Andrzej A.
Kucharski

Electromagnetic Scattering by Dielectric Bodies

Oficyna Wydawnicza
Politechniki Wrocławskiej

Scientific Papers of the Institute of Telecommunications and Acoustics
No. 82 of the Wrocław University of Technology No. 82

Monographs No. 43 2001

Andrzej A. KUCHARSKI

Electromagnetic Scattering by Dielectric Bodies

Prace Naukowe Instytutu Telekomunikacji i Akustyki
Politechniki Wrocławskiej 82

Seria:
Monografie 43

Andrzej A. Kucharski

Electromagnetic Scattering by Dielectric Bodies

Oficyna Wydawnicza Politechniki Wrocławskiej · Wrocław 2001

Opiniodawcy
Daniel Józef BEM
Ryszard KATULSKI

Opracowanie redakcyjne i korekta
Halina MARCINIAK

OFICYNA WYDAWNICZA POLITECHNIKI WROCŁAWSKIEJ
Wybrzeże Wyspiańskiego 27, 50-370 Wrocław

ISSN 0324-9328

Drukarnia Oficyny Wydawniczej Politechniki Wrocławskiej. Zam. nr 519/2001.

Contents

Prace Naukowe Instytutu Telekomunikacji i Akustyki
Nr 82 Politechniki Wrocławskiej Nr 82
Monografie Nr 43 2001

Electromagnetic scattering,
dielectric bodies,
integral equations,
moment methods,
multilayer media

Andrzej A. KUCHARSKI*

Electromagnetic scattering by dielectric bodies

Two basic integral-equation formulations for scattering by dielectric bodies are discussed: the surface integral equation and the volume integral equation. Special attention is given to the problem of scattering by dielectrics in a multilayer environment, which is important in a variety of contemporary microwave applications. A new formulation for inhomogeneous bodies with rotational symmetry is introduced both for the case of free-space and for layered media. A new type of divergenceless basis functions is developed for this formulation, which together with the mixed-potential integral-equation technique considerably enhances the algorithm efficiency. New formulas for modal decomposition of incident plane wave fields and far-field approximations are also stated for the multilayer environment. The methods presented are validated through a great number of examples concerning scattering, radiation as well as resonance problems. Example applications of the methods are also outlined.

* Institute of Telecommunications and Acoustics, Wrocław University of Technology, Wybrzeże Wyspiańskiego 27, 50-370 Wrocław, Poland.

Major notations

$\boldsymbol{A}$ – magnetic vector potential,
A, B – auxiliary coefficients in vector potential kernel expressed in polar coordinate system,
C^{Φ} – correction factor,
C^{Φ} – correction term,
$\boldsymbol{D}$ – electric flux density, vector of coefficients describing electric flux density,
$\boldsymbol{E}$ – electric field,
$\boldsymbol{F}$ – electric vector potential,
f – frequency,
$f_n(\boldsymbol{r})$ – basis or testing function,
$G^F(\boldsymbol{r}\,|\,\boldsymbol{r}')$ – scalar Green's function for free-space electric vector potential calculations,
$G^A(\boldsymbol{r}\,|\,\boldsymbol{r}')$ – scalar Green's function for free-space magnetic vector potential calculations,
$G(\boldsymbol{r}\,|\,\boldsymbol{r}')$ – scalar Green's function,
G_m – modal Green's function,
$\underline{\underline{\boldsymbol{G}}}^{EJ}(\boldsymbol{r}\,|\,\boldsymbol{r}')$ – dyadic Green's function for calculation of electric field due to electric current,
$\underline{\underline{\boldsymbol{G}}}^{EM}(\boldsymbol{r}\,|\,\boldsymbol{r}')$ – dyadic Green's function for calculation of electric field due to magnetic current,
$\underline{\underline{\boldsymbol{G}}}^{HJ}(\boldsymbol{r}\,|\,\boldsymbol{r}')$ – dyadic Green's function for calculation of magnetic field due to electric current,
$\underline{\underline{\boldsymbol{G}}}^{HM}(\boldsymbol{r}\,|\,\boldsymbol{r}')$ – dyadic Green's function for calculation of magnetic field due to magnetic current,
$\underline{\underline{\boldsymbol{G}}}(\boldsymbol{r}\,|\,\boldsymbol{r}')$ – dyadic Green's function,
$\underline{\underline{\boldsymbol{G}}}^{A}(\boldsymbol{r}\,|\,\boldsymbol{r}')$ – magnetic vector potential dyadic Green's function,
$\underline{\underline{\boldsymbol{G}}}^{F}(\boldsymbol{r}\,|\,\boldsymbol{r}')$ – electric vector potential dyadic Green's function,
$\boldsymbol{g}_{mi}(\rho, z)$ – ρ-type modal basis functions,
$\boldsymbol{h}_{mi}(\rho, z)$ – z-type modal basis functions,
$\boldsymbol{H}$ – magnetic field,
$\boldsymbol{I}$ – vector integral,
$\underline{\underline{\boldsymbol{I}}}$ – unit dyadic,
i^p, v^p – equivalent current and voltage sources in the transmission line model of the layered medium,
$\boldsymbol{J}$ – electric current density,
J_n – Bessel function of the first kind and order n,
$\boldsymbol{K}$ – electric or magnetic current,
$\underline{\underline{\boldsymbol{K}}}^{A}$ – corrected vector potential kernel,
$\underline{\underline{\boldsymbol{K}}}^{A}_{m}$ – modal corrected vector potential kernel,

K^{Φ} – scalar potential kernel,

K_m^{Φ} – modal scalar potential kernel,

$k = \omega\sqrt{\varepsilon\mu} = 2\pi/\lambda$ – wave number,

k_x, k_y – coordinates in the spectral domain,

$\boldsymbol{k}_\rho = \hat{\boldsymbol{x}}k_x + \hat{\boldsymbol{y}}k_y$ – parameter of the two-dimensional Fourier transform,

$k_\rho = \sqrt{k_x^2 + k_y^2}$ – distance from the origin of the coordinate system in spectral domain, integration variable in Sommerfeld integrals,

$k_z = \sqrt{k^2 - k_\rho^2}$ – propagation constant in the equivalent transmission line circuit,

L – generating arc of the rotationally symmetric body,

$L_{tt}^m, L_{tz}^m, L_{zt}^m, L_{zz}^m$ – auxiliary functions in the modal vector potential kernel for multilayer media,

$\boldsymbol{M}$ – magnetic current density,

m – magnetic charge density, or the mode number,

$\hat{\boldsymbol{n}}$ – unit vector normal to the surface,

$\underline{\underline{\boldsymbol{Q}}}$ – rotation matrix in spectral domain,

Q – quality factor,

q – electric charge density,

$\boldsymbol{R} = \boldsymbol{r} - \boldsymbol{r}'$ – vector joining source and observation points,

$\hat{\boldsymbol{R}}$ – unit vector in the direction of $\boldsymbol{R}$,

$\underline{\underline{\boldsymbol{R}}}$ – rotation dyadic in DBOR technique,

R – distance between source and observation points,

R_i – homogeneous region of space,

∂R_i – boundary of R_i,

r – distance to the far-field observation point,

$\hat{\boldsymbol{r}}, \hat{\boldsymbol{\theta}}, \hat{\boldsymbol{\varphi}}$ – unit vectors in spherical coordinate system,

(r, θ, ϕ) – coordinates in spherical coordinate system,

$\boldsymbol{r}, \boldsymbol{r}'$ – observation and source point vectors,

$\boldsymbol{S}$ – impedance matrix,

S – surface of the body of interest,

$\boldsymbol{S_m}$ – impedance matrix for mode m,

S_{ij} – surface boundary between regions i and j,

$S_n\{\ \}$ – Sommerfeld integral,

T – transverse plane of the rotationally symmetric body,

(u, v, z) – coordinates in the rotated spectrum-domain coordinate system,

$\hat{\boldsymbol{u}}, \hat{\boldsymbol{v}}, \hat{\boldsymbol{z}}$ – unit vectors in the rotated spectrum-domain coordinate system,

V – volume of the body of interest,

V^p, I^p – voltage and current in the equivalent transmission line circuit,

$V_i^p, V_v^p, I_i^p, I_v^p$ – transmission-line Green's functions,

(x, y, z) – coordinates in Cartesian coordinate system,

$\hat{\boldsymbol{x}}, \hat{\boldsymbol{y}}, \hat{\boldsymbol{z}}$ – unit vectors in Cartesian coordinate system,

Z^p, Y^p – impedance and admittance of the equivalent transmission line circuit,

ε – dielectric permittivity,

ε_r – relative dielectric permittivity,

Φ – electric scalar potential,

$\underline{\underline{\Gamma}}$ – vector potential kernel in azimuthal coordinates,

$\underline{\underline{\Gamma}}_m$ – modal vector potential kernel,

$\eta = \sqrt{\mu / \varepsilon}$ – medium intrinsic impedance,

$\Im_{mv}\{\ \}$ – modal Sommerfeld integral,

κ – contrast ratio,

λ – wavelength,

μ – magnetic permeability,

$\hat{\rho}, \hat{z}, \hat{\varphi}$ – unit vectors in polar coordinate system,

(ρ, z, ϕ) – coordinates in polar coordinate system,

σ – conductivity,

σ_e – surface electric charge density,

$\sigma\left(\hat{r}, \hat{k}\right)$ – radar cross-section,

$\omega = 2\pi f$ – angular frequency,

ξ – rotation angle of the coordinate system in the spectral domain,

Ψ – magnetic scalar potential,

(ς, z, φ) – coordinates in the polar coordinate system associated with the source point.

Abbreviations and acronyms

ABC – Absorbing Boundary Condition
BEM – Boundary Element Method
BOR – Body of Revolution
CDR – Cylindrical Dielectric Resonator
CFIE – Combined Field Integral Equation
CGM – Conjugate Gradient Method
DBOR – Discrete Body of Revolution
DCIM – Discrete Complex Image Method
DGF – Dyadic Green's Function
DR – Dielectric Resonator
DRA – Dielectric Resonator Antenna
EBC – Extended Boundary Condition
EFIE – Electric Field Integral Equation
FD-TD – Finite Differences Time Domain
FEM – Finite Element Method
FFT – Fast Fourier Transform
FIA – Finite Integration Algorithm
GMT – Generalized Multipole Technique
HEM – Hybrid Electro-Magnetic
IBC – Impedance Boundary Condition
MBC – Magnetically Conducting Sheet Boundary Condition
MFIE – Magnetic Field Integral Equation
MIC – Microwave Integrated Circuit
MM – Mode Matching
MMP – Multiple Multipoles
MoM – Method-of-Moments
MPIE – Mixed Potential Integral Equation
PEC – Perfect Electric Conductor
POFM – Pencil-Of-Function Method
RBC – Resistive Sheet Boundary Condition
RCS – Radar Cross-Section
SIE – Surface Integral Equation
TE – Transverse Electric
TLGF – Transmission Line Green's Function
TLM – Transmission Line Matrix
TM – Transverse Magnetic
VFT – Vector Fourier Transform
VIE – Volume Integral Equation

Chapter 1. Introduction

1.1. Numerical methods in electromagnetics

The works of Richmond [170, 171, 172] published in the mid-sixties enounced an era of modern computers used to solve problems in the scientific branch called "electromagnetics". Since that time an extraordinary amount of research has been devoted to the development of new methods and computer codes allowing us to solve more or less specific topics arising when solving Maxwell's equations according to the given boundary and initial conditions [165, 213].

Earlier software was written with strong limitations of computer power in mind, which resulted in much "preprocessing" work concerning analytical developments, going on as far as possible for the given types of problems and applying a numerical method at the last stage of the solution process. Among the techniques dealing with radiation and scattering problems special attention should be given to the method-of-moments (MoM) introduced by Harrington [61]. This method of solving partial integro-differential equations has been successfully applied both in frequency and time domains, for solving problems concerning so-called perfect electric conductors (PECs): wires, thin plates or solid bodies [42, 85, 124, 125, 160, 161, 168, 170], non-perfect conductors [131, 148] and homogeneous [42, 123, 197, 217], partially homogeneous [93, 128, 130, 181] or inhomogeneous [25, 55, 54, 178, 195] material bodies. The method-of-moments is usually used in conjunction with integral equation techniques [58, 61, 59] because of their "global" nature, which among other features, results in a particularly easy incorporation into the solution of the "radiation conditions", i.e., dealing with problems arising when the spatial analysis domain is unbounded. It should be noted that the term "method-of-moments" in its generalized sense [118, 208] is used for a wide class of methods which are known under other names because of historical reasons. Representative examples [12, 68, 208] include the boundary element method (BEM), the mode matching (MM) method, the multiple multipoles (MMP) method or Rumsey's reaction method [173] as well as iterative solutions like the conjugate gradient method (CGM) [208].

The other class of techniques called variational methods has been adapted to electromagnetic field solutions from mechanical engineering. Among those methods, an extremely important role is played by the finite element method (FEM). An interesting point is that the final FEM procedure can also be obtained through the use of the moments method applied to equations with differential operators [47, 146], instead of the classical approach of finding and minimizing a certain proper expression [68]. An important feature of FEM is that the final step of this method includes an inversion of a matrix that can be referred to as "sparse" [68] (contrary to MoM where matrices are "dense") for which a set of very efficient algorithms has been developed.

The fascinating growth of computational power of contemporary computer systems resulted in the development of numerical methods reducing to a minimum the "analytical" portion of the work, starting instead with the discrete approximation of Maxwell's equations. The leaders in this area include the finite-differences time-domain (FD-TD) method, the transmission line matrix (TLM) method or the finite integration algorithm (FIA). In those techniques, the research effort concentrates on incorporating original approaches for various types of the geometry investigated, such as thin wires, edges and strips [34, 158, 167, 38], the exact representation of complicated shapes [38, 53], breaking up larger problems into smaller ones [157], etc.

An important feature of all techniques where a part of space is "digitized" into some sort of a mesh structure is the "local" character of (usually differential) operators involved. It makes these methods particularly well suited for dealing with highly inhomogeneous problems with well-defined boundary conditions, for example, closed configurations of microwave circuits or electromagnetic compatibility testing devices. In order to model open structures one must define an artificial boundary for which some kind of local absorbing boundary conditions (ABCs) is applied [12, 65, 68]. A promising alternative is to apply global boundary conditions, which results in a number of hybrid techniques [9, 14], where "mesh" techniques are used for solving the internal problem, whilst an integral equation method is used for the transition into an unbounded region. It should also be noticed that "mesh" methods as "purely" numerical ones, generally often sacrifice the knowledge of physical phenomena associated with the analyzed structures. It is well known that the analytical or semi-analytical solutions give information about a whole set of similar situations, whilst with the numerical methods, the resulting solution pertains only to one particular problem and therefore any generalizations are rather difficult. It is also a rather trivial statement that computer resources needed for solving a given problem based on the full general code resulting from a direct approximation of Maxwell's equations are usually a few magnitudes greater than the resources needed for more specialized programs. The difference in the calculation time can be as much as weeks or months as compared to minutes. Considering this, such methods are sometimes referred to as "brute force" as opposed to more sophisticated however much less general techniques.

1.2. Problems concerning dielectric bodies

Interaction of electromagnetic fields with dielectric bodies has been in the focus of attention almost since the first numerical methods were developed. The problems of interest can be subdivided into two independent types. First, we investigate material bodies, which can be considered as rather small "islands" of matter existing in surrounding space for which analytical field solutions (in the absence of a body) are known, a typical example here being the "free space". Such situations are encountered when investigating scattering by dielectrics in antenna problems [84, 149], propagation through rainy regions or other hydrometeors [163], field interactions with human body [164], radar science [74], waveguide techniques [206], and many others. On the other hand, similar phenomena are considered when dealing with resonators in microwave integrated circuits (MICs) [52, 149], or more recently in dielectric resonator antennas (DRAs) [117]. Problems of the second type include cases where dielectrics cannot be considered as "small regions", or when material parts constitute an "environment" for other more specific problems. Examples of such situations are dielectric half-space (realistic ground) problems in antenna theory [85, 188], microstrip antennas [155, 159] or layered dielectric configurations in closed or opened waveguide problems [174]. Both kinds of the problems mentioned will be addressed here, however two general assumptions are made throughout the monograph. First, we focus our attention only on purely dielectric isotropic bodies, although some of the concepts presented can also be easily extended to other classes, of which issues concerning both dielectrics and conductors are of particular interest. Second, the situations under consideration are thought of as "three-dimensional", whilst we bear in mind a wide class of "two-dimensional" solutions, which are especially useful in microwave applications [174]. The latter assumption results mainly from the author's key interest in a wide class of "antenna problems" and, on the other hand, it also imposes a logical boundary on the scope of the study.

A great number of methods for solving the scattering problems have been developed [57, 147, 208]. As mentioned in the previous section, special attention is usually given to techniques which use the method-of-moments (MoM) as the solution scheme [61], or more recently, the hybrid techniques [9, 13, 14, 30, 31, 36, 47], which apply the MoM to properly model radiation condition at the boundary of a dielectric region and another technique, such as the finite element method to model fields inside that region. The MoM solutions have been developed for various dielectric bodies including: homogeneous [42, 89, 123, 197], partially homogeneous [48, 128, 130, 181, 182], or heterogeneous [116, 178, 191, 192, 195, 209] ones. In three-dimensional models, the number of unknowns in the matrix equation is usually very large. In order to overcome this, researchers often take advantage of certain symmetries characteristic of the given classes of objects in order to reduce the total number of unknowns.

Among the techniques of interest, the case of bodies of revolution (BOR) plays an important role [6, 42, 125, 128]. As to the methods developed for BORs some of them pertain to homogeneous bodies [40, 42, 123], whilst others to inhomogeneous ones [48, 130]. However, most of these methods rely on surface currents in order to satisfy the boundary conditions. This leads to serious computational problems, when a great number of very small homogeneous parts have to be treated in a model. This is particularly true when one wants to model objects with a continuously varying dielectric constant. Up to now, mainly hybrid methods mentioned earlier are suitable enough for solving such problems, which usually seriously complicates the solution scheme.

Recently, the works of Viola [200, 201] have given a theoretical background for efficient modeling of highly heterogeneous BORs using the MoM techniques. Electric field integral equations (EFIEs) presented in [200, 201] are characteristic in that differential operators do not affect the field components, which enables the application of a simple expansion scheme (pulse basis functions). However, the above can only be done when we assume that the dielectric constant ε_r is a well-behaved (continuously differentiable) function of position. In fact, it means that incorporating for example step discontinuities in the permittivity profiles requires that additional surface integrals should be taken into account [203].

Of the problems with more complex environments, the case of multilayer, laterally infinite media with vertical stratification is of particular interest. Up to now most techniques have been developed for conductive bodies [137, 141] and only a few solutions deal with dielectrics [40, 41, 36, 74]. As will be shown later on, ideas particularly useful for generalization in the case of dielectric bodies embedded in stratified media can be attributed to Michalski and co-workers [134, 135, 140, 141, 142], because of their natural treatment of current sources oriented arbitrarily in space.

As already mentioned, the problem of electromagnetic scattering by the material bodies is closely related to the problem of *internal resonance*. This resonance causes rapid changes of the scattering parameters of the given body at discrete frequencies (called resonant frequencies). This fact is widely used in the *dielectric resonators* (DRs), which are commonly applied to microwave circuits because of their low cost, small size and temperature stability. In recent years, they have also been often utilized as so-called resonant dielectric cavity antennas (DRAs – Dielectric Resonator Antennas) [37, 77, 78, 79, 88, 92, 109, 112, 117, 127, 187]. Although most of the practical solutions are devoted to homogeneous resonator structures, recent efforts have also been directed towards inhomogeneous ones, mainly because of the search for bandwidth enhancement techniques. Example applications of heterogeneous configurations comprise stacked resonators [91, 119], resonators with an air gap [180], or dielectric-coated DRs [26, 216].

A number of analysis methods for dielectric resonators have been proposed in literature, most of them concerning isolated structures, bodies placed on PEC ground or shielded resonators [32, 44, 52, 72, 80, 81, 97, 145, 149, 196, 223]. Considering the

subject of this monograph it is interesting to state that the solutions are often based on scattering methods, which stems from the resonance definition describing this phenomenon as the existence of non-zero field solutions (*resonant modes*) when no incident fields are present [83, p. 269], [93]. However, again there is much interest in the analysis of resonators placed in a more general multilayer environment. Furthermore, the current state of the art in the area of inhomogeneous structure modeling is in the author's opinion far from being satisfactory.

* * *

The monograph is organized as follows: first, general concepts useful in modeling the various types of dielectric bodies are presented and discussed, assuming that field solutions for an "empty" environment surrounding the body are available (Chapter 2). Next, in Chapter 3 we address the method based on the concept of Green's functions, which is of particular importance considering the solutions put forward. We focus here on two special cases, including a free space environment and multilayer media. Special attention is given to the problem of how to deal with singularities encountered in the equations introduced. Chapter 4 is devoted to an important set of problems pertaining to bodies with rotational symmetry. New original equations for analyzing such structures are also introduced. In Chapter 5, we discuss the methods for solving integral equations given in the preceding sections.

Chapters 6 and 7 provide formulas needed for scattering calculations, i.e., we discuss plane wave impressed fields and far-field approximations. Chapter 8 gives a number of computational examples, which validate techniques developed by the author, concerning both scattering and resonator problems. Chapter 9 presents the conclusions.

Other aspects not essential for understanding the main part of this monograph, but necessary for the sake of completeness of the numerical methods presented, are grouped in the Appendices. The $e^{j\omega t}$ time dependence is assumed throughout the monograph and has been suppressed.

It should be noted that the author's essential contribution has been included in Chapters 4–8 and is devoted mainly to scattering by dielectric bodies-of-revolution. Chapters 2 and 3, although incorporating some original ideas, can be treated as a general background introducing concepts developed further on. However, it has to be stated that although BOR geometries may be considered as special cases of three-dimensional (3D) bodies, the BOR solutions theory is based on full 3D formulas. In other words, the correctness of (more sophisticated) BOR methods proves also the correctness of the underlying 3D formulas.

Some parts of the material presented in this monograph have been adapted (with permission) from author's papers appearing in, or submitted to *IEEE Transactions on Microwave Theory and Techniques*, *IEEE Transactions on Antennas and Propagation*

(ref. [104, 105, 107], © 2000, 2001 IEEE). Some other fragments are written based on author's papers printed in *Microwave and Optical Technology Letters* (ref. [100, 101, 103], © 1999, 2000 John Wiley&Sons) and submitted to *Electronics and Telecommunications Quarterly* (ref. [106]). All adapted sections, plots and tables are properly referenced in the text.

Chapter 2. Integral equation formulations for scattering by dielectrics

Consider an arbitrarily shaped dielectric body embedded in an environment, for which explicit formulas relating elementary, infinitesimal sources to electric and magnetic fields (Green's functions) are known (Fig. 2.1). Examples of such environments examined in the present study include free-space and multilayer media (see Chapter 3).

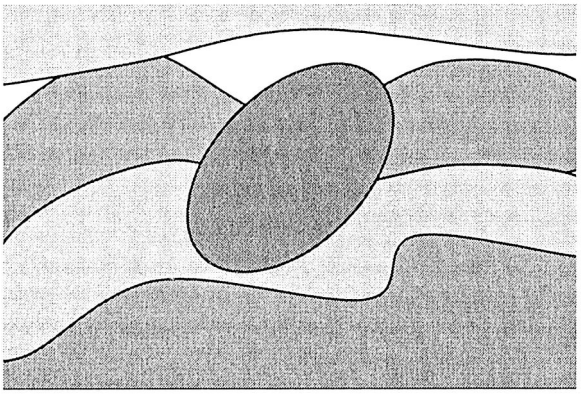

Fig. 2.1. Dielectric body (shown in dark gray) embedded in the general "environment"

The fields within the whole area of interest (including the body) are excited by known electric and magnetic currents ($\boldsymbol{J}^i$, $\boldsymbol{M}^i$). In the absence of dielectric body, the said sources produce so-called *incident* or *impressed* fields ($\boldsymbol{E}^i$, $\boldsymbol{H}^i$) within the environment. The scattering phenomena can be described using the *equivalence principles* [62], which allow the body (scatterer) to be replaced with a system of (equivalent) electric and/or magnetic currents ($\boldsymbol{J}$, $\boldsymbol{M}$) radiating in the unperturbed medium. Those additional sources produce *scattered* fields ($\boldsymbol{E}^s$, $\boldsymbol{H}^s$), which together with incident fields give correct *total* fields in the region of interest ($\boldsymbol{E}$, $\boldsymbol{H}$) = ($\boldsymbol{E}^i + \boldsymbol{E}^s$, $\boldsymbol{H}^i + \boldsymbol{H}^s$). Formulas relating scattered fields to their sources, along with the correctly set boundary conditions define a number of integro-differential equations, which can be solved using numerical methods, pro-

vided that they form a complete and unique description of the situation analyzed [61, 62]. In this chapter, we shall consider two general applications of the equivalence principle: the first one traditionally employed for homogeneous (or partially homogeneous) bodies using fictitious surface currents, and the second one applicable to heterogeneous bodies and using volume (polarization) currents. The idea of the equivalence principles has been described in detail by Harrington [62]. In general, it states that the various configurations of sources can give the same fields inside a given region.

2.1. Equivalence principle for homogeneous material bodies

In this section, we will consider a set of problems which can be solved using surface electric and/or magnetic currents. Typical situations are illustrated in Fig. 2.2. Figure (a), presenting a homogeneous body in a homogeneous space, can be recognized as an example widely described in literature [42, 123, 166, 197]. Figure (b),

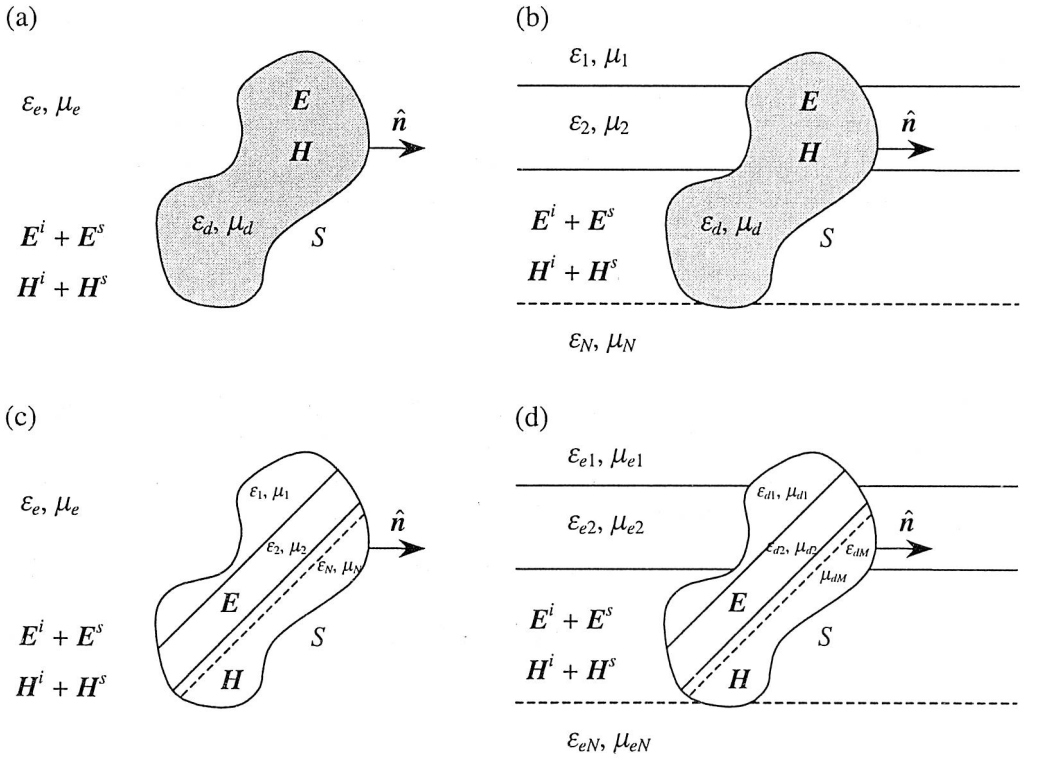

Fig. 2.2. Example problems solvable using the equivalent surface currents

showing a homogeneous body in a layered environment, differs from (a) only in formulas relating equivalent currents and the "scattered" fields [140]. Problems illustrated in figures (c) and (d) do not seem at first glance to belong to situations concerning "homogeneous" bodies. However, in (c) the situation is dual to example (b), which means that we can consider the outer space as an infinite homogeneous "body" immersed in the layered medium. Another interpretation, suitable also for (d), is that we can replace the word "homogeneous" by the statement "filled with a medium for which relations between sources and fields are known". With this in mind and referring to Fig. 2.2, we can now provide a more detailed description of the *surface* equivalence principle and show how to obtain integral equations for such problems. In order to keep things simple, we will remain within the "homogeneous" case of Fig. 2.2(a), however the subsequent analysis can be used without modification for the other situations mentioned.

2.1.1. Internal and external problems

The problem that we would like to solve is to find electric and magnetic field values everywhere throughout a given space, including the interior of the body. To this end, we can replace the original problem of Fig. 2.2(a) with two equivalent problems[*)]: one in which the external fields, sources and medium remain unchanged, whilst we fill the internal space with the external medium and place there some convenient fields distribution (Fig. 2.3(a)). To maintain those fields we must introduce surface currents $\boldsymbol{J}^a$ and $\boldsymbol{M}^a$ flowing on the surface S according to equations [62]:

$$\boldsymbol{J}^a = \hat{\boldsymbol{n}} \times \left(\boldsymbol{H}^s - \boldsymbol{H}^a \right), \tag{2.1}$$

$$\boldsymbol{M}^a = \left(\boldsymbol{E}^s - \boldsymbol{E}^a \right) \times \hat{\boldsymbol{n}} . \tag{2.2}$$

Then we construct a second situation (Fig. 2.3(b)) in which we fill the outer region with the medium from inner region and postulate the external fields distribution, whilst we leave the correct fields inside the body. Of course, another pair of electric and magnetic currents is needed to maintain this situation:

$$\boldsymbol{J}^b = \hat{\boldsymbol{n}} \times \left(\boldsymbol{H}^b - \boldsymbol{H} \right), \tag{2.3}$$

$$\boldsymbol{M}^b = \left(\boldsymbol{E}^b - \boldsymbol{E} \right) \times \hat{\boldsymbol{n}} . \tag{2.4}$$

[*)] In this work we prefer so-called *field formulations*, in contrast to equivalent *source formulations* [60].

Two things should be stressed at this point. First, the number of equivalent problems (both external and internal) is infinite*), because we can postulate arbitrary "artificial" fields to formulate the equations. Second, fictitious equivalent currents radiate in "homogeneous" (in the sense described above) media, which allows application of known formulas for the calculation of fields resulting from the given sources.

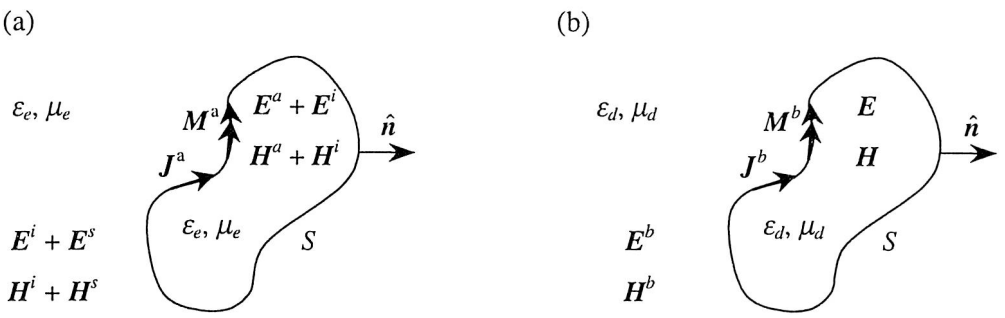

Fig. 2.3. Problems equivalent to the original problem in Fig. 2.2(a).
(a) External equivalence. (b) Internal equivalence

2.1.2. Formulation of integral equations

As indicated in the preceding paragraph, various problem formulations are possible depending on the choice of supporting fields. The most common choice is to assume a zero total field inside the body contour for the external equivalent problem and a zero field outside the body for the internal equivalent problem. In this case, we have:

$$\boldsymbol{E}^a = -\boldsymbol{E}^i, \quad \boldsymbol{H}^a = -\boldsymbol{H}^i, \tag{2.5}$$

$$\boldsymbol{E}^b = 0, \quad \boldsymbol{H}^b = 0. \tag{2.6}$$

Taking into account the boundary conditions in the original problem:

$$\hat{\boldsymbol{n}} \times \boldsymbol{E} = \hat{\boldsymbol{n}} \times \left(\boldsymbol{E}^i + \boldsymbol{E}^s\right), \tag{2.7}$$

$$\hat{\boldsymbol{n}} \times \boldsymbol{H} = \hat{\boldsymbol{n}} \times \left(\boldsymbol{H}^i + \boldsymbol{H}^s\right), \tag{2.8}$$

*) A review of the most popular approaches is given by Harrington [60].

as well as relations (2.1)–(2.4) we can find that in this case the currents for the external equivalent problem are negatives of those for the internal equivalent problem [123, 140]:

$$\boldsymbol{J}^a = -\boldsymbol{J}^b, \qquad \boldsymbol{M}^a = -\boldsymbol{M}^b. \tag{2.9}$$

Therefore, it is sufficient to determine the two current distributions on the body surface S in order to find the electromagnetic fields in the entire space.

The integral equations relating unknown current distributions to incident fields and object geometry can be obtained from boundary conditions associated with the two equivalent problems.

Thus, based on the external equivalent problem we obtain:

$$\boldsymbol{J} = \hat{\boldsymbol{n}} \times \left(\boldsymbol{H}^s(\boldsymbol{J}, \boldsymbol{M}) + \boldsymbol{H}^i\right)_{S+}, \tag{2.10}$$

$$\boldsymbol{M} = -\hat{\boldsymbol{n}} \times \left(\boldsymbol{E}^s(\boldsymbol{J}, \boldsymbol{M}) + \boldsymbol{E}^i\right)_{S+}, \tag{2.11}$$

whilst based on the internal problem:

$$\boldsymbol{J} = \hat{\boldsymbol{n}} \times \boldsymbol{H}(-\boldsymbol{J}, -\boldsymbol{M})_{S-}, \tag{2.12}$$

$$\boldsymbol{M} = -\hat{\boldsymbol{n}} \times \boldsymbol{E}(-\boldsymbol{J}, -\boldsymbol{M})_{S-}, \tag{2.13}$$

where we suppressed the superscript "a" from $\boldsymbol{J}$ and $\boldsymbol{M}$. Subscripts $S+$ and $S-$ indicate that the fields are evaluated as the observation point approaches S from the exterior and interior regions, respectively.

We can see that for two unknown currents we have obtained a set of four equations. The usual methods of equation solving apply when the number of equations is equal to the number of unknowns [123]. The number of equations can be reduced by forming the linear combinations of (2.10) with (2.12) and (2.11) with (2.13). The typical choice [7, 42, 123, 166, 197] is a pair of equations also resulting from continuity of tangential field components in the original problem:

$$\hat{\boldsymbol{n}} \times \boldsymbol{H}(-\boldsymbol{J}, -\boldsymbol{M})_{S-} = \hat{\boldsymbol{n}} \times \left(\boldsymbol{H}^s(\boldsymbol{J}, \boldsymbol{M}) + \boldsymbol{H}^i\right)_{S+}, \tag{2.14}$$

$$\hat{\boldsymbol{n}} \times \boldsymbol{E}(-\boldsymbol{J}, -\boldsymbol{M})_{S-} = \hat{\boldsymbol{n}} \times \left(\boldsymbol{E}^s(\boldsymbol{J}, \boldsymbol{M}) + \boldsymbol{E}^i\right)_{S+}, \tag{2.15}$$

however other possibilities have been considered as well [123, 156] (see also the last paragraph of section 3.2.1.1.). Let us remember that fields on the left sides of (2.14) and (2.15) are calculated for currents radiating in space filled with "internal" medium, whilst fields on the right sides of the equations are for currents radiating in space filled with "external" medium.

The linear combinations like the above set are often referred to as combined field integral equations (CFIE) because they involve calculation of both electric and magnetic fields resulting from equivalent sources [60, 197].

Another possible choice for supporting fields is that the tangential electric field components on the surface S match for both situations*):

$$\hat{\boldsymbol{n}}\times\boldsymbol{E}^a=\hat{\boldsymbol{n}}\times\boldsymbol{E}^s, \tag{2.16}$$

$$\hat{\boldsymbol{n}}\times\boldsymbol{E}^b=\hat{\boldsymbol{n}}\times\boldsymbol{E}. \tag{2.17}$$

This choice results in the lack of magnetic currents in the formulation. Instead we use two electric currents and based on (2.7)–(2.8) we have:

$$\hat{\boldsymbol{n}}\times\boldsymbol{E}\left(\boldsymbol{J}^b\right)_{S-}=\hat{\boldsymbol{n}}\times\left(\boldsymbol{E}^i+\boldsymbol{E}^s\left(\boldsymbol{J}^a\right)\right)_{S+}, \tag{2.18}$$

$$\hat{\boldsymbol{n}}\times\boldsymbol{H}\left(\boldsymbol{J}^b\right)_{S-}=\hat{\boldsymbol{n}}\times\left(\boldsymbol{H}^i+\boldsymbol{H}^s\left(\boldsymbol{J}^a\right)\right)_{S+}, \tag{2.19}$$

where again $\boldsymbol{J}^a$ and $\boldsymbol{J}^b$ radiate in a space filled with external and internal media, respectively. A useful interpretation of this formulation is that currents flow on different sides of S (Fig. 2.4) and produce correct fields in their respective regions [181].

The drawbacks of formulations using only electric currents is that the choice (2.16)–(2.17) gives a unique solution with the exception of some discrete frequencies for which the body contour forms a resonant cavity [43, 60, 62]. For those frequencies, specification of the tangential magnetic field components on S is needed in order to uniquely determine the solution. Instead, we obtain some simplifications of the computational routines.

An interesting approach alternative to the above method has been introduced by Marx [121] and defined using common notation by Glisson [43]. In this approach the continuity of tangential electric field components resulting in the absence of the magnetic current is assumed for the external equivalent problem, whilst zero fields are assumed for the internal equivalent problem in the exterior region. As a result, we obtain a single surface integral equation for a single electric current. This electric current solution produces the correct scattered electric and magnetic fields external to the body. Again, the presented solution suffers non-uniqueness at discrete frequencies corresponding to the resonant frequencies of the perfectly conducting cavity formed by the surface S. A solution to this problem has been given by Mautz [126], who proposed using so-called combined sources [122] instead of simple electric current distribution. The Marx–Glisson approach outlined in this paragraph is however not popular because its generalization for cases of bodies consisting of a number of homogeneous regions (see section 2.1.3) is not obvious. Another similar formulation, as well as example application of a single-current approach can be found in [222].

In all of the above formulations, we assumed that (equivalent) current distributions are associated with the body surface S. However, it can be shown [111] that under certain assumptions, sources distributed on some artificial mathematical surface can

*) This choice is equivalent to the *electric current formulation* given in [60], based on the *source formulation*.

also be used to produce the correct fields in the region of interest. In particular, it is possible to use currents flowing on the surface enclosed within S producing the correct fields in the region exterior to S and currents flowing on the surface outside S, which produce correct fields in the interior region (Fig. 2.4).

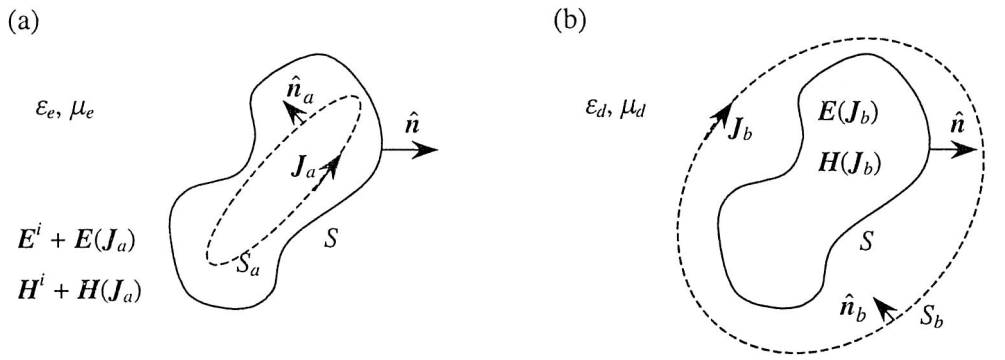

Fig. 2.4. The use of auxiliary mathematical surfaces.
(a) External equivalence. (b) Internal equivalence

Obviously, such sources also produce some fields in regions between the mathematical surface and S. Those fields are understood in terms of the analytical continuation [111] of the true fields, and the existence of the solution is related to the analytic continuity of the scattered field towards the interior region and the internal field towards the exterior region. One can notice that a similar approach is well known from a class of methods concerning thin-wire metal scatterers where we postulate that one-dimensional current flowing along the wire's axis produces correct fields at the surface and outside of it. The advantage of this approach as compared to the classical ones presented earlier is that it is possible to apply simple source distribution over the mathematical surfaces (for example, pulse functions), whilst correct smooth fields in the vicinity of S are obtained. This also enables application of simple testing schemes such as point matching. Note that because the sources are no longer positioned at surfaces where boundary conditions are enforced, there is no need to calculate the fields in source regions. Thus, we do not have to worry about possible singularities present in the equation kernels (see Chapters 3 and 5). On the other hand, if the surface S is not smooth, i.e., incorporates some edges or vertices, this method will fail, because a sum of smooth fields produced at some distance by simple impulsive sources is not well suited for representing singular fields. Also the correct choice and approximation of the auxiliary mathematical surfaces requires that the user should have some experience and in fact can only be judged afterwards based of the boundary conditions check.

We should note that subdividing and collapsing the mathematical surfaces into point sources of the field, leads to another class of methods, such as the T-matrix method [189] or the Generalized Multipole Technique (GMT) [68]. In those techniques field expansions rather than source expansions are used. Consequently, one has to find the number, locations and amplitudes of some auxiliary sources producing fields satisfying the given boundary conditions on S. These methods are also best suited for dealing with bodies with smooth surfaces [68, 110].

The approach that is in some sense dual to the idea of moving sources away from the body surface is the Extended Boundary Condition (EBC)*) method in which the observation points are not situated on S [3].

We also have to mention a wide class of methods developed for imperfectly conducting scatterers, where instead of a detailed investigation of material properties and boundary conditions at the surface, approximate impedance (Leontovich) boundary conditions (IBCs) are imposed onto the electromagnetic fields [148]. It should be noted that in this case the integral equations applied are similar to those applicable for perfect electric conductors, so we can find solutions based on the magnetic field integral equation (MFIE), the electric field integral equation (EFIE) or the above-mentioned combined field integral equation (CFIE). Anyone further interested in this subject should read the especially well written paper contributed by Medgyesi-Mitschang and Putnam [131], where also other similar boundary conditions, such as resistive sheet (RBC) or magnetically conducting sheet (MBC), are investigated.

2.1.3. Partially homogeneous bodies

Although homogeneous dielectric bodies are of interest in many practical cases, there are many problems in which we are interested in electromagnetic scattering by inhomogeneous bodies. The simplest case pertains to scattering by a body comprising a number of homogeneous regions [48, 130].

An example of the said situation is shown in Fig. 2.5, where the scatterer consists of two homogeneous regions. To analyze the problem we can apply again the equivalence principle. As an example, let us use a procedure that is a generalization of the first approach from the preceding section.

We can define three equivalent situations associated with each of the regions R_i ($i = 0, 1, 2$) involved (Fig. 2.6).

*) There is some inconsistency concerning this term in literature. Sometimes the name "EBC" method is used as a synonym for the T-matrix (null-field) method [225].

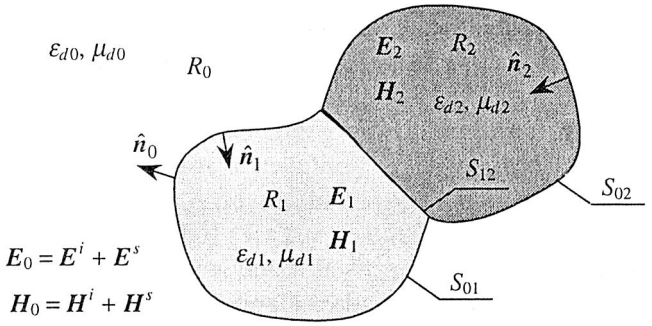

Fig. 2.5. Scattering by a partially homogeneous material body

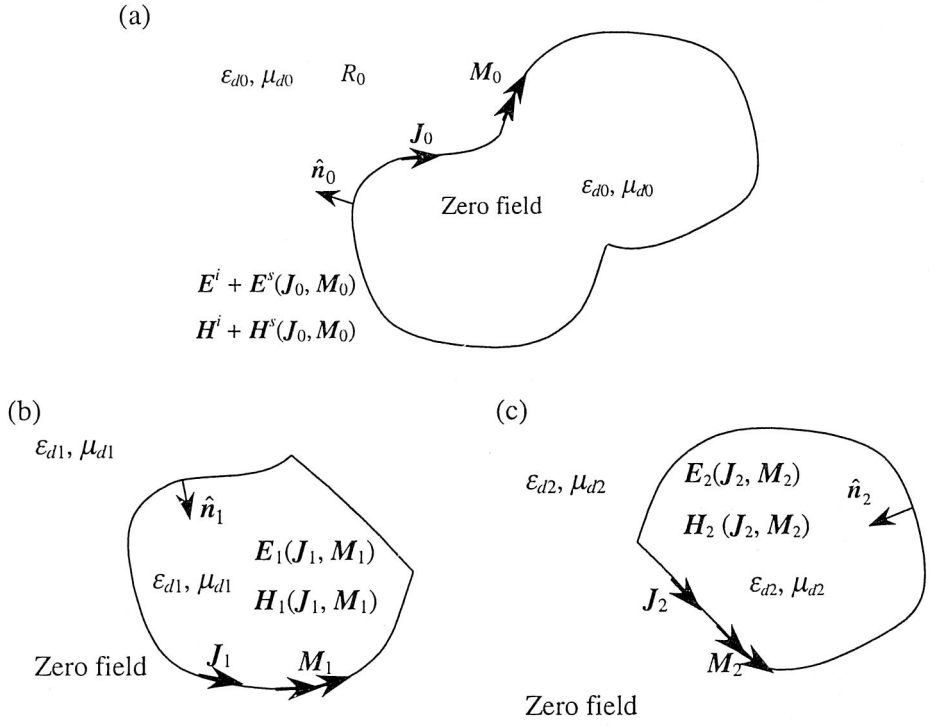

Fig. 2.6. Situations equivalent to the problem of Fig. 2.5.
(a) External equivalence. (b) Equivalence for the region R_1. (c) Equivalence for the region R_2

Let us take $S_{ij} = R_i \cap R_j$, $(i, j = 0,1, \ldots n)$ to denote the surface boundary between regions i and j, $(i \neq j)$, and ∂R_i as the boundary of region R_i, with $\hat{\boldsymbol{n}}_i$ being the surface

normal on ∂R_i, pointing to the region R_i (Fig. 2.5). Of course, $\partial R_i = \bigcup_{i \neq j} S_{ij}$. Similarly to (2.1)–(2.4) or (2.10)–(2.13), we can specify the surface currents as:

$$\boldsymbol{J}_i = \hat{\boldsymbol{n}}_i \times \boldsymbol{H}_i\big|_{\partial R_i}, \qquad \boldsymbol{M}_i = -\hat{\boldsymbol{n}}_i \times \boldsymbol{E}_i\big|_{\partial R_i}. \tag{2.20}$$

Again, based on the continuity of the field tangential components at the media interfaces we have:

$$\left(\hat{\boldsymbol{n}}_i \times \boldsymbol{E}_i + \hat{\boldsymbol{n}}_j \times \boldsymbol{E}_j\right)\Big|_{S_{ij}} = 0, \tag{2.21}$$

$$\left(\hat{\boldsymbol{n}}_i \times \boldsymbol{H}_i + \hat{\boldsymbol{n}}_j \times \boldsymbol{H}_j\right)\Big|_{S_{ij}} = 0. \tag{2.22}$$

Fields in (2.21), (2.22) are produced by current distributions according to equivalent problems associated with each region (Fig. 2.6).

Note that $\left(\hat{\boldsymbol{n}}_i = -\hat{\boldsymbol{n}}_j\right)\Big|_{S_{ij}}$. We can also find that at a given interface S_{ij} we have $\boldsymbol{J}_i\big|_{S_{ij}} = -\boldsymbol{J}_j\big|_{S_{ij}}$ and $\boldsymbol{M}_i\big|_{S_{ij}} = -\boldsymbol{M}_j\big|_{S_{ij}}$, so for each media interface we have two unknown currents and two equations (2.21), (2.22). If our problem consists of k interfaces, we can then form a set of $2k$ equations with $2k$ unknowns. The equations for different S_{ij} interfaces are coupled because tangential fields calculated at each interface "side" are produced by currents flowing on the whole ∂R_i surface of the corresponding region. We can see that as before, the fields associated with region R_i are calculated as the observation point approaches the surface S_{ij} from that region.

Generalizing the solution which involves only electric currents to the case of partially homogeneous bodies is straightforward and can be found in [181, 182].

It is to be noted that using the surface current approach it is relatively easy to model objects which are built of a metal and dielectric combination. For cases like this, we use formulations similar to those presented above for modeling interfaces between dielectrics, while formulations typical of PEC bodies are applied for the metal surfaces*) (free space [69, 90, 93, 128, 129, 130]; layered medium [36]). This approach results in a coupled set of equations relating both equivalent and true currents.

2.2. Inhomogeneous dielectric bodies

As opposed to situations from the previous section, heterogeneous bodies (the ones in which dielectric parameters are in general a function of position) cannot be

*) Including also the so-called thin wire approximation.

modeled using the techniques outlined, because analytic formulas relating fields to their sources (Green's functions) are not available for the interior equivalent problem [140]. Possible solutions to these problems, involving integral equation techniques, are discussed in the following sections.

2.2.1. Volume integral equation

Consider again the general situation presented in Fig. 2.1. This time we assume that the body being evaluated is heterogeneous. We denote the "environment" as region 1 and the body as region 2.

Maxwell's equations for both regions (taking into account the assumed $e^{j\omega t}$ time convention) can be written as:

$$\nabla \times \boldsymbol{E}_1 = -j\omega\mu_1 \boldsymbol{H}_1, \quad \nabla \times \boldsymbol{H}_1 = j\omega\varepsilon_1 \boldsymbol{E}_1, \tag{2.23}$$

for region 1, and

$$\nabla \times \boldsymbol{E}_2 = -j\omega\mu_2 \boldsymbol{H}_2, \quad \nabla \times \boldsymbol{H}_2 = j\omega\varepsilon_2 \boldsymbol{E}_2, \tag{2.24}$$

for region 2.

We note that the field sources in the above equations are outside the region of interest. As stated above, the material parameters of region 2 are the function of position. Let us remember that region 1 does not have to be homogeneous, but we assume that Green's functions (see Chapter 3) for this region are available. We can rewrite equations (2.24) as:

$$\begin{aligned} \nabla \times \boldsymbol{E}_2 &= -j\omega\mu_1 \boldsymbol{H}_2 - j\omega(\mu_2 - \mu_1)\boldsymbol{H}_2, \\ \nabla \times \boldsymbol{H}_2 &= j\omega\varepsilon_1 \boldsymbol{E}_2 + j\omega(\varepsilon_2 - \varepsilon_1)\boldsymbol{E}_2. \end{aligned} \tag{2.25}$$

If we define equivalent volume magnetic and electric currents [62, 166]:

$$\boldsymbol{M} = j\omega(\mu_2 - \mu_1)\boldsymbol{H}_2, \quad \boldsymbol{J} = j\omega(\varepsilon_2 - \varepsilon_1)\boldsymbol{E}_2, \tag{2.26}$$

we can treat the situation as if the whole space were filled with parameters of region 1 and the body volume represented in terms of polarization currents (2.26) radiating in the "homogeneous" environment of region 1. The example situation, in which the region 1 is represented by a multilayer, horizontally stratified environment is shown in Fig. 2.7.

The scattered fields in Fig. 2.7(b) are due to polarization currents $\boldsymbol{J}$ and $\boldsymbol{M}$. We note that in the equivalent situation "scattered" fields are present also in volume V (body interior). We can thus formulate the integral equations:

$$\boldsymbol{E}\big|_V = \left(\boldsymbol{E}^i + \boldsymbol{E}^s(\boldsymbol{J},\boldsymbol{M})\right)\Big|_V = \left(\boldsymbol{E}^i + \boldsymbol{E}^s(\boldsymbol{E},\boldsymbol{H})\right)\Big|_V, \tag{2.27}$$

$$\boldsymbol{H}\big|_V = \left(\boldsymbol{H}^i + \boldsymbol{H}^s(\boldsymbol{J},\boldsymbol{M})\right)\Big|_V = \left(\boldsymbol{H}^i + \boldsymbol{H}^s(\boldsymbol{E},\boldsymbol{H})\right)\Big|_V. \tag{2.28}$$

We have dropped out the subscripts relating fields to their regions above, because the integral equations are specified for the volume V (body interior).

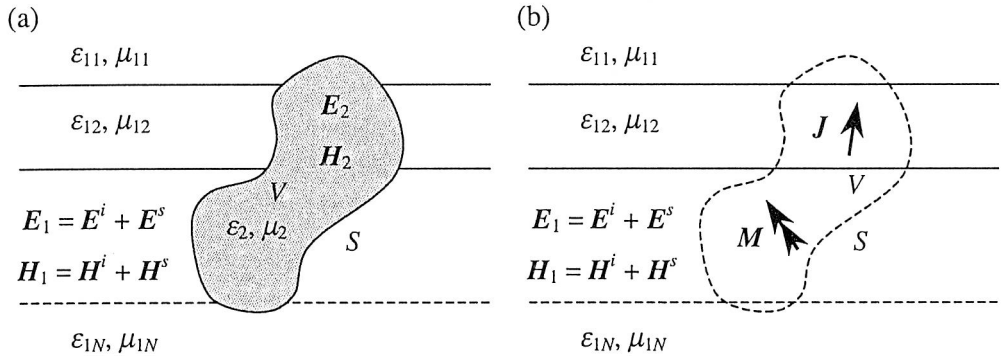

Fig. 2.7. Inhomogeneous body within a layered environment.
(a) Original problem. (b) Equivalent problem

Equations (2.27), (2.28) involve two unknown distributions of vector quantities (electric and magnetic fields or corresponding polarization currents). However, these quantities are generally not independent, as they are related by Maxwell's equations. Therefore, after certain manipulations we can reduce the number of unknowns. Several interesting alternative formulations, developed for the case of free-space environment have been introduced by Volakis [203].

An important case, which is a subject of this work, concerns the situation where the magnetic permeability of the scatterer is the same as that of the surrounding medium. In this instance, the magnetic polarization current disappears and the situation can be described by a single integral equation:

$$\boldsymbol{E}\big|_V = \left(\boldsymbol{E}^i + \boldsymbol{E}^s(\boldsymbol{J})\right)\Big|_V = \left(\boldsymbol{E}^i + \boldsymbol{E}^s(\boldsymbol{E})\right)\Big|_V. \tag{2.29}$$

Equation (2.29) has been extensively applied by several researchers for investigating problems concerning inhomogeneous dielectrics in a free-space environment [25, 54, 55, 169, 172, 178, 195, 200, 201]. Examples of applications of (2.29) for free space and multilayer media will be presented further in this monograph. It is to be noted that although in general equation (2.29) looks simpler than equations presented in section 2.1, the numerical solutions to it are usually more cumbersome because we

have to deal with three-dimensional current distributions and volume integrals. These difficulties can however be greatly reduced if certain symmetries exist, the most important case concerning the so-called bodies-of-revolution (BORs), see Chapters 4 and 5.

2.2.2. Volume-surface integral formulation

If the outer region in the problem considered in the previous section has complex permittivity/permeability distributions (for example, layered media), the volume integrals needed for the electromagnetic field calculations can be very time consuming for general three-dimensional scatterers. An alternative approach enables calculation of the fields in the exterior region using only surface integrals, whilst volume integrals are evaluated only for the homogeneous-space environment [140, 219, 220].

Let us reconsider the situation from Fig. 2.7(a). We can again formulate two equivalent problems using the approach described in section 2.1.2 (Fig. 2.8).

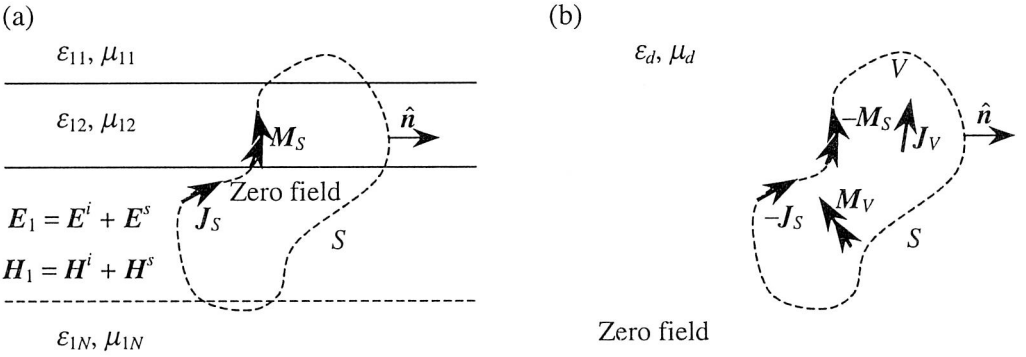

Fig. 2.8. Equivalent problems for inhomogeneous body.
(a) External equivalence. (b) Internal equivalence

For the external problem equivalent currents $\boldsymbol{J}_S$ and $\boldsymbol{M}_S$ defined by (2.10)–(2.11) radiate in the layered environment and produce correct fields outside the body and a zero field inside the contour S. For the interior problem their negatives together with the polarization currents $\boldsymbol{J}_V$ and $\boldsymbol{M}_V$ defined in the preceding section radiate in the homogeneous space and produce a zero field outside and the correct fields inside S. Considering the continuity of tangential field components on S we have the following integral equations:

$$\hat{\boldsymbol{n}} \times \left(\boldsymbol{H}(-\boldsymbol{J}_S, -\boldsymbol{M}_S) + \boldsymbol{H}(\boldsymbol{J}_V, \boldsymbol{M}_V) \right)_{S-} = \hat{\boldsymbol{n}} \times \left(\boldsymbol{H}^s(\boldsymbol{J}_S, \boldsymbol{M}_S) + \boldsymbol{H}^i \right)_{S+}, \qquad (2.30)$$

$$\hat{n}\times\left(E(-J_S,-M_S)+E(J_V,M_V)\right)_{S-}=\hat{n}\times\left(E^s(J_S,M_S)+E^i\right)_{S+},\qquad(2.31)$$

whereas in volume V:

$$E\big|_V=\left(E(-J_S,-M_S)+E(J_V,M_V)\right)\big|_V,\qquad(2.32)$$

$$H\big|_V=\left(H(-J_S,-M_S)+H(J_V,M_V)\right)\big|_V.\qquad(2.33)$$

The relations (2.30)–(2.33) form a set of four equations with four unknowns which can be solved to obtain the unknown surface and volume current distributions. When those currents are known one can easily calculate the fields in the interior and exterior regions.

We can note that when the exterior region is homogeneous (for example, free-space) we can choose the medium parameters for the internal problem*) the same as in the external problem. Taking into account the fact that the surface currents give zero fields inside S and referring to the linearity of field operators, we can prove that for this case

$$E(-J_S,-M_S)\big|_V=E^i\big|_V,\qquad H(-J_S,-M_S)\big|_V=H^i\big|_V.\qquad(2.34)$$

Thus, equations (2.32), (2.33) reduce to (2.27), (2.28), and the surface currents are not needed in the formulation.

The volume-surface integral equation approach utilizing two surface electric currents has been proposed in [219], while the dual method (magnetic surface currents) is applied in [220]. Both methods have been used for modeling the two-dimensional scattering by inhomogeneous cylinders in layered environment. The interesting feature of those formulations is that only one surface current is necessary for the exterior equivalent problem. However, the approach introduced above is expected not to suffer from the problem of internal resonances, when considering general three-dimensional scatterers.

2.2.3. Hybrid integro-differential techniques

An alternative procedure for dealing with electromagnetic scattering by inhomogeneous objects consists in completing the external equivalent problem with differential equations governing the fields for the interior equivalent problem. For example, based on Maxwell's equations, we can easily derive the differential equation for the electric field as:

*) Medium parameters for the interior equivalent problem ε_d, μ_d are somewhat artificial quantities, and usually may be chosen as convenient.

$$\nabla \times \left(\frac{1}{\mu} \nabla \times \boldsymbol{E} \right) = \omega^2 \varepsilon \boldsymbol{E} \,. \tag{2.35}$$

Equation (2.35) or its dual concerning the magnetic field is related to the external problem through the boundary conditions on the body surface S. Thus, we get a set of coupled equations relating the equivalent currents flowing on S, the fields inside the body and the incident fields. Again, various formulations, such as EFIE, MFIE or CFIE are possible. The internal problem differential equation is usually enforced in a "weak" form [30, 66] and subjected to an approximation using a popular Finite Element Method (FEM) [13, 30, 66, 151, 224] although other formulations are possible as well [31]. Using a "hybrid" formulation like this is sometimes interpreted by other researchers dealing with "mesh" methods (FEM, FDTD, TLM) as application of "global" radiation conditions in contrast to many "local" formulations [31]. Most of the achievements so far in the field of hybrid methods pertain to free-space environment, however recent developments also concern layered media [36].

* * *

It should be stated that in all of the cases concerning inhomogeneous dielectrics the body surface S is somewhat "artificial", because the surrounding dielectric parts of the "environment" could often be incorporated into the "body" region as well. Therefore, in many cases the proper choice of S enables a more efficient treatment of the problem. For example, Su [191] in his volume integral formulation assumes without loss of generality that the dielectric body forms an orthorhomboid, Morgan and co-workers [151, 152] use a spherical regions boundary in their unimoment method, while Cwik *et al.* [30] choose S as a surface with rotational symmetry (SOR – Surface-of-revolution) for hybrid FEM/MoM solutions.

At the end of this section, we should mention again the formulations combining the solutions for dielectric bodies with the solutions for perfect electric conductors. There exist solutions using a VIE/SIE approach [175], or hybrid-SIE/SIE formulations [36]. In the former, the VIE is used for the modeling of dielectric bodies, whilst the SIE part is responsible for modeling metal surfaces. In the latter, a hybrid-SIE formulation is related to dielectrics, whereas again the SIE model is used for PECs.

It should be noted that the material presented in this chapter is widely spread in various literature. The author's contribution consists in a systematic treatment of the various formulations outlined. Of particular interest is section 2.2.2 devoted to volume-surface formulations, because even though similar formulations have been described earlier in literature, to the author's knowledge, the formulas introduced herein have never been discussed before.

Chapter 3. Calculation of fields based on the specific current distributions

In the preceding chapter, we have assumed that we can calculate electric and magnetic fields within the analyzed media based on the given electric and magnetic current distributions ($\boldsymbol{J}, \boldsymbol{M}$). The analysis is greatly simplified if we use the superposition rule and evaluate the fields relative to the electric and magnetic currents separately [62, p. 99].

First, let us consider the case where only electric currents are present. We can express the fields in terms of vector and scalar potentials [62]:

$$\boldsymbol{E} = -j\omega \boldsymbol{A} - \nabla \Phi , \tag{3.1}$$

$$\mu \boldsymbol{H} = \nabla \times \boldsymbol{A} .^{*)} \tag{3.2}$$

As equation (3.2) does not specify $\boldsymbol{A}$ uniquely, we can impose an additional condition:

$$\nabla \cdot \boldsymbol{A} = \frac{k^2}{j\omega} \Phi , \tag{3.3}$$

where $k = \omega\sqrt{\varepsilon\mu}$ denotes the wave number.

The relation (3.3) is known as the Lorentz condition. Implementing the above assumption, it can be shown that in homogeneous media[**)] the vector potential (now referred to as the magnetic vector potential) satisfies the inhomogeneous Helmholtz equation:

$$\nabla^2 \boldsymbol{A} + k^2 \boldsymbol{A} = -\mu \boldsymbol{J} . \tag{3.4}$$

Using condition (3.3), we can rewrite (3.1) and (3.2) in terms of the magnetic vector potential:

---

*) Note that in (3.2) the permeability is used as a multiplicative constant on the left-hand side of the equation. This convention follows from the fact that when we consider anisotropic materials media parameters become tensors.

**) The term "homogeneous" does not mean "of infinite extent". The given medium may be homogenous only locally with some boundary conditions defined at the border of this homogeneous region.

$$\boldsymbol{E} = -\frac{j\omega}{k^2}\left(k^2 + \nabla\nabla\right)\boldsymbol{A}\,, \tag{3.5}$$

$$\mu\boldsymbol{H} = \nabla\times\boldsymbol{A}\,. \tag{3.6}$$

Furthermore, if we want to establish the fields produced by the given electrical current distribution, first we have to find the vector potential from (3.4) and then apply (3.5) and (3.6).

The solution of equation (3.4) is usually obtained using the concept of *Green's function* [62] where we replace the general problem of finding $\boldsymbol{A}$ related to $\boldsymbol{J}$ by the problem of finding the potential caused by elementary sources, and then apply the superposition:

$$\boldsymbol{A} = \left\langle \underline{\underline{\boldsymbol{G}}}^{A}; \boldsymbol{J} \right\rangle. \tag{3.7}$$

Following the notation of [140] we use $\langle\ ,\ \rangle$ to denote the integrals of products of two functions separated by a comma over their common spatial base, while a dot over the comma indicates a dot product.

$\underline{\underline{\boldsymbol{G}}}^{A}$ which is the dyadic Green's function (DGF) satisfies the equation:

$$\left(k^2 + \nabla^2\right)\underline{\underline{\boldsymbol{G}}}^{A}(\boldsymbol{r}\,|\,\boldsymbol{r}') = -\mu\underline{\underline{\boldsymbol{I}}}\,\delta(\boldsymbol{r}-\boldsymbol{r}'), \tag{3.8}$$

as well as appropriate boundary conditions which characterize the medium of interest. In the above equation $\boldsymbol{r}$ and $\boldsymbol{r}'$ denote the observation and source points, respectively, whilst $\underline{\underline{\boldsymbol{I}}} = \hat{\boldsymbol{x}}\hat{\boldsymbol{x}} + \hat{\boldsymbol{y}}\hat{\boldsymbol{y}} + \hat{\boldsymbol{z}}\hat{\boldsymbol{z}}$ is the unit dyad*).

Substituting (3.7) into (3.5) and (3.6) we get:

$$\boldsymbol{E} = -\frac{j\omega}{k^2}\left(k^2 + \nabla\nabla\right)\left\langle \underline{\underline{\boldsymbol{G}}}^{A}; \boldsymbol{J} \right\rangle, \tag{3.9}$$

$$\mu\boldsymbol{H} = \nabla\times\left\langle \underline{\underline{\boldsymbol{G}}}^{A}; \boldsymbol{J} \right\rangle. \tag{3.10}$$

The differentiation in (3.9) and (3.10) is usually undesirable when those equations are evaluated numerically in the case of surface or volume current distribution [141]. However, other forms of these relations can be obtained by introducing the differential operators under integral signs. In general, this is possible because the differentiation is performed at the observation point, whilst the integration is performed over the source regions. Thus, we obtain the equations:

---

*) Note that $\underline{\underline{\boldsymbol{G}}}^{A}$ should be understood as the operator acting on the current. Thus, also $\nabla\cdot\underline{\underline{\boldsymbol{G}}}^{A}$ or $\nabla\times\underline{\underline{\boldsymbol{G}}}^{A}$ have to be taken as operators [193, p. 9], [194, p. 121].

$$\boldsymbol{E} = \left\langle -\frac{j\omega}{k^2}\left(k^2 + \nabla\nabla\right)\underline{\underline{\boldsymbol{G}}}^{A}; \boldsymbol{J}\right\rangle, \tag{3.11}$$

$$\mu\boldsymbol{H} = \left\langle \nabla\times\underline{\underline{\boldsymbol{G}}}^{A}; \boldsymbol{J}\right\rangle. \tag{3.12}$$

The case where only magnetic currents are present in the problem formulation can be easily handled by observing the duality of Maxwell's equations [62, p. 98]. Thus, we can express electric and magnetic fields using another pair of vector and scalar potentials:

$$\varepsilon\boldsymbol{E} = -\nabla\times\boldsymbol{F}, \tag{3.13}$$

$$\boldsymbol{H} = -j\omega\boldsymbol{F} - \nabla\Psi. \tag{3.14}$$

Next, we can apply an analysis similar to that presented above and introducing the electric vector potential Green's function $\underline{\underline{\boldsymbol{G}}}^{F}$ related to the elementary magnetic current, arrive at formulas:

$$\varepsilon\boldsymbol{E} = -\left\langle \nabla\times\underline{\underline{\boldsymbol{G}}}^{F}; \boldsymbol{M}\right\rangle, \tag{3.15}$$

$$\boldsymbol{H} = \left\langle -\frac{j\omega}{k^2}\left(k^2 + \nabla\nabla\right)\underline{\underline{\boldsymbol{G}}}^{F}; \boldsymbol{M}\right\rangle. \tag{3.16}$$

When electric and magnetic currents are both present, we can express electric and magnetic fields as:

$$\boldsymbol{E} = -j\omega\boldsymbol{A} - \nabla\Phi - \frac{1}{\varepsilon}\nabla\times\boldsymbol{F}, \tag{3.17}$$

$$\boldsymbol{H} = -j\omega\boldsymbol{F} - \nabla\Psi + \frac{1}{\mu}\nabla\times\boldsymbol{A}. \tag{3.18}$$

Alternatively, after applying the Lorentz conditions:

$$\boldsymbol{E} = -\frac{j\omega}{k^2}\left(k^2 + \nabla\nabla\right)\boldsymbol{A} - \frac{1}{\varepsilon}\nabla\times\boldsymbol{F}, \tag{3.19}$$

$$\boldsymbol{H} = -\frac{j\omega}{k^2}\left(k^2 + \nabla\nabla\right)\boldsymbol{F} + \frac{1}{\mu}\nabla\times\boldsymbol{A}. \tag{3.20}$$

Above, the potentials $\boldsymbol{A}$ and Φ are due to $\boldsymbol{J}$, while $\boldsymbol{F}$ and Ψ are due to $\boldsymbol{M}$.

We can also write the formulas for $\boldsymbol{E}$ and $\boldsymbol{H}$ using *electric* and *magnetic field dyadic Green's functions*:

$$\boldsymbol{E} = \left\langle \underline{\underline{\boldsymbol{G}}}^{EJ}; \boldsymbol{J} \right\rangle + \left\langle \underline{\underline{\boldsymbol{G}}}^{EM}; \boldsymbol{M} \right\rangle, \tag{3.21}$$

$$\boldsymbol{H} = \left\langle \underline{\underline{\boldsymbol{G}}}^{HJ}; \boldsymbol{J} \right\rangle + \left\langle \underline{\underline{\boldsymbol{G}}}^{HM}; \boldsymbol{M} \right\rangle, \tag{3.22}$$

where $\underline{\underline{\boldsymbol{G}}}^{EJ}$, $\underline{\underline{\boldsymbol{G}}}^{HJ}$, $\underline{\underline{\boldsymbol{G}}}^{EM}$, and $\underline{\underline{\boldsymbol{G}}}^{HM}$ are related to vector potential DGFs by:

$$\underline{\underline{\boldsymbol{G}}}^{EJ} = -\frac{j\omega}{k^2}\left(k^2 + \nabla\nabla\right)\underline{\underline{\boldsymbol{G}}}^{A}, \tag{3.23}$$

$$\mu\underline{\underline{\boldsymbol{G}}}^{HJ} = \nabla\times\underline{\underline{\boldsymbol{G}}}^{A}, \tag{3.24}$$

$$\varepsilon\underline{\underline{\boldsymbol{G}}}^{EM} = -\nabla\times\underline{\underline{\boldsymbol{G}}}^{F}, \tag{3.25}$$

$$\underline{\underline{\boldsymbol{G}}}^{HM} = -\frac{j\omega}{k^2}\left(k^2 + \nabla\nabla\right)\underline{\underline{\boldsymbol{G}}}^{F}. \tag{3.26}$$

The notation $\underline{\underline{\boldsymbol{G}}}^{PQ}\left(\boldsymbol{r}\,|\,\boldsymbol{r}'\right)$ is used for dyadic Green's function relating P-type fields at $\boldsymbol{r}$ and Q-type currents at $\boldsymbol{r}'$ [140].

It should be pointed out that the permeability μ and the permittivity ε in the above equations may in general take complex values, representing lossy media. In the derivations above, we have used the method of potentials as a starting point. This, together with the assumption about the homogeneity of the medium in the region of interest allowed us to treat the permittivity and permeability of the regions as constants in Maxwell's equations, thus putting them outside differential operators. Consequently, we have found that magnetic and electric vector potentials or associated DGFs can be obtained from Helmholtz equations augmented by proper boundary conditions. In general, however, in some cases we can derive the field and vector potential DGFs directly from Maxwell's equations, without assuming the homogeneity of the region, which will be shown later.

It is also important to note that the field sources (i.e., electric and magnetic currents) do not need to be confined to the region for which Helmholtz equations are considered. Some problems may however arise when the currents cross the boundaries between homogeneous regions, which will also be discussed for the case of a multilayer environment.

Finally, we should remember that the potentials $\boldsymbol{A}$ and $\boldsymbol{F}$ are not exclusively associated with the electric and magnetic currents, respectively [155]. For example, even if the electric currents are absent in the given problem we can still define a non-zero $\boldsymbol{A}$ satisfying a homogeneous counterpart of (3.4). It is also known that in source-free regions only two *scalar* quantities are enough to completely define the fields, therefore several choices of potentials are used, as discussed by Mosig [155] (see also [141]).

For a homogeneous medium of infinite extent characterized by permittivity ε and permeability μ the vector and scalar potentials are given by [212]

$$A(r)=\mu\langle J(r');G(r\,|\,r')\rangle, \tag{3.27}$$

$$F(r)=\varepsilon\langle M(r');G(r\,|\,r')\rangle, \tag{3.28}$$

$$\Phi(r)=\frac{1}{\varepsilon}\langle q(r');G(r\,|\,r')\rangle, \tag{3.29}$$

$$\Psi(r)=\frac{1}{\mu}\langle m(r');G(r\,|\,r')\rangle, \tag{3.30}$$

where q and m denote the electric and magnetic charge densities related to the corresponding current distributions by continuity equations:

$$\nabla\cdot J(r)=-j\omega q(r), \tag{3.31}$$

$$\nabla\cdot M(r)=-j\omega m(r). \tag{3.32}$$

The kernel in (3.27)–(3.30) is a three-dimensional scalar Green's function

$$G(r\,|\,r')=\frac{e^{-jk|r-r'|}}{4\pi|r-r'|}. \tag{3.33}$$

It is of particular interest that in (3.29) and (3.30) we relate the scalar potentials to charges. The advantages of this step will be apparent later. The formulations in which such relations are used along with (3.17), (3.18), are widely known as mixed-potential integral equation (MPIE) formulations. In contrast, formulations based on (3.19), (3.20) are referred to as vector potential formulations.

3.1. Green's functions

Using the assumptions outlined at the end of the previous paragraph, the magnetic and electric vector potential Green's functions $\underline{\underline{G}}^A$ and $\underline{\underline{G}}^F$ for a given environment can be obtained by solving directly equation (3.8) and its dual, subject to appropriate boundary conditions. In the simplest case of homogeneous space of infinite extent, those solutions are particularly easy, because the DGFs reduce to scalars. Since there are no media boundaries, the only condition that must be taken into account is the *radiation condition*, which assures that only outgoing waves are chosen in the solu-

tion. In dissipative media, this choice is equivalent to the fields vanishing as the observation point approaches infinity. Thus for this case we have [62]:

$$G^A(\boldsymbol{r}|\boldsymbol{r}')=\frac{\mu}{4\pi}\frac{e^{-jk|\mathbf{r}-\mathbf{r}'|}}{|\boldsymbol{r}-\boldsymbol{r}'|}=\mu G(\boldsymbol{r}|\boldsymbol{r}'), \tag{3.34}$$

or by duality

$$G^F(\boldsymbol{r}|\boldsymbol{r}')=\frac{\varepsilon}{4\pi}\frac{e^{-jk|\boldsymbol{r}-\boldsymbol{r}'|}}{|\boldsymbol{r}-\boldsymbol{r}'|}=\varepsilon G(\boldsymbol{r}|\boldsymbol{r}'). \tag{3.35}$$

Of course, based on (3.23)–(3.26) we have immediately:

$$\underline{\underline{G}}^{EJ}(\boldsymbol{r}|\boldsymbol{r}')=-\frac{j\omega}{k^2}\left(k^2+\nabla\nabla\right)\underline{\underline{I}}G^A(\boldsymbol{r}|\boldsymbol{r}'), \tag{3.36}$$

$$\underline{\underline{G}}^{HJ}(\boldsymbol{r}|\boldsymbol{r}')=\frac{1}{\mu}\nabla\times\underline{\underline{I}}G^A(\boldsymbol{r}|\boldsymbol{r}'), \tag{3.37}$$

$$\underline{\underline{G}}^{EM}(\boldsymbol{r}|\boldsymbol{r}')=-\frac{1}{\varepsilon}\nabla\times\underline{\underline{I}}G^F(\boldsymbol{r}|\boldsymbol{r}'), \tag{3.38}$$

$$\underline{\underline{G}}^{HM}(\boldsymbol{r}|\boldsymbol{r}')=-\frac{j\omega}{k^2}\left(k^2+\nabla\nabla\right)\underline{\underline{I}}G^F(\boldsymbol{r}|\boldsymbol{r}'). \tag{3.39}$$

For layered media, also investigated in this monograph, the vector Green's functions remain tensors. As we have mentioned before, they can be obtained by solving directly equation (3.8) and its dual (see, for example, [134]). However, it is a well-established procedure [135, 140] to obtain $\underline{\underline{G}}^{EJ}$ and $\underline{\underline{G}}^{HJ}$ directly from Maxwell's equation, and then using (3.23)–(3.26) to get the entries of $\underline{\underline{G}}^{A}$ and/or $\underline{\underline{G}}^{F}$. The solution procedure summarized in [140] will be outlined in the next sections. It should be noted that the reference [142] addressing similar topics has not been published as widely available literature. In the author's opinion, it is also a good point to explain some details that were not commented on in [140].

3.1.1. Spectral domain formulation for multilayer media

Let us consider a multilayer medium of infinite lateral extent, which is characterized by z-dependent permittivity and permeability. In general, the subsequent analysis remains the same if we assume that some parts, or the whole medium, are uniaxially

anisotropic with the optical axis parallel to the z-axis. However, in order to keep the notation simple, we will assume the media in the formulation as isotropic, because only such cases are considered in examples presented in Chapter 8. Anyone interested in uniaxial media analysis is referred to [135, 140].

We want to compute the electric and magnetic fields specific to the given electric and magnetic current sources. These fields are obviously governed by Maxwell's equations

$$\nabla \times \boldsymbol{E} = -j\omega\mu \boldsymbol{H} - \boldsymbol{M}\,, \tag{3.40}$$

$$\nabla \times \boldsymbol{H} = j\omega\varepsilon \boldsymbol{E} + \boldsymbol{J}\,. \tag{3.41}$$

It is convenient to split all quantities involved in (3.40) and (3.41) into their transverse and longitudinal components:

$$\boldsymbol{E} = \boldsymbol{E}_t + \hat{z}E_z\,, \tag{3.42}$$

$$\boldsymbol{H} = \boldsymbol{H}_t + \hat{z}H_z\,, \tag{3.43}$$

$$\boldsymbol{J} = \boldsymbol{J}_t + \hat{z}J_z\,, \tag{3.44}$$

$$\boldsymbol{M} = \boldsymbol{M}_t + \hat{z}M_z\,, \tag{3.45}$$

$$\nabla = \nabla_t + \hat{z}\frac{\partial}{\partial z}\,. \tag{3.46}$$

After some manipulations the transverse and longitudinal parts of Maxwell's equations can be written as [142]

$$\frac{d}{dz}\boldsymbol{E}_t = \frac{1}{j\omega\varepsilon}\left(k^2 + \nabla_t\nabla_t\cdot\right)\left(\boldsymbol{H}_t \times \hat{z}\right) - \frac{1}{j\omega\varepsilon}\nabla_t J_z - \boldsymbol{M}_t \times \hat{z}\,, \tag{3.47}$$

$$\frac{d}{dz}\boldsymbol{H}_t = \frac{1}{j\omega\mu}\left(k^2 + \nabla_t\nabla_t\cdot\right)\left(\hat{z} \times \boldsymbol{E}_t\right) - \frac{1}{j\omega\mu}\nabla_t M_z - \hat{z} \times \boldsymbol{J}_t\,, \tag{3.48}$$

$$j\omega\varepsilon E_z = \nabla_t \cdot \left(\boldsymbol{H}_t \times \hat{z}\right) - J_z\,, \tag{3.49}$$

$$j\omega\mu H_z = \nabla_t \cdot \left(\hat{z} \times \boldsymbol{E}_t\right) - M_z\,, \tag{3.50}$$

where $k = \omega\sqrt{\varepsilon\mu}$.

Because of the assumed homogeneity of media in the planes transverse to z, further analysis can be facilitated through Fourier transformation of all fields and currents with respect to x and y coordinates. Hence, we introduce the Fourier transform pair [140]

$$F[f(\boldsymbol{r})] \equiv \tilde{f}\left(\boldsymbol{k}_\rho; z\right) = \int_{-\infty}^{+\infty}\int_{-\infty}^{+\infty} f(\boldsymbol{r}) e^{jk_\rho \cdot \rho}\, dxdy\,, \tag{3.51}$$

$$F^{-1}\left[\tilde{f}(\boldsymbol{k}_\rho;z)\right]\equiv f(\boldsymbol{r})=\frac{1}{(2\pi)^2}\int_{-\infty}^{+\infty}\int_{-\infty}^{+\infty}\tilde{f}(\boldsymbol{k}_\rho;z)e^{-j\boldsymbol{k}_\rho\cdot\boldsymbol{\rho}}dk_x dk_y, \tag{3.52}$$

where $f(\boldsymbol{r})\equiv f(\boldsymbol{\rho};z)$ denotes any scalar field component, $\boldsymbol{\rho}=\hat{\boldsymbol{x}}x+\hat{\boldsymbol{y}}y$ is the projection of $\boldsymbol{r}$ onto the (x, y) plane, and $\boldsymbol{k}_\rho=\hat{\boldsymbol{x}}k_x+\hat{\boldsymbol{y}}k_y$.

After applying (3.51) to (3.47) through (3.50) we get:

$$\frac{d}{dz}\tilde{\boldsymbol{E}}_t=\frac{1}{j\omega\varepsilon}\left(k^2-\boldsymbol{k}_\rho\boldsymbol{k}_\rho\cdot\right)\left(\tilde{\boldsymbol{H}}_t\times\hat{\boldsymbol{z}}\right)+\boldsymbol{k}_\rho\frac{\tilde{J}_z}{\omega\varepsilon}-\tilde{\boldsymbol{M}}_t\times\hat{\boldsymbol{z}}, \tag{3.53}$$

$$\frac{d}{dz}\tilde{\boldsymbol{H}}_t=\frac{1}{j\omega\mu}\left(k^2-\boldsymbol{k}_\rho\boldsymbol{k}_\rho\cdot\right)\left(\hat{\boldsymbol{z}}\times\tilde{\boldsymbol{E}}_t\right)+\boldsymbol{k}_\rho\frac{\tilde{M}_z}{\omega\mu}-\hat{\boldsymbol{z}}\times\tilde{\boldsymbol{J}}_t, \tag{3.54}$$

$$-j\omega\varepsilon\tilde{E}_z=j\boldsymbol{k}_\rho\cdot\left(\tilde{\boldsymbol{H}}_t\times\hat{\boldsymbol{z}}\right)+\tilde{J}_z, \tag{3.55}$$

$$-j\omega\mu\tilde{H}_z=j\boldsymbol{k}_\rho\cdot\left(\hat{\boldsymbol{z}}\times\tilde{\boldsymbol{E}}_t\right)+\tilde{M}_z. \tag{3.56}$$

Note that in the spectral domain introduced the transverse *nabla* operator takes on a simple form

$$\nabla_t=-j\boldsymbol{k}_\rho. \tag{3.57}$$

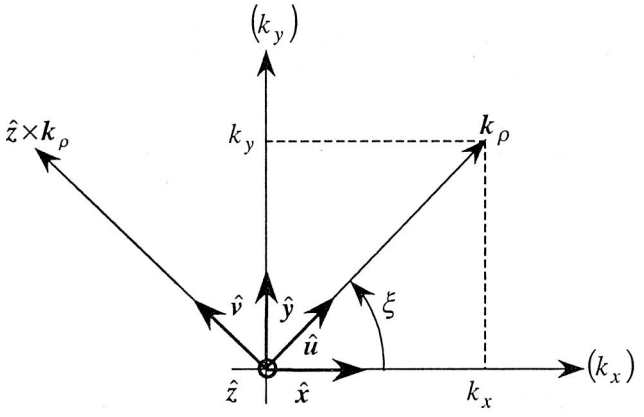

Fig. 3.1. Rotated spectrum-domain coordinate system [140]

It is now useful [140] to transform (3.53)–(3.56) into a rotated coordinate system (u, v, z) in the spectral domain (see Fig. 3.1) with the unit vectors $(\hat{\boldsymbol{u}},\hat{\boldsymbol{v}})$ defined by

$$\hat{\boldsymbol{u}} = \frac{k_x}{k_\rho}\hat{\boldsymbol{x}} + \frac{k_y}{k_\rho}\hat{\boldsymbol{y}}, \qquad \hat{\boldsymbol{v}} = -\frac{k_y}{k_\rho}\hat{\boldsymbol{x}} + \frac{k_x}{k_\rho}\hat{\boldsymbol{y}}, \tag{3.58}$$

where $k_\rho = \sqrt{k_x^2 + k_y^2}$.

The transformation from (k_x, k_y, z) space to (u, v, z) space can be expressed in terms of the matrix equation [142]

$$\begin{bmatrix} \tilde{E}_u \\ \tilde{E}_v \\ \tilde{E}_z \end{bmatrix} = \begin{bmatrix} \cos\xi & \sin\xi & 0 \\ -\sin\xi & \cos\xi & 0 \\ 0 & 0 & 1 \end{bmatrix} \begin{bmatrix} \tilde{E}_x \\ \tilde{E}_y \\ \tilde{E}_z \end{bmatrix} = \underline{\underline{Q}}(\xi) \begin{bmatrix} \tilde{E}_x \\ \tilde{E}_y \\ \tilde{E}_z \end{bmatrix}, \tag{3.59}$$

where

$$\cos\xi = \frac{k_x}{k_\rho}, \qquad \sin\xi = \frac{k_y}{k_\rho}. \tag{3.60}$$

In view of the orthogonality of the rotation matrix, we find that $\underline{\underline{Q}}^{-1} = \underline{\underline{Q}}^{T}$.

It should be noted that the Fourier transformation and the space rotation operations may be grouped together resulting in the following Vector Fourier Transform (VFT) pair [28, 142]:

$$\tilde{\boldsymbol{E}}(\boldsymbol{k}_\rho; z) = \int_{-\infty}^{+\infty} d\boldsymbol{\rho}\, e^{j\boldsymbol{k}_\rho \cdot \boldsymbol{\rho}}\, \underline{\underline{Q}}(\xi) \cdot \boldsymbol{E}(\boldsymbol{r}), \tag{3.61}$$

$$\boldsymbol{E}(\boldsymbol{r}) = \frac{1}{(2\pi)^2} \int_{-\infty}^{+\infty} d\boldsymbol{k}_\rho\, e^{-j\boldsymbol{k}_\rho \cdot \boldsymbol{\rho}}\, \underline{\underline{Q}}^{T}(\xi) \cdot \tilde{\boldsymbol{E}}(\boldsymbol{k}_\rho; z), \tag{3.62}$$

where we introduce the notation:

$$\int_{-\infty}^{+\infty} d\boldsymbol{\rho} \equiv \int_{-\infty-\infty}^{+\infty+\infty} dxdy, \qquad \int_{-\infty}^{+\infty} d\boldsymbol{k}_\rho \equiv \int_{-\infty-\infty}^{+\infty+\infty} dk_x dk_y. \tag{3.63}$$

Let us now focus our interest on equations (3.53) and (3.54) relating transverse spectral field components. If we could solve those equations for $\tilde{\boldsymbol{E}}_t$ and $\tilde{\boldsymbol{H}}_t$, the longitudinal field components would be immediately given by (3.55) and (3.56).

From (3.53) we have in rotated space:

$$\frac{d}{dz}\tilde{E}_u = \frac{1}{j\omega\varepsilon}\left(k^2 - k_\rho^2\right)\tilde{H}_v + \frac{k_\rho}{\omega\varepsilon}\tilde{J}_z - \tilde{M}_v, \tag{3.64}$$

$$\frac{d}{dz}\tilde{E}_v = \frac{1}{j\omega\varepsilon}k^2\left(-\tilde{H}_u\right) + \tilde{M}_u, \tag{3.65}$$

whilst from (3.54) we have:

$$\frac{d}{dz}\left(-\tilde{H}_u\right) = \frac{1}{j\omega\mu}\left(k^2 - k_\rho^2\right)\tilde{E}_v - \frac{k_\rho}{\omega\mu}\tilde{M}_z - \tilde{J}_v, \tag{3.66}$$

$$\frac{d}{dz}\tilde{H}_v = \frac{1}{j\omega\mu}k^2\tilde{E}_u - \tilde{J}_u. \tag{3.67}$$

Note that the above set of four equations splits into two independent pairs: (3.64) and (3.67) as a pair of equations with two unknowns $\tilde{E}_u, \tilde{H}_v$, whilst (3.65) and (3.66) form a pair with the unknowns $\tilde{E}_v, -\tilde{H}_u$.

Performing the substitutions:

$$V^e = \tilde{E}_u, \quad I^e = \tilde{H}_v, \tag{3.68}$$

$$v^e = \frac{k_\rho}{\omega\varepsilon}\tilde{J}_z - \tilde{M}_v, \quad i^e = -\tilde{J}_u, \tag{3.69}$$

$$I^h = -\tilde{H}_u, \quad V^h = \tilde{E}_v, \tag{3.70}$$

$$i^h = -\frac{k_\rho}{\omega\mu}\tilde{M}_z - \tilde{J}_v, \quad v^h = \tilde{M}_u, \tag{3.71}$$

and defining

$$k_z = \sqrt{k^2 - k_\rho^2}, \quad Z^e \equiv \frac{1}{Y^e} = \frac{k_z}{\omega\varepsilon}, \quad Z^h \equiv \frac{1}{Y^h} = \frac{\omega\mu}{k_z}, \tag{3.72}$$

we can rewrite (3.64) through (3.67) as two sets:

$$\begin{aligned} \frac{dV^p}{dz} &= -jk_z Z^p I^p + v^p, \\ \frac{dI^p}{dz} &= -jk_z Y^p V^p + i^p, \end{aligned} \tag{3.73}$$

where the superscript p stands for e or h.

The sets (3.73) can be easily recognized as familiar transmission line equations for transmission lines characterized by the propagation wave number k_z*) and the characteristic impedance and admittance denoted by Z^p and Y^p, respectively. It should be noted that the square root in (3.72) has an associated two-sheeted Riemann surface, where the "proper" sheet is identified by the condition that $\mathrm{Im}\, k_z < 0$ [140].

Thus, the problem of finding electric and magnetic fields in the layered medium has been reduced to a problem of finding the voltages and currents in two transmission-line networks.

In order to complete the derivation let us transfer equations (3.55) and (3.56) to the rotated space. We get:

$$\tilde{E}_z = -\frac{1}{j\omega\varepsilon}\left(jk_\rho \tilde{H}_v + \tilde{J}_z\right), \tag{3.74}$$

$$\tilde{H}_z = \frac{1}{j\omega\mu}\left(jk_\rho \tilde{E}_v - \tilde{M}_z\right). \tag{3.75}$$

An important conclusion resulting from (3.74) and (3.75) is that the longitudinal electric and magnetic field components are associated only with transmission-line equations denoted by superscripts e and h, respectively. It simply means that the set e describes (outside the source region) the fields that are TM to z, while the set h the fields that are TE to z, which was in fact anticipated by the choice of the superscripts. In view of (3.69) and (3.71) we also note that the transverse electric or transverse magnetic currents excite both the TM and TE transmission lines, whilst the z-directed electric or magnetic current excites only the respective TM or TE transmission line.

Finally, the spectral fields may be expressed in terms of voltages and currents in the equivalent transmission lines as [140]

$$\tilde{\boldsymbol{E}} = \hat{u}V^e + \hat{v}V^h - \hat{z}\frac{1}{j\omega\varepsilon}\left(jk_\rho I^e + \tilde{J}_z\right), \tag{3.76}$$

$$\tilde{\boldsymbol{H}} = -\hat{u}I^h + \hat{v}I^e + \hat{z}\frac{1}{j\omega\mu}\left(jk_\rho V^h - \tilde{M}_z\right). \tag{3.77}$$

The space-domain fields $\boldsymbol{E}$ and $\boldsymbol{H}$ may be obtained from (3.76) and (3.77) by applying an inverse VFT (3.62).

*) When considering uniaxial media different values of k_z are associated with the two sets of equations, therefore in this case the transmission lines have different propagation constants. This phenomenon is referred to as birefringence [142].

3.1.2. Derivation of dyadic Green's functions for multilayer media

In the preceding section we have replaced the original field problem with the equivalent transmission line problem, i.e., we have reduced the field calculations to the problem of obtaining voltages and currents in the transmission lines due to the given voltage and current sources. The relation between sources and voltages and currents may again be conveniently expressed using Green's functions (this time called the transmission line Green's functions – TLGF's). Let $V_i^p(z \mid z')$ and $I_i^p(z \mid z')$ denote the voltage and the current, respectively, at the position z caused by a 1-A shunt current source at z', whilst $V_v^p(z \mid z')$ and $I_v^p(z \mid z')$ the voltage and the current at z caused by the 1-V series voltage at z' (Fig. 3.2).

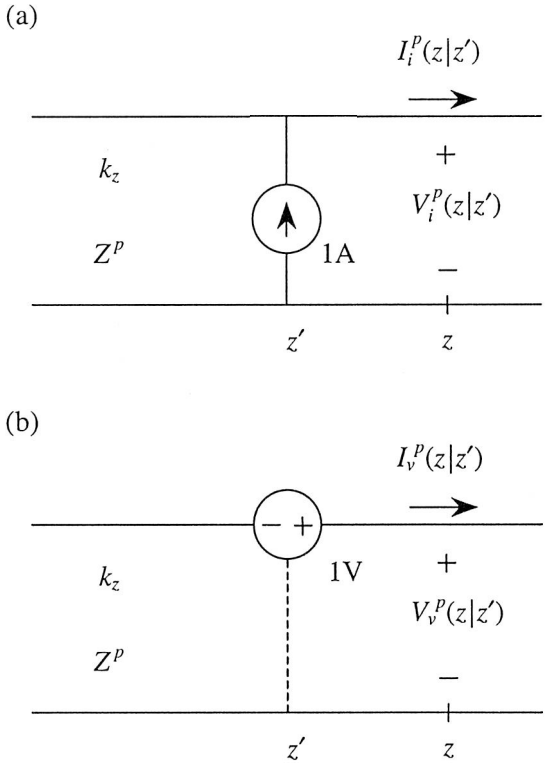

Fig. 3.2. Network problems used to determine the transmission-line Green's functions [140]. (a) 1-A shunt current source. (b) 1-V series voltage source

In view of (3.73) we may easily formulate the relations between the TLGF's introduced, namely [140]:

$$\frac{dV_i^p}{dz} = -jk_z Z^p I_i^p,$$

$$\frac{dI_i^p}{dz} = -jk_z Y^p V_i^p + \delta(z - z'), \tag{3.78}$$

$$\frac{dV_v^p}{dz} = -jk_z Z^p I_v^p + \delta(z - z'),$$

$$\frac{dI_v^p}{dz} = -jk_z Y^p V_v^p. \tag{3.79}$$

The TLGF's also satisfy the following reciprocity relations [39, p. 194], [140, 142]:

$$V_i^p(z \mid z') = V_i^p(z' \mid z),$$

$$I_v^p(z \mid z') = I_v^p(z' \mid z),$$

$$V_v^p(z \mid z') = -I_i^p(z' \mid z),$$

$$I_i^p(z \mid z') = -V_v^p(z' \mid z). \tag{3.80}$$

If for a given configuration of layers the TLGF's are known, we can apply the superposition rule and express the voltage and current at point z of an equivalent transmission line in terms of integrals:

$$V^p = \left\langle V_i^p, i^p \right\rangle + \left\langle V_v^p, v^p \right\rangle,$$

$$I^p = \left\langle I_i^p, i^p \right\rangle + \left\langle I_v^p, v^p \right\rangle. \tag{3.81}$$

If we now substitute (3.81) into (3.76) and (3.77) and use (3.69) and (3.71), we can obtain the spectrum-domain counterparts of (3.21) and (3.22) [140]

$$\tilde{\boldsymbol{E}} = \left\langle \underline{\underline{\tilde{\boldsymbol{G}}}}^{EJ}; \tilde{\boldsymbol{J}} \right\rangle + \left\langle \underline{\underline{\tilde{\boldsymbol{G}}}}^{EM}; \tilde{\boldsymbol{M}} \right\rangle, \tag{3.82}$$

$$\tilde{\boldsymbol{H}} = \left\langle \underline{\underline{\tilde{\boldsymbol{G}}}}^{HJ}; \tilde{\boldsymbol{J}} \right\rangle + \left\langle \underline{\underline{\tilde{\boldsymbol{G}}}}^{HM}; \tilde{\boldsymbol{M}} \right\rangle, \tag{3.83}$$

where the spectral dyadic Green's functions dependent on $\boldsymbol{k}_\rho$ and $z|z'$ are given as

$$\underline{\underline{\tilde{\boldsymbol{G}}}}^{EJ} = -\hat{\boldsymbol{u}}\hat{\boldsymbol{u}} V_i^e - \hat{\boldsymbol{v}}\hat{\boldsymbol{v}} V_i^h + \hat{\boldsymbol{z}}\hat{\boldsymbol{u}} \frac{k_\rho}{\omega\varepsilon} I_i^e + \hat{\boldsymbol{u}}\hat{\boldsymbol{z}} \frac{k_\rho}{\omega\varepsilon'} V_v^e - \hat{\boldsymbol{z}}\hat{\boldsymbol{z}} \left(\frac{k_\rho^2}{\omega^2 \varepsilon' \varepsilon} I_v^e + \frac{1}{j\omega\varepsilon} \delta(z - z') \right), \tag{3.84}$$

$$\underline{\underline{\tilde{G}}}^{HJ} = \hat{u}\hat{v}I_i^h - \hat{v}\hat{u}I_i^e - \hat{z}\hat{v}\frac{k_\rho}{\omega\mu}V_i^h + \hat{v}\hat{z}\frac{k_\rho}{\omega\varepsilon'}I_v^e, \tag{3.85}$$

$$\underline{\underline{\tilde{G}}}^{EM} = -\hat{u}\hat{v}V_v^e + \hat{v}\hat{u}V_v^h + \hat{z}\hat{v}\frac{k_\rho}{\omega\varepsilon}I_v^e - \hat{v}\hat{z}\frac{k_\rho}{\omega\mu'}V_i^h, \tag{3.86}$$

$$\underline{\underline{\tilde{G}}}^{HM} = -\hat{u}\hat{u}I_v^h - \hat{v}\hat{v}I_v^e + \hat{z}\hat{u}\frac{k_\rho}{\omega\mu}V_v^h + \hat{u}\hat{z}\frac{k_\rho}{\omega\mu'}I_i^h - \hat{z}\hat{z}\left(\frac{k_\rho^2}{\omega^2\mu'\mu}V_i^h + \frac{1}{j\omega\mu}\delta(z-z')\right). \tag{3.87}$$

We use the convention that the primed media parameters are evaluated at the source point. The Dirac *delta* symbols that appear in (3.84) and (3.87) arise from the direct presence of electric and magnetic current components in (3.76), (3.77). Because these parts give non-zero contributions to the spectral fields only when the observation point meets the source point on the z axis, in fact it makes no difference whether we use primed or not primed parameters in front of the deltas.

The space-domain DGF's may be obtained from the spectral DGF's listed above using an inverse VFT (3.62), which is equivalent to projecting the unit vectors $(\hat{u}, \hat{v})$ onto the (k_x, k_y)-coordinate system and then applying (3.52). Consequently, we obtain the formula [135, 142]:

$$\underline{\underline{G}}^{PQ}(\boldsymbol{\rho}; z|z') = \frac{1}{(2\pi)^2}\int_{-\infty}^{+\infty} d\mathbf{k}_\rho e^{-j\mathbf{k}_\rho\cdot\boldsymbol{\rho}}\underline{\underline{Q}}^T(\xi)\cdot\underline{\underline{\tilde{G}}}^{PQ}(\mathbf{k}_\rho; z|z')\cdot\underline{\underline{Q}}(\xi). \tag{3.88}$$

Taking into account the translational symmetry of medium with respect to transverse coordinates, we may write

$$\underline{\underline{G}}^{PQ}(\mathbf{r}|\mathbf{r}') \equiv \underline{\underline{G}}^{PQ}(\boldsymbol{\rho} - \boldsymbol{\rho}'; z|z'). \tag{3.89}$$

The entries of the spectral domain DGF's depend on variables k_x and k_y exclusively through k_ρ. When we carry out the transformation (3.88) in the polar spectral coordinates (k_ρ, ξ), and perform integration with respect to variable ξ, the integrals that arise are easily recognized as Sommerfeld-type integrals [135]:

$$F^{-1}\left\{\begin{matrix}\sin\\ \cos\end{matrix} n\xi\, \tilde{f}(k_\rho)\right\} = (-j)^n \begin{matrix}\sin\\ \cos\end{matrix} n\phi\, S_n\left\{\tilde{f}(k_\rho)k_\rho^{-n}\right\}, \quad n = 0, 1, 2, \tag{3.90}$$

where

$$S_n\left\{\tilde{f}(k_\rho)\right\} = \frac{1}{2\pi}\int_0^\infty \tilde{f}(k_\rho)J_n(k_\rho\rho)k_\rho^{n+1}dk_\rho\,. \tag{3.91}$$

In the formula above, J_n is the Bessel function of the order n, and (ρ,ϕ) are the cylindrical coordinates of the projection of the field point onto the (x,y) plane. Formulas (3.90) and (3.91) correspond to a case where the source is on the z-axis. The generalization for arbitrary source locations may be easily obtained by substituting:

$$\rho \to \varsigma = |\rho - \rho'|, \qquad \phi \to \varphi = \arctan\frac{y-y'}{x-x'}. \tag{3.92}$$

Although Green's functions (3.84)–(3.87) and their spatial domain counterparts may be used directly for solving scattering problems [17], it is often useful, (for reasons discussed in further paragraphs), to use the potential representations outlined at the beginning of this chapter. The procedure of obtaining the vector potential DGF's will be shown for a magnetic vector potential, assuming again that only electric currents exist in the given problem.

As already mentioned, equation (3.2) does not define the vector potential $\boldsymbol{A}$ uniquely. Based on several possible formulations (discussed, for example, in [140, 141, 155]), we have chosen the so-called "traditional" form of vector potential for further analysis. This form is historically related to the name of Sommerfeld [185], because of his contribution to the analysis of contiguous half-space problems, useful, for example, in the analysis of antennas in the presence of lossy ground. Sommerfeld used a vertical component of vector potential to characterize radiation of vertical (z-directed) sources, whilst for horizontal (transverse to z) sources the vertical potential component had to be accompanied by an additional horizontal component.

The above choice of potentials is equivalent to postulating the following form of $\underline{\underline{\tilde{G}}}^A$

$$\underline{\underline{\tilde{G}}}^A = (\hat{u}\hat{u}+\hat{v}\hat{v})\tilde{G}^A_{vv} + \hat{z}\hat{u}\tilde{G}^A_{zu} + \hat{z}\hat{z}\tilde{G}^A_{zz}. \tag{3.93}$$

The consistency of this choice with the choice of Sommerfeld is evident when we project (3.93) on the Cartesian coordinate system and present it in the matrix form [140]

$$\left[\tilde{G}^A\right] = \begin{bmatrix} \tilde{G}^A_{vv} & 0 & 0 \\ 0 & \tilde{G}^A_{vv} & 0 \\ \dfrac{k_x}{k_\rho}\tilde{G}^A_{zu} & \dfrac{k_y}{k_\rho}\tilde{G}^A_{zu} & \tilde{G}^A_{zz} \end{bmatrix}, \tag{3.94}$$

where we see that both horizontal and vertical components of the vector potential are associated with a horizontal current source.

The components of $\underline{\underline{\tilde{G}}}^{A}$ can be found if we substitute (3.93) into the spectral domain counterparts of (3.23) or (3.24) and then compare the resulting equations with (3.84) or (3.85), respectively.

For example, based on (3.23) we have:

$$\underline{\underline{\tilde{G}}}^{EJ} = \hat{u}\hat{u}\left(-j\omega\tilde{G}_{vv}^{A} + j\omega\frac{k_\rho^2}{k^2}\tilde{G}_{vv}^{A} - \frac{\omega k_\rho}{k^2}\frac{d}{dz}\tilde{G}_{zu}^{A}\right) - \hat{v}\hat{v}j\omega\tilde{G}_{vv}^{A}$$

$$-\hat{z}\hat{u}\left(\frac{\omega k_\rho}{k^2}\frac{d}{dz}\tilde{G}_{vv}^{A} + \frac{j\omega}{k^2}\frac{d^2}{dz^2}\tilde{G}_{zu}^{A}\right) - \hat{u}\hat{z}\frac{\omega k_\rho}{k^2}\frac{d}{dz}\tilde{G}_{zz}^{A} - \hat{z}\hat{z}\left(j\omega\tilde{G}_{zz}^{A} + \frac{j\omega}{k^2}\frac{d^2}{dz^2}\tilde{G}_{zz}^{A}\right). \quad (3.95)$$

Now, comparing the $\hat{u}\hat{u}$, $\hat{v}\hat{v}$ and $\hat{u}\hat{z}$ components of (3.95) and (3.84) we get the equations:

$$j\omega\tilde{G}_{vv}^{A} - j\omega\frac{k_\rho^2}{k^2}\tilde{G}_{vv}^{A} + \frac{\omega k_\rho}{k^2}\frac{d}{dz}\tilde{G}_{zu}^{A} = V_i^e, \quad (3.96)$$

$$j\omega\tilde{G}_{vv}^{A} = V_i^h, \quad (3.97)$$

$$\frac{\omega k_\rho}{k^2}\frac{d}{dz}\tilde{G}_{zz}^{A} = -\frac{k_\rho}{\omega\varepsilon'}V_v^e. \quad (3.98)$$

Substituting (3.97) into (3.96) leads to the relation:

$$\frac{d}{dz}\left(j\omega\tilde{G}_{zu}^{A}\right) = \frac{k^2}{jk_\rho}\left(-V_i^e + V_i^h - \frac{k_\rho^2}{k^2}V_i^h\right). \quad (3.99)$$

Further, using (3.78) and (3.72), we can transform (3.99) into:

$$j\omega\tilde{G}_{zu}^{A} = \frac{\omega\mu}{k_\rho}\left(I_i^h - I_i^e\right), \quad (3.100)$$

similarly, using (3.98) together with (3.79) and (3.72), leads to:

$$j\omega\tilde{G}_{zz}^{A} = \frac{\mu}{\varepsilon'}I_v^e. \quad (3.101)$$

Relations (3.97), (3.100) and (3.101) define the components of $\underline{\underline{\tilde{G}}}^{A}$ in terms of TLGF's introduced earlier.

Alternatively, in order to obtain those equations we can start with equation (3.24) and express $\underline{\underline{\tilde{G}}}^{HJ}$ in terms of the components of $\underline{\underline{\tilde{G}}}^{A}$:

$$\mu\underline{\underline{\tilde{G}}}^{HJ} = -\hat{u}\hat{v}\frac{d}{dz}\tilde{G}^{A}_{vv} + \hat{v}\hat{u}\left(\frac{d}{dz}\tilde{G}^{A}_{vv} + jk_{\rho}\tilde{G}^{A}_{zu}\right) - \hat{z}\hat{v}\,jk_{\rho}\tilde{G}^{A}_{vv} + \hat{v}\hat{z}\,jk_{\rho}\tilde{G}^{A}_{zz}. \tag{3.102}$$

Comparing the $\hat{z}\hat{v}$ components of (3.102) and (3.85) we immediately get equation (3.97), comparing $\hat{v}\hat{z}$ we get (3.101), whilst comparing the $\hat{v}\hat{u}$ components and applying (3.97) together with (3.78) and (3.72) we obtain relation (3.100).

An important conclusion may be drawn at this point. Note that when using the expressions for $\underline{\underline{\tilde{G}}}^{HJ}$ deriving the $\underline{\underline{\tilde{G}}}^{A}$ components we make no assumption as to the nature of the medium stratification. It means that $\underline{\underline{\tilde{G}}}^{A}$ obtained with the above procedure is valid for any isotropic multilayer environment. In contrast to this, equation (3.23) resulting from (3.5) assumes (as was pointed out earlier) that we deal with a homogeneous layer. This assumption is then also made for equation (3.95). We can prove the generality of the resulting equations by assuming an auxiliary condition relating scalar and vector potentials [140]:

$$\nabla\cdot\left(\frac{1}{\mu}\boldsymbol{A}\right) = -j\omega\varepsilon\Phi, \tag{3.103}$$

in place of the Lorentz condition (3.3). It should be possible to show that using (3.103) to obtain $\boldsymbol{E}$ in terms of $\boldsymbol{A}$ and then $\underline{\underline{\boldsymbol{G}}}^{EJ}$ in terms of $\underline{\underline{\boldsymbol{G}}}^{A}$, we finally arrive at the same form of (3.97), (3.100) and (3.101).

Performing an analysis dual to the one presented above we can readily find spectral components of the electric vector potential DGF $\underline{\underline{\tilde{G}}}^{F}$

$$j\omega\tilde{G}^{F}_{vv} = I^{e}_{v}, \tag{3.104}$$

$$j\omega\tilde{G}^{F}_{zu} = \frac{\omega\varepsilon}{k_{\rho}}\left(V^{e}_{v} - V^{h}_{v}\right), \tag{3.105}$$

$$j\omega\tilde{G}^{F}_{zz} = \frac{\varepsilon}{\mu'}V^{h}_{i}. \tag{3.106}$$

Thus, we have found the formal expressions defining components of the multilayer media DGF's relating the electric and magnetic fields, as well as the magnetic and electric vector potentials to the electric and magnetic current sources, in terms of inverse VFT and TLGF's.

The multilayer environments are important from a practical point of view and concern media with piecewise-constant parameters, i.e., consisting of a number of homogeneous layers. The TLGF's for this case are widely presented in literature and have been listed in Appendix 2.

* * *

In this section, we present the Green's function for two cases, for which examples are given in Chapter 8. Both cases are associated with dielectric antenna applications, which are the main subject of the author's interest. One should bear in mind, however, that the formulations given in Chapter 2 are valid for any environment for which Green's functions are known. This fact has been emphasized in the introduction of this chapter. Thus, we can apply the solution procedures, for example, to dielectric obstacles in waveguides [5, 193, 206] or bodies in the presence of conducting or dielectric spheres, wedges and cones [193].

3.2. Singularities of Green's functions – fields within the source region

The DGF's presented in the previous section are easy to handle in numerical algorithms if the observation point, i.e., the point of space where we want to calculate the fields, is outside the source region. However, in the integral equation techniques, which are discussed in this monograph, a typical task is to evaluate field components *in* the source region. For surface integral equations (sections 2.1.2. and 2.1.3), we have to calculate fields at points approaching the surfaces on which the equivalent currents flow (equations (2.14)–(2.15), (2.18)–(2.19) and (2.21)–(2.22)). In volume integral equation formulations (section 2.2.1) we need to specify fields inside the volume occupied by the polarization currents (equations (2.27)–(2.29)).

Unfortunately, when the observation point approaches the source point, the Green's functions discussed before exhibit a singular behavior. This is evident when examining formulas developed for free-space (see equations (3.34)–(3.39)). For layered media, the singularity of DGF's components becomes more obvious when the transmission line Green's function formulas listed in Appendix 2 are substituted into (3.84)–(3.87)[*)].

Although we will not present any direct proof here, the order of singularity of various DGF's components is in general the same for multilayer media as for free-space [208, p. 239]. Therefore, we will discuss shortly the arising problems using as a basis free-space Green's functions[**)].

[*)] The reader should remember that singularities generally appear when the spatial domain is recovered via the inverse Fourier transform. In the spectral domain, the corresponding Sommerfeld integrals at singular points do not converge.

[**)] In layered media, if the *surface* of interest in the vicinity of the singular point is situated *at* the interface between dissimilar media, one has to take into account also the contributions from the quasi-static image sources of Green's function. However, the procedure remains generally the same [36].

Let us denote the distance between the source and observation points by R, i.e.,

$$R = |\boldsymbol{r} - \boldsymbol{r}'|. \tag{3.107}$$

It can be shown [208, p. 79] that components of $\underline{\underline{\boldsymbol{G}}}^{A}$ and $\underline{\underline{\boldsymbol{G}}}^{F}$ present the $1/R$ singularity, first derivatives of vector potential DGF's are of $1/R^2$ singularity, while second derivatives (associated with the scalar potential terms) are of $1/R^3$ singularity. Therefore, generally when using electric and magnetic field DGF's directly we have to deal with $1/R^2$ singularity when applying $\underline{\underline{\boldsymbol{G}}}^{HJ}$ and $\underline{\underline{\boldsymbol{G}}}^{EM}$ and $1/R^3$ singularity when applying $\underline{\underline{\boldsymbol{G}}}^{EJ}$ and $\underline{\underline{\boldsymbol{G}}}^{HM}$.

At this point, it should be emphasized that Green's functions discussed must be thought of in terms of distributions rather than ordinary functions [208, p. 80], and therefore any singular point has to be understood in conjunction with its immediate spatial surroundings. The above corresponds to the fact that Green's functions are always used in the kernels of *integrals*. Therefore, the question that arises when investigating the singularity of Green's function is whether this singularity is integrable or not. In this study, we discuss two types of integrals, i.e., surface and volume ones. As pointed out in [208, p. 78] the surface and volume integrals converge if the order of the kernel singularity is less than 2 or 3, respectively.

In the light of the above discussion, we see that when using surface integral formulations we always have to take special steps in order to calculate fields in the source regions, whilst when dealing with volume integrals this special treatment is confined to cases where $\underline{\underline{\boldsymbol{G}}}^{EJ}$ and $\underline{\underline{\boldsymbol{G}}}^{HM}$ are involved. We also have to remember that even when the singularity is analytically integrable, the numerical treatment of such a situation usually requires special care.

In the subsequent paragraphs, methods of dealing with singularities in surface and volume integral equations are outlined for a case of homogeneous unbounded media (free-space case). Later we will discuss whether some techniques presented below can be extended into multilayer environments.

3.2.1. Surface integral formulations

Let us consider a situation depicted in Fig. 3.3. We have the surface S with the electric or magnetic current distribution. This surface current (let us denote it by $\boldsymbol{K}$) is a source of the electric and magnetic fields at the observation point specified by the vector $\boldsymbol{r}$. Note that according to equivalent situations introduced in Chapter 2 the surface current radiates in homogeneous media (we assume the same media parameters

inside and outside S). Our task is to calculate fields when $\boldsymbol{r}$ approaches S. This requires calculating three types of (vector) integrals:

$$\boldsymbol{I}_1(\boldsymbol{r}) = \int_S \boldsymbol{K}(\boldsymbol{r}')\left(\nabla \times \underline{\underline{\boldsymbol{I}}} G(\boldsymbol{r}\,|\,\boldsymbol{r}')\right) dS', \tag{3.108}$$

$$\boldsymbol{I}_2(\boldsymbol{r}) = \int_S \boldsymbol{K}(\boldsymbol{r}') G(\boldsymbol{r}\,|\,\boldsymbol{r}') dS', \tag{3.109}$$

$$\boldsymbol{I}_3(\boldsymbol{r}) = \int_S \boldsymbol{K}(\boldsymbol{r}') \nabla\nabla G(\boldsymbol{r}\,|\,\boldsymbol{r}') dS'. \tag{3.110}$$

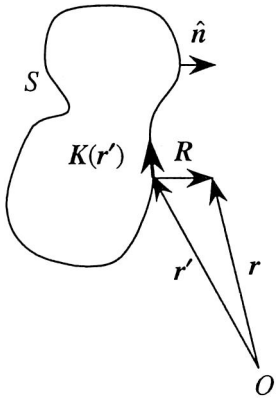

Fig. 3.3. Geometry for a general problem with a field point outside the surface S

The integral $\boldsymbol{I}_1$ arises when we consider $\underline{\underline{\boldsymbol{G}}}^{HJ}$ or $\underline{\underline{\boldsymbol{G}}}^{EM}$ while $\boldsymbol{I}_2$ and $\boldsymbol{I}_3$ result from formulas applying $\underline{\underline{\boldsymbol{G}}}^{EJ}$ and $\underline{\underline{\boldsymbol{G}}}^{HM}$ Green's functions. Of the above integrals, only $\boldsymbol{I}_2$ is easily integrable, because its kernel exhibits $1/R$ weak singularity only, which is obviously integrable on the surface S. In order to perform the remaining integrations, special steps must be applied.

3.2.1.1. Principal value integrals

The integrals (3.108) and (3.110) for an observation point lying on S can be evaluated using a properly applied *limiting procedure* [166, 154] in which we *exclude* the contribution from the infinitesimal neighbourhood of the singular point $\boldsymbol{r} = \boldsymbol{r}'$. This results in calculating the remaining integrals in the sense of a Cauchy principal-value.

After applying the limiting procedure to the integral $\boldsymbol{I}_1$, we get for the case of a *smooth* surface S

$$\boldsymbol{I}_1(\boldsymbol{r})=\int_S \nabla G(\boldsymbol{r}\,|\,\boldsymbol{r}')\times \boldsymbol{K}(\boldsymbol{r}')dS'=\mp\frac{1}{2}\hat{\boldsymbol{n}}\times\boldsymbol{K}(\boldsymbol{r})+\text{⨍}_S \nabla G(\boldsymbol{r}\,|\,\boldsymbol{r}')\times \boldsymbol{K}(\boldsymbol{r}')dS', \quad \boldsymbol{r}\in S, \quad (3.111)$$

where the dashed integral symbol signifies a principal-value integral, and the upper (lower) sign pertains to the outside (inside) surface limit. Note that in (3.111) we have transformed the kernel into a more convenient form using common vector identities.

In practical applications, we formulate the integral equations taking into account field components tangential to S (see Chapter 2). Thus, we are usually interested in the tangential component of $\boldsymbol{I}_1$:

$$\hat{\boldsymbol{n}}\times\boldsymbol{I}_1(\boldsymbol{r})=\pm\frac{1}{2}\boldsymbol{K}(\boldsymbol{r})+\hat{\boldsymbol{n}}\times\text{⨍}_S \nabla G(\boldsymbol{r}\,|\,\boldsymbol{r}')\times \boldsymbol{K}(\boldsymbol{r}')dS', \quad \boldsymbol{r}\in S. \quad (3.112)$$

A careful reader may find that although the principal part has been extracted from the integral in (3.108), calculation of the second right hand component of (3.112) is in general a non-trivial task for S of any shape. Note that in order to obtain (3.112) we have assumed S to be smooth in the vicinity of the singular point. However, as will be seen in Section 5, we typically approximate S with a number of *flat* sub-surfaces. Note also that in the calculation of the integral part associated with the sub-domain to which the observation point belongs (for example, the *self-term* in the method-of-moments expansion) the vector $\boldsymbol{R}$ lies *in* that planar sub-surface. On the other hand, we have:

$$\nabla G=-\frac{1+jkR}{4\pi R^2}e^{-jkR}\hat{\boldsymbol{R}}. \quad (3.113)$$

Therefore, the vector expression under the integral sign in (3.112) is normal to the surface. Consequently, its cross product with the normal $\hat{\boldsymbol{n}}$ equals zero. We conclude that in this case it is not necessary to evaluate the integral [64]. When the surface (or its approximation) is not flat around the singular point, we have to go through additional steps to extract the singularity and enable numerical integration [15, 16].

Let us now consider the integral $\boldsymbol{I}_3$ defined by equation (3.110). We should keep in mind that the double differentiation has appeared in this formula from equation (3.5), i.e., at the beginning it was considered *outside* the integral, which was also related to the particular form of the Lorentz condition (3.3). The sense and existence of the operator $\nabla\nabla\cdot\text{⨍}$ has been investigated by Wang when considering the treatment of volume integrals [208, p. 230]. We recall here that in order to keep the differentiation outside the integral sign we must assume that the current distribution $\boldsymbol{K}(\boldsymbol{r}')$ satisfies a particular form of *Hölder condition* which is stronger than continuity, however, weaker than differentiability [208, p. 231]. In what follows, we will assume that the

first derivatives of the current exist. This is a somewhat strong assumption from a purely mathematical point of view, but enables a relatively simple and clear analysis. Note that if we kept the *nabla* operators outside the integral sign, we could integrate the kernel without difficulty as it would simply be of the integral form $\boldsymbol{I}_2$. Unfortunately, this approach is undesirable in numerical procedures and is therefore avoided. The numerical treatment of differentiation is much less troublesome if we introduce *one* of *nabla* operators under the integral sign. In this case, we have:

$$\boldsymbol{I}_3(\boldsymbol{r}) = \nabla \int_S \boldsymbol{K}(\boldsymbol{r}') \nabla G(\boldsymbol{r} \mid \boldsymbol{r}') dS' . \tag{3.114}$$

Taking into account the relation:

$$\nabla G(\boldsymbol{r} \mid \boldsymbol{r}') = -\nabla' G(\boldsymbol{r} \mid \boldsymbol{r}'), \tag{3.115}$$

where ∇' operates on the source coordinates, and using well known integral relationships in the vector analysis on a surface [208, p. 460], as well as recalling that the surface S is closed, we can transform (3.114) into:

$$\boldsymbol{I}_3(\boldsymbol{r}) = \nabla \int_S (\nabla' \cdot \boldsymbol{K}(\boldsymbol{r}')) G(\boldsymbol{r} \mid \boldsymbol{r}') dS' . \tag{3.116}$$

Note that we have, in fact, transformed the "internal" differential operator to act on the current instead of G. This is, of course, allowed due to the above assumption about the existence of the first spatial derivatives of $\boldsymbol{K}$. In view of the continuity equations (3.31), (3.32) the term $(\nabla' \cdot \boldsymbol{K}(\boldsymbol{r}'))$ can be immediately recognized as the surface charge distribution associated with the current $\boldsymbol{K}$. In some formulations, these (equivalent) charges are written in terms of normal field components [166], [208, p. 173]. One should also note that the integral in (3.116) now represents the scalar potential produced by the charge distribution and is consistent with (3.29) and (3.30). Obviously, the kernel singularity associated with (3.116) has been reduced to $1/R$.

Now, we must deal with the second *nabla* operator in (3.116), which up to now remained outside the integral sign. The first possibility is to leave this differentiation as in (3.116) and neutralize it in a process of reducing the system of integral equations corresponding to the particular problem [168, 197] to a set of linear equations. This approach, which will be described in Chapter 5, is equivalent to the *reaction matching* concept [173], [208, p. 195]. An alternative solution is to transfer this operator also under the integral sign, which is consistent with the notation of (3.110). Thus, we get:

$$\boldsymbol{I}_3(\boldsymbol{r}) = \int_S (\nabla' \cdot \boldsymbol{K}(\boldsymbol{r}')) \nabla G(\boldsymbol{r} \mid \boldsymbol{r}') dS' . \tag{3.117}$$

Note that in comparison with (3.110) which has a singularity of an $1/R^3$ order, the singularity in (3.117) is of $1/R^2$ order which is still too high to perform the integration

on the surface. One should also note that such an order of singularity is the same as that of (3.108). Therefore, the solution is to apply the principal part extraction again. This time the procedure of extracting the infinitesimal portion of S around the singularity leads to the formula:

$$\boldsymbol{I}_3(\boldsymbol{r}) = \mp\hat{\boldsymbol{n}}\frac{(\nabla\cdot\boldsymbol{K}(\boldsymbol{r}))}{2} + \int_S (\nabla'\cdot\boldsymbol{K}(\boldsymbol{r}'))\nabla G(\boldsymbol{r}\,|\,\boldsymbol{r}')dS', \qquad \boldsymbol{r}\in S. \tag{3.118}$$

Again, we are interested in the tangential component of $\boldsymbol{I}_3$:

$$\hat{\boldsymbol{n}}\times\boldsymbol{I}_3(\boldsymbol{r}) = \hat{\boldsymbol{n}}\times\int_S (\nabla'\cdot\boldsymbol{K}(\boldsymbol{r}'))\nabla G(\boldsymbol{r}\,|\,\boldsymbol{r}')dS', \quad \boldsymbol{r}\in S. \tag{3.119}$$

The important observation in this case is the principal part (which is normal to S in view of (3.118)) annihilated to zero in (3.119).

At the end of this section, we present some interesting features related to the choice of (2.14)–(2.15) as the integral equations describing the scattering problem. In this case, the principal parts associated with $\underline{\underline{\boldsymbol{G}}}^{HJ}$ and $\underline{\underline{\boldsymbol{G}}}^{EM}$ Green's functions arising from the interior and exterior problems cancel out [166, 208, 197] (see also section 3.2.1.3). The physical meaning of this observation relates to the fact that the field values in the immediate neighborhood of the singular point depend only on the distance R and *do not depend* on the propagation constants of the surrounding media. The mathematical equivalent of this is the neglecting of "phase factors" in the above extractions of principal parts.

A similar procedure can in fact be used when investigating integrals $\underline{\underline{\boldsymbol{G}}}^{EJ}$ and $\underline{\underline{\boldsymbol{G}}}^{HM}$, and more precisely, their parts associated with scalar potentials, or equivalently with the second derivatives of G. As indicated by Morita [153], although the second derivative of G (present in the integral $\boldsymbol{I}_3$) produces the $1/R^3$ singularity which is not integrable on the surface, the second derivative of the difference $G_d - G_e = \dfrac{e^{-jk_dR}}{4\pi R} - \dfrac{e^{-jk_eR}}{4\pi R}$ has a singularity of an order $1/R$ and therefore *is* integrable on S[*]. This approach may be attractive because it does not require transferring the derivative operators to act on the current, which was necessary in our handling of $\boldsymbol{I}_3$ above. Consequently, simple current approximations can be used in the transformation of integral equations. However, in order to get the difference $G_d - G_e$ under the double *nabla* operator we have to apply special linear combinations of (2.10) with (2.12) and (2.11) with (2.13). This results in so-called *Müller equations* [156] and was investigated by Mautz and Harrington in [123].

[*] Subscripts d and e pertain to internal and external equivalent problems, respectively.

3.2.1.2. Singularity extraction in view of the equivalence principle

In the previous section, we have investigated field singularities taking into account an arbitrary current distribution on S. Now, let us match the obtained results to sources that arise when the equivalence principle is applied to model the presence of a dielectric body.

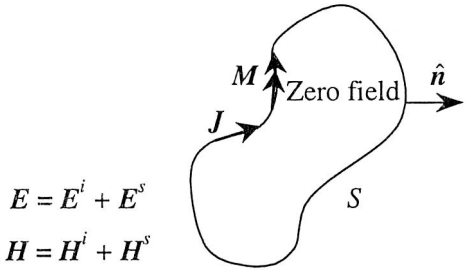

Fig. 3.4. Geometry for an equivalent problem for the exterior region

Let us consider, as an example, the situation depicted in Fig. 3.4, which illustrates the exterior equivalent problem in the form of a surface integral formulation described by the choice (2.5), (2.6).

According to (2.10) and (2.11), the equivalent surface currents are given as:

$$\boldsymbol{J} = \hat{\boldsymbol{n}} \times \boldsymbol{H}^{+}, \qquad \boldsymbol{M} = \boldsymbol{E}^{+} \times \hat{\boldsymbol{n}}, \tag{3.120}$$

where $\hat{\boldsymbol{n}}$ is again the outward unit vector normal to S and ($\boldsymbol{E}^{+}$, $\boldsymbol{H}^{+}$) are the total electric and magnetic fields evaluated just outside S. We also assume that the external medium has been extended into the internal region, and that the appropriate Green's functions exist for the extended medium.

Note that fields radiated by ($\boldsymbol{J}$, $\boldsymbol{M}$) are discontinuous at S. Therefore one must carefully evaluate the surface limits of the fields in the integral equation formulations outlined in Chapter 2. The fields given by (3.17) and (3.18) for homogeneous media have the following limits as the observation point approaches a *smooth* point on the surface S [212] (see also [75, p. 334], [114, p. 188]):

$$\boldsymbol{E}^{s\pm} = \pm \hat{\boldsymbol{n}} \times \frac{\boldsymbol{M}}{2} \pm \hat{\boldsymbol{n}} \frac{q}{2\varepsilon} - j\omega \boldsymbol{A} - \overline{\nabla \Phi} - \frac{1}{\varepsilon} \overline{\nabla \times \boldsymbol{F}}, \tag{3.121}$$

$$\boldsymbol{H}^{s\pm} = \pm \frac{\boldsymbol{J}}{2} \times \hat{\boldsymbol{n}} \pm \hat{\boldsymbol{n}} \frac{m}{2\mu} - j\omega \boldsymbol{F} - \overline{\nabla \Psi} + \frac{1}{\mu} \overline{\nabla \times \boldsymbol{A}}, \tag{3.122}$$

where the superscript s stands for scattered fields, while upper (lower) signs pertain to the outside (inside) surface limit. A line over a formula denotes the *average* value of

a discontinuous quantity as S is approached from the opposite sides. The average terms may be written as:

$$\overline{\nabla \times \boldsymbol{A}(\boldsymbol{r})} = \mu \int\!\!\!\!\!\!- \int_S \nabla G(\boldsymbol{r} \mid \boldsymbol{r}') \times \boldsymbol{J}(\boldsymbol{r}') dS', \tag{3.123}$$

$$\overline{\nabla \times \boldsymbol{F}(\boldsymbol{r})} = \varepsilon \int\!\!\!\!\!\!- \int_S \nabla G(\boldsymbol{r} \mid \boldsymbol{r}') \times \boldsymbol{M}(\boldsymbol{r}') dS', \tag{3.124}$$

$$\overline{\nabla \Phi(\boldsymbol{r})} = \frac{1}{\varepsilon} \int\!\!\!\!\!\!- \int_S \nabla G(\boldsymbol{r} \mid \boldsymbol{r}') q(\boldsymbol{r}') dS', \tag{3.125}$$

$$\overline{\nabla \Psi(\boldsymbol{r})} = \frac{1}{\mu} \int\!\!\!\!\!\!- \int_S \nabla G(\boldsymbol{r} \mid \boldsymbol{r}') m(\boldsymbol{r}') dS', \tag{3.126}$$

where the dashed integral symbols signify that these are principal-value integrals, which exclude the contribution from the source point $\boldsymbol{r} = \boldsymbol{r}'$ on S. Note that the vector potentials $\boldsymbol{A}$ and $\boldsymbol{F}$ in (3.121)–(3.122) do not require special treatment. This is because the integrals (3.27), (3.28) are weakly-singular convergent on surface S (in terms of the notation introduced in the preceding section they correspond to integral $\boldsymbol{I}_2$).

The source terms appearing outside the potential integrals in (3.121), (3.122) account for the well-known discontinuities in the fields at the source-bearing surface S [212]. Note that these formulas may be obtained immediately by applying (3.111) and (3.118). It is worth pointing out that these terms may also be derived through simple physical reasoning, which would give the same result. Namely, as the observation point $\boldsymbol{r}$ approaches a smooth point on S, the effect of curvature vanishes and the fields at $\boldsymbol{r}$ approach those fields calculated directly above or below a flat source-bearing sheet of infinite extent. Hence, applying the boundary conditions at a source-bearing surface [114, p. 70] and invoking symmetry, we obtain the source terms given in (3.121)–(3.122), where $\hat{\boldsymbol{n}} \frac{q}{2\varepsilon}$ and $\hat{\boldsymbol{n}} \frac{m}{2\mu}$ arise respectively from the discontinuities in $\nabla \Phi$ and $\nabla \Psi$, and $\hat{\boldsymbol{n}} \times \frac{\boldsymbol{M}}{2}$ and $\frac{\boldsymbol{J}}{2} \times \hat{\boldsymbol{n}}$ are related to the discontinuities in $\nabla \times \boldsymbol{F}$ and $\nabla \times \boldsymbol{A}$, respectively.

The total fields on both sides of S may be obtained by adding the incident fields to (3.121)–(3.122). In particular, on the exterior side of S we obtain:

$$\frac{1}{2}\boldsymbol{E}^+ = \boldsymbol{E}^i - j\omega \boldsymbol{A} - \overline{\nabla \Phi} - \frac{1}{\varepsilon}\overline{\nabla \times \boldsymbol{F}}, \tag{3.127}$$

$$\frac{1}{2}\boldsymbol{H}^+ = \boldsymbol{H}^i - j\omega \boldsymbol{F} - \overline{\nabla \Psi} + \frac{1}{\mu}\overline{\nabla \times \boldsymbol{A}}, \tag{3.128}$$

where we have used (3.120), relations [114, p. 70]:

$$\frac{q}{\varepsilon} = \hat{\boldsymbol{n}} \cdot \boldsymbol{E}^{+}, \qquad \frac{m}{\mu} = \hat{\boldsymbol{n}} \cdot \boldsymbol{H}^{+}, \tag{3.129}$$

and the vector identity:

$$\boldsymbol{E} = \hat{\boldsymbol{n}} \times (\boldsymbol{E} \times \hat{\boldsymbol{n}}) + (\hat{\boldsymbol{n}} \cdot \boldsymbol{E})\hat{\boldsymbol{n}} . \tag{3.130}$$

After combining the integrals in (3.127)–(3.128) and using (3.115), we obtain the alternative expressions:

$$\frac{1}{2}\boldsymbol{E}^{+} = \boldsymbol{E}^{i} - \iint_{S} \left[j\omega\mu G\boldsymbol{J} + \boldsymbol{M} \times \nabla' G - \frac{q}{\varepsilon} \nabla' G \right] dS' , \tag{3.131}$$

$$\frac{1}{2}\boldsymbol{H}^{+} = \boldsymbol{H}^{i} - \iint_{S} \left[j\omega\varepsilon G\boldsymbol{M} - \boldsymbol{J} \times \nabla' G - \frac{m}{\mu} \nabla' G \right] dS' . \tag{3.132}$$

These equations have been previously derived by Poggio and Miller [166], who used the Stratton–Chu formulas [188] as the starting point. To perform the procedure of taking the surface limit, Poggio and Miller have used the *hemispherical indentation* approach, which since then has been quoted in books [71, 208] and journal articles [24, 36]. An alternative method known as a *flat disk* approach has been described in [154].

3.2.1.3. Example SIE formulation

We should know now how to deal with singularities in surface integral formulations of electromagnetics. As an example, let us consider the formulation based on the zero-field approach (electric and magnetic currents for both exterior and interior equivalent problem) and the linear combinations (2.14)–(2.15). This approach has been developed by Poggio and Miller [166], and then applied by Chang and Harrington [22], as well as Wu and Tsai [218]. It is known in literature as the *PMCHW* formulation (the term composed of the initials of the names).

Equations relating fields and their sources for the exterior problem are given by (3.131), (3.132) with the media parameters set for an external environment. Similarly, for the interior equivalent problems we find (bearing in mind that there is no incident field in the internal equivalence, see Fig. 2.3):

$$\frac{1}{2}\boldsymbol{E}^{-} = \iint_{S} \left[j\omega\mu_d G_d \boldsymbol{J} + \boldsymbol{M} \times \nabla' G_d - \frac{q}{\varepsilon_d} \nabla' G_d \right] dS' , \tag{3.133}$$

$$\frac{1}{2}\boldsymbol{H}^{-} = \iint_{S} \left[j\omega\varepsilon_d G_d \boldsymbol{M} - \boldsymbol{J} \times \nabla' G_d - \frac{m}{\mu_d} \nabla' G_d \right] dS' , \tag{3.134}$$

where the currents are those defined for the exterior problem (their negatives produce fields internal to S). Applying (2.14), (2.15) and after some rearrangements, we arrive at:

$$\hat{\boldsymbol{n}}\times\boldsymbol{E}^i=\hat{\boldsymbol{n}}\times\oint_S\left[j\omega(\mu_e G_e+\mu_d G_d)\boldsymbol{J}+\boldsymbol{M}\times\nabla'(G_e+G_d)\right.$$
$$\left.-q\left(\frac{\nabla' G_e}{\varepsilon_e}+\frac{\nabla' G_d}{\varepsilon_d}\right)\right]dS', \tag{3.135}$$

$$\hat{\boldsymbol{n}}\times\boldsymbol{H}^i=\hat{\boldsymbol{n}}\times\oint_S\left[j\omega(\varepsilon_e G_e+\varepsilon_d G_d)\boldsymbol{M}-\boldsymbol{J}\times\nabla'(G_e+G_d)\right.$$
$$\left.-m\left(\frac{\nabla' G_e}{\mu_e}+\frac{\nabla' G_d}{\mu_d}\right)\right]dS'. \tag{3.136}$$

In view of (3.119), we may also express (3.135), (3.136) in the mixed-potential form:

$$\hat{\boldsymbol{n}}\times\boldsymbol{E}^i=\hat{\boldsymbol{n}}\times\left[j\omega(\boldsymbol{A}_e+\boldsymbol{A}_d)+\nabla\times\left(\frac{\boldsymbol{F}_e}{\varepsilon_e}+\frac{\boldsymbol{F}_d}{\varepsilon_d}\right)+\nabla(\Phi_e+\Phi_d)\right], \tag{3.137}$$

$$\hat{\boldsymbol{n}}\times\boldsymbol{H}^i=\hat{\boldsymbol{n}}\times\left[j\omega(\boldsymbol{F}_e+\boldsymbol{F}_d)-\nabla\times\left(\frac{\boldsymbol{A}_e}{\mu_e}+\frac{\boldsymbol{A}_d}{\mu_d}\right)+\nabla(\Psi_e+\Psi_d)\right], \tag{3.138}$$

where:

$$\boldsymbol{A}_i(\boldsymbol{r})=\mu_i\int_S\boldsymbol{J}(\boldsymbol{r}')G_i(\boldsymbol{r}\,|\,\boldsymbol{r}')dS', \tag{3.139}$$

$$\boldsymbol{F}_i(\boldsymbol{r})=\varepsilon_i\int_S\boldsymbol{M}(\boldsymbol{r}')G_i(\boldsymbol{r}\,|\,\boldsymbol{r}')dS', \tag{3.140}$$

$$\Phi_i(\boldsymbol{r})=\frac{1}{\varepsilon_i}\int_S q(\boldsymbol{r}')G_i(\boldsymbol{r}\,|\,\boldsymbol{r}')dS', \tag{3.141}$$

$$\Psi_i(\boldsymbol{r})=\frac{1}{\mu_i}\int_S m(\boldsymbol{r}')G_i(\boldsymbol{r}\,|\,\boldsymbol{r}')dS'. \tag{3.142}$$

In (3.139)–(3.142), i appropriately stands for e or d.

Bearing in mind the previous discussion as well as (3.135), (3.136), we note that the curl terms in (3.137), (3.138) may be calculated as:

$$\nabla\times\left(\frac{\boldsymbol{A}_e(\boldsymbol{r})}{\mu_e}+\frac{\boldsymbol{A}_d(\boldsymbol{r})}{\mu_d}\right)=\oint_S \boldsymbol{J}(\boldsymbol{r}')\times\nabla' G_e(\boldsymbol{r}\,|\,\boldsymbol{r}')dS'+\oint_S \boldsymbol{J}(\boldsymbol{r}')\times\nabla' G_d(\boldsymbol{r}\,|\,\boldsymbol{r}')dS', \quad (3.143)$$

$$\nabla\times\left(\frac{\boldsymbol{F}_e(\boldsymbol{r})}{\varepsilon_e}+\frac{\boldsymbol{F}_d(\boldsymbol{r})}{\varepsilon_d}\right)=\oint_S \boldsymbol{M}(\boldsymbol{r}')\times\nabla' G_e(\boldsymbol{r}\,|\,\boldsymbol{r}')dS'+\oint_S \boldsymbol{M}(\boldsymbol{r}')\times\nabla' G_d(\boldsymbol{r}\,|\,\boldsymbol{r}')dS'. \quad (3.144)$$

Thus, in the MPIE formulation (3.137), (3.138) only terms (3.143), (3.144) are evaluated as the principal-value integrals. Note also that no source terms outside integrals are present in the *PMCHW* formulation. This is because the "charge" terms normal to S have been annihilated in the process of obtaining the tangential components, whilst the "current" terms arising from both equivalent situations cancelled out in the linear combinations (2.14), (2.15). The MPIE version of the *PMCHW* formulation has been applied in practice by Umashankar, Taflove and Rao [197].

3.2.2. Volume integrals

When volume integrals concerning source region singularity are taken into account, the only problem is related to the scalar potential terms that appear in Green's functions. This is because (as stated at the beginning of section 3.2) those terms have the singularity of an order of $1/R^3$, which are not integrable in the ordinary sense. Note that all other Green's function terms have singularities of an order of $1/R^2$ or lower so no additional steps are needed to perform volume integrations. It is a different case as regards surface integrals discussed in the previous section, especially when $\underline{\underline{\boldsymbol{G}}}^{HJ}$ and $\underline{\underline{\boldsymbol{G}}}^{EM}$ Green's functions are taken into account.

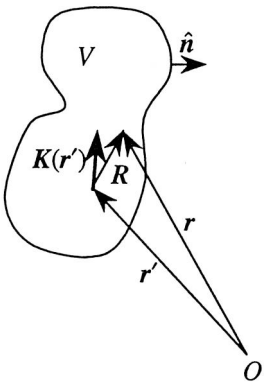

Fig. 3.5. Diagram of a general problem with the field point lying within the current region V

Therefore, the only integral we have to consider here is of the form:

$$\boldsymbol{I}(\boldsymbol{r}) = \int_V \boldsymbol{K}(\boldsymbol{r}')\nabla\nabla G(\boldsymbol{r}\,|\,\boldsymbol{r}')dV'. \tag{3.145}$$

The above-mentioned situation is depicted in Fig. 3.5, where the observation point $\boldsymbol{r}$ lies within the current carrying region V.

Because the integral of interest is performed over V, obviously a singular point when $\boldsymbol{r}$ approaches $\boldsymbol{r}'$ must be considered.

One way of handling this singularity is to use a technique similar to that presented in the previous section, i.e., exclude an infinitesimal volume V_0 from the integral and extract the principal part (Fig. 3.6).

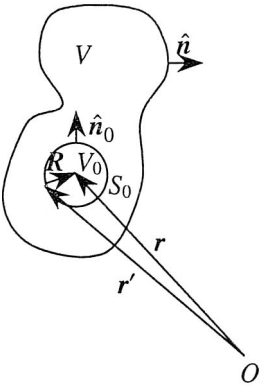

Fig. 3.6. Diagram of the principal value integration with a spherical principal volume V_0 centered around the observation point excluded from the volume V

Thus, we can write:

$$\boldsymbol{I}(\boldsymbol{r}) = \int\!\!\!\!\!\!-_V \boldsymbol{K}(\boldsymbol{r}')\nabla\nabla G(\boldsymbol{r}\,|\,\boldsymbol{r}')dV' + \boldsymbol{I}_0(\boldsymbol{r}). \tag{3.146}$$

The extracted principal part of the integral denoted by $\boldsymbol{I}_0$ is given by [208, p. 227]

$$\boldsymbol{I}_0(\boldsymbol{r}) = \lim_{R\to 0}\left[\boldsymbol{K}(\boldsymbol{r})\cdot\int_{S_0}\frac{\hat{\boldsymbol{R}}\hat{\boldsymbol{n}}_0}{4\pi R^2}\,dS'\right]. \tag{3.147}$$

The limit of the integral around S_0 in (3.147) represents the dyad that is dependent on the shape of the principal volume (non-uniform convergence), which was recognized by Van Bladel [198]. It means also that the principal value integration in (3.146) must be performed with care because it depends on the particular shape of the chosen

principal volume. Three-dimensional source dyadics for various principal volume shapes have been given by Yaghjian [221] and repeated by Wang [208, p. 228]. The calculation is particularly easy when we assume the spherical shape of V_0 (Fig. 3.6). If later we introduce the local spherical coordinate system centered at $\boldsymbol{r}$ and with the polar axis in the direction of $\boldsymbol{K}$ we get:

$$\boldsymbol{I}_0(\boldsymbol{r}) = -\frac{\boldsymbol{K}(\boldsymbol{r})}{3}. \tag{3.148}$$

This choice has been used in the volume integral equation solution given by Livesay and Chen [116], which has been obtained on the basis of the volume equivalence principle, for the case where only electric currents are present (eq. (2.29)). The application of (3.146) together with (3.21), (3.33) and (3.36) yields in the EFIE:

$$\boldsymbol{E}(\boldsymbol{r}) = \boldsymbol{E}^i - \int_V \frac{j\omega\mu}{k^2}\left(k^2 + \nabla\nabla\right)\underline{\underline{\boldsymbol{I}}}G(\boldsymbol{r}\,|\,\boldsymbol{r}')\boldsymbol{J}(\boldsymbol{r}')dV' - \frac{\boldsymbol{J}(\boldsymbol{r})}{3j\omega\varepsilon}. \tag{3.149}$$

We have to note that although the principal part has been extracted from the integral (3.145) (or (3.149)), the remaining part (the principal value) is still an improper integral, which is difficult to evaluate. Therefore, in numerical computation it may be preferable to use a small but *finite* principal volume. The formulas needed for such computations together with suitable proofs may be found in [208, Ch. 7-2]. Recently, a similar attitude has been exploited in [96].

In the principal part extraction an assumption has been applied that the current $\boldsymbol{K}$ has at least first spatial derivatives. This allows us to transform one of the divergence operators in order to operate on it, thus reducing the singularity order of the corresponding volume integral.*) This however does not mean that the functions used in the numerical solution for the current representation must also be differentiable. In fact, in calculation of (3.145), (3.149) type integrals it is a common habit to use simple (for example, pulse) expansion schemes [116, 191, 206, 208]. This however leads to convergence problems indicated in section 5.1.2.

The alternative approach of handling the integrals of (3.145) (which has been mentioned in the section devoted to SIE formulations, and which is further employed throughout this monograph) is to remain within the mixed potential representation rather than to use the dyadic Green's function to directly relate fields to the (equivalent) currents. In this approach only *one* of *nabla* operators remains inside the integral (3.145), which leads to the form:

$$\boldsymbol{I}(\boldsymbol{r}) = \nabla\int_V \boldsymbol{K}(\boldsymbol{r}')\nabla G(\boldsymbol{r}\,|\,\boldsymbol{r}')dV'. \tag{3.150}$$

*) For details, see [208].

The "outside" differential operator is still not convenient for numerical applications. However, as shown in [178], it can be neutralized in the process of reducing the initial equations to a linear set, similarly to the gradient operator present in surface current formulations; see the comments following equation (3.116). Another way of treating this operator in a numerical solution is to approximate it with finite differences, which has been applied in [176].

Now let us focus our interest on the second *nabla* operator remaining under the integral sign. Although the kernel in (3.150) is integrable even when the observation current lies within the source region, it is convenient to further reduce the singularity by transferring the differentiation to act on the current:

$$\int_V \boldsymbol{K}(\boldsymbol{r}')\nabla G(\boldsymbol{r}\,|\,\boldsymbol{r}')dV' = -\int_V \boldsymbol{K}(\boldsymbol{r}')\nabla' G(\boldsymbol{r}\,|\,\boldsymbol{r}')dV'$$

$$= -\int_V \nabla'\cdot(\boldsymbol{K}(\boldsymbol{r}')G(\boldsymbol{r}\,|\,\boldsymbol{r}'))dV' + \int_V (\nabla'\cdot\boldsymbol{K}(\boldsymbol{r}'))G(\boldsymbol{r}\,|\,\boldsymbol{r}')dV'$$

$$= -\int_S \boldsymbol{K}(\boldsymbol{r}')G(\boldsymbol{r}\,|\,\boldsymbol{r}')\hat{\boldsymbol{n}}'\,dS' + \int_V (\nabla'\cdot\boldsymbol{K}(\boldsymbol{r}'))G(\boldsymbol{r}\,|\,\boldsymbol{r}')dV', \tag{3.151}$$

where S is the surface surrounding the volume V, and $\hat{\boldsymbol{n}}$ denotes the vector normal to S pointing outside volume V. The normal component of the current in the surface integral in (3.151) can be easily interpreted when recalling the polarization current definitions (2.26) and applying the continuity equation. Applying the above procedure to EFIE (2.29), we get

$$\boldsymbol{E}(\boldsymbol{r}) = \boldsymbol{E}^i - j\omega\mu\int_V G(\boldsymbol{r}\,|\,\boldsymbol{r}')\boldsymbol{J}(\boldsymbol{r}')dV' + \nabla\frac{1}{j\omega\varepsilon}\int_V G(\boldsymbol{r}\,|\,\boldsymbol{r}')(\nabla'\cdot\boldsymbol{J}(\boldsymbol{r}'))dV'$$

$$-\nabla\frac{1}{j\omega\varepsilon}\int_S \boldsymbol{J}(\boldsymbol{r}')G(\boldsymbol{r}\,|\,\boldsymbol{r}')\hat{\boldsymbol{n}}'\,dS' \tag{3.152}$$

which, in view of (3.31) and noting that

$$\hat{\boldsymbol{n}}\cdot\boldsymbol{J}(\boldsymbol{r}) = j\omega\sigma_e(\boldsymbol{r}), \qquad \boldsymbol{r}\in S, \tag{3.153}$$

where σ_e denotes the surface electric charge density associated with the permittivity jump at S, finally gives us:

$$\boldsymbol{E}(\boldsymbol{r}) = \boldsymbol{E}^i - j\omega\mu\int_V G(\boldsymbol{r}\,|\,\boldsymbol{r}')\boldsymbol{J}(\boldsymbol{r}')dV'$$

$$-\nabla\frac{1}{\varepsilon}\int_V G(\boldsymbol{r}\,|\,\boldsymbol{r}')q(\boldsymbol{r}')dV' - \nabla\frac{1}{\varepsilon}\int_S \sigma_e(\boldsymbol{r}')G(\boldsymbol{r}\,|\,\boldsymbol{r}')dS'. \tag{3.154}$$

We see that the surface integral is simply a scalar potential of the *surface* charge, which has been noted by many authors [166, 176, 198]. This charge exists when we have a permittivity jump at the body surface (otherwise there is no equivalent current there). On the other hand, the divergence of the current in the right hand volume integral in (3.152) obviously represents the *volume* charge associated with the polarization current $\boldsymbol{J}$. Of course, to arrive at the final form of (3.154), we have to assume that the polarization current is differentiable in V. This however is not true when the body of interest has permittivity jumps *inside* (for example, it consists of a number of homogeneous regions with different electric parameters). The polarization current is then discontinuous at some boundaries of sub-regions, which can be easily checked recalling the definitions (2.26) and noting that in the absence of free charges the normal component of the flux density is continuous across the media interfaces. In this case, we can either perform the differentiation referring to the distributions theory or use formulas like (3.151) independently for each of the sub-regions with currents in a form of well-behaved functions of position. Both approaches lead to surface integrals associated with surface charges distributions [178]. Those surface charges are simply related to all permittivity (or permeability) profile jumps in the same way as (even for homogeneous body) the existing surface charge is associated with a jump between the parameters of the body and of the surrounding space*). This topic will be further investigated in Chapter 5.

For the simplest case of a homogeneous dielectric body characterized by the permittivity $\hat{\varepsilon}$, we may specify more precisely (3.154) recalling the polarization current definition (2.26). For this case we have:

$$\nabla \cdot \boldsymbol{J}(\boldsymbol{r}) = \nabla \cdot j\omega(\hat{\varepsilon} - \varepsilon)\boldsymbol{E}(\boldsymbol{r}) = j\omega \frac{(\hat{\varepsilon} - \varepsilon)}{\varepsilon} \nabla \cdot (\varepsilon \boldsymbol{E}(\boldsymbol{r})) = 0, \tag{3.155}$$

which holds in V because in the absence of impressed sources the electric flux density is divergenceless.

Consequently, the second integral in (3.154) disappears, yielding:

$$\boldsymbol{E}(\boldsymbol{r}) = \boldsymbol{E}^i - j\omega\mu \int_V G(\boldsymbol{r} \mid \boldsymbol{r}')\boldsymbol{J}(\boldsymbol{r}')dV' - \nabla \frac{1}{\varepsilon} \int_S \sigma_e(\boldsymbol{r}')G(\boldsymbol{r} \mid \boldsymbol{r}')dS', \tag{3.156}$$

or, in terms of the internal electric field

$$\boldsymbol{E}(\boldsymbol{r}) = \boldsymbol{E}^i + \omega^2\mu(\hat{\varepsilon} - \varepsilon) \int_V G(\boldsymbol{r} \mid \boldsymbol{r}')\boldsymbol{E}(\boldsymbol{r}')dV' - \frac{\hat{\varepsilon} - \varepsilon}{\varepsilon} \nabla \int_S \boldsymbol{E}(\boldsymbol{r}')G(\boldsymbol{r} \mid \boldsymbol{r}')\hat{\boldsymbol{n}}'dS'. \tag{3.157}$$

Equation (3.157) has been given in [166] and used, for example, in [176].

*) This surface charge obviously exists in the *equivalent* situation.

Summarizing the second approach presented in this section, we can state that the particularly effective procedure of handling the $1/R^3$ singularity consists in relating the scalar potential to the charges that arise from the equivalent current distribution. Note that in this solution we have to integrate only the kernels with $1/R$ singularities for which a number of effective integration techniques (both analytic as well as numerical) have been developed [49, 214, 33, 94, 113].

3.3. Mixed potential representation for multilayer media

From the discussion regarding singular integrals in the preceding section, we gather that the particularly convenient ways of handling the singularities concern the use of so-called mixed-potential fields representations, which do not require extraction of principal parts. This approach generally uses vector potentials calculated from the distribution of currents and scalar potentials related to the charges. For the free space situation this can be summarized with the field formulas (3.17), (3.18) and potential representations (3.27)–(3.30).

The most important feature of these formulations is the fact that integrals (3.27)–(3.30) have the kernels with only $1/R$ singularity, which means that they are integrable without referring to principal integration techniques. On the other hand, the presence of derivatives of currents (or fields) inherent in this formulation imposes additional requirements on the basis functions used in the process of transformation of equations into a set of linear equations (see section 5.1).

Unfortunately, the approach outlined above cannot be transposed to the case of multilayer environments in a straightforward manner, because during the development of (3.116) and (3.151) specific properties of the *free space* Green's function have been used extensively. Those properties (like equation (3.115)) are however not valid if multilayer media Green's functions are considered. It is because scalar potential kernels associated with horizontal and vertical dipoles placed in stratified environments are in general different [17, 133, 140, 141]. However, the solution to this problem exists, and we will shortly discuss it in the subsequent paragraphs. For the sake of clarity, we will assume that only electric currents are present in the formulation. Of course, corresponding formulas for magnetic currents and related potentials may be easily obtained by duality.

A general situation is presented in Fig. 3.7. The dielectric body, which may be either homogeneous or heterogeneous, is embedded in a general multilayer medium with horizontal stratification. Note that the body penetrates some interfaces between homogeneous media.

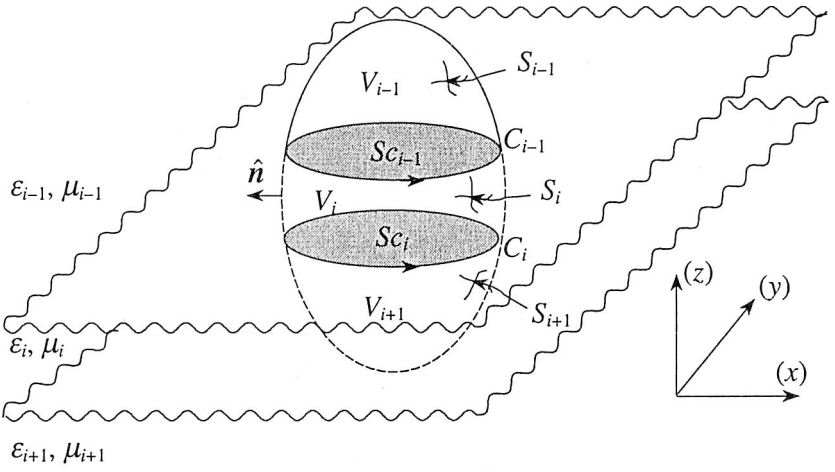

Fig. 3.7. Dielectric body in a multilayer environment

In the next two sections we will discuss cases where only surface currents flowing on the body surface S are present in the formulation (homogeneous body) or when volume currents are present in the body volume V (heterogeneous body). In view of the assumption about the presence of only electric currents, we note that our interest is focused on the $\underline{\underline{G}}^{EJ}$ dyadic Green's function. We also note that in section 3.1.2 we have already obtained the expressions for $\underline{\underline{G}}^{A}$ Green's function, so we are able to calculate the vector potential from the given current distribution. What remains to be done is to deal with the second derivatives of $\underline{\underline{G}}^{A}$ present in (3.23), which are responsible for the undesired $1/R^3$ kernel singularity. The solution that we want to achieve, is to leave one of *nabla* operators outside the integrals concerning the kernel $\nabla\nabla\underline{\underline{G}}^{A}$, and to transfer the remaining one to act on the current in the way similar to (3.116) or (3.150). Summarizing the above comments: for a case of electric currents we want to be able to calculate the electric field from a "multilayer" counterpart of (3.1), when the vector and scalar potentials are calculated from the respective current and charge distributions.

It can be shown [140, 141] that this is possible to accomplish if we find a scalar function G^{Φ}, such that:

$$\nabla\cdot\left(\frac{1}{\mu}\underline{\underline{G}}^{A}(\boldsymbol{r}\,|\,\boldsymbol{r}')\right)=-\varepsilon\,\nabla' G^{\Phi}(\boldsymbol{r}\,|\,\boldsymbol{r}'), \tag{3.158}$$

which can be treated as a counterpart of (3.115) with the difference that the left-hand *nabla* operator acts on a dyadic rather than on a scalar function.

Unfortunately, there is in general no G^{Φ} such that would satisfy (3.158) [133]. Therefore, instead of (3.158) the following decomposition is used [141]:

$$\frac{1}{\varepsilon}\nabla\cdot\left(\frac{1}{\mu}\underline{\underline{G}}^{A}(\boldsymbol{r}\,|\,\boldsymbol{r}')\right)=-\nabla' K^{\Phi}(\boldsymbol{r}\,|\,\boldsymbol{r}')+\boldsymbol{C}^{\Phi}(\boldsymbol{r}\,|\,\boldsymbol{r}'). \tag{3.159}$$

The only difference between (3.158) and (3.159) is the "correction term" comprising the vector $\boldsymbol{C}^{\Phi}$. The decomposition (3.159) is not unique [141], providing for a possibility of many formulations. Three formulations denoted by A, B and C have been introduced and discussed in [141]. Here we will concentrate on formulation C, the advantages of which will be seen later.

In this case, we assume a correction term of the following form:

$$\boldsymbol{C}^{\Phi}(\boldsymbol{r}\,|\,\boldsymbol{r}')=C^{\Phi}(\boldsymbol{r}\,|\,\boldsymbol{r}')\hat{z}, \tag{3.160}$$

where C^{Φ} is referred to as the *Michalski correction factor.*

The expressions for K^{Φ} and C^{Φ} are most easily found in the spectral domain, where:

$$\tilde{\nabla}' = j\boldsymbol{k}_{\rho}+\hat{z}\frac{d}{dz'}. \tag{3.161}$$

Later, substituting (3.93) into the spectral domain counterpart of (3.159), and using (3.96)–(3.101), as well as (3.78)–(3.80), we get:

$$-\frac{\tilde{K}^{\Phi}}{j\omega}=\frac{1}{k_{\rho}^{2}}\left(V_{i}^{h}-V_{i}^{e}\right), \tag{3.162}$$

$$-\frac{\tilde{C}^{\Phi}}{j\omega}=\frac{j\omega\mu'}{k_{\rho}^{2}}\left(V_{v}^{h}-V_{v}^{e}\right). \tag{3.163}$$

Let us now focus our interest on the scalar potential term

$$\Phi(\boldsymbol{r})=-\frac{1}{j\omega\varepsilon}\left\langle\nabla\cdot\left(\frac{1}{\mu}\underline{\underline{G}}^{A}(\boldsymbol{r}\,|\,\boldsymbol{r}')\right);\boldsymbol{J}(\boldsymbol{r}')\right\rangle, \tag{3.164}$$

which for the case of homogeneous region could be given in a more familiar form (see equations (3.1) and (3.9)):

$$\Phi(\boldsymbol{r})=\frac{j\omega}{k^{2}}\left\langle\nabla\cdot\underline{\underline{G}}^{A}(\boldsymbol{r}\,|\,\boldsymbol{r}');\boldsymbol{J}(\boldsymbol{r}')\right\rangle. \tag{3.165}$$

We want to use (3.159) to transform the differentiation to act on the current instead of $\underline{\underline{G}}^A$. Further calculations depend on whether we deal with the surface or volume integral formulations.

3.3.1. MPIE for the surface current-based problems

The formula for a scalar potential for currents belonging to one particular layer i has the form:

$$\Phi^i(\boldsymbol{r}) = -\frac{1}{j\omega\varepsilon}\int_{S_i} \nabla\cdot\left(\frac{1}{\mu}\underline{\underline{G}}^A(\boldsymbol{r}\,|\,\boldsymbol{r}')\right)\boldsymbol{J}(\boldsymbol{r}')dS', \tag{3.166}$$

where S_i denotes the part of S within the layer i (see Fig. 3.7).

Substituting (3.159) into (3.166), we get

$$\Phi^i(\boldsymbol{r}) = \frac{1}{j\omega}\int_{S_i} \nabla' K^\Phi(\boldsymbol{r}\,|\,\boldsymbol{r}')\boldsymbol{J}(\boldsymbol{r}')dS' - \frac{1}{j\omega}\int_{S_i} \boldsymbol{C}^\Phi(\boldsymbol{r}\,|\,\boldsymbol{r}')\boldsymbol{J}(\boldsymbol{r}')dS'. \tag{3.167}$$

The first integral in (3.167) may be further transformed using vector [199, p. 487] and the Gauss theorem [199, p. 503]. Finally, we get

$$\Phi^i(\boldsymbol{r}) = -\frac{1}{j\omega}\int_{S_i} K^\Phi(\boldsymbol{r}\,|\,\boldsymbol{r}')(\nabla'\cdot\boldsymbol{J}(\boldsymbol{r}'))dS' - \frac{1}{j\omega}\int_{S_i} \boldsymbol{C}^\Phi(\boldsymbol{r}\,|\,\boldsymbol{r}')\boldsymbol{J}(\boldsymbol{r}')dS'$$

$$+\frac{1}{j\omega}\left[\oint_{C_i} K^\Phi(\boldsymbol{r}\,|\,\boldsymbol{r}')\boldsymbol{J}(\boldsymbol{r}')\cdot\hat{\boldsymbol{u}}_i dC' - \oint_{C_{i-1}} K^\Phi(\boldsymbol{r}\,|\,\boldsymbol{r}')\boldsymbol{J}(\boldsymbol{r}')\cdot\hat{\boldsymbol{u}}_{i-1} dC'\right]. \tag{3.168}$$

C_i and C_{i-1} are the contours formed by the intersection of S_i with interfaces at $z = z_i$ and $z = z_{i-1}$, respectively, and $\hat{\boldsymbol{u}}_i$ and $\hat{\boldsymbol{u}}_{i-1}$ are the unit vectors perpendicular at $\boldsymbol{r}'$ to C_i and C_{i-1}, respectively, in the planes tangent to S_i [141] (see Fig. 3.8).

In this particular formulation (formulation C), the kernel K^Φ is a continuous function of z' [141], due to which the contour integrals from adjacent layers cancel out and therefore there is no need for their remaining in the expressions*).

*) We perform the calculations assuming that we deal with the layered structure consisting of a number of homogeneous layers, which is shown in Fig. 3.7. However, the expression is also correct for media with other than stepped parameter profiles in the z direction. A situation like this could be thought of as a medium with an infinite number of infinitesimally thin homogeneous layers. In this context, the statements concerning cancelling out the contour integrals remain valid.

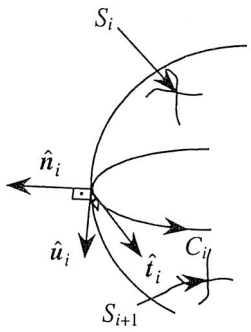

$$\hat{u}_i = \hat{t}_i \times \hat{n}_i$$

Fig. 3.8. Detail of contour C_i with unit vectors $\hat{u}_i$, $\hat{t}_i$ and $\hat{n}_i$ [141]

Finally, taking into account the continuity equation, we obtain a formula for the electric field:

$$\boldsymbol{E}(\boldsymbol{r}) = -j\omega \int_S \underline{\underline{\boldsymbol{G}}}^A(\boldsymbol{r}\,|\,\boldsymbol{r}') \cdot \boldsymbol{J}(\boldsymbol{r}')dS' - \nabla \int_S K^{\Phi}(\boldsymbol{r}\,|\,\boldsymbol{r}')q(\boldsymbol{r}')dS'$$

$$+ \frac{1}{j\omega} \nabla \int_S C^{\Phi}(\boldsymbol{r}\,|\,\boldsymbol{r}')\hat{z} \cdot \boldsymbol{J}(\boldsymbol{r}')dS'. \tag{3.169}$$

We note that the integral arising from the correction term may now be grouped with the vector potential term giving:

$$\boldsymbol{E}(\boldsymbol{r}) = -j\omega \int_S \underline{\underline{\boldsymbol{K}}}^A(\boldsymbol{r}\,|\,\boldsymbol{r}') \cdot \boldsymbol{J}(\boldsymbol{r}')dS' - \nabla \int_S K^{\Phi}(\boldsymbol{r}\,|\,\boldsymbol{r}')q(\boldsymbol{r}')dS', \tag{3.170}$$

with:

$$\underline{\underline{\boldsymbol{K}}}^A(\boldsymbol{r}\,|\,\boldsymbol{r}') = \underline{\underline{\boldsymbol{G}}}^A(\boldsymbol{r}\,|\,\boldsymbol{r}') + \frac{1}{\omega^2} \nabla C^{\Phi}(\boldsymbol{r}\,|\,\boldsymbol{r}')\hat{z}. \tag{3.171}$$

We note that (3.170) is in the desired mixed potential form, which may be recognized as a multilayer counterpart of (3.17) (if the magnetic currents are not present the term concerning $\boldsymbol{F}$ potential disappears). The only difference is the dyadic character of the vector potential kernel.

The explicit form of $\underline{\underline{\boldsymbol{K}}}^A$ may be easily obtained in the spectral domain directly from (3.171) by using (3.93) as well as (3.163). Thus, based on (3.171) we have:

$$\underline{\underline{\tilde{\boldsymbol{K}}}}^A = \underline{\underline{\tilde{\boldsymbol{G}}}}^A - \hat{u}\hat{z}\frac{jk_\rho}{\omega^2}\tilde{C}^{\Phi} + \hat{z}\hat{z}\frac{1}{\omega^2}\frac{d}{dz}\tilde{C}^{\Phi}. \tag{3.172}$$

Substituting (3.93) into (3.172), we get:

$$\underline{\underline{\tilde{K}}}^{A} = (\hat{u}\hat{u} + \hat{v}\hat{v})\tilde{G}_{vv}^{A} + \hat{z}\hat{u}\tilde{G}_{zu}^{A} + \hat{u}\hat{z}\tilde{K}_{uz} + \hat{z}\hat{z}\tilde{K}_{zz}^{A}, \tag{3.173}$$

which expressed in a matrix form gives:

$$\left[\tilde{K}^{A}\right] = \begin{bmatrix} \tilde{G}_{vv}^{A} & 0 & \frac{k_x}{k_\rho}\tilde{K}_{uz}^{A} \\ 0 & \tilde{G}_{vv}^{A} & \frac{k_y}{k_\rho}\tilde{K}_{uz}^{A} \\ \frac{k_x}{k_\rho}\tilde{G}_{zu}^{A} & \frac{k_y}{k_\rho}\tilde{G}_{zu}^{A} & \tilde{K}_{zz}^{A} \end{bmatrix}. \tag{3.174}$$

We see that in comparison with (3.94) we have two additional entries in the dyadic kernel, and that one of the existing kernels is modified.

Using (3.163), we get the formula for $\tilde{K}_{uz}^{A}$:

$$j\omega\tilde{K}_{uz}^{A} = \frac{\omega\mu'}{k_\rho}\left(V_v^h - V_v^e\right). \tag{3.175}$$

Based on (3.101), (3.172) and (3.163), we get:

$$j\omega\tilde{K}_{zz}^{A} = \frac{\mu}{\varepsilon'}I_v^e + \frac{j\omega\mu'}{k_\rho^2}\frac{d}{dz}\left(V_v^h - V_v^e\right), \tag{3.176}$$

which after applying (3.79) gives us:

$$j\omega\tilde{K}_{zz}^{A} = \frac{\mu}{\varepsilon'}\left[\left(1 + \frac{k'^2}{k^2}\right)I_v^e + \frac{k'^2}{k_\rho^2}\left(I_v^h - I_v^e\right)\right]. \tag{3.177}$$

Again, the space-domain counterparts of the spectral kernels can be expressed in terms of Sommerfeld integrals (3.90)–(3.91). Finally, we have:

$$G_{xx}^{A}(\boldsymbol{\rho}; z \mid z') = G_{yy}^{A}(\boldsymbol{\rho}; z \mid z') = S_0\left\{\tilde{G}_{vv}^{A}(k_\rho; z \mid z')\right\}, \tag{3.178}$$

$$G_{zz}^{A}(\boldsymbol{\rho}; z \mid z') = S_0\left\{\tilde{G}_{zz}^{A}(k_\rho; z \mid z')\right\}, \tag{3.179}$$

$$G_{zx}^{A}(\boldsymbol{\rho}; z \mid z') = -j\cos\varphi S_1\left\{\tilde{G}_{zu}^{A}(k_\rho; z \mid z')/k_\rho\right\}, \tag{3.180}$$

$$G_{zy}^{A}(\boldsymbol{\rho}; z \mid z') = -j\sin\varphi S_1\left\{\tilde{G}_{zu}^{A}(k_\rho; z \mid z')/k_\rho\right\}, \tag{3.181}$$

$$K^{\Phi}(\rho; z \mid z') = S_0\left\{\tilde{K}^{\Phi}(k_\rho; z \mid z')\right\}, \tag{3.182}$$

$$C^{\Phi}(\rho; z \mid z') = S_0\left\{\tilde{C}^{\Phi}(k_\rho; z \mid z')\right\}, \tag{3.183}$$

$$K^{A}_{xz}(\rho; z \mid z') = -j\cos\varphi S_1\left\{\tilde{K}^{A}_{uz}(k_\rho; z \mid z')/k_\rho\right\}, \tag{3.184}$$

$$K^{A}_{yz}(\rho; z \mid z') = -j\sin\varphi S_1\left\{\tilde{K}^{A}_{uz}(k_\rho; z \mid z')/k_\rho\right\}, \tag{3.185}$$

$$K^{A}_{zz}(\rho; z \mid z') = S_0\left\{\tilde{K}^{A}_{zz}(k_\rho; z \mid z')\right\}. \tag{3.186}$$

Note that, in fact, only three distinct Sommerfeld integrals appear in $\underline{\underline{G}}^{A}$, and four in $\underline{\underline{K}}^{A}$.

3.3.2. MPIE for the volume current-based problems

When the problem is described in terms of volume electric current, we can obtain the scalar potential based on (3.167) by replacing the surface integrals with volume integrals:

$$\Phi^{i}(\boldsymbol{r}) = -\frac{1}{j\omega}\int_{V_i}\nabla' K^{\Phi}(\boldsymbol{r} \mid \boldsymbol{r}')\boldsymbol{J}(\boldsymbol{r}')dV' - \frac{1}{j\omega}\int_{V_i} C^{\Phi}(\boldsymbol{r} \mid \boldsymbol{r}')\boldsymbol{J}(\boldsymbol{r}')dV'. \tag{3.187}$$

Steps similar to those from the previous section give us:

$$\Phi^{i}(\boldsymbol{r}) = -\frac{1}{j\omega}\int_{V_i} K^{\Phi}(\boldsymbol{r} \mid \boldsymbol{r}')(\nabla' \cdot \boldsymbol{J}(\boldsymbol{r}'))dV' - \frac{1}{j\omega}\int_{V_i} C^{\Phi}(\boldsymbol{r} \mid \boldsymbol{r}')\boldsymbol{J}(\boldsymbol{r}')dV'$$

$$+\frac{1}{j\omega}\left[-\int_{Sc_i} K^{\Phi}(\boldsymbol{r} \mid \boldsymbol{r}')\boldsymbol{J}(\boldsymbol{r}')\cdot\hat{z}\,dS' + \int_{Sc_{i-1}} K^{\Phi}(\boldsymbol{r} \mid \boldsymbol{r}')\boldsymbol{J}(\boldsymbol{r}')\cdot\hat{z}\,dS'\right.$$

$$\left.+\int_{S_i} K^{\Phi}(\boldsymbol{r} \mid \boldsymbol{r}')\boldsymbol{J}(\boldsymbol{r}')\cdot\hat{\boldsymbol{n}}'\,dS'\right]. \tag{3.188}$$

In view of (3.153), the surface integrals in (3.188) are easily recognized as scalar potentials of surface charges present at the surface of a "slice" of the body confined to the layer i. We note that the "side" surface integral (integral over S_i) exists also in free-space counterpart of (3.188). In contrast to the surface current approach given in

the preceding section, the remaining two integrals, in general, do not disappear even when the scalar potential kernel is a continuous function of z' at the interfaces of media, because the component of the equivalent current normal to the intersection is not continuous even for a homogeneous dielectric body. We can however treat the related charges in exactly the same way as other surface charges existing inside the body because of jumps in the permittivity profile, as discussed at the end of section 3.2.2.

We also note the first volume integral in (3.188) represents a scalar potential of volume charge distributions, while the second one, which is related to the correction term can be easily grouped with the vector potential kernel. This leads to the same expressions for the modified vector potential kernel as in the surface current approach.

* * *

In this section, we have discussed the case where only electric currents are present. In a case of only magnetic currents being present, the analysis is dual to that presented above. We can obtain the mixed-potential representations for the magnetic field $\boldsymbol{H}$ by the replacement of symbols [140]: $\boldsymbol{E} \to \boldsymbol{H}$, $\boldsymbol{J} \to \boldsymbol{M}$, $q \to m$, $\boldsymbol{A} \to \boldsymbol{F}$, $\Phi \to \Psi$, $\varepsilon \to \mu$, $\mu \to \varepsilon$, $V \to I$, $I \to V$, $v \to i$, $i \to v$, $e \to h$, and $h \to e$. When both types of currents are required, we simply apply the superposition principle.

The author considers the systematic description of singular terms arising in the surface integral formulations as his original contribution. Up to now, those aspects have not been deeply understood within the electromagnetics community, which resulted in inconsistent or wildly erratic derivations [17, 36]. Also the discussion of VIE problems in section 3.3.2 is presented for the first time.

Chapter 4. Bodies of revolution

In the preceding chapter we have provided useful formulas enabling the calculation of fields for the given current distributions, both for the case of bodies within free space and bodies within a general multilayer environment. We also know how to deal with the singularities encountered when we want to calculate fields within the source regions. Now, what we have to deal with is the problem of performing the surface or volume integrations. The integrations for bodies of arbitrary shape and/or permittivity/permeability distribution are usually performed numerically. Those numerical integrations are in most cases very time consuming, taking into account that, especially in the method-of-moments solution (Chapter 5), they must be repetitively calculated for a large number of observation points. This seriously limits the application of the techniques presented, especially when volume integrals are concerned [178]. However, it is possible to greatly reduce this problem if the specified geometrical structure is characterized by some symmetries. For example, we can reduce the computational effort making use of *reflection* symmetries within the formulation. In this case we can simply modify Green's functions, taking into account images in perfect electric or perfect magnetic conductors [62] and thus confine the solution to a fraction of the original problem. Another example is the *translational* symmetry encountered in so-called *periodic* structures. Here, by applying an expansion into Fourier series, we can reduce the solution to a single "period" of the original problem. As a special case of this type of symmetry, we may consider a rectangular waveguide, where through repetitive imaging of the geometry around the waveguide walls we come to this kind of periodic structure [62, 140].

In this chapter, we will present in more detail another possible solution, which is useful if the dielectric body of interest is characterized by *rotational symmetry*. Problems of such kind are known in literature as Body-of-Revolution (BOR) formulations [6, 20, 42, 125, 130, 202]. As the representative case, we will closely investigate volume current models using only electric currents (which is equivalent to the assumption that the magnetic permeability of the body is the same as that of the surrounding environment). Next, we will generalize the specification to a case of multilayer media.

The material given in this chapter is, with the exception of section 4.4, the author's original contribution.

4.1. Azimuthal modes; modal MPIE for free space*)

Let us assume that the inhomogeneous dielectric body of interest with a complex dielectric constant $\hat{\varepsilon}(\boldsymbol{r}) = \varepsilon(\boldsymbol{r}) - j\sigma(\boldsymbol{r})/\omega$, (where ε and σ are the media permittivity and conductivity at the position $\boldsymbol{r}$), is immersed in a medium characterized by parameters ε_0 and μ_0.

This body is illuminated by an incident field $\boldsymbol{E}^i$, defined as the field present in the absence of the body.

In the presence of the body the total electric field consists of the „incident" and „scattered" fields (2.29):

$$\boldsymbol{E}(\boldsymbol{r}) = \boldsymbol{E}^i(\boldsymbol{r}) + \boldsymbol{E}^s(\boldsymbol{r}), \tag{4.1}$$

where the scattered field is excited by the polarization current $\boldsymbol{J}$ (2.26):

$$\boldsymbol{J}(\boldsymbol{r}) = j\omega[\hat{\varepsilon}(\boldsymbol{r}) - \varepsilon_0]\boldsymbol{E}(\boldsymbol{r}). \tag{4.2}$$

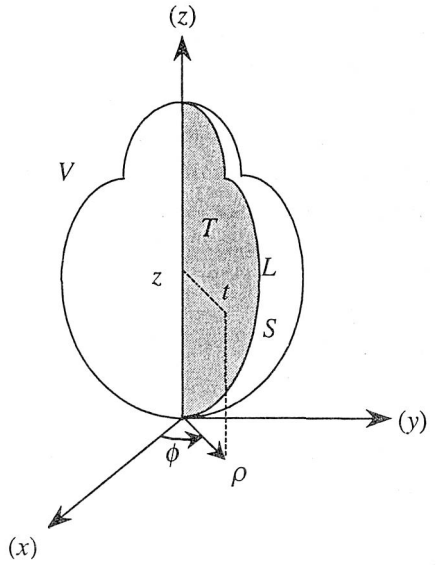

Fig. 4.1. Body of revolution and coordinate system

$\boldsymbol{E}^s$ is related to the polarization current $\boldsymbol{J}$ through the following formulas (see Chapter 3):

*) This section has been written on the basis of the author's articles [104, 105].

$$\boldsymbol{E}^s(\boldsymbol{r}) = -j\omega \boldsymbol{A}(\boldsymbol{r}) - \nabla \Phi(\boldsymbol{r}), \tag{4.3}$$

$$\boldsymbol{A}(\boldsymbol{r}) = \frac{\mu_0}{4\pi} \int_V G(\boldsymbol{r}, \boldsymbol{r}') \boldsymbol{J}(\boldsymbol{r}') dV', \tag{4.4}$$

$$\Phi(\boldsymbol{r}) = \frac{1}{4\pi\varepsilon_0} \int_V G(\boldsymbol{r}, \boldsymbol{r}') q(\boldsymbol{r}') dV', \tag{4.5}$$

where:

$$G(\boldsymbol{r}, \boldsymbol{r}') = \frac{e^{-jk_0|\boldsymbol{r}-\boldsymbol{r}'|}}{|\boldsymbol{r}-\boldsymbol{r}'|}, \tag{4.6}$$

$$k_0 = \omega\sqrt{\varepsilon_0\mu_0} = 2\pi/\lambda_0. \tag{4.7}$$

The charge density $q(\boldsymbol{r})$ is related to the polarization current in (4.2) by the continuity equation:

$$\nabla \cdot \boldsymbol{J}(\boldsymbol{r}) = -j\omega q(\boldsymbol{r}). \tag{4.8}$$

Formula (4.1) is in fact an integro-differential equation for the polarization current $\boldsymbol{J}$. We can see that in the above formulas we have referred to the mixed-potential field representation.

Now let us further assume that the body is characterized by a rotational symmetry (Fig. 4.1). First, we shall rewrite the formulas above for the polar coordinate system associated with the axis of symmetry of the body. Formulas (4.1) through (4.3), as well as (4.8) will, of course, remain in the same form, with the position vector $\boldsymbol{r}$ expressed in terms of (ρ, z, ϕ), which are the usual cylindrical coordinates. The potential formulas will be slightly modified:

$$\boldsymbol{A}(\rho, z, \phi) = \frac{\mu_0}{4\pi} \int_V \boldsymbol{J}(\rho', z', \phi') \underline{\underline{\Gamma}}(\rho, z, \phi, \rho', z', \phi') dV', \tag{4.9}$$

$$\Phi(\rho, z, \phi) = \frac{1}{4\pi\varepsilon_0} \int_V q(\rho', z', \phi') G(\rho, z, \phi, \rho', z', \phi') dV', \tag{4.10}$$

where:

$$\underline{\underline{\Gamma}} = \begin{bmatrix} G\cos(\phi - \phi') & 0 & G\sin(\phi - \phi') \\ 0 & G & 0 \\ -G\sin(\phi - \phi') & 0 & G\cos(\phi - \phi') \end{bmatrix}, \tag{4.11}$$

$$G = G(\rho, z, \phi, \rho', z', \phi') = \frac{e^{-jk_0 R}}{R}, \tag{4.12}$$

$$R = \sqrt{\rho^2 + \rho'^2 - 2\rho\rho'\cos(\phi - \phi') + (z - z')^2} \,. \tag{4.13}$$

Remember that all media parameters are independent of the azimuthal variable ϕ. This fact allows us to expand all fields, currents, charges and potentials into Fourier series in ϕ [42], which leads to the formulas:

$$\boldsymbol{E}^i = \sum_{m=-\infty}^{\infty} \boldsymbol{E}^i_m(\rho, z) e^{jm\phi} \,, \tag{4.14}$$

$$\boldsymbol{J} = \sum_{m=-\infty}^{\infty} \boldsymbol{J}_m(\rho, z) e^{jm\phi} \,, \tag{4.15}$$

$$q = \sum_{m=-\infty}^{\infty} q_m(\rho, z) e^{jm\phi} \,, \tag{4.16}$$

$$\boldsymbol{A} = \sum_{m=-\infty}^{\infty} \boldsymbol{A}_m(\rho, z) e^{jm\phi} \,, \tag{4.17}$$

$$\Phi = \sum_{m=-\infty}^{\infty} \Phi_m(\rho, z) e^{jm\phi} \,. \tag{4.18}$$

Substituting these expansions into formulas (4.1) to (4.8), applying the orthogonality of azimuthal harmonics [6, 42, 125] and performing the integrations over ϕ' we get:

$$\boldsymbol{E}_m(\rho, z) = \boldsymbol{E}^i_m(\rho, z) + \boldsymbol{E}^s_m(\rho, z), \tag{4.19}$$

$$\boldsymbol{J}_m(\rho, z) = j\omega[\hat{\varepsilon}(\rho, z) - \varepsilon_0]\boldsymbol{E}_m(\rho, z), \tag{4.20}$$

$$\boldsymbol{E}^s_m(\rho, z) = -j\omega\, \boldsymbol{A}_m(\rho, z) - \nabla_m \Phi_m(\rho, z), \tag{4.21}$$

where:

$$\boldsymbol{A}_m = \frac{\mu_0}{4\pi} \int_T \underline{\underline{\boldsymbol{\Gamma}}}_m \boldsymbol{J}_m \rho' dT' \,, \tag{4.22}$$

$$\underline{\underline{\boldsymbol{\Gamma}}}_m = \begin{bmatrix} \Gamma^m_{\rho\rho} & \Gamma^m_{\rho z} & \Gamma^m_{\rho\phi} \\ \Gamma^m_{z\rho} & \Gamma^m_{zz} & \Gamma^m_{z\phi} \\ \Gamma^m_{\phi\rho} & \Gamma^m_{\phi z} & \Gamma^m_{\phi\phi} \end{bmatrix} = \begin{bmatrix} \dfrac{G_{m-1} + G_{m+1}}{2} & 0 & \dfrac{G_{m-1} - G_{m+1}}{2j} \\ 0 & G_m & 0 \\ \dfrac{G_{m+1} - G_{m-1}}{2j} & 0 & \dfrac{G_{m-1} + G_{m+1}}{2} \end{bmatrix}. \tag{4.23}$$

Here, we have introduced the "modal" Green's function defined by:

$$G(\rho, z, \rho', z', \phi - \phi') = \frac{e^{-jk_0 R}}{R} = \frac{1}{2\pi} \sum_{m=-\infty}^{\infty} G_m(\rho, z, \rho', z') e^{jm(\phi - \phi')}, \tag{4.24}$$

$$G_m(\rho, z, \rho', z') = \int_0^{2\pi} G(\rho, z, \rho', z', \alpha) e^{-jm\alpha} d\alpha. \tag{4.25}$$

The integration (4.22) is on the transverse surface of the BOR (see Fig. 4.1). Note that $R = |\boldsymbol{r} - \boldsymbol{r}'|$ is periodic with respect to variable $(\phi - \phi')$ (equation 4.13) from which the Fourier expansion (4.24), (4.25) follows.

The scalar potential is defined as:

$$\Phi_m = \frac{1}{4\pi\varepsilon_0} \int_T q_m G_m \rho' dT', \tag{4.26}$$

where the electric charge density q_m is related to the current J_m through the modal continuity equation:

$$q_m = -\frac{1}{j\omega} \nabla_m \cdot \boldsymbol{J}_m = -\frac{1}{j\omega} \left[\frac{1}{\rho'} \frac{\partial (\rho' J_m^{\rho})}{\partial \rho} + \frac{\partial J_m^{z}}{\partial z} + \frac{jm}{\rho'} J_m^{\phi} \right]. \tag{4.27}$$

In equation (4.27) we introduce the harmonic divergence. We also define the harmonic gradient operator:

$$\nabla_m \Phi_m = \hat{\boldsymbol{\rho}} \frac{1}{\rho} \frac{\partial (\rho \Phi_m)}{\partial \rho} + \hat{z} \frac{\partial \Phi_m}{\partial z} + \hat{\boldsymbol{\varphi}} \frac{jm}{\rho} \Phi_m. \tag{4.28}$$

Note that although the above modal formulas look a little bit more complicated than their full three-dimensional counterparts in the Cartesian coordinate system, we have the advantage of reducing the problem dimensions. The integrations needed to calculate the potentials are now surface integrals instead of volume integrals in the original expressions. This reduces considerably the number of unknowns needed in the approximation procedure and thus enables the handling of basically impossible situations (from a practical point of view, e.g., limited computer resources) in full 3D models. An observant reader may find that theoretically we should solve an infinite number of equations (4.19). In practice, however, the solution is usually limited to the first few modes, which follows from the modal expansion of incident fields (see Chapter 6).

The idea of modal decomposition of the problem presented here may be easily applied to surface current models. In this case, we gain a reduction of surface integrals to line integrals along the generating arc of the body denoted by L in Fig. 4.1. Furthermore, since the equivalent currents flow *on* the surface of the body, the components ρ and z in the corresponding equations are usually grouped together to form one

transverse (to $\hat{\varphi}$) unknown current [6, 42, 125, 130]. An additional requirement in this case is also to calculate the magnetic fields related to electric currents (and maybe the electric and magnetic fields related to the magnetic currents). In order to accomplish this we also need to define the Fourier-harmonic curl operator [42]:

$$\nabla_m \times A_m = \begin{vmatrix} \frac{1}{\rho}\hat{\rho} & \hat{\varphi} & \frac{1}{\rho}\hat{z} \\ \frac{\partial}{\partial \rho} & jm & \frac{\partial}{\partial z} \\ A_m^{\rho} & \rho A_m^{\phi} & A_m^{z} \end{vmatrix}. \tag{4.29}$$

4.2. Modal VIE in layered media*)

An approach similar to the above may be easily applied to the case of multilayer environments, under the assumption that the symmetry axis of the BOR is perpendicular to the stratification (Fig. 4.2).

If we apply the MPIE approach again, the only difference in comparison with formulas presented in section 4.1 is the character of the kernels used to calculate the vector and scalar potentials. According to (3.170) in the case of volume current approach we have:

$$A(r) = \int_V \underline{\underline{K}}^A(r \mid r') \cdot J(r') dV', \tag{4.30}$$

$$\Phi(r) = \int_V K^{\Phi}(r \mid r') q(r') dV'. \tag{4.31}$$

For the sake of completeness, let us list the final formulas (3.178)–(3.186) for the entries of $\underline{\underline{K}}^A$ and K^{Φ}:

$$K_{xx}^A = K_{yy}^A = \frac{1}{j\omega} S_0 \{V_i^h\}, \tag{4.32}$$

$$K_{zz}^A = \frac{1}{j\omega} \frac{\mu}{\varepsilon'} S_0 \left\{ \left(1 + \frac{k'^2}{k^2} \right) I_v^e + \frac{k'^2}{k_\rho^2} \left(I_v^h - I_v^e \right) \right\}, \tag{4.33}$$

*) The material presented in this section has been previously published by the author in [100, 101, 102, 103].

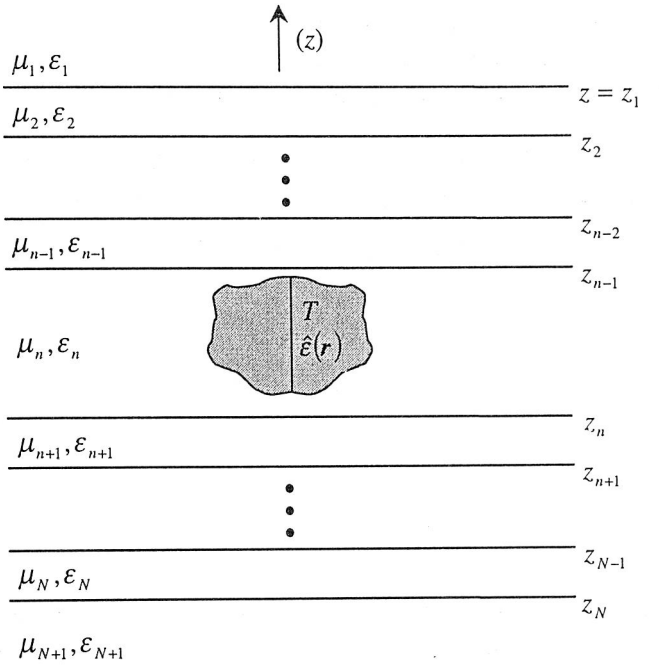

Fig. 4.2. An inhomogeneous dielectric body of revolution embedded within a stratified medium

$$K_{zx}^{A} = -\mu \cos\varphi \, S_1 \left\{ \frac{I_i^h - I_i^e}{k_\rho^2} \right\}, \tag{4.34}$$

$$K_{zy}^{A} = -\mu \sin\varphi \, S_1 \left\{ \frac{I_i^h - I_i^e}{k_\rho^2} \right\}, \tag{4.35}$$

$$K_{xz}^{A} = -\mu' \cos\varphi \, S_1 \left\{ \frac{V_v^h - V_v^e}{k_\rho^2} \right\}, \tag{4.36}$$

$$K_{yz}^{A} = -\mu' \sin\varphi \, S_1 \left\{ \frac{V_v^h - V_v^e}{k_\rho^2} \right\}, \tag{4.37}$$

and finally:

$$K^{\Phi} = -j\omega S_0 \left\{ \frac{V_i^h - V_i^e}{k_\rho^2} \right\}. \tag{4.38}$$

The angle φ above is defined by (3.92).

Following the procedure given in the previous section we start off by writing (4.30) and (4.31) in polar (ρ, z, ϕ) coordinates, which yields:

$$\underline{\underline{K}}^{A} = \begin{bmatrix} K_{xx}^{A}\cos(\phi-\phi') & A\cos(\phi-\varphi) & K_{xx}^{A}\sin(\phi-\phi') \\ B\cos(\phi'-\varphi) & K_{zz}^{A} & B\sin(\varphi-\phi') \\ -K_{xx}^{A}\sin(\phi-\phi') & A\sin(\varphi-\phi) & K_{xx}^{A}\cos(\phi-\phi') \end{bmatrix}, \tag{4.39}$$

where:

$$A = -\mu' S_1 \left\{ \frac{V_v^h - V_v^e}{k_\rho^2} \right\}, \tag{4.40}$$

$$B = -\mu S_1 \left\{ \frac{I_i^h - I_i^e}{k_\rho^2} \right\}. \tag{4.41}$$

Now, we can expand (4.38) and (4.39) in Fourier series in $(\phi - \phi')$. When making the analysis, we should keep in mind the fact that we deal with two different systems of polar coordinates, one associated with the BOR symmetry axis, the other one with

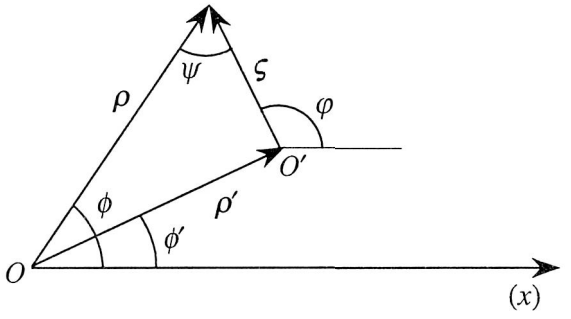

Fig. 4.3. Translation of the reference system

the particular source point. The latter situation occurs when we return from the spectral to the spatial domain using Sommerfeld integrals. Let us point out once again that the actual relation between the source and the field (observation points) has to be considered in the light of (3.92). During calculation, it is advisable to use the addition theorem, which allows us to express quantities in one of the systems in terms of the other [188, p. 373]:

$$J_n(k_\rho \varsigma)e^{jn\psi} = \sum_{m=-\infty}^{\infty} J_m(k_\rho \rho')J_{n+m}(k_\rho \rho)e^{jm(\phi-\phi')}. \tag{4.42}$$

The parameters found in (4.42) are shown in Fig. 4.3. J_m is the Bessel function of the order m.

After applying the Fourier series expansion to the kernel components and using (4.42), and after some algebraic transformations we finally arrive at:

$$\underline{\underline{K}}_m^A = \begin{bmatrix} \dfrac{L_{tt}^{m-1} + L_{tt}^{m+1}}{2} & -\dfrac{L_{tz}^{m} + L_{tz}^{-m}}{2} & \dfrac{L_{tt}^{m-1} - L_{tt}^{m+1}}{2j} \\ -\dfrac{L_{zt}^{m-1} + L_{zt}^{-(m+1)}}{2} & L_{zz}^{m} & -\dfrac{L_{zt}^{m-1} - L_{zt}^{-(m+1)}}{2j} \\ \dfrac{L_{tt}^{m+1} - L_{tt}^{m-1}}{2j} & -\dfrac{L_{tz}^{m} - L_{tz}^{-m}}{2j} & \dfrac{L_{tt}^{m-1} + L_{tt}^{m+1}}{2} \end{bmatrix}, \tag{4.43}$$

with:

$$L_{tt}^m = \frac{1}{j\omega}\Im_{m0}\{V_i^h\}, \quad L_{zz}^m = \frac{1}{j\omega}\frac{\mu}{\varepsilon'}\Im_{m0}\left\{\left(1+\frac{k'^2}{k^2}\right)I_v^e + \frac{k'^2}{k_\rho^2}\left(I_v^h - I_v^e\right)\right\},$$

$$L_{zt}^m = \mu\Im_{m1}\left\{\frac{I_i^h - I_i^e}{k_\rho^2}\right\}, \quad L_{tz}^m = \mu'\Im_{m1}\left\{\frac{V_v^h - V_v^e}{k_\rho^2}\right\}, \tag{4.44}$$

and

$$K_m^\phi = -j\omega\Im_{m0}\left\{\frac{V_i^h - V_i^e}{k_\rho^2}\right\}. \tag{4.45}$$

The notation used above follows the one introduced in [1]. The operator $\Im$ denotes a modal Sommerfeld integral:

$$\Im_{mv}\{.\} = \frac{1}{2\pi}\int_0^\infty dk_\rho k_\rho^{v+1} J_{m+v}(k_\rho \rho)J_m(k_\rho \rho')\{.\}, \quad v = 0,1. \tag{4.46}$$

Modal kernels (4.44) and (4.45) allow us to calculate scattered fields needed in the multilayer counterpart of (4.1).

However, in the surface current approach, we must remember that we should use the kernel $\underline{\underline{G}}^A$ for magnetic field calculations and in the case of BOR we should perform its modal decomposition.

4.3. TE, TM and HEM fields*)

The interesting features of the volume integral equations presented above may be found for the zeroth mode ($m = 0$). First, let us consider equations (4.27) and (4.28) describing the modal divergence and gradient, respectively. We note that in this case:

1) there is no charge related to the azimuthal field (or equivalent current) component (4.27);

2) in view of (4.28), the scalar potential term of (4.21) produces no azimuthal field.

Additionally, we shall consider the behavior of kernels (4.23) and (4.43). Noting that $G_1 = G_{-1}$ we get for the free-space kernel:

$$\underline{\underline{\Gamma}}_0 = \begin{bmatrix} G_1 & 0 & 0 \\ 0 & G_0 & 0 \\ 0 & 0 & G_1 \end{bmatrix}. \tag{4.47}$$

Similarly, for the "layered" kernel we find that $L^1_{tt} = L^{-1}_{tt}$, which yields:

$$\underline{\underline{K}}^A_0 = \begin{bmatrix} L^1_{tt} & -L^0_{tz} & 0 \\ -L^{-1}_{zt} & L^0_{zz} & 0 \\ 0 & 0 & L^1_{tt} \end{bmatrix}. \tag{4.48}$$

Based on (4.47) and (4.48) we see that the vector potential kernels do not introduce any coupling between "transverse" (ρ, z) and "azimuthal" ϕ field components. In view of 1) and 2) above, we conclude that the general EFIE (4.19) for $m = 0$ decouples into two independent equations describing "transverse" and "azimuthal" fields. For free space we arrive at:

$$E_\phi(\rho, z) = E^i_\phi(\rho, z) - j\omega \frac{\mu_0}{4\pi} \int_T G_1 J_\phi(\rho', z') \rho' dT', \tag{4.49}$$

for azimuthal fields, and

*) See also the author's articles [100, 101, 103, 104].

$$\boldsymbol{E}_T(\rho,z)=\boldsymbol{E}_T^i(\rho,z)-j\omega\frac{\mu_0}{4\pi}\int_T \underline{\underline{\boldsymbol{\Gamma}}}_T\cdot\boldsymbol{J}_T(\rho',z')\rho'dT'$$

$$+\frac{1}{j\omega}\frac{1}{4\pi\varepsilon_0}\nabla_T\int_T G_0\left(\nabla'_T\cdot\boldsymbol{J}_T(\rho',z')\right)\rho'dT', \tag{4.50}$$

where

$$\underline{\underline{\boldsymbol{\Gamma}}}_T=\begin{bmatrix}G_1 & 0\\ 0 & G_0\end{bmatrix}, \tag{4.51}$$

for transverse fields, while for stratified media we get the counterparts of (4.49) and (4.50):

$$E_\phi(\rho,z)=E_\phi^i(\rho,z)-2\pi j\omega\int_T L_{tt}^1 J_\phi(\rho',z')\rho'dT', \tag{4.52}$$

$$\boldsymbol{E}_T(\rho,z)=\boldsymbol{E}_T^i(\rho,z)-2\pi j\omega\int_T \underline{\underline{\boldsymbol{K}}}_T^A\cdot\boldsymbol{J}_T(\rho',z')\rho'dT'$$

$$+\frac{2\pi}{j\omega}\nabla_T\int_T K_0^\phi\left(\nabla'_T\cdot\boldsymbol{J}_T(\rho',z')\right)\rho'dT', \tag{4.53}$$

where

$$\underline{\underline{\boldsymbol{K}}}_T^A=\begin{bmatrix}L_{tt}^1 & -L_{tz}^0\\ -L_{zt}^{-1} & L_{zz}^0\end{bmatrix}. \tag{4.54}$$

In the equations above, we have used the "transverse" divergence and gradient operators:

$$\nabla'_T\cdot\boldsymbol{J}_T=\frac{1}{\rho'}\frac{\partial\left(\rho' J^\rho\right)}{\partial\rho'}+\frac{\partial J^z}{\partial z'}, \tag{4.55}$$

$$\nabla_T\Phi=\hat{\rho}\frac{1}{\rho}\frac{\partial(\rho\Phi)}{\partial\rho}+\hat{z}\frac{\partial\Phi}{\partial z}. \tag{4.56}$$

Using the "transverse" plane T as the reference and the usual terminology, we can say that equations (4.49) and (4.52) describe the transverse electric (TE) fields, whilst (4.50) and (4.53) describe the transverse magnetic (TM) fields. For $m\neq 0$ the equations do not exhibit such features (no decoupling into particular field modes can be found), so the fields are recognized as having a hybrid nature. This terminology is widely used when we classify the resonance phenomena in cylindrical dielectric bod-

ies, which will be shown in the examples. The resonant modes are then subdivided into TE, TM and HEM (hybrid electromagnetic).

4.4. DBOR techniques

Another solution technique, related to the above BOR formulation (worked out for bodies with rotational symmetry), is the so-called *discrete body of revolution* (DBOR) approach [5, 212, 215]. This approach has been developed for bodies characterized by K-fold rotational symmetry. The evaluated body belongs to this category if it consists of K identical slices, where each transforms to the other via the rotation through an angle $\frac{2\pi}{K}k$, $k = 0, 1, ..., K-1$. According to Fig. 4.4, we can distinguish the *generating slice* with an angular width of $\Delta\phi = \frac{2\pi}{K}$, which rotated through $\Delta\phi$ K times gives us the geometry of the body.

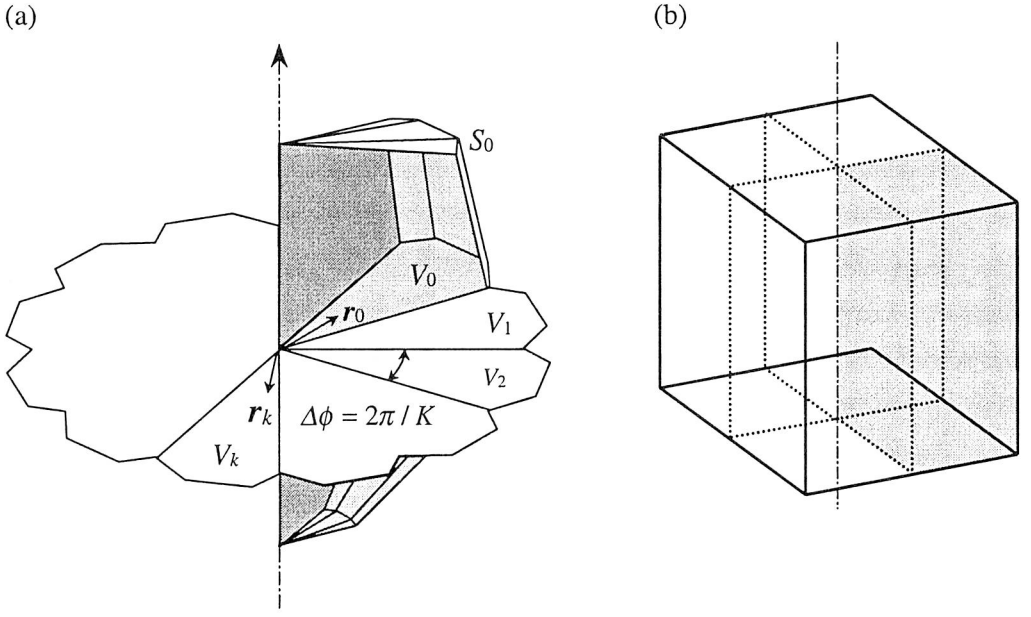

Fig. 4.4. Cylindrical symmetry in DBOR geometry (a) and a cuboid with 4-fold DBOR symmetry (b); in both cases one of the "slices" is shown in gray

The position vector $\boldsymbol{r}$ indicating a point lying within the k-th slice may be described in terms of a corresponding vector in the 0^{th} (generating) slice as

$$\boldsymbol{r} = \underline{\underline{\boldsymbol{R}}}^{k} \cdot \boldsymbol{r}_0, \quad \boldsymbol{r}_0 \in V_0, \tag{4.57}$$

where $\underline{\underline{\boldsymbol{R}}}$ is the dyadic of the rotation through an angle $\Delta\phi$:

$$[\boldsymbol{R}] = \begin{bmatrix} \cos\Delta\phi & -\sin\Delta\phi & 0 \\ \sin\Delta\phi & \cos\Delta\phi & 0 \\ 0 & 0 & 1 \end{bmatrix}. \tag{4.58}$$

We note that

$$\underline{\underline{\boldsymbol{R}}}^{-1} = \underline{\underline{\boldsymbol{R}}}^{T}, \quad \underline{\underline{\boldsymbol{R}}}^{n}(\Delta\phi) = \underline{\underline{\boldsymbol{R}}}(n\Delta\phi). \tag{4.59}$$

If we now define the coordinate system associated with each slice, so that the unit vectors in slice k may be obtained from unit vectors in slice 0 through a rotation k-times by an angle $\Delta\phi$, we may find that the electromagnetic quantities (currents, fields, etc.) at corresponding points are functions of the type $f(\boldsymbol{r}_0, k\Delta\phi)$, where $\boldsymbol{r}_0$ is the vector in the 0^{th} slice. Thus all scalar quantities (also vector components) may be treated as a series of K samples with the sampling period $\Delta\phi$. Consequently, we find that we may expand them in *discrete* Fourier series [215]. We have for example for the current*):

$$J(\boldsymbol{r}) = \sum_{m=1}^{K-1} J_m(\boldsymbol{r}_0) e^{jkm\Delta\phi}, \tag{4.60}$$

where k is the slice number, while the index m denotes the discrete Fourier modes.

Green's functions are in general functions of both source and observation points, where each of them can possibly belong to a different slice:

$$\underline{\underline{\boldsymbol{G}}}(\boldsymbol{r}, \boldsymbol{r}') = \underline{\underline{\boldsymbol{G}}}(\boldsymbol{r}_0, \boldsymbol{r}_0', k\Delta\phi, n\Delta\phi). \tag{4.61}$$

Above, we have assumed that the source vector $\boldsymbol{r}'$ indicates a point in the n-th slice, while the observation vector $\boldsymbol{r}$ indicates a point in the k-th slice. Bearing in mind the symmetry, we may conclude that Green's function depends on the *relative*, and not the *absolute* position of the respective slices [5]. Thus, we may further describe $\underline{\underline{\boldsymbol{G}}}$ as a function of $(\boldsymbol{r}_0, \boldsymbol{r}_0', (k-n)\Delta\phi)$, which allows us to expand all entries of it (let us denote the particular entry by G) in terms of discrete series:

*) We note that the meaning of "vector" series components pertains to the statement above about expressing all of the vectors in terms of local coordinates relative to each of the slices.

$$G(\boldsymbol{r},\boldsymbol{r}')=G(\boldsymbol{r}_0,\boldsymbol{r}_0',(k-n)\Delta\phi)=\sum_{m=0}^{K-1}G_m(\boldsymbol{r}_0,\boldsymbol{r}_0')e^{jm(k-n)\Delta\phi}. \tag{4.62}$$

The surface or volume integrals relating currents and scattered fields may thus be described as a sum of K integrals over the single slices. Substituting expansions like (4.60) and (4.62) into the full 3D formulas and performing the summations in k we find that, after invoking the orthogonality of Fourier components, the modal equations decouple. Then, for each discrete mode, it is enough to solve the integral equation related to the 0^{th} slice only, i.e., with integrals over V_0 or S_0, depending on whether we deal with VIE or SIE, respectively. Obviously in order to do so, we have also to expand the incident fields in the discrete Fourier series.

The procedure outlined above may be considered as a generalization of the classical BOR theory. Indeed, the full rotational symmetry corresponds to applying the limit $K\to\infty$, for which the expansions (4.60), (4.62) become Fourier series like (4.15) and (4.24). As $\Delta\phi\to 0$, the integration domains diminish to the generating (transverse) surface, or to the generating arc within the volume and surface integrals, respectively.

One aspect of the DBOR technique should be especially mentioned. In certain applications (for example, for DBOR objects inside cylindrical waveguides), it is convenient to express the incident field in terms of (continuous) azimuthal modes. For a single azimuthal mode, say m, the incident field has an azimuthal variation $e^{jm\phi}$. In the discrete Fourier expansion, such variation results in a *single* discrete mode [5]. However, that relation is not symmetrical, i.e., the single discrete mode is related to an infinite number of azimuthal modes, each of them possibly appearing in the scattered field formulas. As a result, for a given mode m within the incident field, the harmonics with the numbers

$$n=m+\nu N,\qquad \nu\in\mathbf{Z}, \tag{4.63}$$

are reflected back [5].

Closing this section we should also mention the efforts associated with so-called *partial bodies of revolution*, which constitutes similar kinds of problems [70].

* * *

In this chapter, we have shown how the application of special kinds of symmetries (here, of the rotational type) may reduce the order of the solution, resulting in efficient computational algorithms. However, even if the observed kind of symmetry is not used within the full 3D formulation of the problem, it is still present in the physical relations serving as a basis for the solution. For example, the relation between the source and field (observation) points in many cases does not depend on the absolute

location of those points, but on their relative position (i.e., their distance to each other). It means that relations between the pairs of source/field points are expressed using the same formulas and do not have to be recalculated for all possible combinations. Speaking in terms of the method-of-moments solution outlined in the next chapter, if only symmetry is preserved during the approximation process, it appears in the form of the MoM impedance matrix. This fact may be taken advantage of both in the process of matrix computation and in the step required to find a solution of a matrix equation. Recently, this approach has been applied to a class of iterative solutions where, in view of the translational symmetry of the medium, the process of matrix-vector multiplication has been accelerated by means of a Fast-Fourier-Transform (FFT) [190, 191, 226].

Chapter 5. Solution of integral equations – the method-of-moments

In the previous chapters, we have formulated the problem of electromagnetic scattering by dielectric homogeneous/heterogeneous bodies, possibly also surrounded by a stratified environment, in terms of surface or volume integral equations. For the unknown quantities in those equations, we have used the fictitious equivalent electric and/or magnetic currents*). Unfortunately, the analytical (or semi-analytical) solutions of the integral equations are at present known only for a small set of bodies having simple geometrical shapes (for example, spheres for which the solution is known in terms of Mie series [188, p. 563]). In practical situations, we have to apply numerical methods, which lead to approximated solutions. For integro-differential equations considered in this monograph the widely recognized solution is known as the "method-of-moments" (MoM). This term, introduced by Harrington [59, 61] is presently used for a wide set of numerical methods [208], incorporating the "classical" method of Harrington, the reaction matching concept of Rumsey [173], mode matching, conjugate gradient method (CGM), etc. A systematic description of the various approaches may be found in a monograph by Wang [208]. Here we only mention the most general classification, subdividing the frequency-domain moment methods into *direct* (where the "impedance" matrix describing the problem is obtained and then inverted) and *iterative* ones (where only the vector describing the unknown quantity (current) is stored, and the solution is obtained in several steps (iterations)**). The efficiency of the iterative solutions may be enhanced by using special techniques, such as the fast multipole method [118], the adaptive integral method [11], the impedance matrix localization method [18], and the fast Fourier transform and wavelet methods [45, 46, 86, 186, 204].

A general trend is to use very simple approximations for the iterative methods, allowing application of simple and fast formulas, and to obtain the desired accuracy

---

*) In view of (2.1)–(2.2) and (2.26), those currents may usually be understood as fields, as well.

**) In the *direct* method-of-moments, the impedance matrix may be inverted directly or iteratively. This second possibility is closely related to the *iterative* method-of-moments [208, p. 12], with the exception that in the latter case the matrix elements are not stored, but calculated each time they are needed.

by using a large number of unknown parameters [190, 191]. In the direct methods we apply more sophisticated approximations for the unknown quantities, but we are usually restricted as regards the number of unknowns because of the computer memory limitations (we must store the N^2 element matrix for N unknowns). In the work herein, we apply the traditional direct solution, which may be outlined as follows.

Each operator equation that may be constructed for the problem of interest based on the previous chapters, may be written in the form:

$$A(x) = y\,, \tag{5.1}$$

where x denotes the unknown (electric and/or magnetic equivalent current), y denotes the given field (in our case the incident one), and A denotes a linear (here integro-differential) operator. Equation (5.1) has to be fulfilled within the spatial domain of the integral operators used in the formulation. For instance, for SIE formulations we require (5.1) to be satisfied on the body surface S, while for VIE formulations (5.1) has to be satisfied within the body volume V. The first step in the MoM solution is to approximate the unknown in the form of a linear combination:

$$x \cong \sum_{n=1}^{N} X_n x_n\,, \tag{5.2}$$

where X_n are complex constants, and x_n is a set of N linearly independent functions, referred to as the *basis functions* or *expansion functions*. The fact that we postulate an *approximate form* of the solution is indicated by the sign $\cong$. Substituting approximation (5.2) into (5.1), and making use of the linearity of the operator A, we get:

$$\sum_{n=1}^{N} X_n A(x_n) \cong y\,. \tag{5.3}$$

Formula (5.3) is an equation with N unknowns, which should be *approximately* satisfied at all points of the spatial domain of the operator. In order to make (5.3) meaningful we follow the procedure given by Harrington [61], i.e., we *test* (5.3) using a set of N properly chosen *weighting* or *testing* functions. The testing procedure consists in taking a symmetric or scalar product of the tested quantity with a testing function from the set [208]. The number of testing functions should be the same as the number of basis functions used for approximation of the unknown quantity. The symmetric product is usually defined as:

$$\langle u; w \rangle = \int_K u \cdot w\, dK\,, \tag{5.4}$$

where the domain of the integration K denotes surface S for the surface integral equation formulations, or volume V for the volume integral equation formulations.

In certain applications, it is convenient to use a scalar product:

$$\langle \boldsymbol{u}; \boldsymbol{w} \rangle = \int_K \boldsymbol{u} \cdot \boldsymbol{w}^* dK . \tag{5.5}$$

If we denote the testing function by $\boldsymbol{w}_1$, $\boldsymbol{w}_2$, ..., $\boldsymbol{w}_N$ and apply the testing procedure to (5.3), we obtain:

$$\sum_{n=1}^{N} X_n \langle \boldsymbol{A}(\boldsymbol{x}_n); \boldsymbol{w}_m \rangle = \langle \boldsymbol{y}; \boldsymbol{w}_m \rangle, \qquad m = 1, 2, ..., N. \tag{5.6}$$

Thus, the initial equation (5.1) has been transformed into a set of N linear equations with N unknowns. This set can be written in a matrix form:

$$[A_{mn}][X_n] = [y_m], \tag{5.7}$$

where $[X_n]$ denotes the column matrix of unknown coefficients of expansion (5.2), while elements of the so-called *impedance matrix* $[A_{mn}]$ and the *excitation vector* $[y_m]$ are given respectively by:

$$A_{mn} = \langle \boldsymbol{A}(\boldsymbol{x}_n); \boldsymbol{w}_m \rangle, \tag{5.8}$$

$$y_m = \langle \boldsymbol{y}; \boldsymbol{w}_m \rangle . \tag{5.9}$$

The equation set (5.7) may now be solved with the standard methods of linear algebra.

Note that we do not consider here problems of the existence or uniqueness of the solution to (5.1). We assume that a solution exists in the sense of MoM. Any reader interested in a more formal mathematical introduction to the method-of-moments is referred for example to monograph [208].

In the MoM solution, the choice of the basis and testing (weighting) functions is of fundamental importance [85]. Note that in the mixed-potential representations, which are in general preferred in this monograph, there is always a divergence operator acting on the current. This causes that at least some linear capabilities of the basis functions are required to enable the differentiation. In contrast to this approach, there are solutions with simpler expansions (pulse) [25, 116, 191], where the principal value techniques must however be used when dealing with the singularities of Green's functions[*)]. The choice of the basis functions will be discussed in the subsequent section.

At the end of these introductory remarks, we should devote a few words to a relatively new technique, which may be used when dealing with scattering problems us-

[*)] The singularities appear in the solution, for example, when so-called "self-terms" are considered, which corresponds to diagonal elements of the impedance matrix.

ing the method-of-moments. The well-known drawback of the MoM is that the matrices produced in this scheme are dense (in contrast to mesh methods like FEM), which in the case of problems concerning electrically large objects, complicates both the matrix storage and inversion. This drawback may be resolved by using the wavelet methods mentioned above [46]. The wavelet methods can be applied either directly (using wavelets as the basis and testing functions) or indirectly (transforming the impedance matrix with the wavelet transform). Both approaches lead to matrices in which several of the elements are small in comparison to others and can be neglected (set to zero) without lowering the quality of the approximated solution.

5.1. Basis functions

As indicated above, the key element in the MoM procedure is the approximation of an unknown quantity, for example, of the surface or volume current. In order to make such an approximation we first have to decide on whether the shape of the body should also be approximated. The shape approximations are used when surfaces bounding the body or its parts are curved. A typical approach is to replace the curved surfaces with planar patches over which the basis functions are spanned*). Of course, the surfaces of the body (including possible media discontinuities) are usually better approximated using a greater number of elementary planar patches. Thus, we have two approximation levels applied in the MoM solution: 1) the approximation of the geometry of the body, and 2) the approximation of fields or equivalent currents. The first approximation is avoided when the body itself is bounded by planar surfaces, or when more sophisticated geometrical techniques are applied. Such techniques are in recent years extensively investigated by a number of researchers. Representative references in this field are given by Wilton and co-workers [15, 16, 21]. In this monograph, however, we focus our interest on the integral equations describing the electromagnetic scattering problems rather than searching for the most accurate geometrical representations. In the light of what has been said, we limit our attention to simple configurations where planar surface segments can be used. The second approximation depends not only on the demanded accuracy, but also on the presumptions made in the formulation. In the next sections, we will shortly introduce typical basis functions, which may be used to represent the surface and volume currents. A general remark that should precede this description follows from Chapter 3 of this book. We concluded there that particular ease with which the singularities in integral equations are treated is associated with their mixed-potential form. Such formulations

*) This introduces non-physical edges into the solution. Different kinds of problems are associated with the modeling of real (existing) sharp edges, due to the singularity in the charge density near an edge [16].

require however the possibility of calculating charges from current distributions (using the continuity equation). Therefore, basis functions applicable within the MPIE formulation have to be at least piecewise differentiable. Any reader interested in more sophisticated higher-order field and current approximations is referred for example to [50, 51].

5.1.1. Rooftop basis functions for surface current representation

The early surface current representations, developed mainly for the modeling of conducting surfaces, were limited to rectangular plates [205]. Simple approaches [4, 17, 95], used "pulse" vector basis functions associated with single elements (patches), for example, in [17] two orthogonal vector basis functions per each patch have been applied. A similar approach where triangles (more flexible in the modeling of surfaces of arbitrary shape) were used as the basis function domains was proposed by Wang [207].

In more sophisticated attempts higher-order functions were spanned over two adjacent patches. In [211] the authors used "two rectangle", piecewise sinusoidal functions to represent current in its flow direction, whilst in the transverse direction perpendicular to the current, the representation still had a simple pulse form. This approach, which in fact relates the basis functions to common edges between the patches (see Fig. 5.1(a)), rather than to patches themselves, laid down the basis for contemporary surface patch modeling techniques. Although attempts at developing a more accurate representation of current distributions in transverse direction are known in literature [160] the complexity introduced to the basis function construction is not, in the author's opinion, justified by the modeling flexibility.

The "two rectangle" or "rooftop" approach was first generalized to non-rectangular (however regular in some aspects) geometry [183], and second, to the very versatile "two quadrilateral" representation (see Fig. 5.1(b)), [162]. Although in the original solution [162] the authors again used a piecewise sinusoidal current representation, other models are also known, using for example linear (triangular) current expansions [182]. It is to be pointed out that triangular domains may also be easily treated in the method of [162], because a triangle can be considered as a degenerated quadrilateral.

A milestone in contemporary three-dimensional surface current modeling techniques was the paper by Rao, Wilton and Glisson [168]. In their formulation, which has also been originally developed for scattering calculations by perfectly conducting bodies, a surface of arbitrary shape was approximated with flat triangles (see Fig. 5.1(c)). Like in some previous attempts, the basis function definition is associated with the edges between adjacent triangles.

These, so called *RWG* functions are defined as follows*):

$$f_n(\boldsymbol{r}) = \begin{cases} \dfrac{l_n}{2A_n^+}\boldsymbol{\rho}_n^+ & \text{for } \boldsymbol{r} \in T_n^+, \\ \dfrac{l_n}{2A_n^-}\boldsymbol{\rho}_n^- & \text{for } \boldsymbol{r} \in T_n^-, \\ 0 & \text{otherwise,} \end{cases} \tag{5.10}$$

where l_n denotes the length of the common edge, and $A_n^{+/-}$ is the area of the triangle $T_n^{+/-}$.

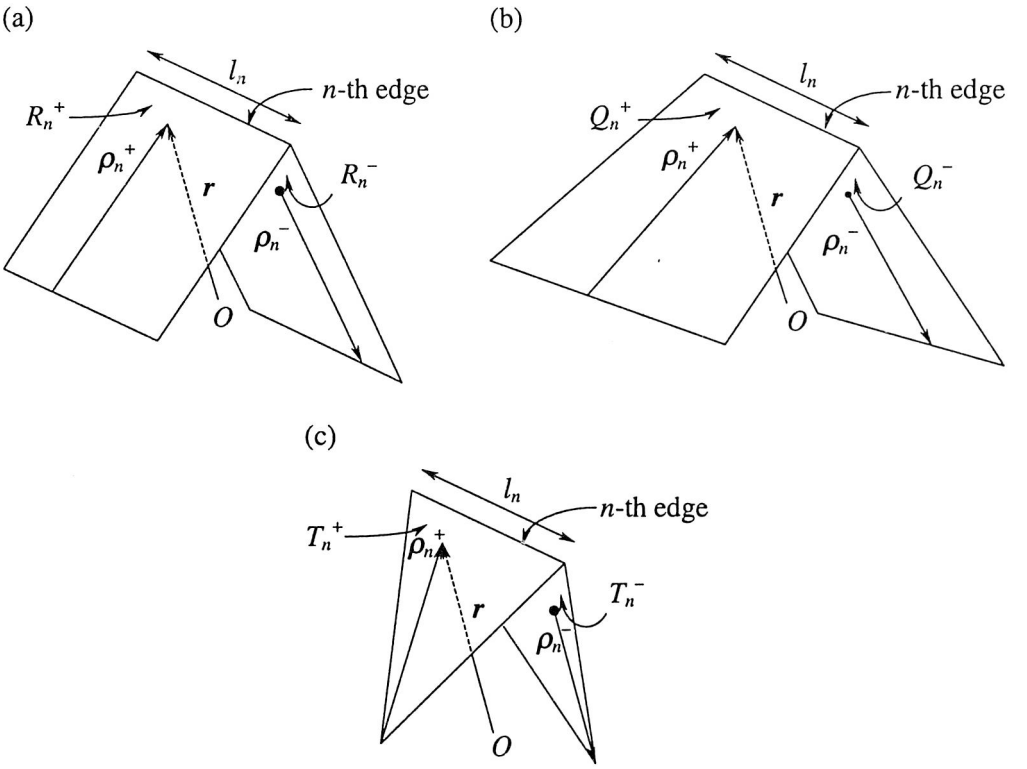

Fig. 5.1. Geometrical parameters associated with the interior edges between: (a) two rectangles; (b) two quadrilaterals; (c) two triangles

*) In recent papers [137, 143] another equivalent formal definition is preferred, where the so-called Λ functions associated with the numbering of local vertices for each triangle are used. Here we apply the traditional definition because of the more natural transition between triangular and quadrilateral domains.

The following properties of the above basis functions make them attractive for surface current modeling [168, 208]:

1) f_n (the current) is tangent to the edges of triangles except at their common edge, and no line charges exist along those edges.

2) The normal component of the current crossing the common edge between the two triangles is continuous, and hence there is no line charge on the common edge.

3) The average of f_n over the two triangles (the moment) can be easily evaluated in terms of vectors pointing towards the triangle centroids.

4) The surface divergence of f_n, which is proportional to the surface charge density associated with the basis function, can be simply evaluated as:

$$\nabla_S \cdot f_n(\boldsymbol{r}) = \begin{cases} \dfrac{l_n}{A_n^+} & \text{for } \boldsymbol{r} \in T_n^+, \\ -\dfrac{l_n}{A_n^-} & \text{for } \boldsymbol{r} \in T_n^-, \\ 0 & \text{otherwise.} \end{cases} \tag{5.11}$$

Feature 4), which in fact means that the charge density is constant in each triangle, makes the basis function particularly well suited for MPIE formulations.

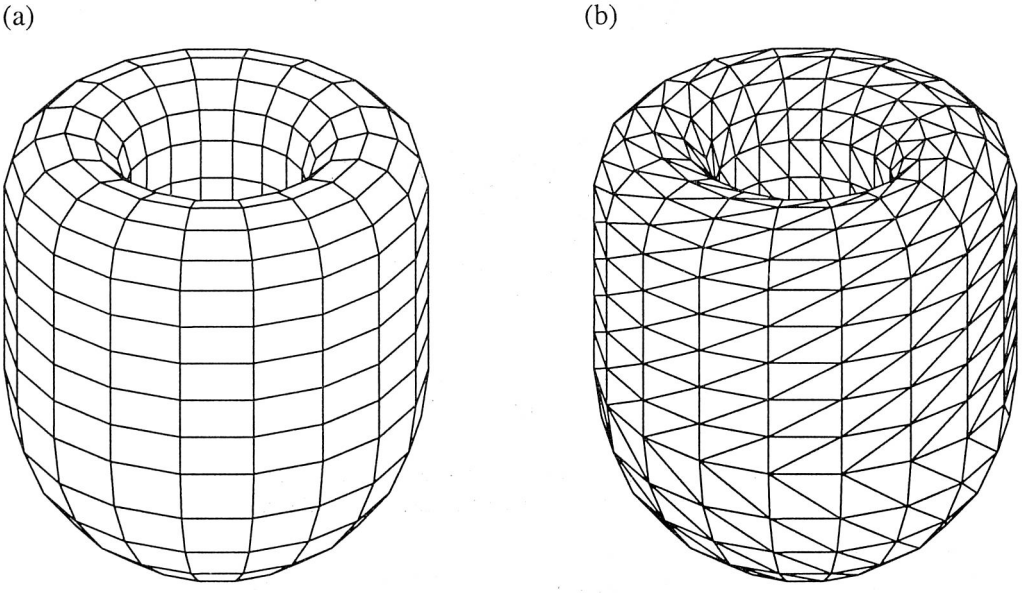

Fig. 5.2. An arbitrary surface modeled using quadrilateral (a) and triangular (b) patches

When dielectric bodies are modeled using the surface current approach we must remember that usually two currents have to be approximated for each of the surfaces. The *RWG* functions have been successfully applied for scattering by homogeneous dielectrics in [197].

Although the *RWG* function described above offers a very flexible tool for surface current modeling, one must remember that in certain cases the quadrilateral modeling may be still of interest, because it can give a model with a smaller number of unknowns and therefore smaller impedance matrix as compared to triangular modeling. Some commercial codes offer the possibility of the choice between these two techniques [182], see also Fig. 5.2.

5.1.2. Generalization of the rooftop functions into VIE techniques

In volume integral equation techniques, the cubical cells play a more important role than rectangular patches, which may be considered as their two-dimensional counterpart, in surface current modeling. The reason for that is twofold: first, it is in some sense "natural" to model an inhomogeneous body with the help of a Cartesian grid, where material parameters are associated with each cuboid (piecewise constant permittivity and/or permeability profiles), second, we are not forced to exactly represent the surface of the body – we are allowed to take any convenient shape as the "body volume" which includes the real body inside and the "rest" being simply filled with material of the surrounding environment (Fig. 5.3).

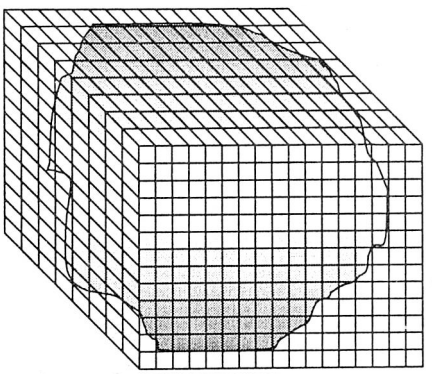

Fig. 5.3. An arbitrary inhomogeneous dielectric body modeled as a cuboid in the Cartesian grid

Let us remain here with purely dielectric bodies, which may be modeled using equivalent electric current only. There are two major ways of treating the scattering problems in this case. Historically the first one, introduced by Livesay and Chen

[116], uses EFIE with a simple pulse basis function for field (or current) representation. Because pulse functions are not differentiable, it is not possible to apply the mixed potential formulation, and therefore principal value integration must be used when "self-terms" of the impedance matrix are evaluated. The interest in this approach (see also [25, 54, 55]) was revived more recently, when the iterative MoM procedures became popular [208, 210, 191, 209]. This approach suffers from two drawbacks. One is that using the Cartesian mesh enforces application of a large number of cells when the surfaces between dissimilar media are of arbitrary shape (staircase approximation). Another one is associated with the pulse field representation that introduces non-physical charges at cells boundaries, which may be a source of convergence problems when more subtle segmentation is applied [61, 178].

The second approach is associated with using MPIE and therefore avoiding the singularity problems. This again requires at least some linearity to be built into the basis functions. This can be easily done when we generalize the rooftop functions from the preceding section to three dimensions. Possible configurations using two cuboids (the counterpart of a surface basis function spanned over two rectangles) or two tetrahedrons [178] (the counterpart of two triangles) are shown in Fig. 5.4. It is obvious that the basis functions are now associated with faces rather than with cells.

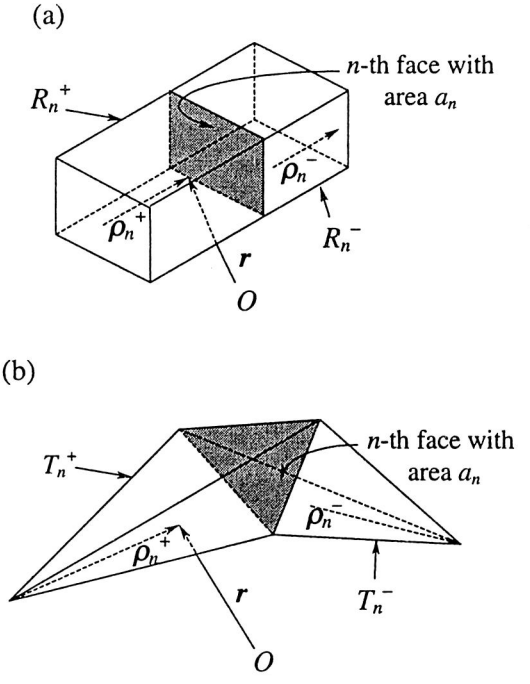

Fig. 5.4. Geometrical parameters associated with the interior face between (a) two cuboids; (b) two tetrahedrons

For the case of two tetrahedrons, the basis function is defined as [178]:

$$f_n(\boldsymbol{r}) = \begin{cases} \dfrac{a_n}{3V_n^+}\boldsymbol{\rho}_n^+ & \text{for } \boldsymbol{r} \in T_n^+, \\ \dfrac{a_n}{3V_n^-}\boldsymbol{\rho}_n^- & \text{for } \boldsymbol{r} \in T_n^-, \\ 0 & \text{otherwise,} \end{cases} \tag{5.12}$$

where a_n denotes the area of the common face, and $V_n^{+/-}$ is the volume of the tetrahedron $T_n^{+/-}$.

The basis functions defined in (5.12) have the following interesting properties [178]:

1) f_n is tangent to the faces of tetrahedrons except at their common face.

2) The normal component of f_n crossing the common face between the two tetrahedrons is continuous.

3) The average of f_n over the two tetrahedrons (the moment) can be easily evaluated in terms of vectors pointing towards the tetrahedron centroids.

4) The divergence of f_n can be simply evaluated as

$$\nabla \cdot f_n(\boldsymbol{r}) = \begin{cases} \dfrac{a_n}{V_n^+} & \text{for } \boldsymbol{r} \in T_n^+, \\ -\dfrac{a_n}{V_n^-} & \text{for } \boldsymbol{r} \in T_n^-, \\ 0 & \text{otherwise.} \end{cases} \tag{5.13}$$

The above basis functions are well suited for field representation, when piecewise constant media parameters are assumed. The dielectric constant associated with each tetrahedron may be different, so in general the normal component of the equivalent current (4.2) may be discontinuous at media interfaces. This contradicts the above feature 2), therefore functions (5.12) are not suitable for equivalent current representation. The same is true about the electric field. However, the dielectric flux density defined as:

$$\boldsymbol{D} = \hat{\varepsilon}\boldsymbol{E}, \tag{5.14}$$

possesses the desired feature of continuity of the normal component across the media interfaces. Therefore it is $\boldsymbol{D}$ that is approximated [178] throughout the body volume V using the double-tetrahedron basis function, as:

$$\boldsymbol{D}(\boldsymbol{r}) = \sum_{n=1}^{N} D_n f_n(\boldsymbol{r}). \tag{5.15}$$

The N above denotes the total number of faces that make up the tetrahedral model of V. Obviously, in this volume model some tetrahedron faces are placed on the surface of the body. If this is the case, a "single-tetrahedron" basis function associated with the "interior" tetrahedron is defined.

When the basis functions are chosen for the problem in question, in the case of the MoM procedure other quantities associated with this elementary block of field expansion, such as currents or charges, have to be calculated. Namely, we have the following formula for the current expansion:

$$\boldsymbol{J}(\boldsymbol{r}) = j\omega \sum_{n=1}^{N} D_n \kappa(\boldsymbol{r}) f_n(\boldsymbol{r}), \tag{5.16}$$

where we have introduced the *contrast ratio* [178]

$$\kappa(\boldsymbol{r}) = \frac{\hat{\varepsilon}(\boldsymbol{r}) - \varepsilon_0}{\hat{\varepsilon}(\boldsymbol{r})}, \tag{5.17}$$

now acting for all discontinuities in the normal current component at media interfaces. Obviously, in a multilayer environment, the free-space permittivity in (5.17) should be replaced with the permittivity of the proper layer.

The charge density can be obtained from (5.16) using the continuity equation, yielding

$$q(\boldsymbol{r}) = -\sum_{n=1}^{N} D_n \boldsymbol{f}_n(\boldsymbol{r}) \cdot \nabla \kappa(\boldsymbol{r}) - \sum_{n=1}^{N} D_n \kappa(\boldsymbol{r}) \nabla \cdot f_n(\boldsymbol{r}). \tag{5.18}$$

It is interesting that, as seen from (5.18), the two kinds of associated charges have been related to functions (5.12). The surface charges (first summation) arise at tetrahedron interfaces when dielectric constants of both tetrahedrons are different, and at interfaces lying on the surface bounding the body (except for the possible "empty" cells mentioned at the beginning of this section). Note that this is consistent with the discussion of MPIEs performed at the end of section 3.2.2 and in section 3.3. The explicit formula for the surface charge associated with the function $\boldsymbol{f}_n$ is:

$$q_{sn}(\boldsymbol{r}) = \begin{cases} D_n\left(\kappa_n^+ - \kappa_n^-\right), & \boldsymbol{r} \in a_n, \\ 0, & \text{otherwise}, \end{cases} \tag{5.19}$$

where $\kappa_n^{+/-}$ is the constant value of $\kappa(\boldsymbol{r})$ in $T_n^{+/-}$.

The second summation in (5.18) represents the volume charge, easily calculated using (5.13):

$$q_{vn}(\boldsymbol{r}) = \begin{cases} -D_n K_n^+ \dfrac{a_n}{V_n^+}, & \boldsymbol{r} \in T_n^+, \\ D_n K_n^- \dfrac{a_n}{V_n^-}, & \boldsymbol{r} \in T_n^-, \\ 0, & \text{otherwise}. \end{cases} \tag{5.20}$$

A careful reader may notice that, in view of the Gauss law, there should be no volume charges in the formulation, because $\boldsymbol{D}$ is divergenceless, and f_n represents a building block for $\boldsymbol{D}$. However, the basis functions defined above are not divergenceless, therefore this condition must be enforced numerically [178]. An alternative approach consists in grouping together double-tetrahedron basis functions with a common edge, which leads to a class of solenoidal bases with no volume charges present [19]. Another simple solution to this problem may be found for the case of a body-of-revolution and will be defined in the next section.

When explicit formulas for elementary currents and charges are known we can calculate numerically the associated potentials and fields at an arbitrary point of space using the Green's functions discussed earlier in this book.

Although the formulation outlined above is preferred by the author, there are also other MPIE approaches using VIE. For example, Tsai *et al.* [195] use linear basis functions spanned over polyhedral domains to represent the electric field in a manner similar to FEM formulations.

5.1.3. Mixed-domain basis function in BOR problems

A special case in basis function construction is associated with bodies with rotational symmetry discussed in Chapter 4. In general, the 3D problem in the BOR case is reduced to a number of 2D problems. In the surface current approach, the surface integrals reduce to line integrals along the "generating arc" of the body. The rooftop functions described in this section reduce to triangle functions spanned over adjacent segments of the generating arc. As shown, for example, in [42, 125], two current components must be approximated: the current flowing along the arc and an azimuthal current component. In [42], it is shown that for the latter case a simple pulse approximation gives stable solutions. Because the BOR techniques with SIE formulations have been known almost from the beginning of the contemporary computational electromagnetics, an interested reader is referred to voluminous literature dealing with

this subject [1, 6, 42, 123, 124, 125, 130]. The VIE basis functions are discussed below because of some interesting possibilities associated with this approach.

First, we would like to underline one aspect of the "azimuthal mode decoupling" procedure associated with BOR analysis. Two interpretations are possible in this case. First [42], we can take the modal equations as they appear in Chapter 4. Note that the domain of the operators in those equations is the transverse area of BOR denoted by T. Thus, the basis function should enable representation of field components, depending on the position of the observation point on T. The azimuthal dependence ($e^{jm\phi}$) is suppressed in the equations and is present in the form of modal operators, such as modal divergence, curl or gradient (eqs. (4.27)–(4.29)). Therefore, let us state again that the basis functions have to be dependent only on (ρ, z) coordinates. The second interpretation [125] allows us to remain within the classical 3D form of the equations (Chapter 3), but the basis functions are understood as combined, mixed domain functions constructed as a multiplication of "transverse" functions (usually spanned over small sub-domains) with the entire domain exponential functions:

$$f_{mn}(\rho, z, \phi) = f_n^T(\rho, z) e^{jm\phi}, \tag{5.21}$$

where the superscript T denotes the function defined in the "transverse" body area.

This second approach is useful when we want, for example, to prove the features of mode decoupling (in view of the orthogonality of exponential $e^{jm\phi}$ functions with different m indices) [125]. On the other hand, the first approach is better suited for immediate application to a numerical procedure, because the analytical work is performed a step further (see for example that in the final equations presented in Chapter 4 we have performed all of the integrations over the variable ϕ analytically). We therefore remain with this (in the author's opinion) more elegant form and will understand the basis function as defined on the "transverse" domain. Consequently, the superscript T from (5.21) will be omitted further on.

5.1.4. Reduction of the number of unknowns through the use of Gauss law*)

In section 5.1.2, it was mentioned that in the original double-tetrahedron method [178] usually the Gauss law is enforced numerically. However, the authors suggest that taking advantage of the fact that the electric flux density is divergenceless within the tetrahedrons, it would be possible to reduce the number of unknowns in the solution when developing the basis function. Indeed, the Gauss law

*) [105].

$$\nabla \cdot \boldsymbol{D} = 0 \tag{5.22}$$

enforces an additional relation on the field components, which are in general not independent. This feature was used previously in BOR schemes for developing specialized EFIEs characterized by a reduced number of unknowns [200, 201]. We will show how (5.22) can be used for the construction of efficient BOR-VIE basis functions.

Based on (5.21) let us denote again the transverse basis function by f_n. If the basis function set is used for $\boldsymbol{D}$ representation, we can state that (5.22) should also apply to f_n, which in cylindrical coordinates gives us (see (4.27)):

$$\nabla_m \cdot f_n = \frac{1}{\rho}\frac{\partial\left(\rho f_n^{\rho}\right)}{\partial\rho} + \frac{\partial f_n^{z}}{\partial z} + \frac{jm}{\rho} f_n^{\phi} = 0, \tag{5.23}$$

where m denotes the azimuthal mode.

One can see that it is possible to easily calculate the azimuthal component f_n^{ϕ} from (5.23) if transverse components f_n^{ρ} and f_n^{z} are known,

$$f_n^{\phi} = -\frac{\rho}{jm}\left[\frac{1}{\rho}\frac{\partial\left(\rho f_n^{\rho}\right)}{\partial\rho} + \frac{\partial f_n^{z}}{\partial z}\right]. \tag{5.24}$$

Note that:

1) the above relation cannot be applied for m = 0, however in this case, as discussed in section 4.3, the equations describing transverse and azimuthal fields are decoupled and have to be solved separately;

2) the transverse field components must be differentiable*).

In view of the above statements, in order to construct a divergenceless basis function for non-zero azimuthal modes, we have to first define a (differentiable) basis function suitable to represent the transverse vector field in the transverse plane T, and then calculate the remaining azimuthal component with the help of (5.24). This reduces the total number of unknowns needed in the solution approximately by a factor of 2/3.

Two possible choices have been introduced in the author's earlier work [105]. The natural choice for "transverse" functions are the rooftop functions from section 5.1.1. Indeed, they represent two-dimensional vector distributions, and possess some linearity features which make them differentiable. The difference in direct application is that rooftop functions described in section 5.1.1 are designed for *current* representation on surfaces of arbitrary shape. In contrast to that, here we use them for *field* rep-

*) In (5.23) and (5.24) we use ρ and z components separately. However, they may be grouped to form a single vector "transverse" component in the equations. The square bracketed part of (5.24) can then be interpreted as a transverse component of the divergence operator $\nabla_T \cdot f_n^T$.

resentation (in view of section 5.1.2 a good choice is the electric flux density). Furthermore, the surface over which the functions are spanned is always *planar*, because it is simply the transverse plane of BOR.

For further development we include two types of rooftop functions: functions defined on rectangular domains, which correspond to "double-cuboid" functions in 3D cases, and functions spanned over triangles (*RWG* functions), which are the counterpart of "double-tetrahedron" functions. Both representations are shown in Fig. 5.5.

We can note that in the divergence relation (5.23) the ρ-directed field component is multiplied by ρ, while the z-directed component appears alone, i.e., without the ρ multiplier. Thus, as will be seen in the subsequent paragraph, it is useful to apply different expansions for both components of $\boldsymbol{D}$. When the "rooftop" functions are used to represent transverse fields, it is appropriate to expand ρD_ρ with the "radial" rooftop functions, whilst in z-directed rooftop functions it is more appropriate to expand D_z directly. Consequently, a constant variation in ρ is assured for both field components in the immediate neighborhood of z-axis.

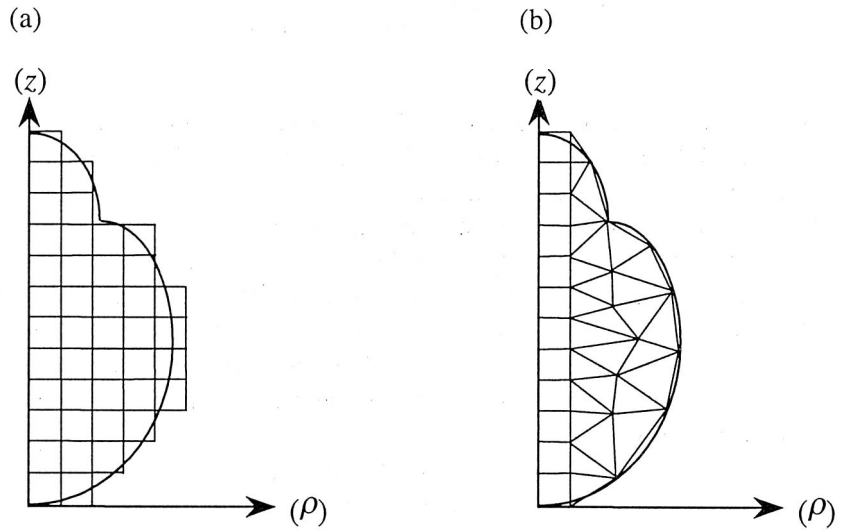

Fig. 5.5. Approximation of the transverse plane of the body;
(a) rectangular basis functions; (b) rectangular and triangular basis functions

Basis functions on rectangular domains

Assuming that the transverse surface of BOR is divided into small rectangles (see Fig. 5.5(a)) characterized by piecewise constant dielectric parameters we define two sets of basis functions (see Fig. 5.6 for notation):

1) type ρ functions defined as:

$$\boldsymbol{g}_{mi}(\rho,z)=\begin{cases}\hat{\boldsymbol{\rho}}\dfrac{1}{\rho}\dfrac{\left(\rho-\rho_i^{+}\right)}{a_i^{+}}-\hat{\boldsymbol{\varphi}}\dfrac{1}{jma_i^{+}}, & \rho\in\left(\rho_i^{+},\rho_i\right),\ z\in\left(z_i^{1},z_i^{2}\right),\\ \hat{\boldsymbol{\rho}}\dfrac{1}{\rho}\dfrac{\left(\rho_i^{-}-\rho\right)}{a_i^{-}}+\hat{\boldsymbol{\varphi}}\dfrac{1}{jma_i^{-}}, & \rho\in\left(\rho_i,\rho_i^{-}\right),\ z\in\left(z_i^{1},z_i^{2}\right),\\ 0, & \text{otherwise,}\end{cases} \tag{5.25}$$

2) type z functions defined as:

$$\boldsymbol{h}_{mi}(\rho,z)=\begin{cases}\hat{\boldsymbol{z}}\dfrac{\left(z-z_i^{+}\right)}{b_i^{+}}-\hat{\boldsymbol{\varphi}}\dfrac{\rho}{jmb_i^{+}}, & \rho\in\left(\rho_i^{1},\rho_i^{2}\right),\ z\in\left(z_i^{+},z_i\right),\\ \hat{\boldsymbol{z}}\dfrac{\left(z_i^{-}-z\right)}{b_i^{-}}+\hat{\boldsymbol{\varphi}}\dfrac{\rho}{jmb_i^{-}}, & \rho\in\left(\rho_i^{1},\rho_i^{2}\right),\ z\in\left(z_i,z_i^{-}\right),\\ 0, & \text{otherwise.}\end{cases} \tag{5.26}$$

If the internal edge of the basis function is on the contour of the body, the basis function is defined based on the rectangles interior to T. No basis functions are associated with edges lying on the z-axis.

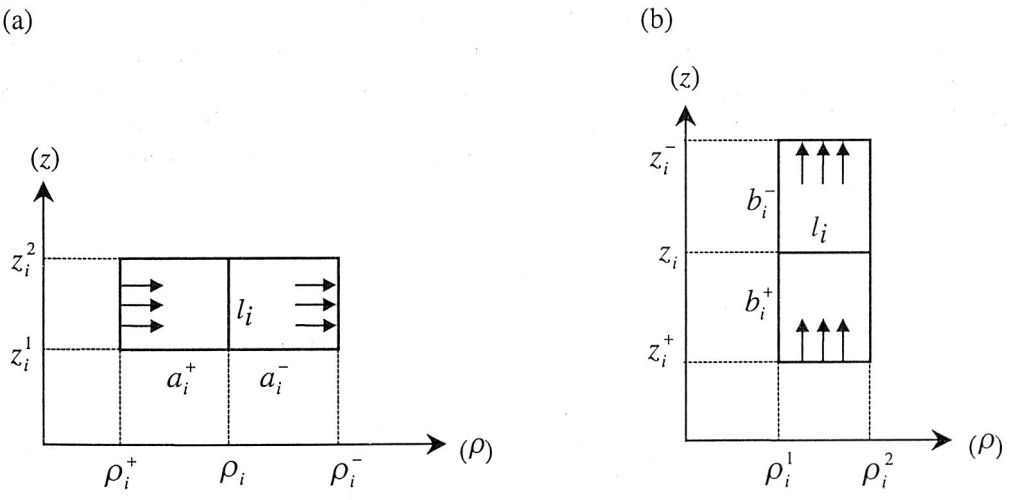

Fig. 5.6. Rectangle pairs and geometrical parameters associated with the rectangular basis function; (a) type ρ; (b) type z

It can be easily checked using (5.23) that functions (5.25) and (5.26) are divergenceless. It should be mentioned once again that „modal" basis functions should be understood in global expansion scheme as multiplied by an $\exp(jm\phi)$ factor.

Thus, we get the following representation of the "modal" $\boldsymbol{D}$:

$$\boldsymbol{D}_m(\rho, z)=\sum_{i=1}^{N_\rho} D_{mi}^{\rho}\boldsymbol{g}_{mi}(\rho, z)+\sum_{i=1}^{N_z} D_{mi}^{z}\boldsymbol{h}_{mi}(\rho, z), \tag{5.27}$$

where N_ρ and N_z are the function numbers defined by (5.25) and (5.26), respectively. Of course, $N_\rho + N_z = N$.

The corresponding currents associated with basis function can be calculated from (5.16). The total modal current at the given point can be expressed as:

$$\boldsymbol{J}_m(\rho, z)= j\omega\sum_{i=1}^{N_\rho} D_{mi}^{\rho}\kappa(\rho, z)\boldsymbol{g}_{mi}(\rho, z)+ j\omega\sum_{i=1}^{N_z} D_{mi}^{z}\kappa(\rho, z)\boldsymbol{h}_{mi}(\rho, z). \tag{5.28}$$

The charge density is represented by:

$$q_m(\rho, z)=-\sum_{i=1}^{N_\rho} D_{mi}^{\rho}\kappa(\rho, z)\nabla_m\cdot\boldsymbol{g}_{mi}(\rho, z)-\sum_{i=1}^{N_\rho} D_{mi}^{\rho}\boldsymbol{g}_{mi}(\rho, z)\cdot\nabla_T\kappa(\rho, z)$$

$$-\sum_{i=1}^{N_z} D_{mi}^{z}\kappa(\rho, z)\nabla_m\cdot\boldsymbol{h}_{mi}(\rho, z)-\sum_{i=1}^{N_z} D_{mi}^{z}\boldsymbol{h}_{mi}(\rho, z)\cdot\nabla_T\kappa(\rho, z), \tag{5.29}$$

where ∇_T denotes the transverse part of the gradient operator.

Similarly to the three-dimensional case, the first and third summations in (5.29) represent volume charge densities, which in the case of divergenceless functions (5.25) and (5.26) are simply equal to zero. The second and fourth summations, assuming piecewise constant profile of the contrast ratio κ, represent surface charge densities associated with the basis functions:

$$q_{msi}^{\rho}(\rho, z)=\begin{cases}\dfrac{1}{\rho} D_{mi}^{\rho}\left(\kappa_i^{\rho+}-\kappa_i^{\rho-}\right), & (\rho, z)\in l_i,\\ 0, & \text{otherwise},\end{cases} \tag{5.30}$$

$$q_{msi}^{z}(\rho, z)=\begin{cases}D_{mi}^{z}\left(\kappa_i^{z+}-\kappa_i^{z-}\right), & (\rho, z)\in l_i,\\ 0, & \text{otherwise},\end{cases} \tag{5.31}$$

where l_i in (5.30) and (5.31) is a "common line" associated with ρ-type and z-type basis functions, respectively.

Based on the above equations, it is easy to see that evaluation of the scalar potential does not require calculation of the surface integrals, because the integral in (4.26), or its multilayer counterpart, now reduces to a contour integral.

Basis functions on triangular domains

As mentioned before for triangular domains basis functions similar to the *RWG* functions [168] can be easily applied. We define the basis functions which span over two adjacent triangles (like the classical rooftop functions over two rectangles). Again, the basis functions are associated with edges rather than with particular triangles. Expanding $\rho \boldsymbol{D}_m^T(\rho, z)$ into the *RWG* functions and calculating D_m^{ϕ} from (5.24) we get the basis function definition:

$$\boldsymbol{f}_{mi}(\rho,z)=\begin{cases} \boldsymbol{t}_i^+ \dfrac{1}{\rho}\dfrac{l_i}{2A_i^+}-\hat{\boldsymbol{\varphi}}\dfrac{1}{jm}\dfrac{l_i}{A_i^+}, & (\rho, z)\in T_i^+, \\ \boldsymbol{t}_i^- \dfrac{1}{\rho}\dfrac{l_i}{2A_i^-}+\hat{\boldsymbol{\varphi}}\dfrac{1}{jm}\dfrac{l_i}{A_i^-}, & (\rho, z)\in T_i^-, \\ 0, & \text{otherwise}, \end{cases} \tag{5.32}$$

where vectors $\boldsymbol{t}_i^{+/-}$ responsible for the transverse fields are defined in Fig. 5.7.

Formulas similar to (5.28) through (5.31) for representing currents and charges can also be easily obtained.

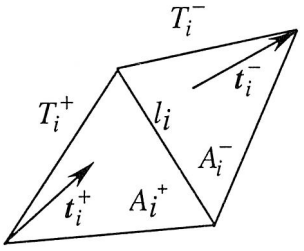

Fig. 5.7. Triangle pair and geometrical parameters associated with the triangular basis function

It should be noted that functions (5.32) are not capable of correctly representing the fields in sub-domains in the immediate vicinity of the z-axis. First, because the piecewise constant character of the *RWG* function in the direction perpendicular to current flow, after multiplying by $1/\rho$ results in an incorrect representation of the D_z component near the z-axis. Second, for similar reasons, no basis function can be defined on triangle edges directly on the z-axis. Taking into account the fact that in or-

der to represent a field in any direction we must use all three basis functions associated with each triangle, we find that fields in the vicinity of the z-axis cannot be correctly represented by functions defined in (5.32). On the other hand, omitting the $1/\rho$ term in the definition results in that the divergence formulas become significantly complex, which obviously cancels out one of the main advantages of applying the *RWG* functions.

One solution is to combine functions defined based on rectangles for representing the fields near the z-axis with functions defined based on triangles for the remaining part of the body. This however would require additional „mixed" basis functions to be defined for the edges separating rectangles and triangles (see Fig. 5.5(b)).

Mode $m = 0$

For the zeroth mode, we have two independent equations concerning transverse and azimuthal field components. These equations can then be solved separately.

Solving the equation for transverse field components, we can for example use the same transverse field representation as in the previous section. However, one must remember that the basis functions constructed in this manner are no longer divergenceless. This means that we must take into account the volume charges which appear in (5.29) when computing the scalar potential. This also means the need to enforce the zero divergence condition numerically.

The equation for the azimuthal mode has a very simple form, because it has no scalar potential term. Also, there is no differentiation operator acting on the field. Therefore, very simple (e.g., pulse) representations may be used in the field expansion.

Note also that because of the decoupling of equations, we never have to solve a system of linear equations with more unknowns than in the case of non-zero modes. It means that in this case we retain the main advantage of this method.

The method of construction, as well as the examples of mixed-domain divergenceless basis functions suitable for electric flux density are the author's exclusive original contribution.

5.2. Advantages of Galerkin formulations in the MPIE framework

In Chapter 3, we have concluded that the easiest treatment of kernel singularities is associated with a mixed-potential representation of the fields, because the scalar potential kernels exhibit only $1/R$ singularity, which present no computational difficulties (see Appendix 1). The disadvantage related to this representation is an additional *nabla* operator (gradient) acting on the scalar potential, i.e. appearing in front

of the scalar potential integral. We will show how this problem can be circumvented in the MoM formulation, when the Galerkin scheme is applied. In the Galerkin formulation, we assume that the basis and testing function sets are the same.

Let us assume that the equation describing the problem of interest is "tested" with the vector function f_p with properties of the functions described in the previous section. We will focus our interest on the contribution of scalar potential terms made to the impedance matrix.

SIE formulations

For SIE approach and *RWG* functions, we have the scalar potential term in the form:

$$\left\langle \nabla\Phi; f_p \right\rangle = \int_S \nabla\Phi \cdot f_p dS$$

$$= \int_{T_p^-} \nabla\Phi^- \cdot f_p^- dS + \int_{T_p^+} \nabla\Phi^+ \cdot f_p^+ dS, \tag{5.33}$$

where superscripts +/– relate scalar potential and basis function components to corresponding triangles. Integrating by parts and applying the Gauss theorem, we transform (5.33) into:

$$\left\langle \nabla\Phi; f_p \right\rangle = -\int_{T_p^-} \Phi^- \nabla \cdot f_p^- dS - \int_{T_p^+} \Phi^+ \nabla \cdot f_p^+ dS$$

$$+ \int_{l_p} \left(\Phi^- f_p^- \cdot \hat{\boldsymbol{u}}_p^- + \Phi^+ f_p^+ \cdot \hat{\boldsymbol{u}}_p^+ \right) dl, \tag{5.34}$$

where the designations are indicated in Fig. 5.8.

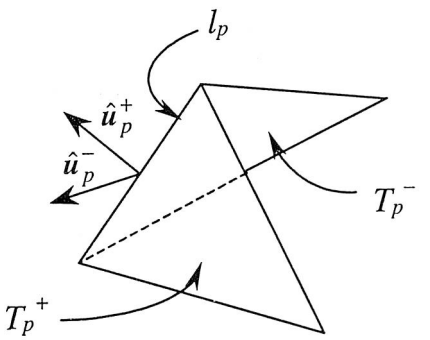

Fig. 5.8. A triangle pair defining an *RWG* test function [141]

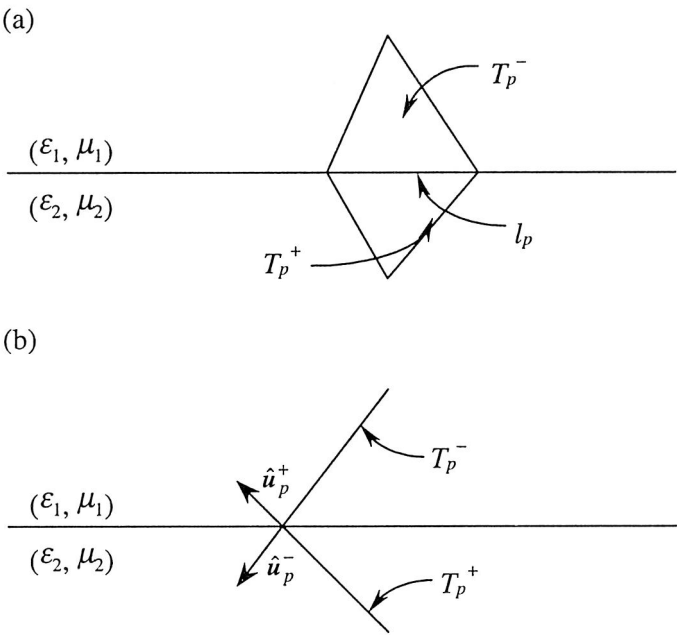

Fig. 5.9. Side view (a) and cross-sectional view (b) of a triangle pair straddling the interface between two adjacent layers [141]

Note that in the derivation of (5.34) we have applied a property of *RWG* functions such that $\boldsymbol{f}_p$ has no components normal to edges other than the common edge between the two triangles. In view of the definition (5.10) $\boldsymbol{f}_p^- \cdot \hat{\boldsymbol{u}}_p^- + \boldsymbol{f}_p^+ \cdot \hat{\boldsymbol{u}}_p^+ = 0$ on l_p. In free space, the scalar potential is a continuous function of position, thus $\Phi^- = \Phi^+$ on l_p, and the line integral in (5.34) disappears. In layered media, no triangular patch is allowed to cross the interface between two adjacent layers [141]. As a result, the triangle patch model must take into account the position of the interface, which leads to a configuration depicted in Fig. 5.9. An arrangement like this ensures the continuity of the current and allows a discontinuity of the charge on the interface [141]. The presence or absence of an additional line integral in (5.34) depends on the particular MPIE used. Fortunately, in the formulation outlined in this monograph (formulation C of Michalski and Zheng [141]), the scalar potential kernel is continuous when the observation point crosses the media interfaces, and the line integral disappears, which makes the situation identical to its free-space counterpart. Finally, for the formulations included herein we have:

$$\left\langle \nabla\Phi; f_p \right\rangle = -\int_{T_p^-} \Phi^- \nabla \cdot f_p^- dS - \int_{T_p^+} \Phi^+ \nabla \cdot f_p^+ dS \,. \tag{5.35}$$

Thus, the differential operator acting on the scalar potential has been neutralized in the testing procedure, and transferred to act on the testing functions which obviously must be differentiable. Equation (5.35) may be easily approximated using the potential values in the centers of the triangles and applying (5.11), [168].

Note also that identical treatment relying on rectangular or quadrilateral-based functions is possible, because the functions on edges opposite to the common edge have a zero value and do not contribute to the line integrals arising from the application of Gauss theorem.

VIE formulations

For VIE formulations, a similar procedure will be shown assuming a double-tetrahedron basis and the testing functions. Again, for double-cuboid functions the procedure remains essentially the same.

Thus, we have:

$$\left\langle \nabla\Phi; f_p \right\rangle = \int_V \nabla\Phi \cdot f_p dV = \int_{T_p^-} \nabla\Phi^- \cdot f_p^- dV + \int_{T_p^+} \nabla\Phi^+ \cdot f_p^+ dV \,. \tag{5.36}$$

Integrating by parts and applying the properties of f_p and the three-dimensional form of Gauss theorem we arrive at the formula:

$$\left\langle \nabla\Phi; f_p \right\rangle = \int_{A_p} \left(\Phi^- f_p^- \cdot \hat{\boldsymbol{u}}_p^- + \Phi^+ f_p^+ \cdot \hat{\boldsymbol{u}}_p^+\right) dS - \int_{T_p^-} \Phi^- \nabla \cdot f_p^- dV - \int_{T_p^+} \Phi^+ \nabla \cdot f_p^+ dV \,, \tag{5.37}$$

where the details are presented in Fig. 5.10.

This time, however, the situation is not a simple extrapolation of the SIE technique. We should remember that, although the essential block in the solution is a "double-tetrahedron" function, "single-tetrahedron" functions might also appear in association with the tetrahedron faces on the outer surface of the body. Therefore, we need to distinguish between these two cases.

When the "interior" function is considered and the scalar potential kernel is a continuous function of the observation point, then in view of the continuity of the normal f_p component on the common face A_p, the surface integral in (5.37) disappears, resulting in:

$$\left\langle \nabla\Phi; f_p \right\rangle = -\int_{T_p^-} \Phi^- \nabla \cdot f_p^- dV - \int_{T_p^+} \Phi^+ \nabla \cdot f_p^+ dV \,. \tag{5.38}$$

For "exterior" faces we have instead:

$$\left\langle \nabla\Phi; f_p \right\rangle = \int_{A_p} \left(\Phi f_p \cdot \hat{\boldsymbol{n}}\right) dS - \int_{T_p} \Phi \nabla \cdot f_p dV \,, \tag{5.39}$$

where the lack of superscripts +/– indicates that only one tetrahedron function is associated with A_p. $\hat{\boldsymbol{n}}$ denotes a unit vector normal to the body surface at A_p.

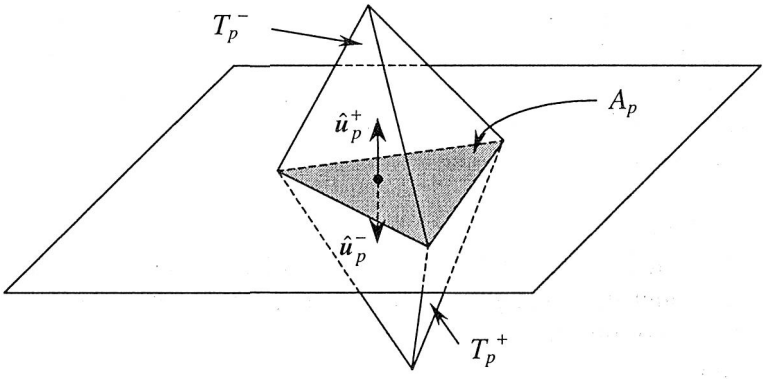

Fig. 5.10. A tetrahedron pair straddling the interface between two adjacent layers

If however the scalar potential kernel is not continuous across the media boundary in the multilayer environment, the surface integrals also remain for the "interior" functions and must be taken into account in the process of filling the impedance matrix. An alternative way is to split the tetrahedrons, with a common face in the layered media interface, to form two separate "single-tetrahedron" basis and testing functions. Afterwards, for each of these functions we should use formulas like (5.39). Note that this corresponds to "cutting" the body of interest into "slices" within the different layers.

BOR-VIE formulation

Note that up to now we have used a symmetric product in the testing procedure. In BOR formulations it is however convenient to apply a scalar product:

$$\langle f; g \rangle = \int_V f \cdot g^* dV \,. \tag{5.40}$$

For the m mode we get:

$$\langle f_m; g_m \rangle = \int_T \int_0^{2\pi} f_m(\rho, z) e^{jm\phi} \cdot g_m^*(\rho, z) e^{-jm\phi} \rho d\phi \, dT \,, \tag{5.41}$$

which, after performing the ϕ integration results in:

$$\langle f_m; g_m \rangle = 2\pi \int_T f_m(\rho, z) \cdot g_m^*(\rho, z) \rho dT \,, \tag{5.42}$$

where T is the „transverse" area of the BOR.

For the scalar potential term and for the "interior" testing function we get:

$$\left\langle \nabla_m \Phi_m ; f_{mp} \right\rangle = -2\pi \int_{T_p^-} \Phi_m^- \nabla_m \cdot f_{mp}^{-*} \rho dT - 2\pi \int_{T_p^+} \Phi_m^+ \nabla_m \cdot f_{mp}^{+*} \rho dT , \qquad (5.43)$$

while for the "exterior" faces we have:

$$\left\langle \nabla_m \Phi_m ; f_{mp} \right\rangle = 2\pi \int_{L_p} \left(\Phi_m f_{mp}^* \cdot \hat{\boldsymbol{n}} \right) \rho dL - 2\pi \int_{T_p} \Phi_m \nabla_m \cdot f_{mp}^* \rho dT . \qquad (5.44)$$

In (5.44) L denotes the generating arc of the BOR (the contour of T).

Note that if divergenceless testing functions are used ($m \neq 0$), then the only integral that remains in (5.43), (5.44) is the integral along the part of L. Thus, only the testing functions associated with the contour of the body introduce non-zero elements into the moment matrix. This fact reduces considerably the amount of computations associated with the scalar potential term. It is also worth pointing out that the singularity problem in this case can be avoided by surrounding the body with a layer consisting of „empty" basis functions (which means sub-domains with dielectric permittivity equal to that of surrounding space). In this case there is no surface charge density on the surface S, which results in the fact that all „self-term" elements are explicitly equal to zero.

For m = 0 we note that all integrals in (5.43) and (5.44) must be taken into account, because the testing functions are not divergenceless. This, however, concerns only TM equations, because in TE equations scalar potential terms are not present.

5.3. Resonance problems

This section is based on VIE formulation, however, it can be easily applied also to SIE formulations [44, 84].

As indicated in the introduction to this chapter, after applying the method-of-moments, equation (2.29) is transformed into a matrix equation:

$$\boldsymbol{S} \left| \boldsymbol{D} \right\rangle = \left| \boldsymbol{E}^i \right\rangle , \qquad (5.45)$$

where $\boldsymbol{S}$ is the moment matrix, $\boldsymbol{D}$ is the vector of unknown coefficients describing the electric flux density in the structure (which according to the previous sections is chosen as the unknown quantity), and $\boldsymbol{E}^i$ is the excitation vector depending on the incident field. Note that we have specialized the formal algebraic notation into our problem of interest. Resonant (natural) frequencies of the structure are defined as

frequencies for which the field can exist without excitation [93]. Such a situation takes place if the moment matrix determinant is equal to zero:

$$\det(\boldsymbol{S}) = 0. \tag{5.46}$$

In general, one has to search for roots of (5.46) in the complex frequency plane. This can be achieved if in all of the equations each ($j\omega$) is replaced by a complex number s. When both real and imaginary parts of the root are obtained one gets the information about resonant frequency and the associated quality factor of the resonator [93].

In the case of BOR structures, the matrix equation (5.45) splits into a number of modal matrix equations of the form:

$$\boldsymbol{S}_m \left| \boldsymbol{D}_m \right\rangle = \left| \boldsymbol{E}_m^i \right\rangle, \tag{5.47}$$

where the subscript m denotes the m-th Fourier mode. Again, for the case of no excitation this matrix equation has non-trivial solutions only when the determinant of the moment matrix $\boldsymbol{S}_m$ is equal to zero:

$$\det(\boldsymbol{S}_m) = 0. \tag{5.48}$$

The roots of (5.48) are designated by:

$$s_{m,\nu} = \sigma_{m,\nu} + j\omega_{m,\nu} \tag{5.49}$$

where $\omega_{m,\nu}$ is the resonant frequency of the mode (m, ν), and $\sigma_{m,\nu}$ is the decay time constant of the mode, which in the case of lossless dielectric materials is inversely proportional to the radiation factor Q

$$Q_{m,\nu} = -\frac{\omega_{m,\nu}}{2\sigma_{m,\nu}}. \tag{5.50}$$

Note that in the VIE-BOR formulation we have included a resonance identification scheme. The first subscript in (5.49) and (5.50), which is simply the azimuthal mode number, describes the azimuthal field variation associated with a given resonance. The second subscript ν is an integer used to count the resonant frequencies in a growing order, i.e., to denote the unique complex frequencies for which (5.48) is satisfied. For each of the m values in (5.48) we can find solutions for $\nu = 1, 2, 3, \ldots$. Each of these solutions corresponds to a different resonant mode. Once the field distribution for a particular mode is known, we can sometimes also replace ν with two other subscripts, which denote the radial and axial behavior of the field [93]. When the resonance frequency is found with a satisfactory accuracy, the field distributions for the particular modes may be found based on (5.48) within a multiplicative constant.

An interesting generalization of the concept of resonant modes is the idea of *characteristic modes* [22, 63], especially useful when considering the problem of synthesis of scattering characteristics [184].

5.4. Convergence and validation of results

Errors related to the given numerical approximate solutions above are caused by [85]:

- physical modeling,
- numerical modeling.

The first type of errors is related to the number of approximations made in the physical description of the problem. In this monograph, an example of approximation like this is the assumption of an infinite lateral extent of the media in problems involving stratified environments. Numerical modeling errors [35] are on the other hand associated with the specific methods of constructing the approximate problem solution. In the method-of-moments these errors arise from:

- the set of basis functions (how closely a finite set of basis functions is able to represent the real physical quantities, such as current or field distributions);
- the testing procedure;
- the approximation of operators (numerical integrations, the quadratures applied);
- round-off errors in numerical calculations (the available floating-point precision level).

Usually it is assumed that using a larger number of unknowns we should get results that are more accurate. This is true for the so-called well-posed problems, for which the moment matrix inversion does not present numerical difficulties. The limitations of increasing the accuracy by increasing the number of unknowns can be twofold. First, the problem solution may become not manageable because of the required computer resources (CPU memory, computation time). Second, the influence of round-off errors may become unacceptable.

The more fundamental limitations can be related to some physical modeling, inherent in the formulation. For example, in VIE procedure of Livesay and Chen [116] the use of pulse functions for the electric field representation causes non-physical charges associated with field jumps between particular sub-domains (cells) to appear. As the number of sub-divisions is increased the influence of these non-physical charges may lead to divergent results [61, p. 59], [178]. Note that these types of errors can be accounted for only by experienced code users who deeply understand the theory behind the particular application (code).

The general trend that can be observed in state-of-art developments is to decrease the number of unknowns needed by using more accurate approximations of the modeled quantities. This is related to the development of higher order basis functions better suited both for representing complex (possibly curvilinear) geometries [15, 16, 21], as well as looking for more accurate field (currents, potentials) representations [50, 51] (see also section 5.1). As indicated in this monograph, a significant reduction of unknowns may be obtained when the problem of interest is characterized by certain

symmetries (BOR schemes), or when some fundamental physical laws are inherent in the formulation instead of being enforced numerically (divergenceless basis function for representation of $\boldsymbol{D}$).

The best way of verifying the modeling results is to compare them with measurement data [85]. Unfortunately, we very rarely have at our disposal reliable measurement data suitable for comparisons. We must say that experiments, particularly in the field of dielectric bodies–EM field interactions, are difficult or sometimes even impossible to perform (for example, internal field distributions in dielectric bodies). Even if measurements of some quantities are possible, they require vast experience, careful preparation of experiment methodology and last but not least, an accurate (and expensive) measuring set-up.

An alternative way (or a kind of supplement to the experimental verification) is to compare the computation results with those obtained independently using other calculation methods. The drawback of such an approach is that when the results differ from each other, it is difficult to indicate which of them are better (closer to the actual values), [85].

Another class of verification methods includes the "intrinsic" methods. The essential element of these methods is to check (with some additional computational effort) whether the results satisfy the initial assumptions, such as boundary conditions, as well as the reciprocity theorem and the conservation of energy.

A good method for validation of numerical code is a systematic verification of particular computational blocks and formulas. The simple steps in validation of the VIE-BOR free-space scattering code may be as follows:

1. We assume that dielectric body has permittivity of the surrounding space, i.e., $\varepsilon_r = 1$ and then we check whether the electric field obtained is equal to the incident field. Thus, we check the ability of the basis function to properly represent the fields. At the same time, we can check the decomposition of the problem into azimuthal modes.

2. We assume a relatively low frequency for the computation. In this case, the solution is dominated by the scalar potential terms. Also, approximate analytical formulas for canonical shapes (sphere) are available for comparison.

3. We go to higher frequencies and check the vector potential calculations.

4. We apply the solution to resonance problems, so that we only check the formulas for the impedance matrix (without excitation).

5. We check the far-field formulas versus the rigorous formulas applied for sufficiently far observation points.

6. Increasing the number of unknowns, we check whether the solutions converge to true values. In this step, we can choose to compromise between the accuracy and the computational time, of course if other limits such as memory requirements do not play an important role. It should be noted that a reasonable accuracy may be that of comparison data.

For the case of multilayer media, additional blocks must be tested. Of particular importance are the calculations of Sommerfeld integrals, which are the basis for the whole procedure. In general, because the multilayer case is a generalization of a free-space problem, the natural procedure is to check whether the multilayer solutions applied to free-space problems reduce to real free-space solutions. As a kind of an intermediate case, we can consider the perfect ground problem.

All of the above methods have been used to carefully validate all programs developed by the author. Validation results are shown in the examples presented in Chapter 8.

Chapter 6. Incident fields

The typical excitation taken into account in scattering calculations is a plane wave with oblique incidence and polarization. Although the mathematical description of a plane wave in free-space is trivial, two aspects require more detailed treatment. First, in BOR schemes we need to decompose a plane wave into azimuthal modes in order to solve the modal equations. Second, the problem of calculating the impressed fields created by the incident plane wave at an arbitrary point of layered medium has to be dealt with. Solutions to the above problems are given below. Finally, we consider the two problems together, i.e., state the explicit formulas for modal impressed field decomposition in multilayer media.

6.1. Decomposition of a plane wave into azimuthal modes

Consider a plane wave with the electric field amplitude E_0 propagating in free space. According to Fig. 6.1, the direction this wave arrives from is specified by the angles (ϑ_i, φ_i) and its polarization by ς_i.

Projected onto the cylindrical coordinate system, the electric and magnetic fields are given by:

$$\boldsymbol{E}_0^i = E_0\left[\left(\hat{\boldsymbol{\rho}}_i \cos\vartheta_i + \hat{\boldsymbol{z}} \sin\vartheta_i\right)\cos\varsigma_i + \hat{\boldsymbol{\varphi}}_i \sin\varsigma_i\right] e^{jk_{zi}(z-z_0)} e^{-j\boldsymbol{k}_{\rho i}\cdot\boldsymbol{\rho}}, \tag{6.1}$$

$$\boldsymbol{H}_0^i = \frac{E_0}{\eta_0}\left[\left(\hat{\boldsymbol{\rho}}_i \cos\vartheta_i + \hat{\boldsymbol{z}} \sin\vartheta_i\right)\sin\varsigma_i - \hat{\boldsymbol{\varphi}}_i \cos\varsigma_i\right] e^{jk_{zi}(z-z_0)} e^{-j\boldsymbol{k}_{\rho i}\cdot\boldsymbol{\rho}}, \tag{6.2}$$

where $\eta_0 = \sqrt{\mu_0 / \varepsilon_0}$ is a free-space intrinsic impedance, z_0 is an arbitrarily chosen phase reference point on the z-axis, $k_{zi} = k_0 \cos\vartheta_i$, $\boldsymbol{k}_{\rho i} = \hat{\boldsymbol{\rho}}_i k_{\rho i}$ with $k_{\rho i} = k_0 \sin\vartheta_i$. Here, $0 \le \vartheta_i \le \pi/2$ and

$$\boldsymbol{k}_{\rho i} \cdot \boldsymbol{\rho} = k_0 \sin\vartheta_i \left(x\cos\varphi_i + y\sin\varphi_i\right). \tag{6.3}$$

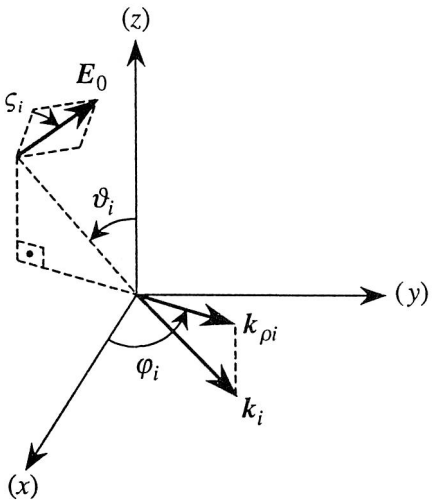

Fig. 6.1. Geometry used for the evaluation of the plane wave incident field

Directions of the unit vectors $\hat{\boldsymbol{\rho}}_i$ and $\hat{\boldsymbol{\varphi}}_i$ are fixed by the angle φ_i, which specifies the *plane of incidence*. In order to find the modal decomposition of (6.1) and (6.2) we must first express the impressed field in terms of cylindrical coordinates (ρ, z, ϕ). Unit vectors $\hat{\boldsymbol{\rho}}_i$ and $\hat{\boldsymbol{\varphi}}_i$ may be expressed as:

$$\hat{\boldsymbol{\rho}}_i = \hat{\boldsymbol{\rho}}\cos\phi - \hat{\boldsymbol{\varphi}}\sin\phi\,, \tag{6.4}$$

$$\hat{\boldsymbol{\varphi}}_i = \hat{\boldsymbol{\rho}}\sin\phi + \hat{\boldsymbol{\varphi}}\cos\phi\,. \tag{6.5}$$

Here, without loss of generality we may also assume that $\varphi_i = 0$. The exponential term thus becomes:

$$-j\boldsymbol{k}_{\rho i}\cdot\boldsymbol{\rho} = -jk_0\sin\vartheta_i\; x = -jk_0\sin\vartheta_i\;\rho\cos\phi\,. \tag{6.6}$$

After substituting (6.4)–(6.6) into (6.1), (6.2), we obtain:

$$\begin{aligned}\boldsymbol{E}_0^i = E_0\big[&\hat{\boldsymbol{\rho}}\big(\cos\vartheta_i\cos\varsigma_i\cos\phi + \sin\varsigma_i\sin\phi\big) + \hat{\boldsymbol{z}}\sin\vartheta_i\cos\varsigma_i \\ &+ \hat{\boldsymbol{\varphi}}\big(-\cos\vartheta_i\cos\varsigma_i\sin\phi + \sin\varsigma_i\cos\phi\big)\big]e^{jk_{zi}(z-z_0)}e^{-jk_0\sin\vartheta_i\rho\cos\varphi}\,,\end{aligned} \tag{6.7}$$

$$\begin{aligned}\boldsymbol{H}_0^i = \frac{E_0}{\eta_0}\big[&\hat{\boldsymbol{\rho}}\big(\cos\vartheta_i\sin\varsigma_i\cos\phi - \cos\varsigma_i\sin\phi\big) + \hat{\boldsymbol{z}}\sin\vartheta_i\sin\varsigma_i \\ &- \hat{\boldsymbol{\varphi}}\big(\cos\vartheta_i\sin\varsigma_i\sin\phi + \cos\varsigma_i\cos\phi\big)\big]e^{jk_{zi}(z-z_0)}e^{-jk_0\sin\vartheta_i\rho\cos\phi}\,.\end{aligned} \tag{6.8}$$

The modal fields are then obtained based on (6.7), (6.8) using an expansion into Fourier series applied with respect to the azimuthal variable ϕ. Taking into account the integral representation of Bessel function [125]

$$J_n(a)=\frac{j^n}{2\pi}\int_0^{2\pi} e^{-ja\cos\phi}e^{-jn\phi}d\phi, \tag{6.9}$$

we finally obtain the following formulas (m denotes the number of the azimuthal mode):

$$\boldsymbol{E}_0^{im}=E_0\frac{1}{j^m}\left[\hat{\boldsymbol{\rho}}\left(\cos\vartheta_i\cos\varsigma_i\frac{J_{m+1}-J_{m-1}}{2j}+\sin\varsigma_i\frac{J_{m+1}+J_{m-1}}{2}\right)+\hat{z}\sin\vartheta_i\cos\varsigma_i J_m\right.$$
$$\left.+\hat{\varphi}\left(-\cos\vartheta_i\cos\varsigma_i\frac{J_{m+1}+J_{m-1}}{2}+\sin\varsigma_i\frac{J_{m+1}-J_{m-1}}{2j}\right)\right]e^{jk_{zi}(z-z_0)}, \tag{6.10}$$

$$\boldsymbol{H}_0^{im}=\frac{E_0}{\eta_0}\frac{1}{j^m}\left[\hat{\boldsymbol{\rho}}\left(\cos\vartheta_i\sin\varsigma_i\frac{J_{m+1}-J_{m-1}}{2j}-\cos\varsigma_i\frac{J_{m+1}+J_{m-1}}{2}\right)+\hat{z}\sin\vartheta_i\sin\varsigma_i J_m\right.$$
$$\left.-\hat{\varphi}\left(\cos\vartheta_i\sin\varsigma_i\frac{J_{m+1}+J_{m-1}}{2}+\cos\varsigma_i\frac{J_{m+1}-J_{m-1}}{2j}\right)\right]e^{jk_{zi}(z-z_0)}, \tag{6.11}$$

where:

$$J_k=J_k(k_0\rho\sin\vartheta_i). \tag{6.12}$$

The above formulas are consistent with those given, for example, in [6, 125]. Based on (6.12), we may also estimate the number of azimuthal harmonics needed in the solution. A rule of thumb for this case is to take $M=k_0\rho_{\max}$ modes, where $\rho_{\max}$ denotes the largest ρ value of the BOR [212].

6.2. Impressed fields in multilayer media*)

Now, we shall consider the case of stratified media. In addition to the assumptions made in section 3.1, we assume that the top layer of the medium forms a half-space

*) This section has been written on the basis of a longer, unpublished version of paper [140], which has been made available to the author by Prof. K. A. Michalski.

filled with air. Our goal is to find the impressed field $(\boldsymbol{E}^i, \boldsymbol{H}^i)$ established at any point in the layered medium, as a result of a plane-wave (6.1), (6.2) incident in the upper half-space.

For the fields to match at the interface, the dependence of $(\boldsymbol{E}^i, \boldsymbol{H}^i)$ in the transverse (to the z-axis) coordinates must be the same in all layers [144] and must match that of the incident plane wave (6.1), (6.2). That dependence is described by the factor

$$e^{-j\boldsymbol{k}_{\rho i}\cdot\boldsymbol{\rho}} = e^{-jk_0 \sin\vartheta_i (x\cos\varphi_i + y\sin\varphi_i)} = e^{-j(k_x x + k_y y)}, \tag{6.13}$$

where we define $k_x = k_0 \sin\vartheta_i \cos\varphi_i$, $k_y = k_0 \sin\vartheta_i \sin\varphi_i$.

With the transverse dependence of all field quantities described by (6.13) and noting that the medium is homogeneous and of infinite extent in any transverse plane we may suppress the lateral dependence in Maxwell's equations assuming $\frac{\partial}{\partial x} = -jk_x$, $\frac{\partial}{\partial y} = -jk_y$.

Thus, after separating the transverse and longitudinal parts we note that the fields satisfy the source free forms of equations (3.47)–(3.50), with $\boldsymbol{k}_\rho = \boldsymbol{k}_{\rho i}$

$$\frac{d}{dz}\tilde{\boldsymbol{E}}_t = \frac{1}{j\omega\varepsilon}\left(k^2 - \boldsymbol{k}_{\rho i}\boldsymbol{k}_{\rho i}\cdot\right)\left(\tilde{\boldsymbol{H}}_t \times \hat{z}\right), \tag{6.14}$$

$$\frac{d}{dz}\tilde{\boldsymbol{H}}_t = \frac{1}{j\omega\mu}\left(k^2 - \boldsymbol{k}_{\rho i}\boldsymbol{k}_{\rho i}\cdot\right)\left(\hat{z} \times \tilde{\boldsymbol{E}}_t\right), \tag{6.15}$$

$$-j\omega\varepsilon\tilde{E}_z = j\boldsymbol{k}_{\rho i}\cdot\left(\tilde{\boldsymbol{H}}_t \times \hat{z}\right), \tag{6.16}$$

$$-j\omega\mu\tilde{H}_z = j\boldsymbol{k}_{\rho i}\cdot\left(\hat{z} \times \tilde{\boldsymbol{E}}_t\right). \tag{6.17}$$

The symbol "~" above field quantities now denotes fields with suppressed lateral dependence.

If we now express the transverse electric and magnetic fields as:

$$\tilde{\boldsymbol{E}}_t = \hat{\boldsymbol{\rho}}_i V^e + \hat{\varphi}_i V^h, \quad \tilde{\boldsymbol{H}}_t = \hat{\boldsymbol{\rho}}_i I^e + \hat{\varphi}_i I^h, \tag{6.18}$$

and moreover, project (6.14)–(6.15) onto $\hat{\boldsymbol{\rho}}_i$ and $\hat{\varphi}_i$, we find that these equations decouple into two sets of source free transmission line equations of the form:

$$\frac{dV^p}{dz} = -jk_{zi}Z^p I^p, \quad \frac{dI^p}{dz} = -jk_{zi}Y^p V^p, \tag{6.19}$$

where $p = e$ or h. Above, the propagation wave numbers and the characteristic impedance and admittance of the transmission line are defined as in Chapter 3, with $k_\rho = k_{\rho i}$:

$$k_z = \sqrt{k^2 - k_{\rho i}^2} = k_{zi}, \tag{6.20}$$

$$Z^e = \frac{1}{Y^e} = \frac{k_{zi}}{\omega\varepsilon}, \quad Z^h = \frac{1}{Y^h} = \frac{\omega\mu}{k_{zi}}. \tag{6.21}$$

Based on (6.19), we see that the components of $\tilde{\boldsymbol{E}}_t$ and $\tilde{\boldsymbol{H}}_t$ may be interpreted as voltages and currents on a transmission-line analog of a medium along the z-axis.

The transverse electric field corresponding to the incident plane wave (6.1), (6.2) can be expressed as:

$$\tilde{\boldsymbol{E}}_{0t}^i = \hat{\boldsymbol{\rho}}_i \tilde{V}^e + \hat{\boldsymbol{\varphi}}_i \tilde{V}^h, \tag{6.22}$$

where:

$$\tilde{V}^e = E_0 \cos\varsigma_i \cos\vartheta_i e^{jk_{zi}(z-z_0)}, \quad \tilde{V}^h = E_0 \sin\varsigma_i e^{jk_{zi}(z-z_0)}. \tag{6.23}$$

$\tilde{V}^e$ and $\tilde{V}^h$ may be interpreted as the leftward propagating incident voltage waves exciting the respective TM and TE transmission-line networks, in a line section corresponding to the upper-half-space.

The z-components of the fields may be easily calculated from (6.16) and (6.17). Thus, the impressed fields in any layer may be obtained as

$$\boldsymbol{E}^i = \left(\hat{\boldsymbol{\rho}}_i V^e + \hat{\boldsymbol{\varphi}}_i V^h - \hat{\boldsymbol{z}} \frac{k_0}{\omega\varepsilon} \sin\vartheta_i I^e \right) e^{-j\boldsymbol{k}_{\rho i}\cdot\boldsymbol{\rho}}, \tag{6.24}$$

$$\boldsymbol{H}^i = \left(-\hat{\boldsymbol{\rho}}_i I^h + \hat{\boldsymbol{\varphi}}_i I^e + \hat{\boldsymbol{z}} \frac{k_0}{\omega\mu} \sin\vartheta_i V^h \right) e^{-j\boldsymbol{k}_{\rho i}\cdot\boldsymbol{\rho}}, \tag{6.25}$$

where $V^p(z)$ and $I^p(z)$ are the total voltage and current at point z on the transmission line network. If the uppermost interface is z_n the total voltage and current on the transmission-line section n corresponding to the upper half-space are given as

$$V^p(z) = \tilde{V}^p(z)\tilde{\tau}_n^p(z), \quad I^p(z) = \tilde{V}^p(z)\tilde{y}_n^p(z), \tag{6.26}$$

where auxiliary functions $\tilde{\tau}_n^p$ and $\tilde{y}_n^p$ are defined in Appendix 2. In any other line section m, $V^p(z)$ and $I^p(z)$ are given by (A.2.10), with $V^p(z_n)$ computed via (6.26). Note again that all calculations are performed with $k_\rho = k_{\rho i}$. Also note that in (6.24)–(6.25) the lateral dependence has been recovered.

6.3. Modal representation for a case of stratified environment

For a body-of-revolution, we have to find the modal counterparts of formulas (6.24) and (6.25). In the subsequent derivation, we assume that the BOR symmetry axis is perpendicular to the medium stratification, i.e., it runs along the z-axis of the coordinate system.

In terms of local coordinates (6.24)–(6.25) may be rewritten as:

$$\boldsymbol{E}^i = \left(\hat{\rho}\left(V^e \cos\phi + V^h \sin\phi\right) + \hat{\varphi}\left(V^h \cos\phi - V^e \sin\phi\right) - \hat{z}\frac{k_0}{\omega\varepsilon}\sin\vartheta_i I^e \right) e^{-jk_{\rho i}\cdot\rho}, \quad (6.27)$$

$$\boldsymbol{H}^i = \left(\hat{\rho}\left(I^e \sin\phi - I^h \cos\phi\right) + \hat{\varphi}\left(I^h \sin\phi + I^e \cos\phi\right) + \hat{z}\frac{k_0}{\omega\mu}\sin\vartheta_i V^h \right) e^{-jk_{\rho i}\cdot\rho}. \quad (6.28)$$

Following the procedure given in section 6.1, i.e., performing the expansion into Fourier series and using (6.9) as well as some algebra we obtain:

$$\boldsymbol{E}^{im} = \frac{1}{j^m}\left[\hat{\rho}\left(V^e \frac{J_{m+1} - J_{m-1}}{2j} + V^h \frac{J_{m+1} + J_{m-1}}{2} \right) \right.$$

$$\left. + \hat{\varphi}\left(V^h \frac{J_{m+1} - J_{m-1}}{2j} - V^e \frac{J_{m+1} + J_{m-1}}{2} \right) - \hat{z}\frac{k_0}{\omega\varepsilon}\sin\vartheta_i I^e J_m \right], \quad (6.29)$$

$$\boldsymbol{H}^{im} = \frac{1}{j^m}\left[\hat{\rho}\left(I^e \frac{J_{m+1} + J_{m-1}}{2} - I^h \frac{J_{m+1} - J_{m-1}}{2j} \right) \right.$$

$$\left. + \hat{\varphi}\left(I^h \frac{J_{m+1} + J_{m-1}}{2} + I^e \frac{J_{m+1} - J_{m-1}}{2j} \right) + \hat{z}\frac{k_0}{\omega\mu}\sin\vartheta_i V^h J_m \right]. \quad (6.30)$$

In problems concerning conducting and homogeneous bodies, the above equations are often formulated in terms of components tangential to the BOR surface. In this case, radial and vertical components can be grouped together giving a single tangential component lying in the transverse T plane [125].

It can be shown that in the degenerated case, when the medium is homogeneous (free-space) the transmission line model reduces to an infinite line with constant parameters, and the formulas given in this section reduce to those given in section 6.1.

The modal decomposition of the impressed field given in this section is considered as the author's original contribution.

Chapter 7. Far-field approximation

7.1. Vector potential components in a radiation zone

A considerable simplification of the formulas relating fields to their sources occurs when the observation point lies in the far-field zone. Let us assume again that the fields are due to electric current distribution. This situation is shown in Fig. 7.1.

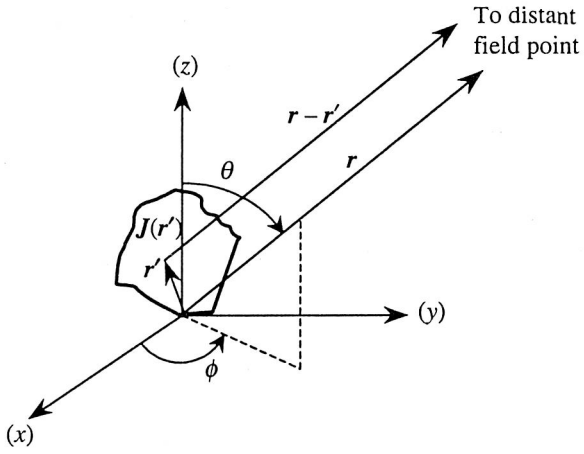

Fig. 7.1. The configuration for calculation of far-zone fields

According to [62, p. 132] for free-space*) the vector magnetic potential may be approximated as:

$$A(r) \xrightarrow{r\to\infty} \frac{\mu_0}{4\pi}\frac{e^{-jk_0 r}}{r}\left\langle e^{jk_0\hat{r}\cdot r'}; J(r')\right\rangle. \tag{7.1}$$

*) Obviously, the formulas are the same for any homogeneous medium. The free-space indices are introduced for notational consistency with section 7.3.

In (7.1) we have taken advantage of the fact that for r approaching infinity the amplitude differences in fields caused by elementary currents forming the whole current distribution may be neglected, while the dependence in phase factors is left unchanged in the formulas. Furthermore, it is known that the fields in the far-zone behave as plane waves, i.e., there is no field component along the direction of propagation, which is caused by the fact that in the far-field the scalar potential field component cancels out the radial field component related to the vector potential. In view of this, we can write the formula for the electric field [212] as:

$$\boldsymbol{E}(\boldsymbol{r}) = j\omega\hat{\boldsymbol{r}} \times (\hat{\boldsymbol{r}} \times \boldsymbol{A}(\boldsymbol{r})). \tag{7.2}$$

The magnetic field may be obtained using the well-known plane wave relation [62, p. 133]:

$$\boldsymbol{H}(\boldsymbol{r}) = \frac{1}{\eta_0}\hat{\boldsymbol{r}} \times \boldsymbol{E}(\boldsymbol{r}), \tag{7.3}$$

where $\eta_0 = \sqrt{\mu_0 / \varepsilon_0}$ is the intrinsic impedance of the medium.

For consistency with the notation used in section 7.3, and as an introduction to modal formulas given in section 7.4 we may express (7.2) using cylindrical coordinates:

$$E_{\theta,\phi} \approx \frac{\omega\mu_0 e^{-jk_0 r}}{4\pi jr}\left\langle f_{\theta,\phi}\, e^{jk_{\rho 0}\cdot\rho'}; \boldsymbol{J}(\boldsymbol{r}')\right\rangle, \tag{7.4}$$

where we have introduced $\boldsymbol{k}_0 = k_0\hat{\boldsymbol{r}} = \boldsymbol{k}_{\rho 0} + \hat{z}k_{z0}$, $k_{z0} = k_0\cos\theta$, $\boldsymbol{k}_{\rho 0} = \hat{\boldsymbol{\rho}}k_{\rho 0}$, $k_{\rho 0} = k_0\sin\theta$.

In (7.4) the auxiliary vector functions $\boldsymbol{f}$ are defined as:

$$\boldsymbol{f}_\theta = e^{jk_{z0}z'}(\hat{\boldsymbol{\rho}}\cos\theta - \hat{z}\sin\theta), \tag{7.5}$$

$$\boldsymbol{f}_\phi = e^{jk_{z0}z'}\hat{\boldsymbol{\varphi}}. \tag{7.6}$$

Additionally, we find that:

$$\boldsymbol{k}_{\rho 0}\cdot\boldsymbol{\rho}' = k_0\sin\theta(x'\cos\phi + y'\sin\phi) = k_0\sin\theta\ \rho'\cos(\phi - \phi'). \tag{7.7}$$

If the magnetic currents are also present, we may as usual apply the duality principle and afterwards the superposition.

7.2. Radar cross-section

A useful measure in plane-wave scattering problems is the *bistatic radar cross-section*, defined as [212]

$$\sigma(\hat{\boldsymbol{r}},\hat{\boldsymbol{k}}) = \lim_{r\to\infty} 4\pi r^2 \frac{|\boldsymbol{E}(\boldsymbol{r})|^2}{|\boldsymbol{E}^{\text{inc}}|^2}, \tag{7.8}$$

where the unit vector $\hat{\boldsymbol{k}}$ describes the direction of propagation of an incident plane wave $\boldsymbol{E}^{\text{inc}}$, whilst the unit vector $\hat{\boldsymbol{r}}$ defines the observation direction (Fig. 7.2).

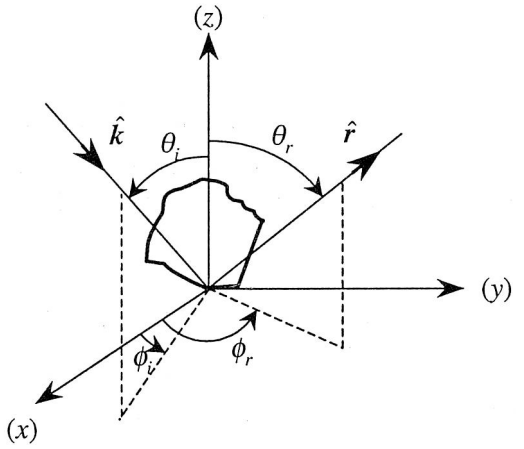

Fig. 7.2. Plane wave scattering by an arbitrary body

In practical cases, we often take into account the polarization of incident and outgoing waves, which leads to the following definition [125]:

$$\sigma_{pq}(\hat{\boldsymbol{r}},\hat{\boldsymbol{k}}) = \lim_{r\to\infty} 4\pi r^2 \frac{|\boldsymbol{E}_p(\boldsymbol{r})|^2}{|\boldsymbol{E}_q^{\text{inc}}|^2}, \tag{7.9}$$

where pq denotes $\theta\theta$, $\theta\phi$, $\phi\theta$, $\phi\phi$.

The *monostatic radar cross-section* is the radar cross-section observed in the back scattering direction, i.e., $\sigma(-\hat{\boldsymbol{k}},\hat{\boldsymbol{k}})$ or $\sigma_{pq}(-\hat{\boldsymbol{k}},\hat{\boldsymbol{k}})$.

7.3. Far-field approximation for layered media

We will consider the far-field approximation for layered media, when the medium of interest is not shielded from above. For the subsequent development we also assume that the upper half-space is filled with air, which is a practical situation. Next, we choose a point on the z-axis, z_0 such that the layered structure and the current distribution (the body) lie below, i.e., are confined to the region $z \le z_0$ (see Fig. 7.3). The procedure outlined here was originally given in a longer, draft version of the paper [140].

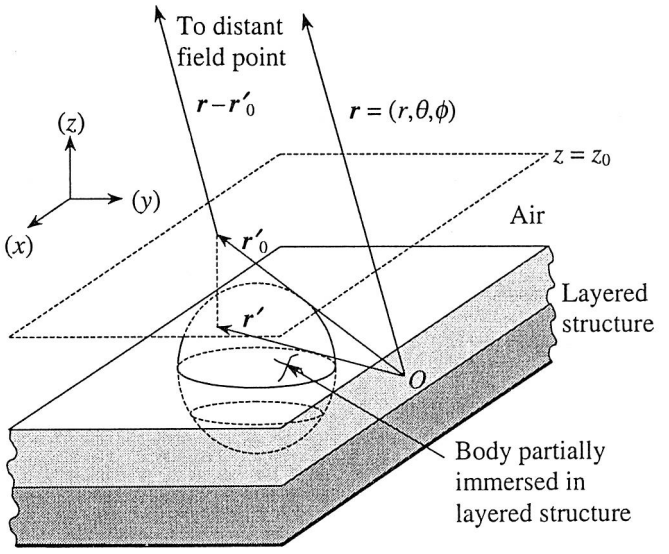

Fig. 7.3. Geometry for the evaluation of the far-zone field in layered media

Based on (3.84)–(3.87) as well as the TLGFs given in Appendix 2 it can be noticed that for the region of interest the spectral DGFs may be expressed in the form:

$$\underline{\underline{\tilde{G}}}^{PQ}\left(\boldsymbol{k}_\rho; z \mid z'\right) = \underline{\underline{\tilde{G}}}^{PQ}\left(\boldsymbol{k}_\rho; z_0 \mid z'\right) e^{-jk_z(z-z_0)}, \qquad z \ge z_0, \tag{7.10}$$

where $k_z = \sqrt{k_0^2 - k_\rho^2}$. The space counterpart of (7.10) may be written as:

$$\underline{\underline{G}}^{PQ}\left(\boldsymbol{r} \mid \boldsymbol{r}'\right) = \frac{1}{(2\pi)^2} \int_{-\infty}^{\infty}\int_{-\infty}^{\infty} jk_z \underline{\underline{\tilde{G}}}^{PQ}\left(\boldsymbol{k}_\rho; z_0 \mid z'\right) \left\{ \frac{e^{-jk\cdot(r-r'_0)}}{jk_z} \right\} dk_x dk_y , \tag{7.11}$$

where $\boldsymbol{k} = \boldsymbol{k}_\rho + \hat{z}k_z$, $\boldsymbol{r}_0' = \boldsymbol{\rho}' + \hat{z}z_0$. The integrand in (7.11) has been factorized into a slowly varying part and a rapidly varying part. The later (enclosed in curly braces) can be integrated in a closed form using the Weyl–Sommerfeld identity [185].

$$\frac{1}{(2\pi)^2}\int_{-\infty}^{\infty}\int_{-\infty}^{\infty}\frac{e^{-j\boldsymbol{k}\cdot(\boldsymbol{r}-\boldsymbol{r}_0')}}{jk_z}dk_x dk_y = \frac{1}{2\pi}\int_0^{\infty}\frac{e^{-jk_z|z-z_0|}}{jk_z}J_0\left(k_\rho|\boldsymbol{\rho}-\boldsymbol{\rho}'|\right)k_\rho dk_\rho = \frac{1}{2\pi}\frac{e^{-jkR}}{R}, \quad (7.12)$$

where

$$R = \sqrt{|\boldsymbol{\rho}-\boldsymbol{\rho}'|^2 + |z-z_0|^2} = |\boldsymbol{r}-\boldsymbol{r}_0'|. \quad (7.13)$$

As $r \to \infty$ (see Fig. 7.3), most of the contribution to the integral comes from the vicinity of the stationary phase point at $k_{x0} = k_0 x/r$, $k_{y0} = k_0 y/r$ [27]. Consequently, we may replace the slowly varying part of the integrand with its value at the stationary-phase point and place it in front of the integral signs and then evaluate the rest of the integral in a closed form using (7.12). As a result, after applying the far-zone approximations described in section 7.1 we get:

$$\underline{\underline{\boldsymbol{G}}}^{PQ}(\boldsymbol{r}\,|\,\boldsymbol{r}') \approx \frac{e^{-jk_0 r}}{2\pi jr}e^{jk_{z0}z_0}k_{z0}\underline{\underline{\tilde{\boldsymbol{G}}}}^{PQ}\left(\boldsymbol{k}_{\rho 0}; z_0\,|\,z'\right)e^{j\boldsymbol{k}_{\rho 0}\cdot\boldsymbol{\rho}'}, \qquad r \to \infty \quad (7.14)$$

where $k_{z0} = k_0\cos\theta$, $\boldsymbol{k}_{\rho 0} = \hat{\boldsymbol{\rho}}k_{\rho 0}$, $k_{\rho 0} = k_0\sin\theta$. Here $0 \le \theta < \pi/2$ and

$$\boldsymbol{k}_{\rho 0}\cdot\boldsymbol{\rho}' = k_0\sin\theta\left(x'\cos\phi + y'\sin\phi\right) = k_0\sin\theta\ \rho'\cos(\phi-\phi'). \quad (7.15)$$

At the stationary-phase point we have $(\hat{\boldsymbol{u}}, \hat{\boldsymbol{v}}) = (\hat{\boldsymbol{\rho}}, \hat{\boldsymbol{\varphi}})$, where the directions of the unit vectors $\hat{\boldsymbol{\rho}}$ and $\hat{\boldsymbol{\varphi}} = \hat{z}\times\hat{\boldsymbol{\rho}}$ are fixed by the observation angle ϕ. Finally, using (3.84) as well as (3.78) and (3.79) we get the far-zone approximation for the electric field component produced by the electric current [137]:

$$E_{\theta,\phi} \approx \frac{e^{-jk_0 r}}{2\pi jr}e^{jk_{z0}z_0}k_0\left\langle f_{\theta,\phi}e^{j\boldsymbol{k}_{\rho 0}\cdot\boldsymbol{\rho}'}; J(\boldsymbol{r}')\right\rangle, \qquad r \to \infty, \quad (7.16)$$

where

$$\boldsymbol{f}_\theta = \hat{\boldsymbol{\rho}}V_i^e(z_0\,|\,z') - \hat{z}\frac{\eta_0^2}{\varepsilon'}\sin\theta\cos\theta\ I_v^e(z_0\,|\,z'), \quad (7.17)$$

$$\boldsymbol{f}_\phi = \hat{\boldsymbol{\varphi}}\cos\theta\ V_i^h(z_0\,|\,z'). \quad (7.18)$$

The TLGFs above are calculated using $k_\rho = k_{\rho 0}$.

A careful reader may note the similarity of (7.16) to its free-space counterpart (7.4). Indeed, when (7.16) is specialized to the trivial case of free-space, the TLGFs become the ones for an infinite uniform transmission line, and it is easy to show that (7.16) with $z_0 = 0$ simply reduces to (7.4).

7.4. Far-field of azimuthal modes

In BOR problems, we are interested in far-fields relative to the particular azimuthal modes. In order to obtain the required formulas the author has developed the procedure consisting in first putting the general three-dimensional formulas into the cylindrical coordinate system, then substituting the current of the mode of interest for $\boldsymbol{J}(\boldsymbol{r}')$, and afterwards performing the integrations in the azimuthal variable. The first step in this scheme has already been done in sections 7.1 and 7.3, resulting in formulas (7.4) and (7.16) for free-space and multilayer media, respectively. We will place these formulas under a common notation:

$$E_{\theta,\phi} \approx E_F \left\langle f_{\theta,\phi} e^{jk_{\rho 0}\cdot\rho'} ; \boldsymbol{J}(\boldsymbol{r}') \right\rangle, \tag{7.19}$$

with

$$f_\theta = \hat{\rho} f_\rho - \hat{z} f_z, \tag{7.20}$$

$$f_\phi = \hat{\varphi} f_\phi, \tag{7.21}$$

where the definitions of E_F, f_ρ, f_ϕ and f_z come from (7.4)–(7.6) and (7.16)–(7.18), and are grouped in Table 7.1.

Table 7.1. Definition of parameters for computing the far-field of azimuthal modes

Parameter	Free-space	Layered media
E_F	$\dfrac{\omega\mu_0 e^{-jk_0 r}}{4\pi jr}$	$\dfrac{e^{-jk_0 r}}{2\pi jr} e^{jk_{z0}z_0} k_0$
f_ρ	$e^{jk_{z0}z'} \cos\theta$	$V_i^e(z_0 \mid z')$
f_ϕ	$e^{jk_{z0}z'}$	$\cos\theta\, V_i^h(z_0 \mid z')$
f_z	$e^{jk_{z0}z'} \sin\theta$	$\dfrac{\eta_0^2}{\varepsilon'} \sin\theta \cos\theta\, I_v^e(z_0 \mid z')$

The modal current distribution is defined by:

$$\boldsymbol{J}(\boldsymbol{r}')=\left(\hat{\boldsymbol{\rho}}'J_m^{\rho}(\rho',z')+\hat{z}'J_m^{z}(\rho',z')+\hat{\boldsymbol{\varphi}}'J_m^{\phi}(\rho',z')\right)e^{jm\phi'}. \tag{7.22}$$

Upon substituting (7.22) into (7.19) and noting that

$$\begin{aligned}
&\hat{\boldsymbol{\rho}}\cdot\hat{\boldsymbol{\rho}}'=\cos(\phi-\phi'), && \hat{\boldsymbol{\varphi}}\cdot\hat{\boldsymbol{\rho}}'=-\sin(\phi-\phi'), && \hat{z}\cdot\hat{\boldsymbol{\rho}}'=0,\\
&\hat{\boldsymbol{\rho}}\cdot\hat{\boldsymbol{\varphi}}'=\sin(\phi-\phi'), && \hat{\boldsymbol{\varphi}}\cdot\hat{\boldsymbol{\varphi}}'=\cos(\phi-\phi'), && \hat{z}\cdot\hat{\boldsymbol{\varphi}}'=0,\\
&\hat{\boldsymbol{\rho}}\cdot\hat{z}'=0, && \hat{\boldsymbol{\varphi}}\cdot\hat{z}'=0, && \hat{z}\cdot\hat{z}'=1,
\end{aligned} \tag{7.23}$$

as well as applying the integral formula for Bessel functions (6.9), we can now perform the integrations in ϕ' in order to get (for the case of volume current distribution):

$$\begin{aligned}
E_{\theta}^{m}=2\pi j^{m}e^{jm\phi}E_F\int_T\Bigg(&f_{\rho}J_m^{\rho}(\rho',z')\frac{J_{m-1}-J_{m+1}}{2j}\\
&-f_{\phi}J_m^{\phi}(\rho',z')\frac{J_{m-1}+J_{m+1}}{2}-f_zJ_m^{z}(\rho',z')J_m\Bigg)\rho'dT',
\end{aligned} \tag{7.24}$$

$$\begin{aligned}
E_{\phi}^{m}=2\pi j^{m}e^{jm\phi}E_F\int_T\Bigg(&f_{\rho}J_m^{\rho}(\rho',z')\frac{J_{m-1}+J_{m+1}}{2}\\
&+f_{\phi}J_m^{\phi}(\rho',z')\frac{J_{m-1}-J_{m+1}}{2j}\Bigg)\rho'dT'.
\end{aligned} \tag{7.25}$$

In (7.24)–(7.25) the Bessel functions are calculated for $k_0\rho'\sin\theta$. The reader may check that for free-space parameters the above formulas are consistent with those given in [6, 125]. For the case of stratified media, no corresponding formulas have been published in the literature.

When we consider SIE formulation, the integrals in (7.24)–(7.25) become line integrals along the generating arc of the body. In addition, it is sometimes convenient to express the transverse current components in terms of a single current, which is tangential to the body surface [125].

The formulas describing the far-field approximation for the case of azimuthal modes in layered environment are the author's original contribution.

Chapter 8. Case studies

In this chapter, we give a number of computational examples which prove the correctness of the formulations presented in this monograph. Wherever possible, comparisons with computed or measured data published in the literature available are given. In the case of the lack of such data published by other authors, comparisons are made between the results obtained by the author using different computational models.

The main contribution of the author is related to the development of BOR-VIE techniques for both free-space and multilayer environments. Therefore, examples given below concern mainly this part of the material presented. However, it should be stated that in general BOR techniques are more sophisticated than their three-dimensional counterparts. Furthermore, 3D models constitute a background for BOR problems, so we may conclude that the correctness of BOR formulation proves also the correctness of the 3D formulation serving as its origin. We also remember that (especially in VIE techniques) BOR models enable us to solve problems which would otherwise be unmanageable using 3D formulations because of computer limitations.

BOR-VIE results, as well as the resonant frequencies and quality factors, have been obtained with the original computer code written by the author using the FORTRAN f77 programming language. Calculations of the 3D-SIE examples have been performed using commercial software CONCEPT II developed at the Technical University of Hamburg–Harburg, Germany [182]. All computations have been done on a SUN Ultra1 Workstation.

Considering that in most cases, the results presented in this chapter have been published previously in articles or conference papers written by the author, we therefore provide appropriate references in captions to each figure. However, all data presented here are the author's original contribution.

8.1. Free space*)

In order to check the methods developed for free-space applications, they have been applied to a few problems for which solutions (either analytical or numerical) obtained by other authors are available. Most of these solutions concern homogeneous or partially homogeneous bodies. In all BOR-VIE calculations (see section 4.2 for the formulation), basis functions defined on rectangular domains (sections 5.1.3 and 5.1.4) have been used. The numerical integrations, needed in the evaluation of the impedance matrix, have been performed using four-point quadrature per rectangle. The number of points resulted from approximating the triangle functions with four-pulse functions in the current flow direction [125]. The integrations in the azimuthal variable needed in the calculation of modal Green's functions have been performed using an adaptive procedure depending on the number of the azimuthal mode. Singular integrals associated with some terms of the impedance matrix have been calculated using the singularity extraction technique outlined in Appendix 1.

In the examples, the incident field has been assumed to be a plane wave, which has been expanded into modes according to procedures given in Chapter 6.

8.1.1. Electric fields in dielectric spheres and cylinders

It is well known that some secondary parameters like radar cross-sections are somewhat insensitive to inaccuracies in internal current distributions. Therefore, as suggested in [178], the calculations of internal fields have been chosen as the first class of examples.

For the first example, we considered a homogeneous dielectric sphere. Next, we modelled a layered sphere, and, finally, we obtained the results for a homogeneous dielectric cylinder using both the VIE and SIE techniques.

8.1.1.1. Dielectric spheres

A simple model of a sphere, with discretization similar to that of Fig. 5.5, has been used to calculate the electric field inside a dielectric sphere. In this model, we have used eight squares per sphere radius, which corresponds to 216 unknowns. First, we assume the axial incidence of the incident field, which requires computations of only the –1 and +1 modes. Field calculations for the low frequencies have shown that the electric field is within 5 percent of $3/(\varepsilon_r + 2)$ times the incident field, which is the theoretical value.

*) [105, 106].

At higher frequencies, we observe a typical standing wave behavior. In Fig. 8.1 a comparison of the results with the analytical solution [178] is presented for a sphere with $k_0 a = 0.408$. One can see that the comparison result is good. In order to verify the procedures for the zeroth mode and more sophisticated modal expansions, the same calculations for different angles of incidence and different polarization have been performed. A small picture in the corner of Fig. 8.1 relates the symbols used in the plot to different scattering situations. The simplest case with the incidence along the z-axis is denoted by diamond symbols. Again, a very good agreement has been obtained which validates the procedures described in the previous sections of the monograph. The reader can notice that the calculated solutions slightly differ from each other and from the analytical solution near the plot ends. This is caused by a rather crude approximation of the sphere surface within the model applied.

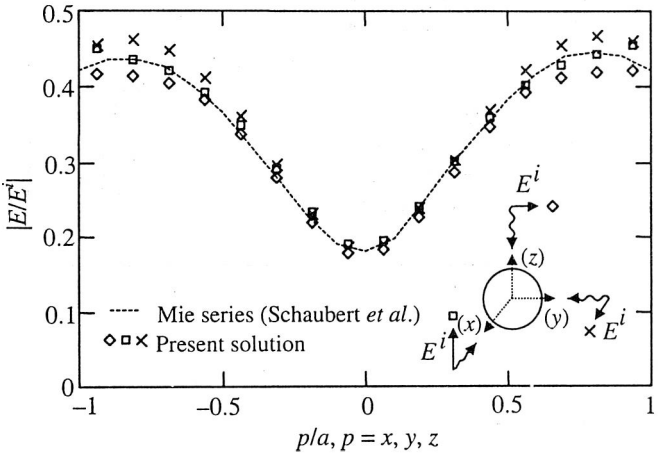

Fig. 8.1. The field along the axis of incidence inside the dielectric sphere; $\varepsilon_r = 36$, $k_0 a = 0.408$ (Ref. [105], ©2000 IEEE)

The field distributions for a layered sphere are presented in Fig. 8.2. The comparison data were again taken from [178].*) The calculations have been performed for two grids. The solutions 1 and 2 denote respectively 8 and 16 squares per outer radius of the sphere. Solution 1 gives some error in the vicinity of the boundary between the materials. This is caused by the fact that the model of the inner sphere was not precise. Solution 2 gives a very good field prediction. It proves the improvement of accuracy when the body under investigation is modeled using smaller volume elements. Note that the jump in the component E_x calculated along the x-axis is predicted perfectly. This is be-

*) In [178], wrong data have been given in the caption of the corresponding figure. Here, we use the correct data supplied by the authors.

cause the correct behavior at media interfaces is built into the basis function in a way similar to that given in [178]. It is also worth mentioning that even in the case of solution 1 the resolution of the model is about twice that of a tetrahedron (full 3D) model [178]. However, thanks to the rotational symmetry the number of unknowns is only 216, compared to 1088 in the tetrahedron model. In solution 2, where the resolution is doubled in comparison to solution 1 we have 828 unknowns, which is still less than in the 3D case.

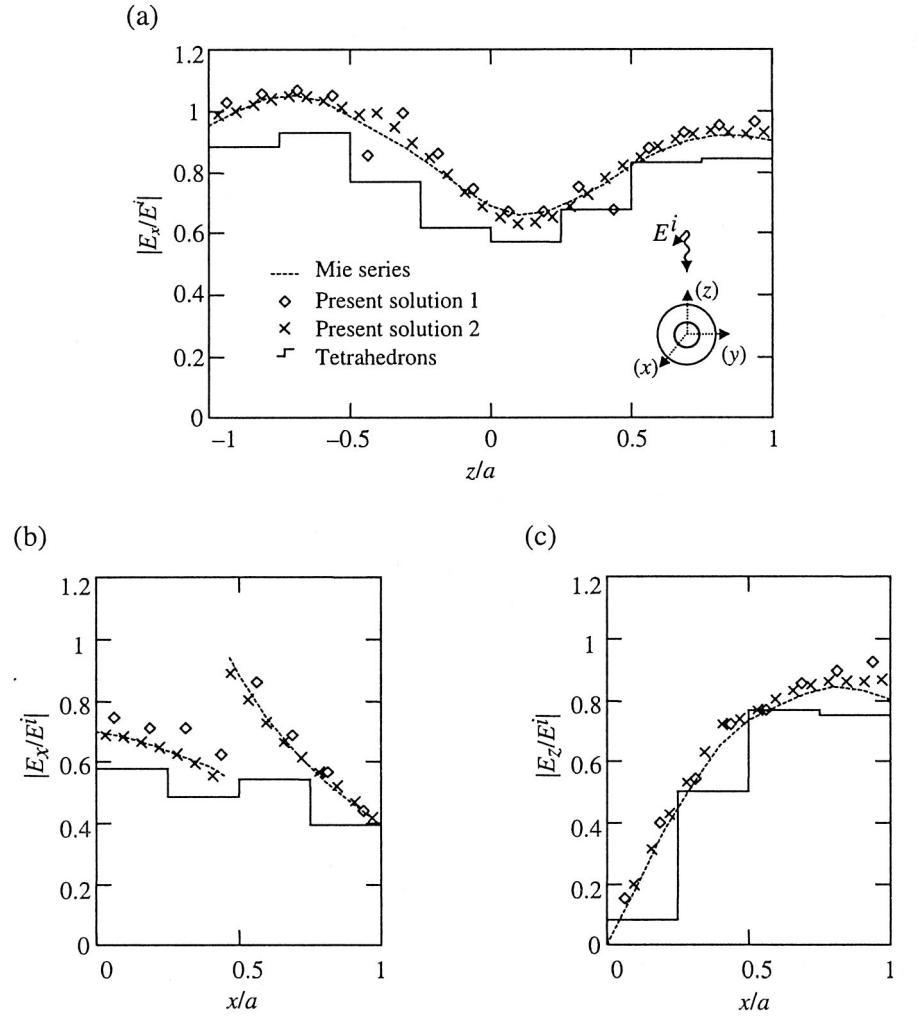

Fig. 8.2. Fields inside an inhomogeneous sphere; $\varepsilon_{r1} = 36$, $k_0 a_1 = 0.3738$, $\varepsilon_{r2} = 9$, $k_0 a_2 = 0.8168$. (a) Relative magnitude of E_x along the z-axis. (b) Relative magnitude of E_x along the x-axis. (c) Relative magnitude of E_z along the x-axis (Ref. [105], ©2000 IEEE)

8.1.1.2. Dielectric cylinder

Calculations similar to the above were performed for a homogeneous dielectric cylinder. The results are presented in Fig. 8.3. One can see that the agreement of the results obtained using different techniques is excellent.

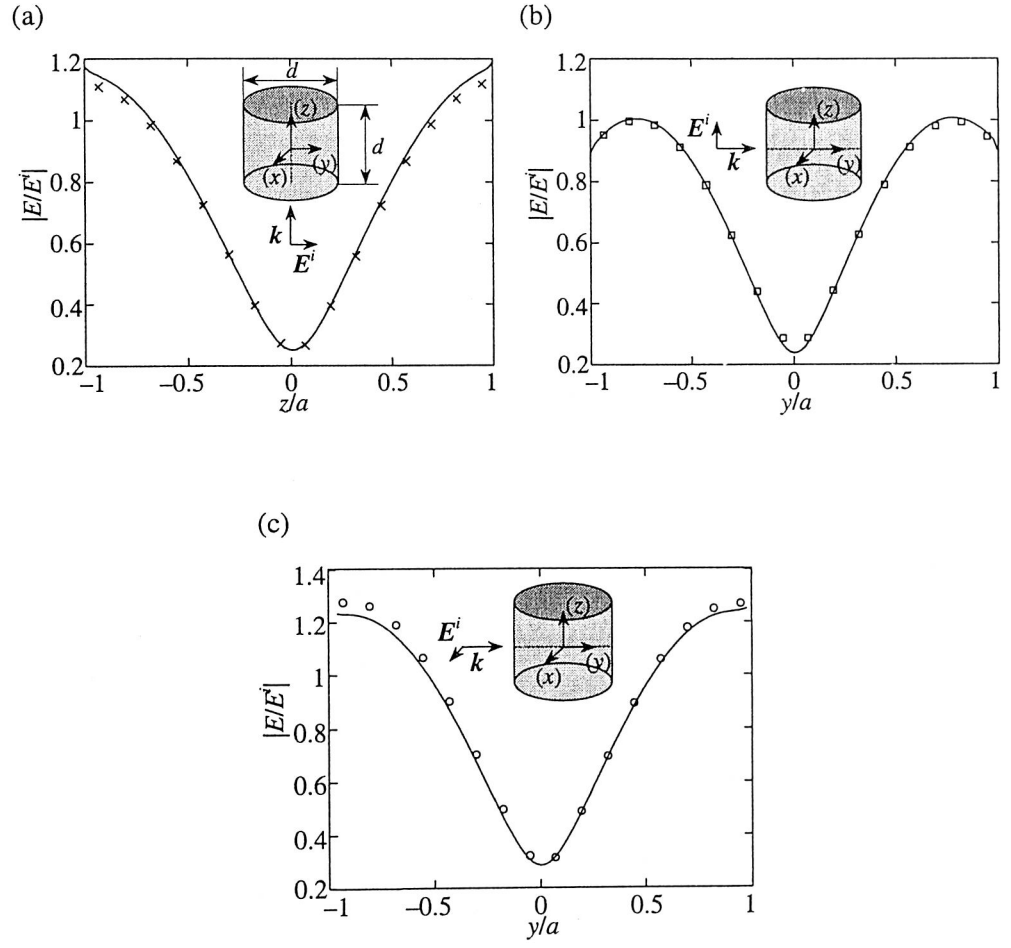

Fig. 8.3. The electric field distributions inside a homogeneous dielectric cylinder; $\varepsilon_r = 36$, $k_0 d = 0.8377$, $a = d/2$. The symbols denote the BOR-VIE solution, the solid line denotes the 3D-SIE solution (CONCEPT II). (Ref. [106])

8.1.2. Scattering calculations

Because of the difficulties to measure fields inside dielectric bodies, and because of the practical importance of this value, the main parameter calculated and published in literature is the radar cross-section defined in section 7.2. In this work, we computed the radar cross-section of a thin dielectric rod and compared it with the results of Richmond [171], Wang and Papanicolopulos [210] and Shaubert, Wilton and Glisson [178]. The BOR model consists of a single column of rectangular cells (in the transverse plane). The results are presented in Fig. 8.4, where the agreement is excellent again.

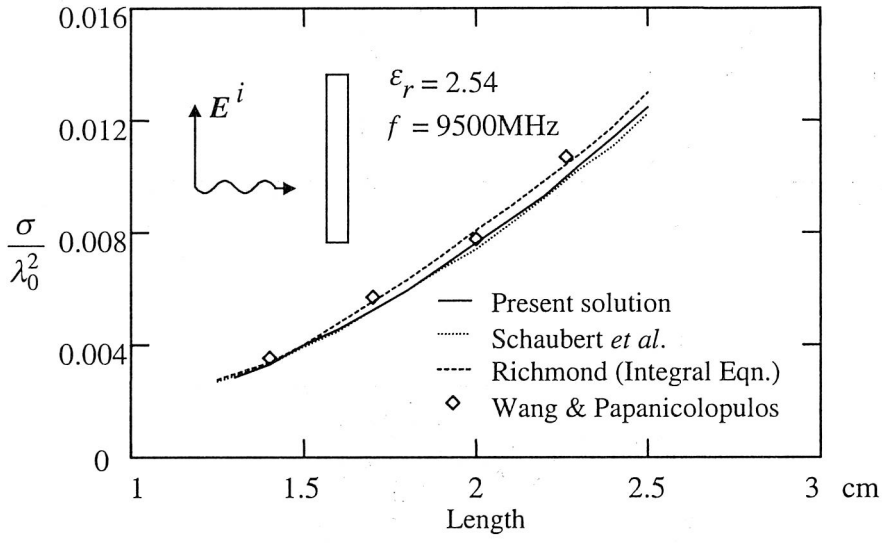

Fig. 8.4. Radar cross-section of a thin dielectric rod; $a = 0.16$ cm $= 0.05\lambda_0$, $\varepsilon_r = 2.54$ (Ref. [105], ©2000 IEEE)

Next, the bistatic radar cross-section of a dielectric cylinder has been calculated and compared with data given by Mautz and Harrington [123]. The comparison has been done in Fig. 8.5.

Finally, some calculations of resonant frequencies of dielectric spheres and cylinders have been performed and compared to the analytical and numerical results given by Barber, Owen and Chang [8]. In all cases the resonant frequencies predicted with the present method were within 0.5 percent of those of Barber *et al.* Note that in contrast to the data given in the next section the resonant frequencies were found as the maximum in the RCS versus frequency plots.

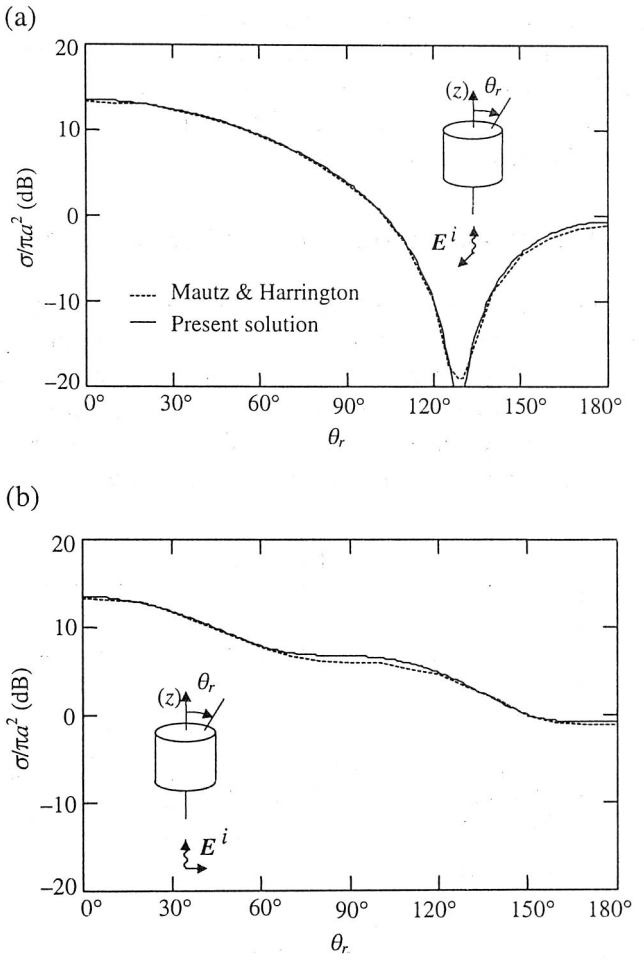

Fig. 8.5. Plane wave scattering patterns for a dielectric cylinder with a radius a and height $2a$. $a = 0.25\lambda_0$, $\varepsilon_r = 4$. (a) $\phi\phi$-polarization. (b) $\theta\theta$-polarization (Ref. [105], ©2000 IEEE)

8.1.3. Resonances in heterogeneous dielectric bodies with rotational symmetry*)

In this section, we provide examples investigating the resonance phenomena in dielectric bodies placed in free-space. The calculations have been performed according to the procedures given in section 5.3. As explained in section 5.3, we use the fol-

*) [104, 106].

lowing notation throughout this monograph, which is convenient for cylindrical structures: first, the resonance is identified according to the behavior of fields as belonging to the TE, TM or HEM type (see section 4.3). Then two subscripts are used: the first one denotes the azimuthal mode and the second one corresponds to the resonance number along the frequency axis.

8.1.3.1. Resonant frequencies and quality factors

First, the resonant frequencies and quality factors of the homogeneous cylindrical resonator DRD105UD046 have been calculated. The process of finding and identifying the resonances is illustrated in Fig. 8.6. This figure shows the determinant of the impedance matrix calculated from modal EFIE for $m = 1$. Consequently, the minima found within the complex frequency plane correspond to the modes denoted by HEM_{1n}. Starting with the lower frequencies the first resonance is found around 6.37 GHz, and we

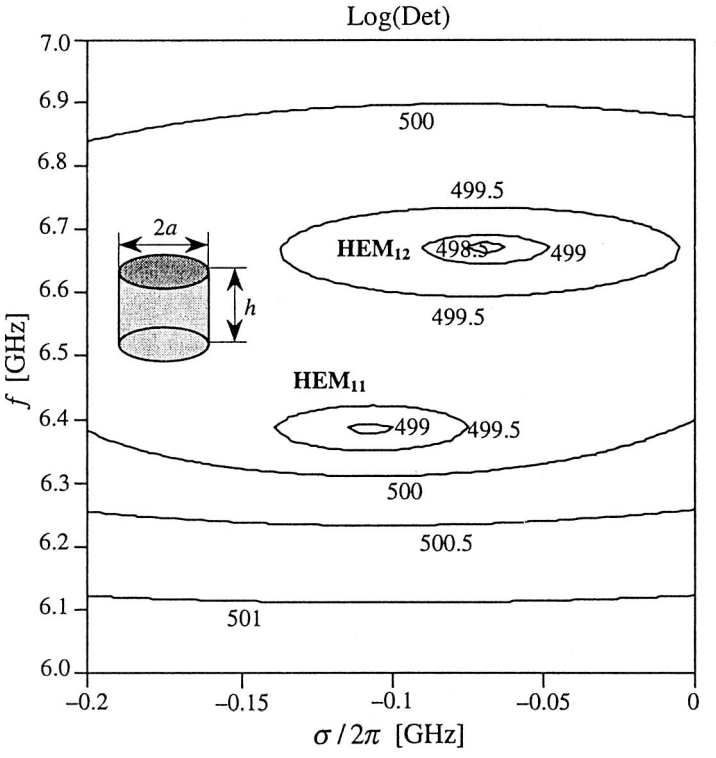

Fig. 8.6. Determinant of the impedance matrix for $m = 1$ in a complex frequency plane for a cylindrical resonator with $\varepsilon_r = 38$, $a = 5.25$ mm, $h = 4.6$ mm. (Ref. [106])

describe it as a HEM_{11} mode. The next one, seen in the plot, (HEM_{12}) is found around 6.66 GHz. Note that due to the relatively low Q-factors the resonance values lie some distance away from the imaginary axis. Some of them could be easily overlooked if the search was done along the frequency axis only, without referring to the idea of complex frequencies. In Fig. 8.6, this is the case of the HEM_{11} resonance.

A comparison of more precise numerical results for a few of the modes is given in Table 8.1 (resonant frequencies) and Table 8.2 (Q-factors). The agreement of the results with the previously reported values seems to be excellent for the resonant frequency values. The result differences for the Q-factors are greater, however it should be remembered that values given in the references also differ much from each other as well as from the actual measured results.

Table 8.1. Comparison of computed and measured resonant frequency results for a resonator with radius $a = 5.25$ mm, height $h = 4.6$ mm, and $\varepsilon_r = 38$. (Ref. [104], ©2000 IEEE)

Mode	Frequency [GHz]			
	Computed Present method	Computed MoM [84]	Measured [44]	Computed T-matrix [225]
TE_{01}	**4.861**	4.829	4.85	4.9604
TM_{01}	**7.594**	7.524	7.60	7.5384
HEM_{11}	**6.373**	6.333	–	6.3450
HEM_{12}	**6.657**	6.638	6.64	6.6520
HEM_{21}	**7.784**	7.752	7.81	7.7621

Table 8.2. Comparison of the computed and measured Q-factor results for a resonator with radius $a = 5.25$ mm, height $h = 4.6$ mm, and $\varepsilon_r = 38$. (Ref. [104], ©2000 IEEE)

Mode	Q			
	Computed Present method	Computed MoM [84]	Measured (Transmission method) [44]	Computed T-matrix [225]
TE_{01}	**40.7**	45.8	51	40.819
TM_{01}	**73.7**	76.8	86	76.921
HEM_{11}	**30.4**	30.7	–	30.853
HEM_{12}	**49.5**	52.1	64	50.316
HEM_{21}	**329.8**	327.1	204	337.66

The next test concerns an inhomogeneous dielectric resonator with a cylindrical dielectric plug. The dielectric constant of the outer ring is equal to 38, whilst the di-

electric constant of the plug was being changed between 1 (ring resonator) and 100. The results are given in Fig. 8.7. The black circles included in the plots correspond to values reported by Zheng [225]. Again, a very good agreement of results has been obtained.

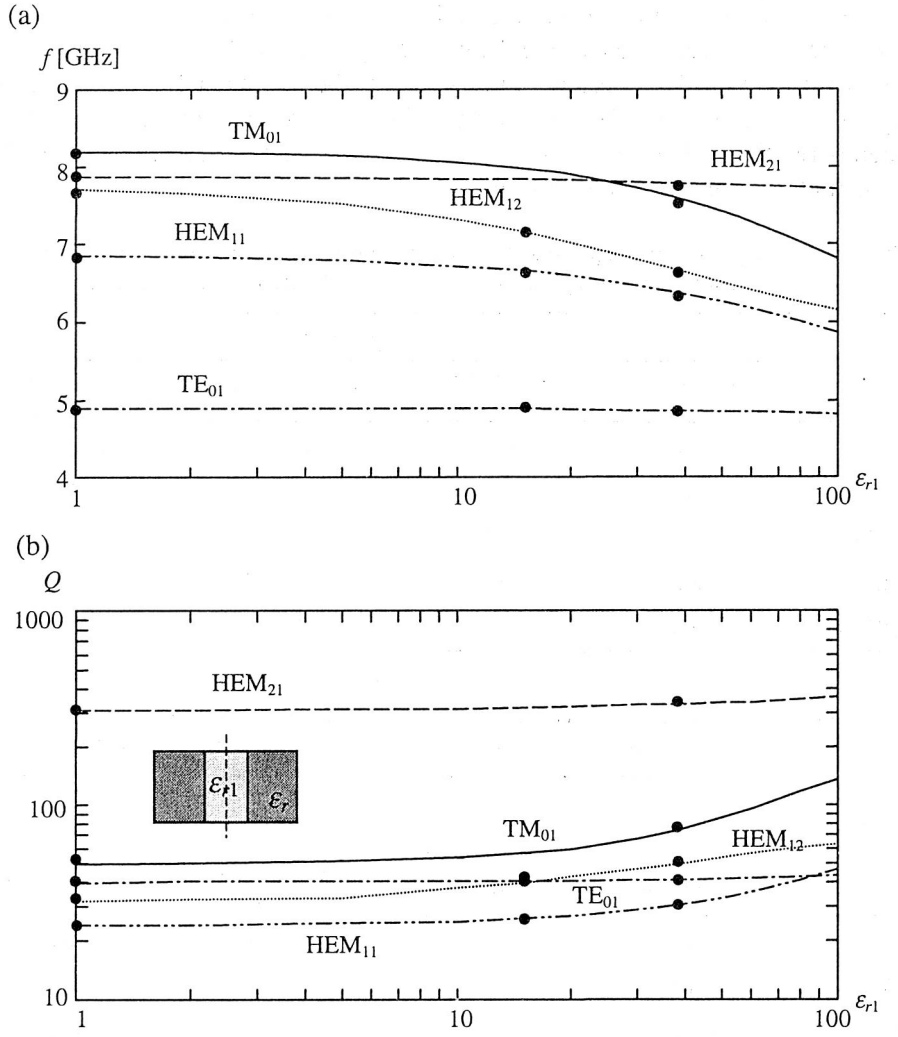

Fig. 8.7. Resonance frequencies and quality factors of five lower modes of a dielectric inhomogeneous resonator versus the permittivity of the inner part. Dimensions: $a = 5.25$ mm, $h = 4.6$ mm, radius of the plug $a_1 = a/4$, $\varepsilon_r = 38$. The circles represent values given in [225]. (a) Resonant frequencies. (b) Quality factors (Ref. [104], ©2000 IEEE)

8.1.3.2. Modal field distributions

When the complex resonant frequency is found with a satisfactory degree of accuracy, the modal field distributions may be easily found using equation (5.48), within the multiplicative constant. For N unknowns in the system we simply assume one of the unknown field coefficients at a certain constant value (say "1"). Then we can solve (5.48) as a set of linear equations with the remaining $N - 1$ unknowns. Some difficulties are associated with the graphical presentation of the results, because the coefficients obtained (field values) are in general complex numbers. Following [83, 84], we recover the suppressed $e^{j\omega t}$ dependence for the presentation and plot the field amplitudes at some chosen time values, ignoring at the same time the decaying nature of the field. In Fig. 8.8, the field distribution for the simplest TE_{01} mode is shown and compared with literature data. In the next figures, the electric field distributions in the representative cut-planes are shown for several TM and HEM modes. The reader can compare this data with plots given, for example, in [83, 84].

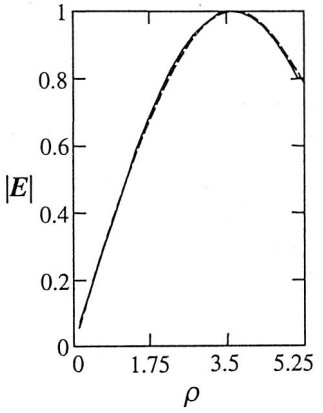

Fig. 8.8. Electric field inside the isolated resonator versus radial distance, mode TE_{01}.
Solid line – present solution; broken line – Kajfez *et al.* [84].
Dimensions: $a = 5.25$ mm, $h = 4.6$ mm, $\varepsilon_r = 38$. (Ref. [106])

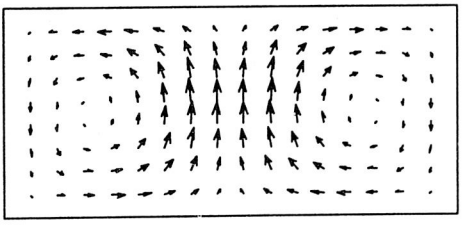

Fig. 8.9. Electric field inside the homogeneous dielectric resonator;
TM_{01} mode; E-field in the meridian plane $\phi = 0$

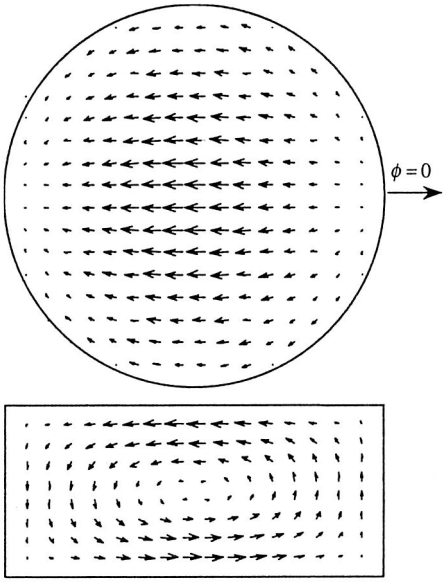

Fig. 8.10. Electric field inside the homogeneous dielectric resonator; HEM_{11} mode; E-field in a plane parallel to the equatorial plane offset by 2.15 mm (upper figure) and E-field in the meridian plane $\phi = 0$ (bottom figure)

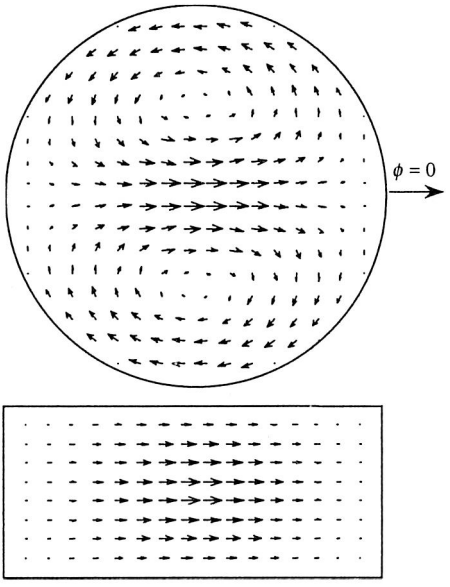

Fig. 8.11. Electric field inside the homogeneous dielectric resonator; HEM_{12} mode; E-field in the equatorial plane (upper figure) and E-field in the meridian plane $\phi = 0$ (bottom figure)

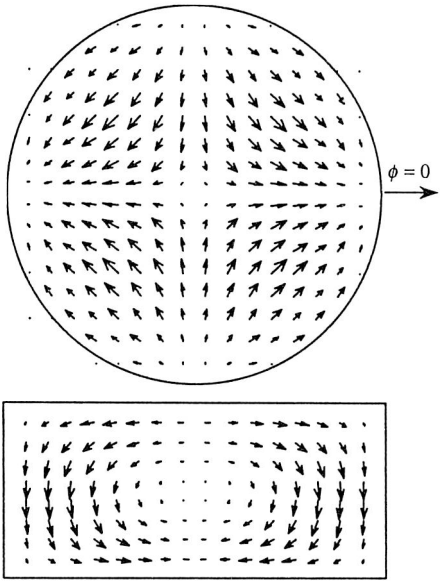

Fig. 8.12. Electric field inside a homogeneous dielectric resonator; HEM_{21} mode; E-field in the plane parallel to the equatorial plane offset by 2.15 mm (upper figure) and E-field in the meridian plane $\phi = 0$ (bottom figure)

As seen in Table 8.1, the resonant modes in the dielectric resonators in some cases have their natural frequencies very close to each other. In fact, for certain geometry the resonant frequencies may even become identical (the so-called degenerate pairs [82]). This fact can be considered a desirable feature, for example, when designing dual-mode band-pass filters. On the other hand, when investigating dielectric resonator antennas (see the next section), small frequency separation of some modes results in the fact that when one of the modes is a desired mode of operation the other one creates spurious resonance nearby. This problem can be eliminated for instance by changing the resonator proportions (radius/height ratio). In certain cases, however, this method fails, because the frequency ratio of two modes may be insensitive to such changes (see the universal mode chart [83, p. 284]). We outline an alternative way of overcoming this problem below, using non-homogeneous resonators.

Let us focus our interest on two mode pairs: HEM_{11}–HEM_{12} and TM_{01}–HEM_{21}, for the resonator and parameters used in the previous examples.

For a HEM_{11}–HEM_{12} pair the difference in resonant frequencies is less than 5 percent. However, it can be easily noticed that in the case of a HEM_{11} mode the electric field is concentrated near the resonator surface [84], whilst in a HEM_{12} mode the field is concentrated in the inner part. This suggests that changing the dielectric permittivity independently for the inner and outer part of the resonator we probably could change the relative position of the resonances in the complex frequency plane. This

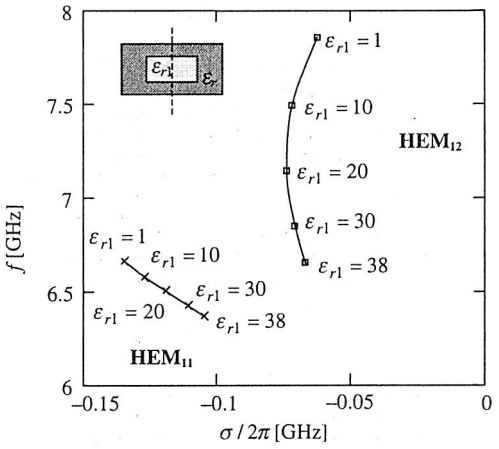

Fig. 8.13. Position change of complex roots associated with HEM_{11} and HEM_{12} modes caused by a decrease of dielectric permittivity of the inner part of the resonator. Dimensions: $a = 5.25$ mm, $h = 4.6$ mm, inner part: $a_1 = 2.625$ mm, $h_1 = 2.3$ mm. $\varepsilon_r = 38$. (Ref. [104], ©2000 IEEE)

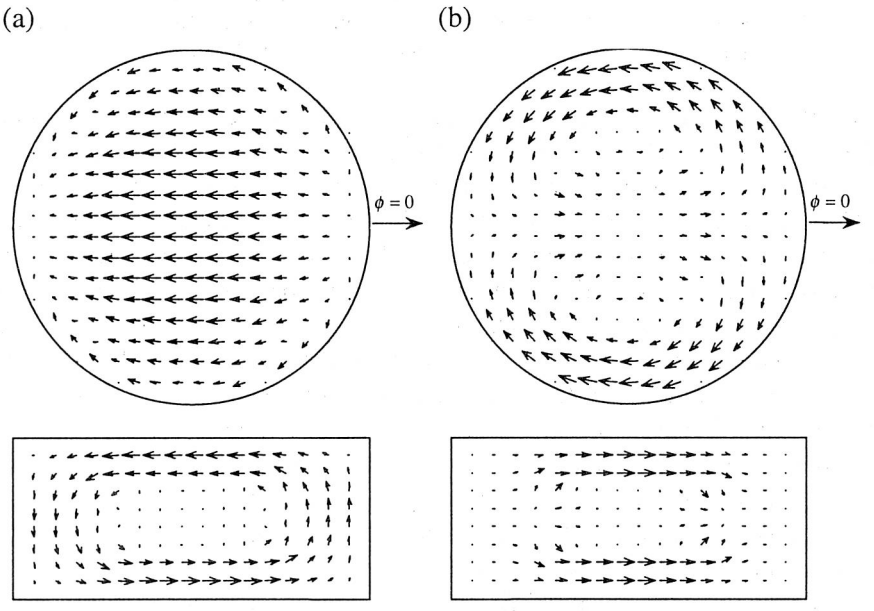

Fig. 8.14. Electric field inside a non-homogeneous dielectric resonator, outer part: $a = 5.25$ mm, $h = 4.6$ mm, $\varepsilon_r = 38$, inner part: $a_1 = 2.625$ mm, $h_1 = 2.3$ mm, $\varepsilon_{r1} = 1$. (a) HEM_{11} mode. E-field in a plane parallel to the equatorial plane offset by 2.15 mm (upper figure) and E-field in the meridian plane $\phi = 0$ (bottom figure), (b) HEM_{12} mode. E-field in an equatorial plane (upper figure) and E-field in the meridian plane $\phi = 0$ (bottom figure). (Ref. [104], ©2000 IEEE)

possibility has been tested in a configuration shown in the upper left corner of Fig. 8.13. The dielectric constant of the outer part has been left unchanged ($\varepsilon_r = 38$), whilst the inner part was being changed between 38 and 1. Based on Fig. 8.13 it can be noticed that whilst the resonant frequency of a HEM_{11} mode is almost unchanged, the resonant frequency of a HEM_{12} mode is moving towards the upper values. For a case of $\varepsilon_{r1} = 1$ the resonant frequency of HEM_{12} is about 18 percent higher than that of HEM_{11} mode. The electric field distributions for both modes have been illustrated in Fig. 8.14.

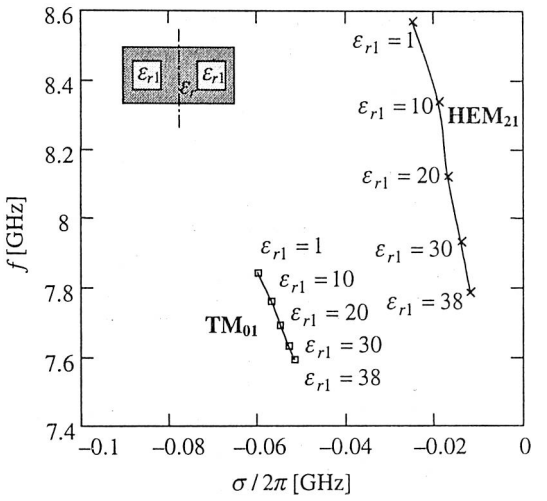

Fig. 8.15. Change of the position of complex roots associated with TM_{01} and HEM_{21} modes caused by a decrease of dielectric permittivity of the inner ring

For the TM_{01}–HEM_{21} pair the difference in resonant frequencies is only 2.5 percent. In this case, based on the source field distributions shown earlier we see that the electric field of TM_{01} mode is very weak near the horizontal plane of symmetry (equatorial plane) at the radial distance of about 0.6÷0.7 of the resonator radius. On the other hand, the electric field of a HEM_{21} mode is rather strong in this region (however, we must bear in mind that it also depends on the azimuthal position). This suggests that any changes to the dielectric constant in the region of interest should have much stronger influence on the HEM_{21} than on the TM_{01} mode. A possible configuration with a ring having a different dielectric constant embedded within the resonator is depicted in the smaller picture in Fig. 8.15. A rectangular cross-section of the ring is chosen quite arbitrarily, merely to simplify the numerical analysis. Changes in the complex resonant frequencies of the modes of interest are shown in Fig. 8.15. It can be observed that for a dielectric constant of the ring equal to 1 ("air ring") the resonant frequencies of TM_{01} and HEM_{21} modes differ by as much as 9.3 percent.

The corresponding field distributions are shown in Figs. 8.16 and 8.17.

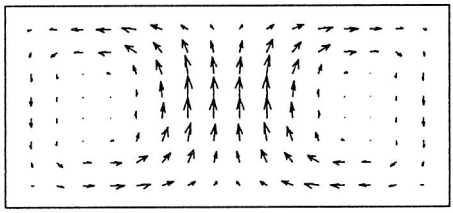

Fig. 8.16. Electric field inside an inhomogeneous dielectric resonator; TM_{01} mode; E-field in the meridian plane $\phi = 0$

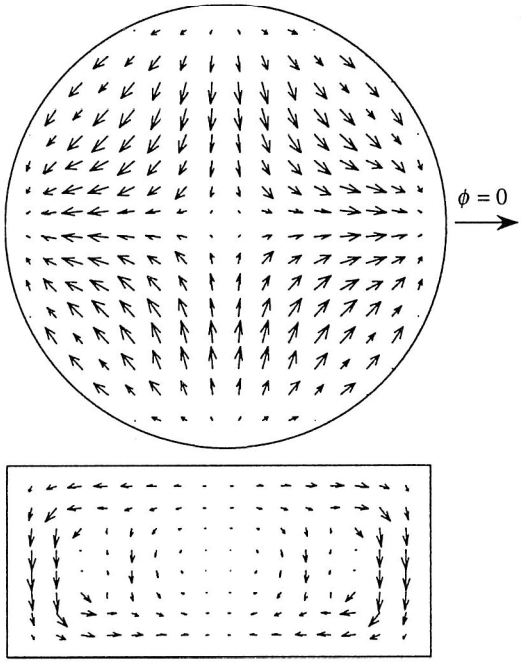

Fig. 8.17. Electric field inside an inhomogeneous dielectric resonator; HEM_{21} mode; E-field in the plane parallel to the equatorial plane offset by 2.15 mm (upper figure) and E-field in the meridian plane $\phi = 0$ (bottom figure)

The last solution may be considered impractical from the technological point of view. However, one must bear in mind that in practical situations (see also the next point) the free-space resonator is replaced with a half-volume resonator over metal ground. In this case one does not have to make a ring inside the resonator volume (Fig. 8.18).

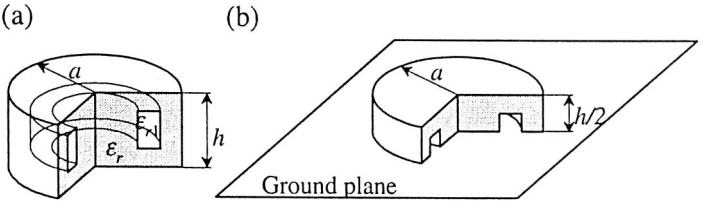

Fig. 8.18. Inhomogeneous dielectric resonator with an "air ring" (a) in free space and (b) half-split, over a metal ground plane

8.1.3.3. Resonant dielectric antennas

Recently, open dielectric resonators have been used as so-called dielectric resonator antennas [117, 93]. The most popular applications employ the HEM_{11} mode because it has a low Q-factor (which indicates that it can act as a good radiator) and because this mode offers a broadside radiation pattern. The typical use consists in placing the DRA over a metal ground plane (which may be a part of the case including a transmitter/receiver). For computation purposes, this ground plane is often assumed to be of infinite lateral extent. The analysis of such a case can be carried out twofold. First we may analyze the resonator with a doubled volume, using the well known mirror principle (Fig. 8.19).

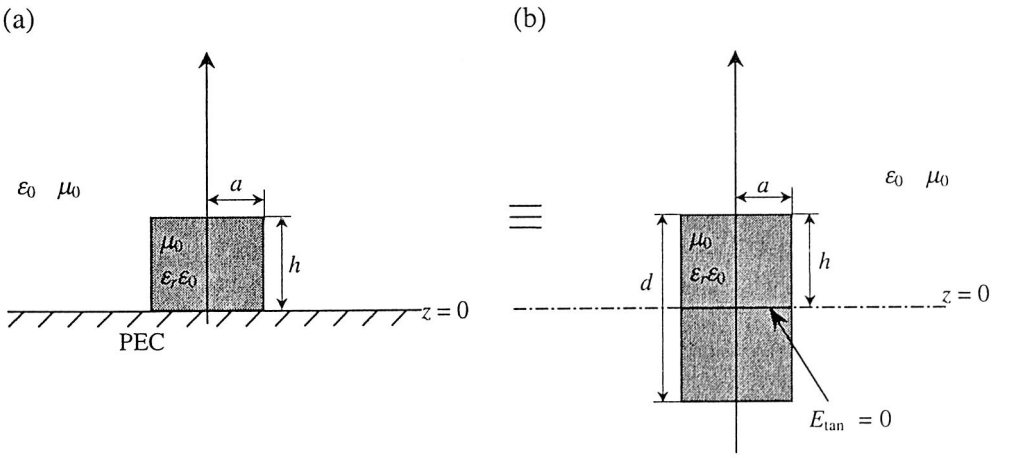

Fig. 8.19. Dielectric resonator over a PEC plate (a) and its equivalent in free-space (b)

Considering this, we can directly apply the free-space code in order to characterize the problem. The cost of this solution is that in general the number of unknowns is approximately twice as that of the original problem. An alternative way is to leave the

problem in the original configuration as depicted in Fig. 8.19(a). This requires a proper modification of the kernels of the governing equations. We may either modify the kernels according to the well-known mirror rules for vertical and horizontal currents over a PEC infinite ground, or (the author's preferred choice), treat the situation as a simple case of stratified media, where we may now directly apply the formulas given in this monograph. We only have to calculate the transmission line Green's functions for a simple transmission line shortened at one end. Of course, both formulations are formally identical. The details concerning the transmission line analysis as well as further computations are shown later for a less trivial case. Here we only state that the methods outlined (i.e., the mirror method and the kernel modification method) have been both tested for the case of a simple cylindrical DRA and the results were undistinguishable.

In Fig. 8.20, simple DRA radiation patterns are given along with a comparison to the results given by Long *et al.* [117]. For a better understanding, we have also included the pseudo-3D plot of the radiation pattern (Fig. 8.21).

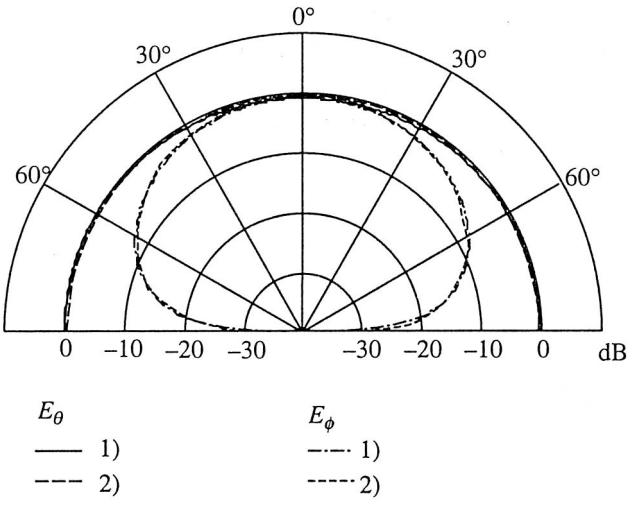

Fig. 8.20. Far-field radiation patterns of cylindrical DRA with $a = 0.5$ cm, $h = 0.3$ cm, $\varepsilon_r = 8.9$. (1) Author's method; (2) Long *et al.* [117]. HEM_{11} mode resonant frequency – 10.3 GHz. (Ref. [106])

Note that if the body-of-revolution technique is used for dielectric antenna analysis, some trouble arises due to the modelling of excitation, which in general introduces a break in the rotational symmetry of the problem. One of the solutions is to use an infinitesimal electric dipole, of which the field properly decomposed into azimuthal modes may be used to obtain the right hand "incident field" parts of the equations. This approach, first proposed in [93] is to some extent equivalent to electric

probe excitation and may be used for the radiation pattern calculations or testing the influence of the probe position on the presence of unwanted mode excitation. However, neither the physical structure of the probe nor the coupling phenomena are modeled rigorously. Consequently, the infinitesimal dipole model cannot be used for input impedance calculations. In addition, the DRA characteristics including the resonant frequency, Q-factor or field distributions are taken as in an unloaded structure. It is also obvious that more sophisticated excitations (for example, slot excitation) cannot be considered in this purely BOR scheme.

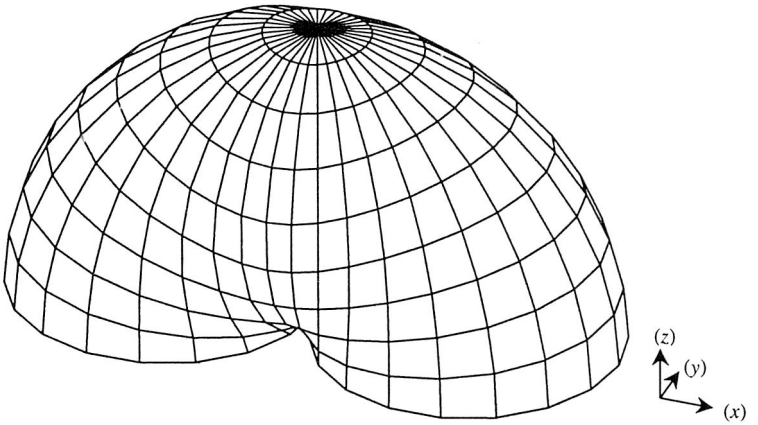

Fig. 8.21. Radiation pattern of DRA with the HEM_{11} mode of operation. (Ref. [106])

The situation where a real physical structure excitation is modeled is much more complicated because it requires completing the body-of-revolution model with the parts that do not possess the rotational symmetry. This causes, in general, that the main advantage of the method presented, i.e., the independent mode-by-mode solution process, is no longer present. Fortunately, it can be shown [78, 179] that even in this situation the matrix describing the case can be inverted part-by-part and that at each step of the solution process one has to invert only relatively small sub-matrices corresponding to the particular modes. The presentation of these techniques is however beyond the scope of this study.

8.2. Stratified media

The problem of electromagnetic scattering in a multilayer environment will be illustrated for the case of BOR immersed in one of the layers, as shown in Fig. 8.22. As was described in the previous chapters, there are two major problems, which

should be addressed and which had not appeared in the free-space configurations. The first one concerns the transmission line analysis for the media stratification considered. The general formulas for such analysis are listed in Appendix 2. In the next sections, these formulas are specialized for the situation at hand. The second problem is related to the Sommerfeld integrals present in the formulations. Those improper integrals are difficult for numerical operations because their kernels, incorporating Bessel functions, are highly oscillatory and divergent [140]. The problems are also related to singularities occurring near the integration path in the complex k_ρ-plane. An important observation is that some of those singularities, which consist of poles and branch points, in the lossless case appear on the real axis. Therefore, the integration path has to be indented into the first quadrant [140] in order to avoid them. Several methods of integration have been proposed in literature, with some of them comprising the deformation of the integration path into complex plane [17, 132]. Sometimes, however, it may be preferred to use real-axis integration methods [76, 159]. So far, there is no unified elegant method enabling an automatic treatment of all possible situations [144]. Different approaches are needed depending on the media configuration (which determines the TLGFs under the integral sign) and on the source and observation point locations. It is important to overcome the difficulty arising from the singularities associated with terms of the moment matrix, when the observation point lies within the source region. This situation usually requires tedious preliminary treatment of the kernels in order to make the Sommerfeld integrals convergent [141]. To speed up further computations some additional techniques are usually also applied [23, 136]. In this work instead of the numerical integrations, a semi-analytic method of solution has been chosen [2, 29, 138, 139]. This method referred to as the discrete complex images method (DCIM) is a very flexible tool, particularly when source and observation points belong to the same layer in stratified environment, which is the case in the examples provided below. The drawback of this method is that it does not have built-in accuracy testing capabilities, and that the overall accuracy can only be evaluated by referring to the classical methods of integration [139]. As noted in [23, 87] the method is not fully general and various practical situations need special treatment. However, recently an automated solution for these problems has been given in [115]. Nevertheless, the method is useful for the purpose of validation of the formulations given in this monograph. Some computational details will be outlined in the next section.

8.2.1. Computation of Sommerfeld integrals

For illustrative purposes, we will consider the modal Sommerfeld integrals introduced in Chapter 4 (eq. (4.46)). First, let us consider the integral:

$$\Im_{m0}\{\cdot\}=\frac{1}{2\pi}\int_0^{\infty} dk_\rho k_\rho J_m(k_\rho\rho)J_m(k_\rho\rho')\{\cdot\}. \tag{8.1}$$

Based on (4.42) taken for $n = 0$, we obtain (see Fig. 4.3 for notation):

$$J_m(k_\rho\rho)J_m(k_\rho\rho')=\frac{1}{2\pi}\int_{-\pi}^{\pi} J_0(k_\rho\varsigma)e^{-jm(\phi-\phi')}d(\phi-\phi'). \tag{8.2}$$

Bearing in mind that the function inside the Sommerfeld operator $\{\cdot\}$ depends only on (z,z'), we can rewrite (8.1) as:

$$\Im_{m0}\{\cdot\}=\frac{1}{4\pi^2}\int_{-\pi}^{\pi} d(\phi-\phi')e^{-jm(\phi-\phi')}\int_0^{\infty} dk_\rho k_\rho J_0(k_\rho\varsigma)\{\cdot\}. \tag{8.3}$$

Now, the essential element in the solution is the approximation of the function under the operator as a sum of exponentials, in the form:

$$\{\cdot\}=\sum_l \Lambda_l \frac{e^{-jk_z h_l}}{jk_z}, \tag{8.4}$$

where l denotes the (not known *a priori*) number of exponential coefficients needed for the approximation, Λ_l is the complex amplitude, h_l is the complex distance and k_z is defined by (3.72). Using the Sommerfeld identity [185, p. 242]:

$$\int_0^{\infty} k_\rho J_0(k_\rho\zeta)\frac{e^{-jk_z h_l}}{jk_z}dk_\rho=\frac{e^{-jkR_l}}{R_l}, \tag{8.5}$$

where

$$R_l=\sqrt{\varsigma^2+h_l^2}=\sqrt{\rho^2+\rho'^2-2\rho\rho'\cos(\phi-\phi')+h_l^2}, \tag{8.6}$$

we finally arrive at

$$\Im_{m0}\{\cdot\}=\sum_l \Lambda_l \frac{1}{4\pi^2}\int_{-\pi}^{\pi}\frac{e^{-jkR_l}}{R_l}e^{-jm(\phi-\phi')}d(\phi-\phi'). \tag{8.7}$$

Because, in general, h_l may be complex, the square root branch with the positive real part in (8.6) should be taken [138].

Note that in certain cases (8.7) exhibits the $1/R$ singularity. This singularity, however, in this formulation is exactly of the same form as in the free-space case. Therefore, it is also treated in exactly the same manner (see Appendix 1 for details).

The second integral that must be considered is

$$\Im_{m1}\{\cdot\}=\frac{1}{2\pi}\int_0^{\infty} dk_\rho k_\rho^2 J_{m+1}(k_\rho\rho)J_m(k_\rho\rho')\{\cdot\}. \tag{8.8}$$

Again, based on (4.42) with $n = 1$ we have

$$J_{m+1}(k_\rho\rho)J_m(k_\rho\rho')=\frac{1}{2\pi}\int_{-\pi}^{\pi} J_1(k_\rho\varsigma)e^{j\psi}e^{-jm(\phi-\phi')}d(\phi-\phi'). \tag{8.9}$$

Differentiating both sides of Sommerfeld identity (8.5) with respect to ς we get

$$\int_0^{\infty} k_\rho^2 J_1(k_\rho\varsigma)\frac{e^{-jk_z h_l}}{jk_z}dk_\rho=\varsigma\frac{e^{-jkR_l}}{R_l^3}(1+jkR_l). \tag{8.10}$$

Assuming again the approximation (8.4) and substituting (8.9) and (8.10) into (8.8) we finally obtain the formula

$$\Im_{m1}\{\cdot\}=\sum_l \Lambda_l\frac{1}{4\pi^2}\int_{-\pi}^{\pi} e^{j\psi}\varsigma\frac{e^{-jkR_l}}{R_l^3}(1+jkR_l)e^{-jm(\phi-\phi')}d(\phi-\phi'), \tag{8.11}$$

which upon using the geometrical relations from Fig. 4.3 may be further transformed into:

$$\Im_{m1}\{\cdot\}=\sum_l \Lambda_l\frac{1}{4\pi^2}\int_{-\pi}^{\pi}(\rho-\rho'\cos(\phi-\phi')$$

$$+\,j\rho'\sin(\phi-\phi'))\frac{e^{-jkR_l}}{R_l^3}(1+jkR_l)e^{-jm(\phi-\phi')}d(\phi-\phi'). \tag{8.12}$$

Thus, we can replace the Sommerfeld integrals with formulas similar to the free-space expressions, assuming that we are able to perform approximations of the form (8.4). These approximations can be made after some preprocessing using the so-called pencil-of-function method (POFM), which is outlined in Appendix 3.

Some comment should be given to the problem of Sommerfeld integral computations for finding resonance. In this case, as outlined in section 5.3, the frequency is a complex number [143]. Consequently, even in a lossless case the wave number k becomes also complex, which causes the integration path to begin within the improper Riemann sheet*). As reported in [41], in this case the deformed integration path in the complex k_ρ-

*) In the case of media considered in the examples presented, where the environment is backed with a perfect electric conductor ground plane, we deal with a two-sheeted Riemann surface [143]. When the two dielectric half-spaces are taken into account we have to consider a four-sheeted Riemann surface [41].

plane (see Appendix 3) may capture a number of so-called "leaky-wave" poles, which normally belong to the improper Riemann surface. The details of generalizing DCIM to incorporate complex frequencies in both lossless and lossy media are given in [41].

8.2.2. Dielectric resonators in a MIC environment*)

Our first example of a dielectric body in a multilayer structure is a cylindrical dielectric resonator in a microwave integrated circuit (MIC) environment (Fig. 8.22).

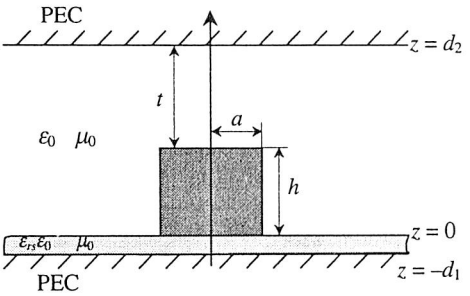

Fig. 8.22. A DR mounted on a grounded dielectric substrate and under a tuning plate

The typical mode of operation in a structure like this is the TE_{01} mode. To analyze this mode we use equation (4.52) together with a simple pulse basis function. Thus, we have to calculate the kernel L_{tt}^{1} which (see eq. (4.44)) is given as:

$$L_{tt}^{1} = \frac{1}{j\omega} \mathfrak{I}_{10}\{V_i^h\}. \tag{8.13}$$

First, we have to calculate the proper TLGF, V_i^h for the configuration in Fig. 8.22. The corresponding transmission line configuration is shown in Fig. 8.23.

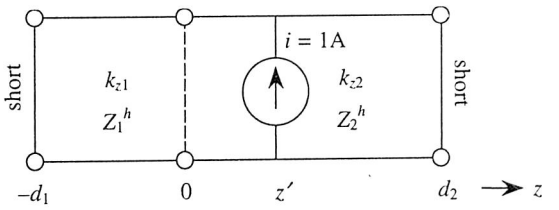

Fig. 8.23. Transmission line circuit for the computation of V_i^h for a source point above a grounded substrate and under a tuning plate

*) [100].

Because we assume that the resonator is placed on a grounded substrate, the source point in the figure is in the second section of the line, corresponding to the region between the substrate and the tuning plate.

According to formulas (3.72), the n-th section has the propagation constant:

$$k_{zn} = \sqrt{k_n^2 - k_\rho^2}, \quad n = 1, 2, \tag{8.14}$$

and the characteristic impedance Z_n^h (for TE waves) given as:

$$Z_n^h = \frac{\omega\mu_0}{k_{zn}}. \tag{8.15}$$

The TLGF can now be easily obtained with the formulas given in Appendix 2. After some transformations we get:

$$V_i^h(z,z') = \frac{\omega\mu_0}{2k_{z2}}[g_d - g_r - f(S_- - S_+)], \tag{8.16}$$

where

$$g_d = e^{-jk_{z2}|z-z'|}, \quad g_r = e^{-jk_{z2}(2d_2-(z+z'))}, \tag{8.17}$$

$$f = \frac{\Gamma}{1+\Gamma t_2}, \quad \Gamma = \frac{Z_1^h(1-t_1) - Z_2^h(1+t_1)}{Z_1^h(1-t_1) + Z_2^h(1+t_1)}, \tag{8.18}$$

$$t_n = e^{-j2k_{zn}d_n}, \quad n = 1, 2, \tag{8.19}$$

$$S_- = \sum_{k=1}^{2} e^{-jk_{z2}\gamma_k}, \quad S_+ = \sum_{k=3}^{4} e^{-jk_{z2}\gamma_k}, \tag{8.20}$$

with

$$\gamma_1 = 2d_2 + (z-z'), \quad \gamma_2 = 2d_2 - (z-z'), \tag{8.21}$$

$$\gamma_3 = 4d_2 - (z+z'), \quad \gamma_4 = (z+z'). \tag{8.22}$$

The essential element in DCIM is now representing f appearing in (8.16) in terms of the approximation (see [1]):

$$f = \sum_{l=1}^{L} A_l e^{-jk_{z2}h_l}. \tag{8.23}$$

As already mentioned, the coefficients $\{A_l\}$ and $\{h_l\}$ may be found using the pencil-of-function method (Appendix 3). Now, (8.16) can be rewritten in the general form:

$$V_i^h(z,z') = \frac{j\omega\mu_0}{2}\left[\sum_{s=1}^{S} a_s \frac{e^{-jk_{z2}c_s}}{jk_{z2}}\right], \tag{8.24}$$

where the coefficients a_s and c_s take into account the direct and reflected rays (g_d and g_r) as well as the complex images. In view of the formulas given in the preceding section, we can now transform (8.13) to:

$$L_{tt}^1 = \frac{1}{j\omega}\Im\{V_i^i\} = \frac{\mu_0}{2}\Re\left\{\sum_{s=1}^{S} a_s \frac{e^{-jk_2R_s}}{R_s}\right\}, \tag{8.25}$$

where

$$\Re\{\cdot\} = \frac{1}{4\pi^2}\int_{-\pi}^{\pi} d(\phi-\phi')e^{-j(\phi-\phi')}\{\cdot\}, \tag{8.26}$$

with

$$R_s = \sqrt{\rho^2 + \rho'^2 - 2\rho\rho'\cos(\phi-\phi') + c_s^2}\ . \tag{8.27}$$

Upon application of the method-of-moments and using the procedure from section 5.3, we can now calculate the resonant frequencies.

Table 8.3 presents the numerical results for the TE_{01} mode, obtained for four types of resonator structures in comparison with values given by other authors.

Table 8.3. Resonant frequencies of the TE_{01} mode for the various resonator parameters. (Ref. [100], ©1999 John Wiley & Sons)

Specifications						Resonant frequency [GHz]			
ε_r	ε_{rs}	a [mm]	h [mm]	d_1 [mm]	d_2 [mm]	Ref. [150]	Ref. [223]	Other methods [Ref.]	Present method
34.19	9.6	7.49	7.48	0.70	8.20	4.34	4.35	4.35 [120]	**4.36**
34.21	9.6	7.00	6.95	0.70	8.20	4.51	4.53	4.52 [120]	**4.53**
36.2	1.0	2.03	5.15	2.93	8.08	10.37	10.86	10.5 [73]	**10.52**
36.2	1.0	4.00	2.14	4.43	6.57	7.69	8.37	7.76 [73]	**7.75**

The results are found to be in good agreement.

The second test concerns the calculation of the TE_{01} mode resonance frequency of the resonator with a = 3.85 mm, h = 3.41 mm, ε_r = 37.7, ε_{rs} = 2.54, d_1 = 0.254 mm, versus the distance t between the resonator and the tuning plate. Results of the computation are compared with those given in [223] (GIBC method) and [83] (variational method) in Fig. 8.24.

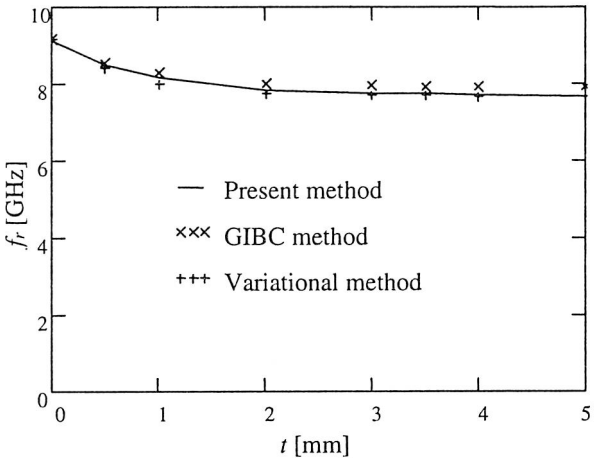

Fig. 8.24. The resonant frequency versus the distance t – comparison of results. (Ref. [100], ©1999 John Wiley & Sons)

The third example concerns an inhomogeneous dielectric body. We consider a structure (a DR with a dielectric tuning device) as shown in Fig. 8.25. For modeling purposes we assume that we deal with the dielectric BOR composed of four parts: the DR itself, the air gap between the DR and the upper dielectric, the tuning dielectric, and the metal screw. The screw is rigorously modeled as a lossy dielectric with a high conductivity σ. Figure 8.26 shows the resonance frequency of the structure versus the distance t, with the thickness g as the parameter. The comparison with the results given in [52] proves the present formulation to be correct.

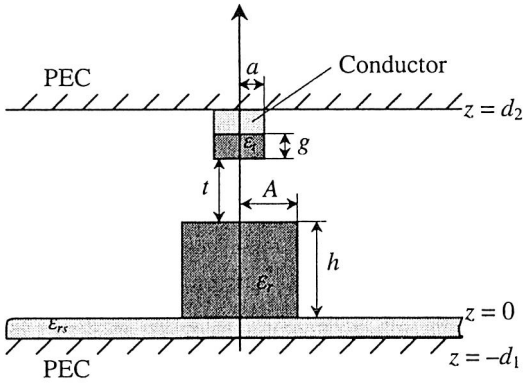

Fig. 8.25. A DR with a dielectric tuning device

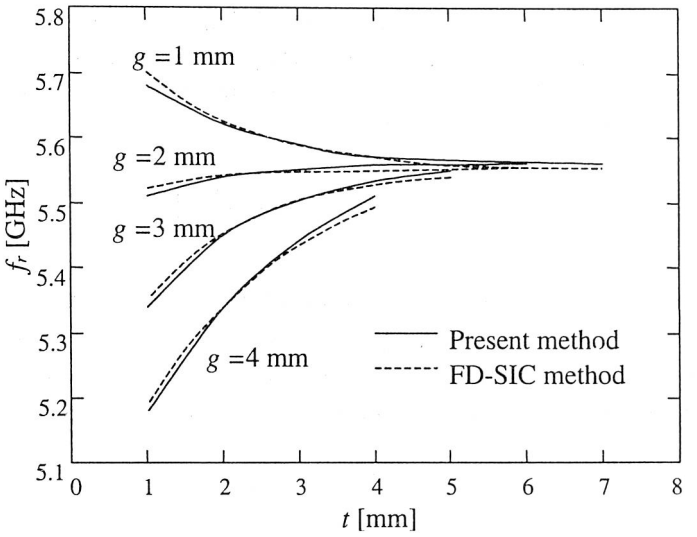

Fig. 8.26. Resonant frequency for the DR with a dielectric tuning device. (a = 5 mm, d_1 = 2 mm, d_2 = 12 mm, h = 4 mm, A = 5 mm, $\varepsilon_r = \varepsilon_t = 38$, $\varepsilon_{rs} = 1$, and $\sigma = 5.336 \cdot 10^7$ S/m).
(Ref. [100], ©1999 John Wiley & Sons)

8.2.3. Dielectric bodies over a grounded dielectric substrate*)

In this section, we give examples of calculations for the configuration shown in Fig. 8.27, where the cylindrical body (either homogeneous or not) is placed in an environment typical of microstrip antennas, i.e., on a grounded dielectric substrate.

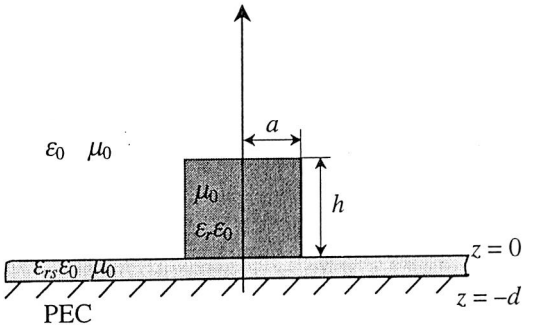

Fig. 8.27. A DR mounted on a grounded dielectric substrate

*) [101, 103].

This time we will focus our attention on HEM and TM modes, so we need to calculate all of the Sommerfeld integrals appearing in the general formulation given by formulas (4.44) and (4.45). For brevity, we will present as an example, the method of calculating the scalar potential kernel.

$$K_m^{\phi} = -j\omega\Im_{m0}\left\{\frac{V_i^h - V_i^e}{k_\rho^2}\right\}. \tag{8.28}$$

A transmission line for the computation of V_i^p for a given media configuration is depicted in Fig. 8.28. Considering our assumption that the resonator is placed on a grounded substrate, the source point in the figure is within the second section of the line, corresponding to the air region above the substrate.

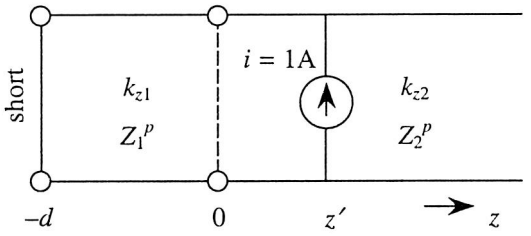

Fig. 8.28. Transmission line circuit for computation of V_i^p for a source point above the grounded substrate

The n-th section has a propagation constant k_{zn} and a characteristic impedance Z_n^e (for TM waves) and Z_n^h (for TE waves) given as:

$$Z_n^e = \frac{\eta_n k_{zn}}{k_n}, \qquad Z_n^h = \frac{\eta_n k_n}{k_{zn}}, \tag{8.29}$$

where η_n denotes the intrinsic impedance of layer n.

Using the formulas from Appendix 2, after some transformations we obtain the following expression for the spectral scalar potential kernel:

$$\frac{V_i^h - V_i^e}{k_\rho^2} = \frac{j}{2\omega\varepsilon_0}\left\{\frac{e^{-jk_{z2}|z-z'|}}{jk_{z2}} + f^{\phi}\frac{e^{-jk_{z2}(z+z')}}{jk_{z2}}\right\}, \tag{8.30}$$

where:

$$f^{\phi} = \frac{k_2^2\Gamma^h - k_{z2}^2\Gamma^e}{k_\rho^2}, \qquad \Gamma^p = \frac{Z_1^p(1-t) - Z_2^p(1+t)}{Z_1^p(1-t) + Z_2^p(1+t)}, \quad p = e, h, \qquad t = e^{-j2k_{z1}d}. \tag{8.31}$$

We note that, despite its appearance, f^{ϕ} is bounded as $k_\rho \to 0$, which is important for later development. When k_ρ goes to infinity f^{ϕ} approaches the value:

$$f^{\phi} \xrightarrow{k_\rho \to \infty} -q, \qquad q = \frac{\varepsilon_r - 1}{\varepsilon_r + 1}. \tag{8.32}$$

This asymptotic part can be subtracted from f^{ϕ} thus enabling the application of DCIM. The "reminder" function is then approximated in terms of the expansion:

$$f^{\phi} + q = \sum_{l=1}^{L} A_l e^{-jk_{z2}h_l}. \tag{8.33}$$

The coefficients $\{A_l\}$ and $\{h_l\}$ may again be found using the POF method. Now, (8.30) can be rewritten in the form:

$$\frac{V_i^h - V_i^e}{k_\rho^2} = \frac{j}{2\omega\varepsilon_0}\left[\sum_{s=1}^{S} a_s \frac{e^{-jk_{z2}c_s}}{jk_{z2}}\right], \tag{8.34}$$

where coefficients a_s and c_s this time take into account the direct ray, the asymptotic (quasi-static) part and the complex images. Following the procedure given in section 8.2.1 we may now calculate (8.28):

$$-j\omega\Im_{m0}\left\{\frac{V_i^h - V_i^e}{k_\rho^2}\right\} = \frac{1}{2\varepsilon_0}\Re_m\left\{\sum_{s=1}^{S} a_s \frac{e^{-jk_2R_s}}{R_s}\right\}, \tag{8.35}$$

where

$$\Re_m\{\cdot\} = \frac{1}{4\pi^2}\int_{-\pi}^{\pi} d(\phi - \phi')e^{-jm(\phi-\phi')}\{\cdot\}, \tag{8.36}$$

with

$$R_s = \sqrt{\rho^2 + \rho'^2 - 2\rho\rho'\cos(\phi - \phi') + c_s^2}. \tag{8.37}$$

In a similar way we can easily evaluate the kernels forming magnetic potential dyadic Green's function. It has to be noted that in the case of Fig. 8.27 $L_{tz} = -L_{zt}$, therefore only three sets of complex images have to be found. It is also worth mentioning that in the process of applying DCIM we do not extract the surface wave terms from the kernel functions, which is often the case when analyzing for example microstrip structures. A step like this is in general possible, but if applied it introduces residues that depend both on z and z', which means that the extraction must be repeated for each z, z' combination. If we do not extract the surface wave terms we need more

complex images to make the method sufficiently accurate, but the sets of complex images can be found once for each of the layer configurations as well as for each frequency [138]. Some inaccuracies may also appear in the far-field computations near the horizon, if the surface wave contribution is strong. This is in general caused by the fact that the surface waves behave in the manner of cylindrical waves and it is physically inappropriate to approximate them with spherical ones [115]. However, if the body of interest is not electrically large and we are not interested in the radiation along the media interfaces, the procedure without extraction of surface waves is much more efficient.

Computational examples for the above formulation are given in the next sections.

8.2.3.1. Resonant frequencies and quality factors

HEM modes

Table 8.4 gives a comparison of the computed HEM_{11} resonant frequencies using the present method for three DRs with the results given by Kishk *et al.* [93]. The comparison data concerns the measured results as well as results of computation using the surface current model (with finite size of the ground plane and the dielectric substrate). In the computations we have considered a substrate with $\varepsilon_{rs} = 2.35$ and thickness $d = 0.795$ mm. The relative dielectric constant of the resonators is $\varepsilon_r = 22$.

Table 8.4. Measured and computed resonant frequencies of the HEM_{11} mode. (Ref. [101], ©1999 John Wiley & Sons)

Resonator dimensions		Resonant frequency [GHz]		
a [mm]	h [mm]	Measured [93]	Computed [93]	Computed Present method
5.2	10.4	5.20	5.189	**5.160**
11.3	4.51	4.39	4.336	**4.347**
7.8	3.0	6.58	6.567	**6.502**

The results are found to be in good agreement, the largest difference being 1.2%.

The second test concerns the calculation of the HEM_{11} mode resonance frequency and the quality factor of a resonator with $a = 6.5$ mm, $h = 5$ mm versus the dielectric constant of the resonator. Results of the computation are compared with those given in [93] in Fig. 8.29.

The third example concerns an inhomogeneous dielectric body. The evaluated structure (stacked dielectric resonator antenna similar to that proposed in [91]) is

shown in Fig. 8.30. Figure 8.31 shows the resonance frequency of the structure versus the dielectric constant of the upper part of the antenna, for several values of the dielectric constant of the lower part. The comparison with the results obtained with the surface current model [182] (finite size of the substrate) proves the present formulation to be correct.

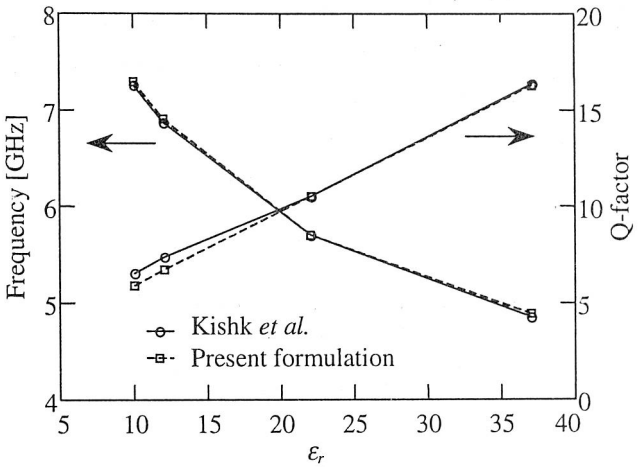

Fig. 8.29. The resonant frequency and radiation Q-factor of a dielectric disk antenna versus dielectric constant of the disk; $a = 6.5$ mm, $h = 5$ mm, $d = 0.795$ mm, $\varepsilon_{rs} = 2.35$. (Ref. [101], ©1999 John Wiley & Sons)

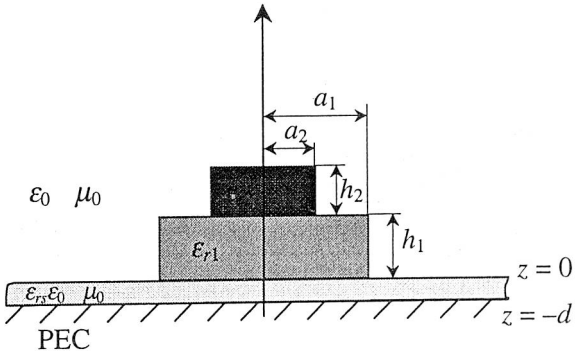

Fig. 8.30. A stacked dielectric resonator mounted on a grounded dielectric substrate

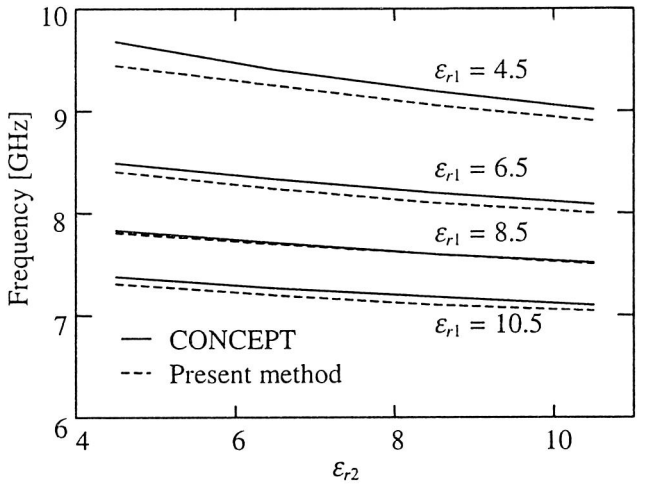

Fig. 8.31. The resonant frequency of a stacked dielectric disk antenna.
$a_1 = 7$ mm, $h_1 = 4$ mm, $a_2 = 3.5$ mm,
$h_2 = 2.4$ mm, $d = 0.795$ mm, $\varepsilon_{rs} = 2.35$.
(Ref. [101], ©1999 John Wiley & Sons)

Finally, the coated dielectric resonator similar to that proposed in [26] has been analyzed (Fig. 8.32). Figure 8.33 shows the structure discretization for the purpose of SIE modelling. The results of resonant frequency computations are shown in Fig. 8.34.

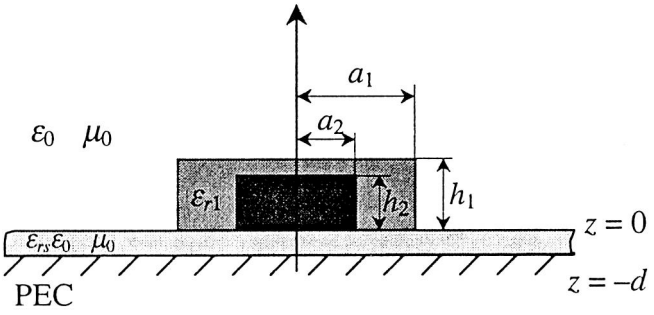

Fig. 8.32. Coated dielectric resonator
on a grounded dielectric substrate

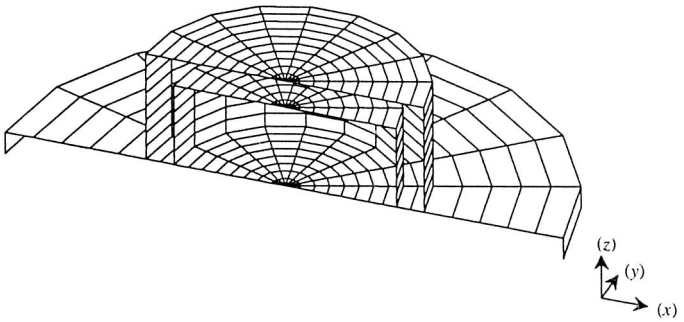

Fig. 8.33. An example of the structure discretization for computation using the CONCEPT II code. Half of the structure is shown. The metal ground plane with $z = 0$ is not shown in the picture

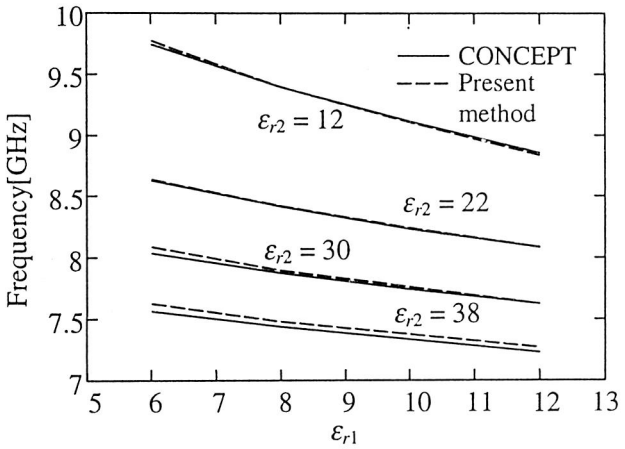

Fig. 8.34. The resonant frequency of a coated dielectric disk antenna $a_1 = 5$ mm, $h_1 = 4$ mm, $a_2 = 4$ mm, $h_2 = 3$ mm, $d = 0.795$ mm, $\varepsilon_{rs} = 2.35$ (Ref. [106])

TM modes

First, a simple homogeneous resonator (Fig. 8.27) with the relative dielectric constant $\varepsilon_r = 36$ has been analyzed. The TM_{01} mode resonant frequencies computed with the present method have been compared with results obtained from the surface current model with finite lateral size of the substrate. The resonator is placed on the substrate with $\varepsilon_{rs} = 2.35$ and thickness $d = 0.795$ mm. Figure 8.35 shows the calculated resonant frequencies against the resonator height. There is a good agreement of results, with the largest difference being 1.7%.

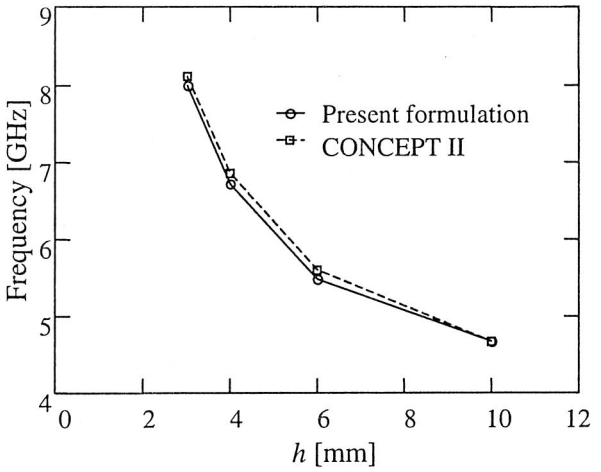

Fig. 8.35. The TM_{01} resonant frequency of a dielectric ring resonator versus the resonator height; $a = 7$ mm, $d = 0.795$ mm, $\varepsilon_r = 36$, $\varepsilon_{rs} = 2.35$
(Ref. [103], ©2000 John Wiley & Sons)

The second test concerns the calculation of the TM_{01} mode resonance frequency and the quality factor of the ring resonator (Fig. 8.36) with $a = 7$ mm, $h = 6$ mm, $b/a = 0.2$ versus the dielectric constant of the resonator. The resonator has been modeled as an inhomogeneous BOR consisting of the ring itself and the air region inside modeled as a dielectric with $\varepsilon_r = 1$. Results of computation of the resonant frequency are compared with results obtained with the surface currents model in Fig. 8.37. The results for Q-factor are also included in the figure.

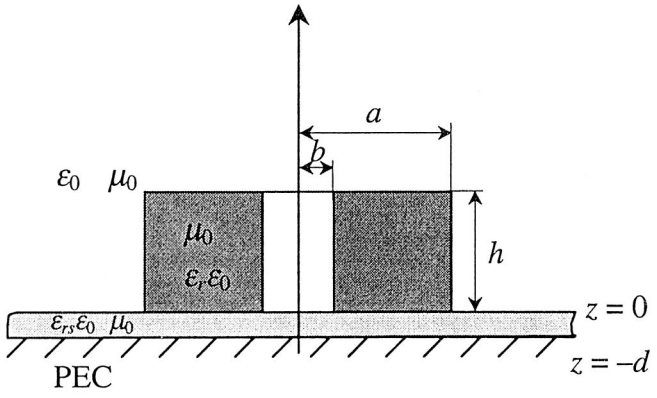

Fig. 8.36. A ring DR mounted on a grounded dielectric substrate

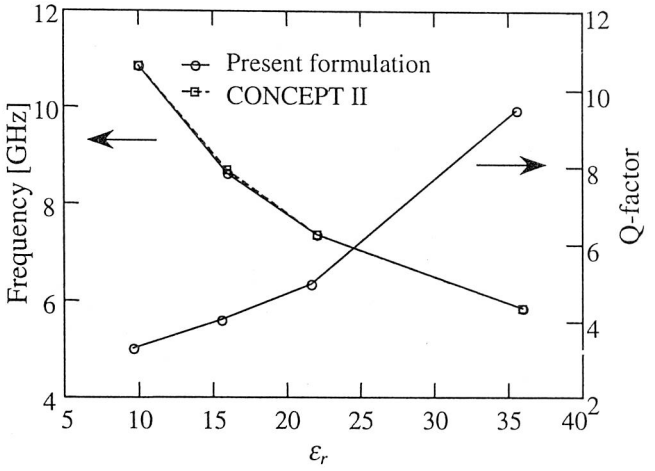

Fig. 8.37. The resonant frequency and radiation Q-factor of a dielectric ring antenna versus the dielectric constant of the resonator; $a = 7$ mm, $h = 6$ mm, $b = 1.4$ mm, $d = 0.795$ mm, $\varepsilon_{rs} = 2.35$ (Ref. [103], ©2000 John Wiley & Sons)

8.2.3.2. Internal electric field distributions*)

In the preceding sections, we have given a number of examples concerning resonant frequency and quality factor computations. All of the examples include comparison data, thus validating the computational procedures developed by the author. However, for such computations we need to calculate only the impedance matrix for a given problem. The convenient aspect of these examples is that the formulas obtained for different mode types have been validated separately. In scattering problems, which are the main subject of this monograph we use all or some of the procedures at the same time, depending on the modal decomposition of the excitation.

In this section, we give computation examples for the electric fields inside dielectric bodies due to plane wave excitation. Based on the comparison given below we are able to prove the correctness of the impressed field formulas provided for layered media in Chapter 6. The configuration used for computations is presented in Fig. 8.27.

First, we have computed the electric field inside a homogeneous dielectric cylinder of moderate size residing on a grounded substrate. The cylinder has been illuminated by a plane wave arriving at an angle $\vartheta_i = 45°$. Two polarizations of

*) [107].

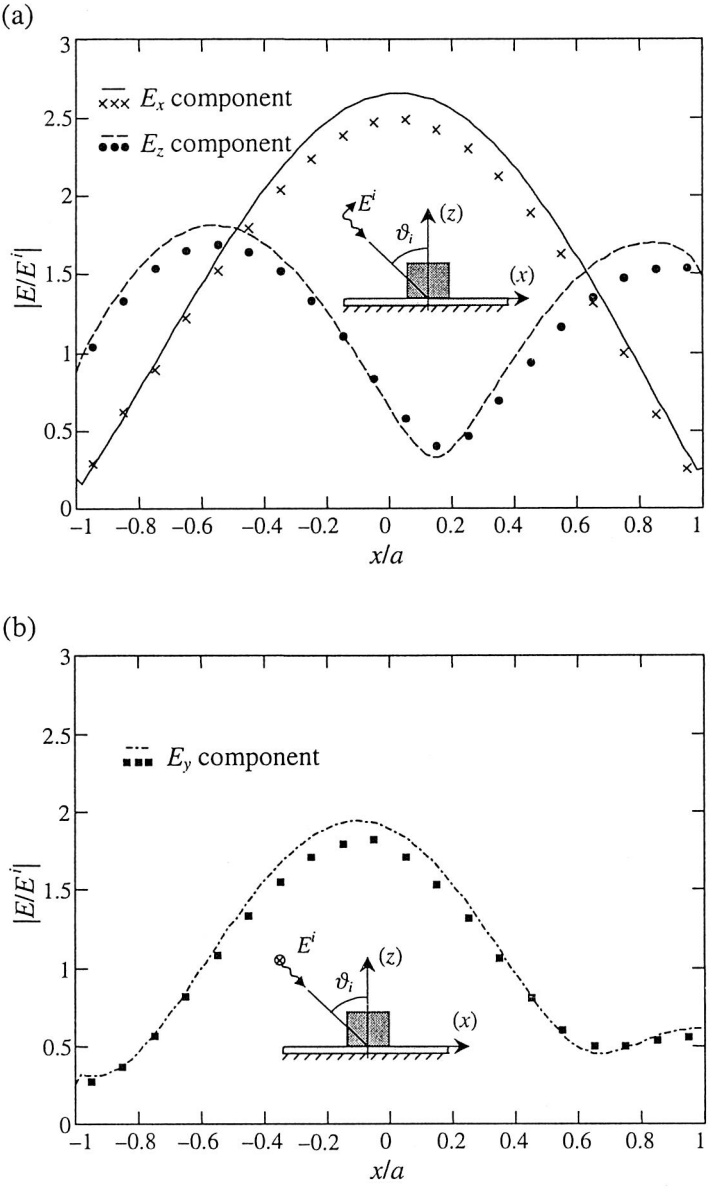

Fig. 8.38. The field along a line parallel to the x-axis at $z = 2.5$ mm inside a homogeneous dielectric cylinder with $\varepsilon_r = 36$, placed in layered media. $a = 7$ mm, $h = 5$ mm, $d = 0.795$, $\varepsilon_{rs} = 2.35$. Angle of incidence $\vartheta_i = 45°$, $k_0 a = 0.733$. Symbols denote the present solution, lines represent the SIE solution. (a) Parallel polarization. (b) Perpendicular polarization. (Ref. [107], ©2001 IEEE)

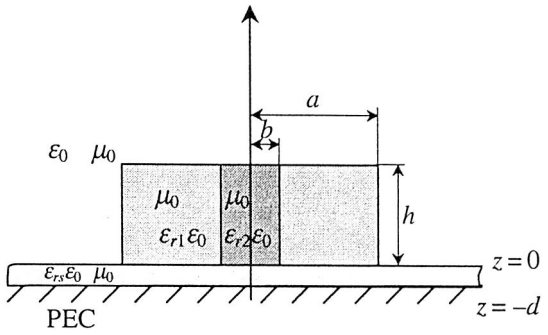

Fig. 8.39. An inhomogeneous CDR in a layered environment

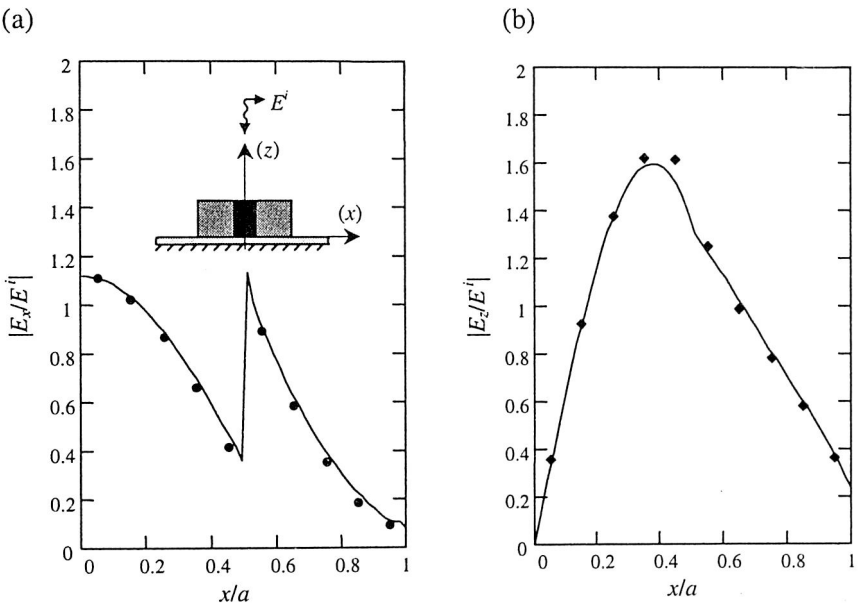

Fig. 8.40. The field along a line parallel to the x-axis at $z = 2.5$ mm inside an inhomogeneous dielectric cylinder, placed in layered media. $a = 7$ mm, $b = 3.5$ mm, $h = 5$ mm, $d = 0.795$, with $\varepsilon_{r1} = 10$, $\varepsilon_{r2} = 36$, $\varepsilon_{rs} = 2.35$, $k_0 a = 1.026$. Symbols denote the present solution, lines represent the SIE solution. (a) Normalized magnitude of the E_x component. (b) Normalized magnitude of the E_z component. (Ref. [107], ©2001 IEEE)

the incident wave have been considered in order to test the various modal decompositions of the problem. Sample results are given in Fig. 8.38. The agreement of the results obtained using the method herein with the CONCEPT II calculations is again very good.

Next, the inhomogeneous dielectric cylinder shown in Fig. 8.39 has been taken into account. This time we have assumed an axial field incidence. The internal electric field distributions are shown in Fig. 8.40. One can notice the perfect prediction of the jump in the electric field component perpendicular to the boundary between the two dielectrics. This again is caused by the appropriate boundary condition being directly built into the basis function definitions.

8.2.3.3. RCS computations*)

Being satisfied with the results of internal field distributions, we can now calculate the radar cross-sections. This will allow us to validate the last building block in the computational scheme, namely the far-field formulas given in Chapter 7. Figure 8.41 shows the bi-

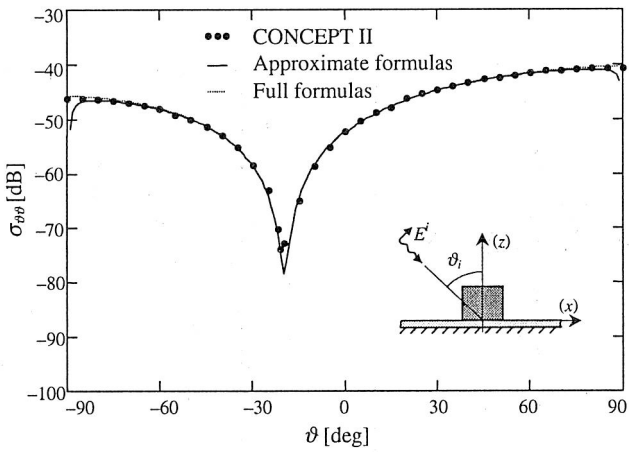

Fig. 8.41. Bi-static RCS of a homogeneous dielectric resonator placed on a grounded dielectric substrate. $\varepsilon_r = 36$, $a = 7$ mm, $h = 5$ mm, $d = 0.795$, $\varepsilon_{rs} = 2.35$, $k_0 a = 0.44$. Angle of incidence $\vartheta_i = 45°$. The symbols denote a SIE solution, dotted and solid lines correspond respectively to the present exact and approximate solutions

static radar cross-section of a homogeneous dielectric cylinder from the first example provided in the previous section. As indicated in the picture, the RCS has been calculated twice using the present method. One of the curves corresponds to simple formulas presented in Chapter 7, the second one has been obtained using a full rigorous field formula (3.170). The agreement between these results as well as in comparison with CONCEPT data is very good with the exception of angles near the horizon, where as was mentioned at the end of Chapter 7, the approximate formulas loose validity.

*) [107].

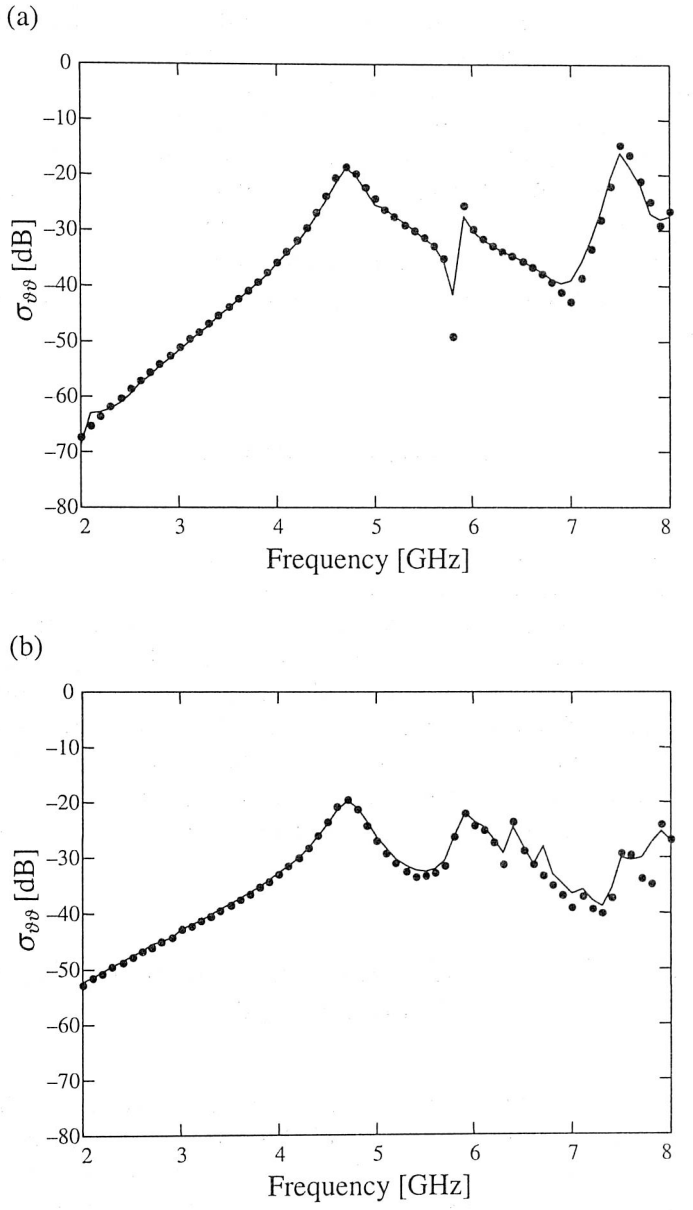

Fig. 8.42. RCS of a homogeneous dielectric resonator
placed on a grounded dielectric substrate.
$\varepsilon_r = 36$, $a = 7$ mm, $h = 5$ mm, $d = 0.795$, $\varepsilon_{rs} = 2.35$.
The symbols denote the present solution, the solid line represents a SIE solution.
(a) Angle of incidence $\vartheta_i = 0°$. (b) Angle of incidence $\vartheta_i = 45°$.
(Ref. [107], ©2001 IEEE)

As the last example, the monostatic RCS of the dielectric cylinder from Fig. 8.27 has been calculated as a function of frequency. The results for two different arrival directions of the incident wave are given in Fig. 8.42.

It should be mentioned that (following [137]) the RCS results presented above do not include the field reflected from the layered structure (physical optics). It may also be of interest for CONCEPT II users that the scattered field necessary for RCS computations was calculated using the near field routines of this program. It was obtained by subtracting from the total fields the incident ones computed in the absence of the dielectric body (however taking into account the finite dielectric substrate).

8.3. Other examples

The examples given in the previous sections included either some canonical problems (scattering by dielectric spheres or cylinders), dielectric resonator problems (resonant frequency and quality factors), or dielectric antenna problems (radiation patterns, radar cross-sections). However, the application possibilities for the theory presented are much wider. Below, we present just two examples: the calculation of fields induced by external fields in a human body and (the example from a completely different branch) the calculation of EM scattering by rain particles, which is an important aspect in propagation models. Other possible applications include underground sensing [40], or thin-films technology [201].

8.3.1. Electric fields induced in a body-of-revolution model of a human head*)

In this example, the free space version of the VIE-BOR method has been used to calculate the electric field inside a simple human-head model presented in Fig. 8.43(a). Step discontinuities of particular borders result from the simple rectangular basis function used in this case. The object is illuminated by a plane wave with a unit amplitude and frequency of 450 MHz coming from the right. The calculated field distribution inside the head model is presented in Fig. 8.43(b).

*) [98].

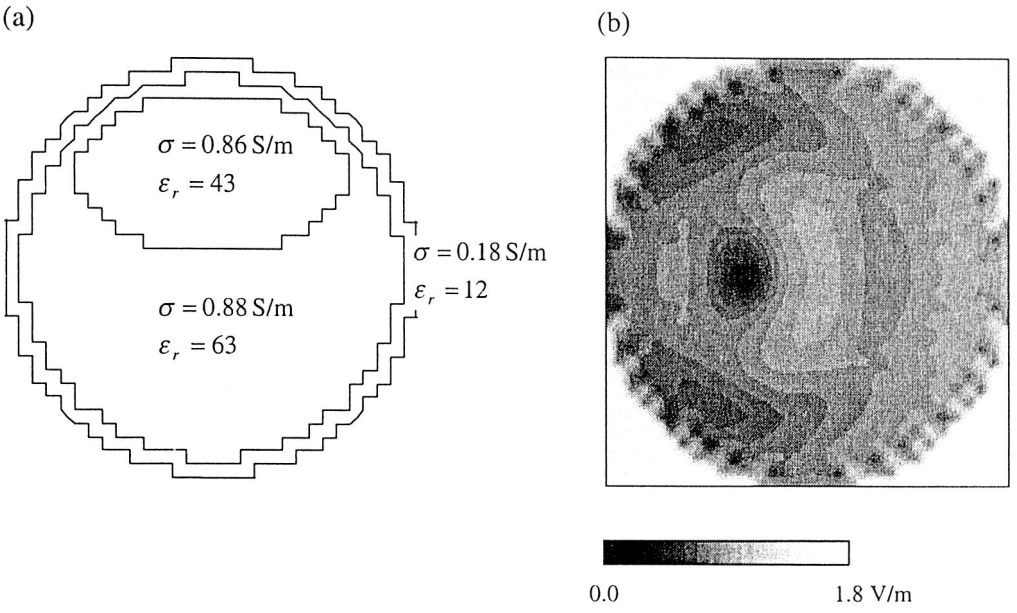

Fig. 8.43. Simplified model of a human head (a)
and the computed field distribution inside the model (b). (Ref. [98])

8.3.2. Electromagnetic scattering by hydrometeors in a resonant frequency region*)

The problem of predicting the electromagnetic field attenuation and scattering due to propagation through hydrometeors plays an extremely important role in the performance of both satellite and terrestrial microwave radio links. The scattering phenomena depend very strongly on the frequency range of the electromagnetic waves.

There are three main frequency regions that are usually defined when considering scattering by rain particles:

1) Rayleigh-scattering region, when rain particles can be considered as electrically small, and where the phase shifts across the particles are small;

2) optical-scattering region, when the incident wavelength is much less than the diameter of the scattering particle; larger raindrops approach this condition at 100 GHz or above;

3) resonance region, which lies between the above Rayleigh and optical regions.

*) [99, 108].

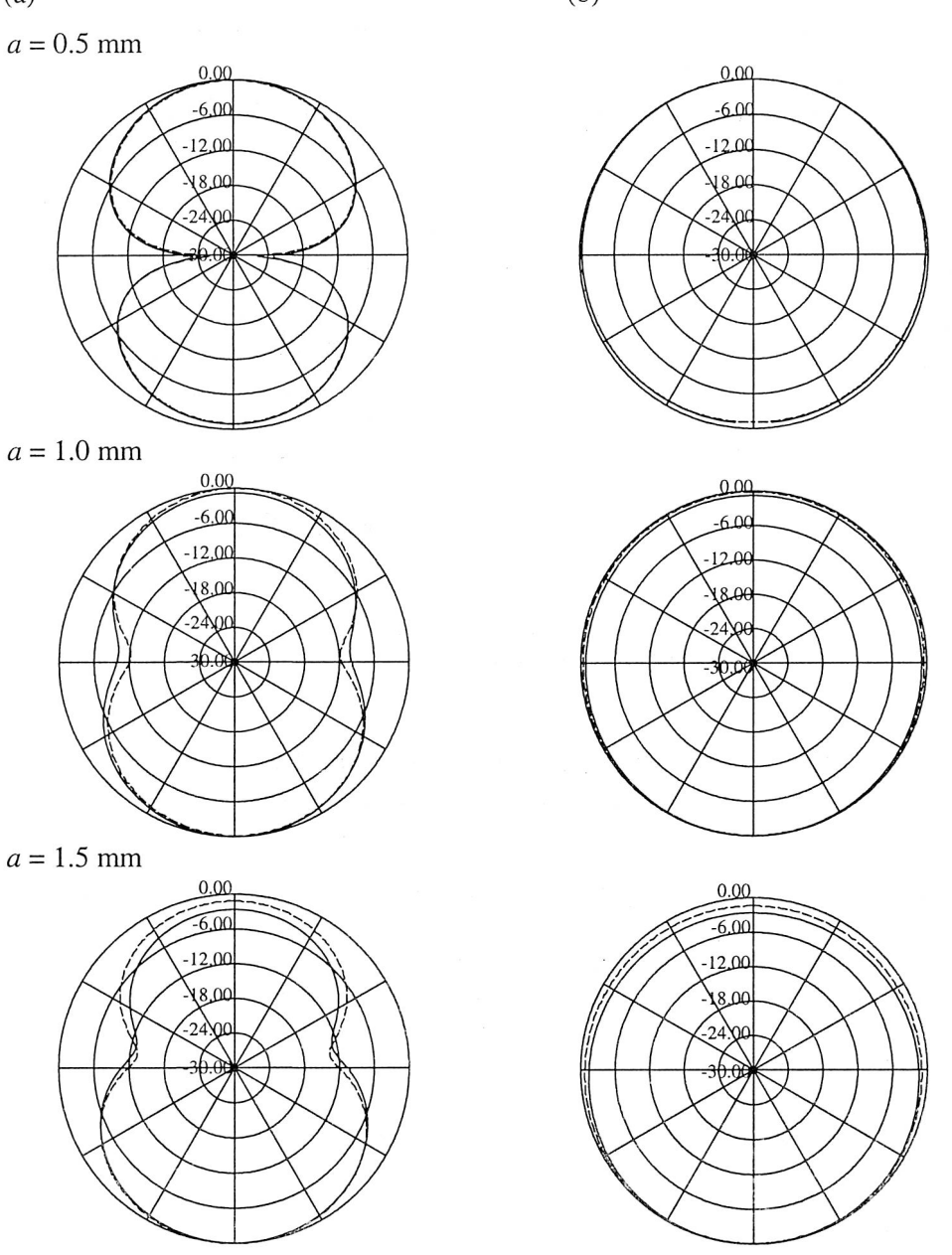

Fig. 8.44. Bi-static radar cross-sections of raindrops at 20 GHz (a) $\theta\theta$ polarization, (b) $\phi\phi$ polarization. Solid lines – SIE formulation, dashed lines – VIE formulation. a denotes the raindrop radius. Scale in dB, incident wave along the z-axis. (Ref. [108])

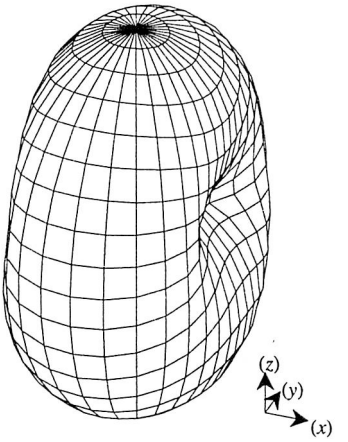

Fig. 8.45. Three dimensional view of the bi-static radar cross-section characteristics. Raindrop radius 1 mm, frequency 20 GHz, incident field along the z-axis, field vector parallel to the x-axis. (Ref. [108])

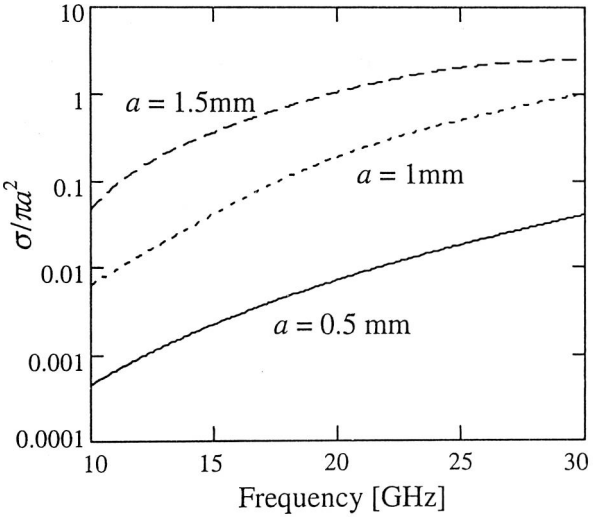

Fig. 8.46. Normalized radar cross-section of the raindrop for three raindrop sizes. a denotes the raindrop radius. (Ref. [108])

In both Rayleigh and optical regions there are well proven asymptotic solutions: at low frequencies there are relatively simple formulas describing the scattering phenomenon and at high frequencies the situation may be described by ray models.

In the resonance region there are no simple asymptotic techniques that could be used to describe the field–rain interactions. In fact, the description of the scattering problem requires a rigorous solution of Maxwell's equations. Unfortunately, when investigating for example the 20–30 GHz frequency band, which is becoming important in contemporary solutions, this third approach must be used.

The analytical or semi-analytical solutions exist only for simple shapes of scatterers. For example, for spheres we can apply the Mie theory. For shapes that are more irregular we have to use purely numerical techniques, like the ones presented in this monograph.

In this example, two numerical methods have been applied to predict the scattering by hydrometeors within the resonance region and compared to each other: the VIE-BOR method developed by the author and the SIE-3D method (CONCEPT code).

The scattering by rain particles has been considered in two aspects. First, an angular dependence of rain scatter at 20 GHz has been given. Figure 8.44 shows the bi-static scattering cross-section of raindrops for various raindrop sizes. Based on data such as presented in Fig. 8.44, concerning the scattering by a single raindrop we can obtain the bi-static cross-section per unit volume and then also the power scattered by a rain region using the raindrop-size distribution [56]. In Figure 8.45, a three-dimensional view of bi-static scattering characteristics has been shown. Next, the radar cross-sections versus frequency for various drop diameters have been given in Fig. 8.46.

Chapter 9. Conclusions

The objective of this study was to develop reliable methods for analysis of electromagnetic wave scattering by general dielectric bodies embedded in various environments. Different forms of the equivalence principles suitable for analysis of homogeneous, partially homogeneous or heterogeneous bodies have been discussed. The equivalence principles allow one to formulate the integral equations describing the problem of interest. In conjunction with the idea of Green's functions, the integral equations method is applicable to various related problems of electromagnetics, where the representative examples include scattering by dielectrics in free-space or in general multilayer environments. Among the various formulation possibilities, particular attention has been devoted to those exploiting the so-called mixed-potential forms of the equations.

The computational methods described usually make extensive use of computer resources. In view of this, every reduction of the problem complexity allows us to treat situations that are not solvable using standard approaches. An important example is the case of bodies characterized by the rotational symmetry, presented in this monograph. The equations based on the volume equivalence approach have been presented and solved using the well-known method-of-moments, both for the case of free-space and for layered media configurations. In the solution we have applied a specially developed basis function set, which allowed further optimization of the procedure.

This monograph also includes examples concerning scattering calculations and resonance phenomena inside dielectric objects. All procedures have been carefully validated using data published in literature or by comparison with other computational methods.

The author's contribution includes the following items:

- A systematized discussion of the various types of the equivalence principle.
- An introduction of a promising volume-surface integral formulation.
- A unified discussion of problems associated with singularities inherent in the surface integral equation formulations.
- A formulation of the volume integral equation for inhomogeneous bodies of revolution for the case of free-space.

• The development of a new class of mixed-domain, divergenceless basis functions suitable for representation of electric flux density. The basis functions enable a considerable reduction in the number of unknowns characterizing the problem of interest.

• The formulation of specialized forms of the general equation, suitable for characterizing different azimuthal field modes inside the cylindrical dielectric bodies. Separate equations have been presented for TE, TM and HEM modes.

• Generalization of the above items into the case of a multilayer environment.

• Development of modal decomposition formulas for the incident plane wave in layered media.

• Development of far-field approximate modal formulas for the case of layered media unbounded from the top.

All of the new formulas presented in the monograph have been carefully validated. The computer codes have been prepared by the author and the results have been compared with measured and computed data available in literature, as well as with the results of computation performed using commercially available software.

Apart from the canonical problems suitable for validation purposes, some of the results given are of practical importance. The methods developed enable a particularly easy identification of resonance phenomena within cylindrical inhomogeneous dielectric resonators. Thanks to that knowledge, new types of dielectric resonators with enhanced mode separation have been proposed. The radar cross-section computations of dielectric resonator antennas backed with layered structures have been given for the first time.

It is to be noted that although the given computational examples concern mainly antenna problems (DRA – dielectric resonator antennas), which become important in contemporary microwave-frequency applications, the methods presented are totally generic. It has also been demonstrated how these methods could be applied in the field of microwave propagation in rainy regions or in human-body/electromagnetic-field interactions. Other possible applications include geoscience, underground sensing, etc.

According to the author, future developments in this area could concern:

• Focusing on Sommerfeld integrals to develop algorithms suitable for general multilayer configurations, enabling treatment of parts belonging to different layers. A promising approach in this direction is the use of classical numerical integration schemes [136], possibly combined with the singularity cancellation technique outlined in Appendix 1, which eliminates the need of treatment of particularly tedious special cases in the computations of Sommerfeld integrals. An alternative way could be the recently enhanced DCIM procedure [115].

• Closer investigation of the volume-surface formulation proposed, which is expected to enhance the efficiency of VIE solution in the case of layered environment.

• A step towards hybrid techniques joining the SIE approach with the mesh methods [36, 66] for layered media.

- The development of algorithms combining the VIE-BOR scheme with non-BOR geometry [179].
- Combining the SIE or VIE approaches for layered media with the DBOR approach outlined in Section 4.4.
- Specializing the given procedures to new application areas, such as underground sensing (buried dielectric bodies), or investigating the influence of imperfections in dielectric substrates on the performance of microstrip structures.
- Application of the computational algorithms to environments characterized by Green's functions other than the ones presented in this monograph (for example, scattering by dielectric obstacles within waveguides).

Appendix 1. Integration of singular integrals

In the computation of MoM impedance matrices, we have to calculate matrix elements associated with situations where the observation (field) point lies in the source region*). This causes the necessity of performing spatial integrations of singular functions. In the MPIE formulations preferred in this monograph the singularity order is (as was indicated many times) $1/R$, where $R=|\boldsymbol{r}-\boldsymbol{r}'|$ is the distance between the observation and source (primed) points. In free-space the integrals that arise are of the type:

$$I_1=\int_D \frac{e^{-jk|r-r'|}}{|\boldsymbol{r}-\boldsymbol{r}'|}dD\,, \tag{A.1.1}$$

$$I_2=\int_D \boldsymbol{\Lambda}(\boldsymbol{r}')\frac{e^{-jk|r-r'|}}{|\boldsymbol{r}-\boldsymbol{r}'|}dD\,, \tag{A.1.2}$$

where the latter corresponds to a linear basis function used in the MPIE schemes (symbol $\boldsymbol{\Lambda}(\boldsymbol{r}')$ denotes a linear vector function of source coordinates). Note that in BOR geometry the same types of singularities are present during the calculation of the modal Green's functions, when the source and field points coincide in the transverse plane of the body (in the case of volume formulations) and on the generating arc (in the case of surface integrals).

The method of integration through singularities, which has been used in the examples presented in Chapter 8, is based on the so-called singularity extraction technique, and will be illustrated for the case of formula (A.1.1). First, we note that as $\boldsymbol{r}'$ approaches $\boldsymbol{r}$, the kernel approaches $1/|\boldsymbol{r}-\boldsymbol{r}'|$. This is evident if we expand the exponential term into Maclaurin series around the observation point $\boldsymbol{r}$, and retain only the first two terms:

$$\frac{e^{-jk|r-r'|}}{|\boldsymbol{r}-\boldsymbol{r}'|}\cong\frac{1-jk|\boldsymbol{r}-\boldsymbol{r}'|}{|\boldsymbol{r}-\boldsymbol{r}'|}=\frac{1}{|\boldsymbol{r}-\boldsymbol{r}'|}-jk\,. \tag{A.1.3}$$

---

*) The presence of singularity is in fact not limited to self-terms in the impedance matrix, because the spatial domains of basis functions may overlap.

We can subtract the singular term from (A.1.1) and then add it back in the form of a separate integral to get:

$$I_1 = \int_D \frac{e^{-jk|r-r'|} - 1}{|r-r'|} dD + \int_D \frac{1}{|r-r'|} dD . \tag{A.1.4}$$

The first integral in (A.1.4) is now bounded and may be computed with the typical numerical integration methods, using quadratures suitable for the integration domains [49]. Alternatively [125], if sufficiently small integration domain is chosen, just around the singularity, the first integral may be approximated with the second term of the expansion (A.1.3) as:

$$\int_D \frac{e^{-jk|r-r'|} - 1}{|r-r'|} dD \cong -jk \int_D dD , \tag{A.1.5}$$

where the right hand integral is simply the surface or volume of the domain D.

The second integral in (A.1.4) may be computed analytically. The formulas for calculation of this integral when the domain D is either a polygonal surface or a polyhedral volume are given in [49, 214]. In particular, in VIE-BOR formulation with a rectangular basis function we need to calculate the singular integral over domains of the type shown in Fig. A.1.1.

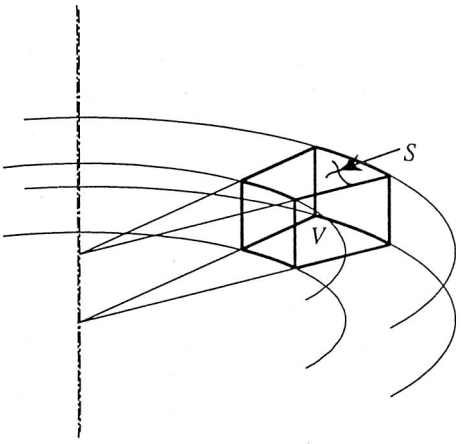

Fig. A.1.1. The elementary integration domains associated with VIE-BOR formulation in the case of a rectangular basis function. V denotes the elementary volume element, S denotes the elementary surface element (one of the faces of V)

Again assuming sufficiently subtle segmentation, we can approximate V using a cuboid with properly adjusted dimensions. The singular part of the integral I_1 (when

D is a cuboid with dimensions $2a_1 \times 2a_2 \times 2a_3$ and the observation vector points into its center of symmetry) is then given by:

$$I_C = \int_{-a_1}^{a_1}\int_{-a_2}^{a_2}\int_{-a_3}^{a_3} \frac{1}{\sqrt{x^2+y^2+z^2}}\,dxdydz$$

$$= 4 \sum_{\substack{i,j,k=1,2,3 \\ i\neq j \\ j\neq k \\ k\neq i}} a_i^2 \arctan\left(\frac{a_j a_k}{a_i^2 + a_k^2 + S_C a_k}\right) - \frac{a_i a_k}{2} \ln\left(\frac{S_C + a_j}{S_C - a_j}\right),$$

$$S_C = \sqrt{a_1^2 + a_2^2 + a_3^2}\,. \tag{A.1.6}$$

Similarly, we can replace the faces with rectangles. The singular part of the integral I_1 (when D is a rectangle with dimensions $2a_1 \times 2a_2$ and the observation vector points into its center of symmetry) is given by:

$$I_R = \int_{-a_1}^{a_1}\int_{-a_2}^{a_2} \frac{1}{\sqrt{x^2+y^2}}\,dxdy = 2 \sum_{\substack{i,j=1,2 \\ i\neq j}} a_i \ln\left(\frac{S_R + a_j}{S_R - a_j}\right), \qquad S_R = \sqrt{a_1^2 + a_2^2}\,. \tag{A.1.7}$$

A similar procedure may be developed for integral (A.1.2) [49, 214]. An alternative way is to approximate the linear function in (A.1.2) with a number of pulse (step) functions and then use the procedures obtained for integral (A.1.1). The approach where the triangle functions have been replaced with four-pulse approximations has been introduced by Mautz and Harrington [125] and then followed by a number of researchers*). This is particularly justified in the BOR case (which was the original Mautz and Harrington application), in view of $1/\rho$ terms appearing in front of the typical linear basis function (see section 5.1.3).

The singularity extraction approach outlined above is also suitable for the case of the multilayer media Green's functions, if the DCIM approach is applied. In this approach the closed form spatial Green's functions are obtained, consisting of a number of terms similar to the free-space scalar Green's function integrated in (A.1.1) and (A.1.2). Therefore, the treatment of possible singularities (which arise when the observation point coincides with the source point in a direct ray or when the observation point meets the location of the image term) is exactly the same as described for the

*) The linear functions are approximated by pulse functions only for performing integrations. When the derivatives of base functions are needed, we remain within the original linear formulation, which causes that the derivatives also have a "pulse" nature.

free-space situation. Unfortunately, this approach fails when we use the classical treatment of Sommerfeld integrals, since dealing here with singularities becomes a very tedious process depending on the particular layers/sources configuration [144].

A promising alternative that becomes popular in recent developments is the cancellation of singularity [212] by means of a special transformation of coordinates. This approach may be outlined as follows.

Let us assume that we deal with the polygonal integration domain, to which the observation point belongs (Fig. A.1.2). We divide the polygon into triangular parts, such that a singular point lies in the vertex of each triangle. Integration over each of the triangles is then performed separately. Next, the elementary triangle is mapped into a local coordinate system depicted in Fig. A.1.3(a). The figure also shows the location of the singular point. The mapping may be described in a vector form [168]:

$$\boldsymbol{r} = \boldsymbol{r}_1(1-\xi_1-\xi_2)+\boldsymbol{r}_2\xi_1+\boldsymbol{r}_3\xi_2\,, \tag{A.1.8}$$

where $\boldsymbol{r}$ indicates the point in Cartesian coordinates, vectors $\boldsymbol{r}_i$ indicate triangle vertices P_i.

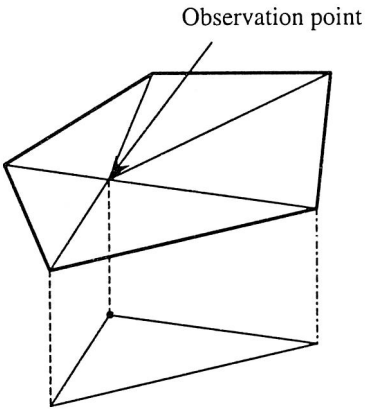

Fig. A.1.2. Subdivision of the polygonal domain into triangles

We see that using transformation (A.1.8) we map point P_1 into point (0, 0), P_2 into (1, 0) and P_3 into (0, 1). We are interested in calculating an integral of the form:

$$I = \int_S \frac{f(\boldsymbol{r})}{|\boldsymbol{r}-\boldsymbol{r}_2|}\,dS\,, \tag{A.1.9}$$

where we assume, according to Fig. A.1.3, that the singular point is placed in vertex P_2. It can be easily shown [168] that after coordinate transformation, (A.1.9) becomes:

$$I = 2T \int_0^1 d\xi_1 \int_0^{1-\xi_1} \frac{f(\xi_1, \xi_2)}{\sqrt{(1-\xi_1)^2 + \xi_2^2}} d\xi_2 \tag{A.1.10}$$

where T is the area of the triangle.

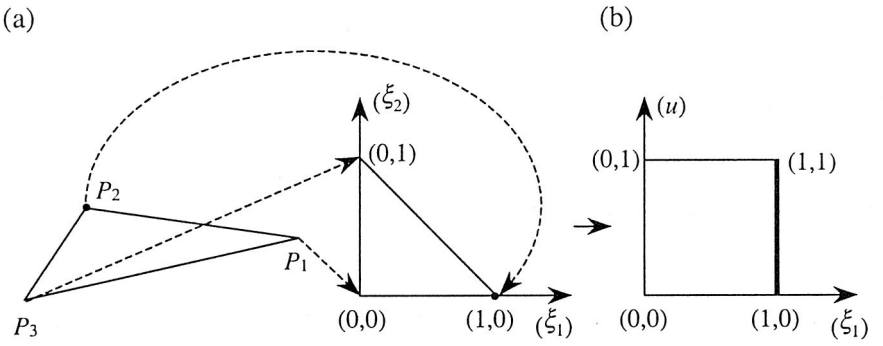

Fig. A.1.3. Elementary triangle mapping (a) into a local coordinate system, (b) into a unit square [212]

Now we make a change of variables [33]:

$$\xi_2 = (1-\xi_1)u\,, \tag{A.1.11}$$

which transforms the "intermediate" triangle into a unit square (Fig. A.1.3(b)), in such a way that the singular point (1, 0) is mapped into the line (1, 0)–(1, 1). After this transformation the integral becomes:

$$I = 2T \int_0^1 d\xi_1 \int_0^1 \frac{f(\xi_1, u)}{\sqrt{(1+u^2)}} du\,. \tag{A.1.12}$$

The kernel of (A.1.12) is now a well-behaved function and may be integrated with standard numerical integration techniques. It may be of interest that the above method easily extends into integration over curvilinear sub-domains, by introducing the proper mapping between the original curvilinear triangular patch and the intermediate triangle [33].

The singularity cancellation method may be generalized into volume integrals by introducing the mapping of the elementary tetrahedron into a unit cube [113], where the singular point is mapped into one of the cube faces.

It should be noted that the coordinate transformation method presented here is only one of a wide set of purely numerical methods suitable for the integration of singular integrals. A detailed description and comparison of those methods lies beyond the scope of this study. A starting point for an interested reader may for example be reference [94].

Appendix 2. Transmission line Green's functions*)

In the formulation of the layered media problems throughout this monograph, we have expressed the kernels in terms of so-called transmission line Green's functions (TLGFs). These TLGFs relate voltages and currents in the transmission line along the layered medium to their sources, according to the telegrapher equations to which the Maxwell's equations reduce in the spectral domain (see section 3.1.1, eq. (3.73)). In order to specialize the equations for the particular configuration of layers we need explicit formulas for calculation of $V_i^p(z|z')$, $I_i^p(z|z')$, $V_v^p(z|z')$ and $I_v^p(z|z')$, $p = e, h$. Note that the DGF formulas presented in Section 3.1.2 are valid for arbitrary media stratification (see the discussion after eq. (3.102)). The case that is important from the practical viewpoint concerns media with parameters that are piecewise constant along the z-axis, although other situations are sometimes found in literature [10].

The transmission line analog of the layered medium consists in our case of a cascade connection of uniform transmission line sections. Let us use n to denote parameters associated with layer n with the boundaries z_n and z_{n+1}. The corresponding section n of the transmission line has terminals at z_n and z_{n+1}, a propagation constant k_{zn} and the characteristic impedance Z_n^p (Fig. A.2.1).

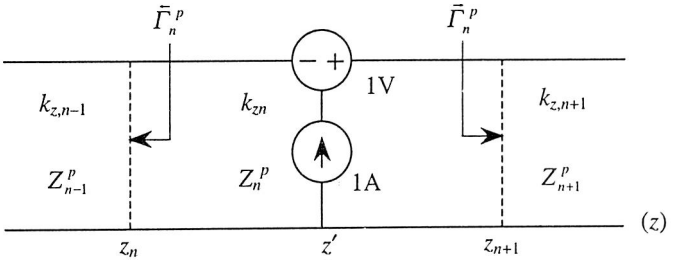

Fig. A.2.1. A transmission line section with voltage and current point sources [140]

*) [140, 137, 134].

In order to find the TLGF's, we excite the transmission line network using unit-strength voltage and current sources at z' in section n and compute the voltage and current at z in section m. As in the main body of the monograph, we assume that the primed media parameters are associated with the source layer n, while the unprimed ones are those of layer m. In Fig. A.2.1, $\overleftarrow{\Gamma}_n^p$ and $\overrightarrow{\Gamma}_n^p$ are the voltage reflection coefficients looking respectively to the left and right from the terminals of section n. These coefficients can be obtained for each line junction using the recursive relations:

$$\overleftarrow{\Gamma}_{n+1}^p = \frac{\Gamma_{n,n+1}^p + \overleftarrow{\Gamma}_n^p t_n}{1+\Gamma_{n,n+1}^p \overleftarrow{\Gamma}_n^p t_n}, \tag{A.2.1}$$

$$\overrightarrow{\Gamma}_{n-1}^p = \frac{\Gamma_{n,n-1}^p + \overrightarrow{\Gamma}_n^p t_n}{1+\Gamma_{n,n-1}^p \overrightarrow{\Gamma}_n^p t_n}, \tag{A.2.2}$$

where

$$\Gamma_{ij}^p = \frac{Z_i^p - Z_j^p}{Z_i^p + Z_j^p}, \tag{A.2.3}$$

$$t_n = e^{-j2k_{zn}d_n}, \quad d_n = z_{n+1} - z_n. \tag{A.2.4}$$

One should apply (A.2.1) and (A.2.2) starting, respectively, from the left and right ends of the transmission line network.

For the case where the observation point lies in the source layer, $m = n$, we can obtain $V_i^p(z \mid z')$ from (3.78) as:

$$V_i^p(z \mid z') = \frac{Z_n^p}{2}\left[e^{-jk_{zn}|z-z'|} + \frac{1}{D_n^p}\sum_{s=1}^{4} R_{ns}^p e^{-jk_{zn}\gamma_{ns}}\right], \tag{A.2.5}$$

where

$$D_n^p = 1 - \overleftarrow{\Gamma}_n^p \overrightarrow{\Gamma}_n^p t_n, \tag{A.2.6}$$

$$\begin{aligned} R_{n1}^p &= \overrightarrow{\Gamma}_n^p, \\ R_{n2}^p &= \overleftarrow{\Gamma}_n^p, \\ R_{n3}^p &= R_{n4}^p = \overleftarrow{\Gamma}_n^p \overrightarrow{\Gamma}_n^p, \end{aligned} \tag{A.2.7}$$

$$\begin{aligned}\gamma_{n1} &= 2z_{n+1} - (z + z'),\\ \gamma_{n2} &= (z + z') - 2z_n,\\ \gamma_{n3} &= 2d_n + (z - z'),\\ \gamma_{n3} &= 2d_n - (z - z').\end{aligned} \tag{A.2.8}$$

The first term in (A.2.5) represents the direct ray between the source and the observation point. Note that if the above formulas are applied to free space, which was the case when for example checking whether the "layered" formulas reduce properly to their free-space counterparts in sections 6.3 and 7.3, this "direct" term is the only one that remains in the solution. The remaining TLGF's may be obtained from (A.2.5) using (3.78)–(3.80). Thus, we get:

$$V_v^p(z \mid z') = \frac{1}{2}\left[\pm e^{-jk_{zn}|z-z'|} - \frac{1}{D_n^p}\sum_{s=1}^{4}(-1)^s R_{ns}^p e^{-jk_{zn}\gamma_{ns}}\right], \tag{A.2.9}$$

where the upper and lower signs pertain to $z > z'$ and $z < z'$, respectively. The formulas for $I_v^p(z \mid z')$ and $I_i^p(z \mid z')$ may be easily obtained respectively from (A.2.5) and (A.2.9), using the duality of (3.78) and (3.79). Consequently, we should replace the impedances by admittances, which also changes the signs of the reflection coefficients. The discontinuous terms that appear in $V_v^p(z \mid z')$ and $I_i^p(z \mid z')$ cancel out in formulas (4.34)–(4.37).

When the observation (field) point z is located in a source free section m of the transmission line network, we can get the voltage $V^p(z)$ and current $I^p(z)$ in terms of the voltage $V^p(z_0)$ across one of the terminal pairs of the source section. Here, $z_0 = z_n$ or $z_0 = z_{n+1}$, depending on whether z is located respectively to the left or to the right of the line section n. Using the homogeneous form of transmission line equations (3.73) for $m < n$ we get:

$$\begin{Bmatrix} V^p(z) \\ I^p(z) \end{Bmatrix} = V^p(z_n)\frac{\prod_{k=m+1}^{n-1}\bar{T}_k^p}{1+\bar{\Gamma}_m^p t_m}\begin{Bmatrix} \bar{\tau}_m^p(z) \\ \bar{y}_m^p(z) \end{Bmatrix} e^{-jk_{zm}(z_{m+1}-z)}, \tag{A.2.10}$$

where

$$\bar{T}_k^p \equiv \frac{V^p(z_k)}{V^p(z_{k+1})} = \frac{(1+\bar{\Gamma}_k^p)e^{-jk_{zk}d_k}}{1+\bar{\Gamma}_k^p t_k}, \tag{A.2.11}$$

$$\bar{\tau}_m^p(z) = \left[1 + \bar{\Gamma}_m^p e^{-jk_{zm}(z-z_m)}\right], \tag{A.2.12}$$

$$\tilde{y}_m^p(z) = -Y_m^p\left[1 - \tilde{\Gamma}_m^p e^{-jk_{zm}(z-z_m)}\right]. \tag{A.2.13}$$

The product in (A.2.10) is equal to one if the lower limit exceeds the upper limit. Note that in the above formulas we have dropped the subscripts v and i, because it makes no difference by what type of source the voltage $V^p(z_0 = z_n)$ is produced. Also the dependence z' has been dropped from the argument, because (A.2.10) only implicitly depends on the source location, which is outside the section m. Hence, if section n is excited by a unit-strength current source at z', then $V^p(z_n) = V_i^p(z_n \mid z')$, thus $V^p(z)$ and $I^p(z)$ represent $V_i^p(z \mid z')$ and $I_i^p(z \mid z')$, respectively. If the section is excited by a unit-strength voltage source at z', then $V^p(z_n) = V_v^p(z_n \mid z')$, thus $V^p(z)$ and $I^p(z)$ represent $V_v^p(z \mid z')$ and $I_v^p(z \mid z')$, respectively. For the case of $m > n$ $(z > z')$ we may obtain analogous formulas. Alternatively, we may apply the reciprocity theorems (3.80). For example, $V_v^p(z \mid z')$ may be computed as $-I_i^p(z' \mid z)$.

Appendix 3. Discrete complex images and the Pencil-of-Function method*)

The essential step in closed form computation of Sommerfeld integrals described in section 8.2.1 is an approximation of the spectral integrand in the form:

$$f(k_\rho) = \sum_{i=1}^{M} a_i e^{-jk_{zn}\xi_i}, \tag{A.3.1}$$

where $\{a_i\}$ and $\{\xi_i\}$ are the complex coefficients to be found.

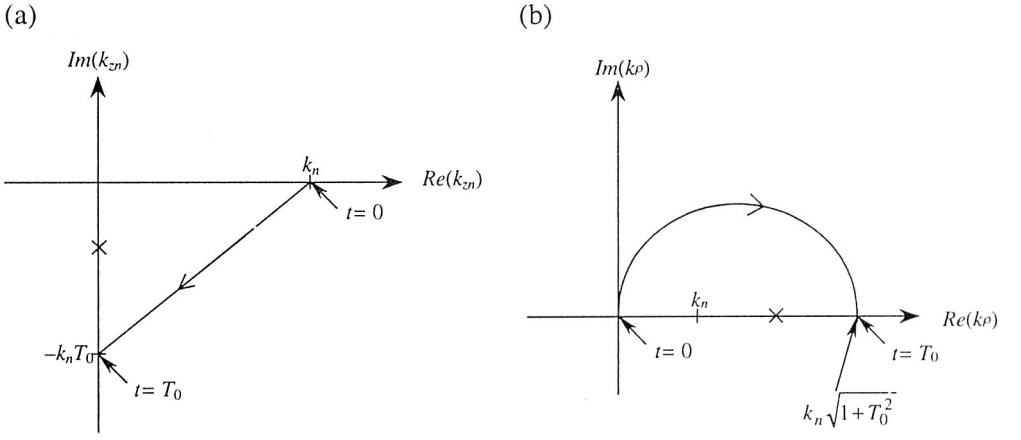

Fig. A.3.1. Paths corresponding to (A.3.2). (a) k_{zn} plane. (b) k_ρ plane [139]

The coefficients can be extracted using parameterization:

$$k_{zn} = k_n\left[\left(1-\frac{t}{T_0}\right) - jt\right], \qquad 0 \le t \le T_0, \tag{A.3.2}$$

*) [138, 139, 67], see also [2, 177].

in terms of a real variable t, where T_0 is a suitably selected parameter. (A.3.2) defines a straight line in the fourth quadrant of the plane k_{zn} (see Fig. A.3.1(a)). When mapped into the plane k_ρ, this segment corresponds to a bow-shaped path in the first quadrant (Fig. A.3.2(b)). After substituting (A.3.2) into (A.3.1) we get the representation of the form:

$$f\left[k_\rho(t)\right]=\sum_{i=1}^{M} b_i e^{s_i t}. \tag{A.3.3}$$

The parameterization (A.3.3) is performed in terms of the *real* variable t. Coefficients $\{b_i\}$ and $\{s_i\}$ may be obtained with the following algorithm. First, we sample the left side of (A.3.3) using a large number (say N) of equidistant points t over an interval $(0, T_0)$. This results in:

$$y_k = f\left[k_\rho(k\delta t)\right]=\sum_{i=1}^{M} b_i e^{s_i k\delta t}, \tag{A.3.4}$$

where $k=0,1,2,...,N-1$; δt denotes the sampling interval. Next, we introduce the notation

$$z_i = e^{s_i \delta t}, \tag{A.3.5}$$

where z_i are the poles in the Z-plane.

We also introduce vectors $\boldsymbol{y}_0, \boldsymbol{y}_1, ..., \boldsymbol{y}_L$ defined as

$$\boldsymbol{y}_i = \left[y_i, y_{i+1}, ..., y_{i+N-L-1}\right]^T. \tag{A.3.6}$$

Moreover, we define the matrices $\boldsymbol{Y}_1$ and $\boldsymbol{Y}_2$ as

$$\boldsymbol{Y}_1 = \left[\boldsymbol{y}_0, \boldsymbol{y}_1, ..., \boldsymbol{y}_{L-1}\right], \tag{A.3.7}$$

$$\boldsymbol{Y}_2 = \left[\boldsymbol{y}_1, \boldsymbol{y}_2, ..., \boldsymbol{y}_L\right]. \tag{A.3.8}$$

It can be shown that if $M \le L \le N-M$ the poles (A.3.5) are the generalized eigenvalues of the matrix pencil $\boldsymbol{Y}_2 - z\boldsymbol{Y}_1$. The algorithm for computing the generalized eigenvalues is given in [67]. Here we note that for $L=M$ (classical Pencil-of-Function method), $\{z_i; i=1,...,M\}$ are the eigenvalues of the $M\times M$ matrix $(\boldsymbol{Y}_1^H \boldsymbol{Y}_1)^{-1}\boldsymbol{Y}_1^H \boldsymbol{Y}_2$, which can be shown to have the form:

$$\left(\boldsymbol{Y}_1^H \boldsymbol{Y}_1\right)^{-1} \boldsymbol{Y}_1^H \boldsymbol{Y}_2 = \begin{bmatrix} 0 & \dots & 0 & -c_M \\ 1 & & 0 & -c_{M-1} \\ & \ddots & & \vdots \\ & & 1 & -c_1 \end{bmatrix}, \tag{A.3.9}$$

where

$$\begin{bmatrix} c_M \\ \vdots \\ c_1 \end{bmatrix} = -\left(\boldsymbol{Y}_1^H \boldsymbol{Y}_1\right)^{-1} \boldsymbol{Y}_1^H \boldsymbol{y}_M . \tag{A.3.10}$$

In order to find the eigenvalues of (A.3.9) the standard methods of linear algebra can be applied.

Once poles z_i are found, the complex amplitudes b_i are easily found as:

$$\boldsymbol{b} = \begin{bmatrix} b_0 \\ \vdots \\ b_{N-1} \end{bmatrix} = \left(\boldsymbol{S}^T \boldsymbol{S}\right)^{-1} \left(\boldsymbol{S}^T \boldsymbol{y}\right), \tag{A.3.11}$$

where

$$\left\{S_{ij}\right\} = \left\{\left(z_j\right)^i\right\}, \qquad \boldsymbol{y} = \left[y_0, y_1, \dots, y_{N-1}\right]^T . \tag{A.3.12}$$

Finally,

$$s_i = \frac{1}{\delta t} \ln\left(z_i\right). \tag{A.3.13}$$

Coefficients $\{a_i\}$ and $\{\xi_i\}$ may then be readily recovered from $\{b_i\}$ and $\{s_i\}$ as

$$\xi_i = -\frac{s_i T_0}{k_n \left(T_0 - j\right)}, \qquad a_i = b_i e^{j k_n \xi_i} . \tag{A.3.14}$$

In order to illustrate the above technique, let us go back to the example presented in section 8.2.3. Namely, we will consider the decomposition (8.33):

$$f\left(k_\rho\right) = f^\phi + q = \sum_{i=1}^{M} a_i e^{-j k_{z2} \xi_i} . \tag{A.3.15}$$

After performing the steps described in this Appendix, for a substrate thickness of 0.795 mm, permittivity $\varepsilon_r = 2.35$ and a frequency of 7 GHz we find the coefficients as given in Table A.3.1.

Table A.3.1. Complex image coefficients of decomposition $f^{\phi}+q$ for the case of Fig. A.3.2 with $M = 4$, $T_0 = 15$, $N = 50$.

i	b_i	s_i	a_i	ξ_i
1	0.00038453 + j0.00004919	−2.12678339 + j3.1062148	−0.01189697 − j0.00101645	0.015839671 − j0.0201192
2	0.10023884 + j0.18491748	−0.29901025 + j0.1136908	0.043951832 + j0.2266961	0.002080789 − j0.0006363
3	−0.69499190 − j0.02595681	−0.22956824 + j0.0003331	−0.661106142 − j0.1800556	0.001558204 + j0.0001016
4	−0.00626253 − j0.05672312	−0.35315219 − j0.15973994	0.010887732 − j0.0462860	0.002324528 + j0.0012439

To illustrate the approximation process, the magnitude and phase plots of $f = f^{\phi} + q$ along the DCIM path are shown in Fig. A.3.2 (solid lines). Their complex image approximations are shown using dashed lines.

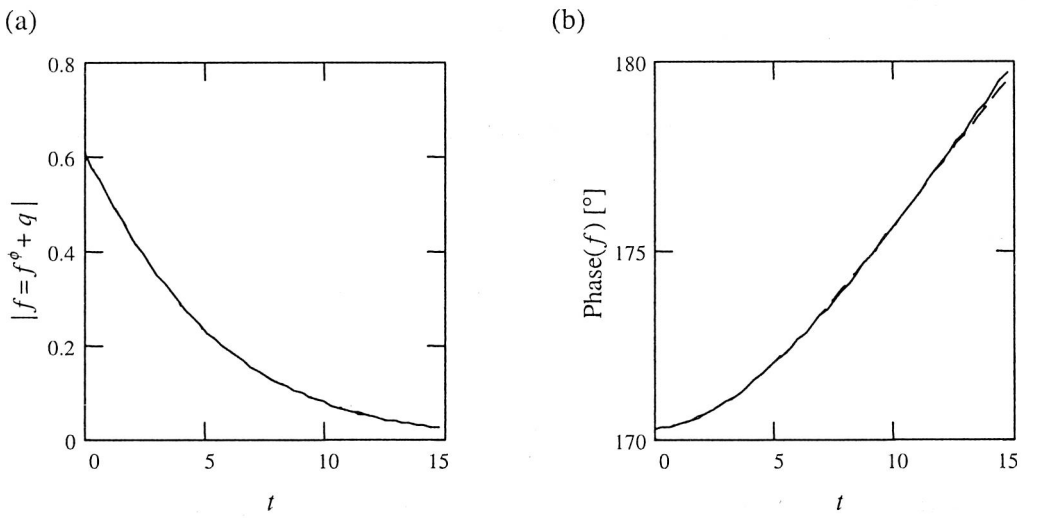

Fig. A.3.2. Magnitude (a) and phase (b) plots of $f = f^{\phi} + q$ (solid lines) and the complex image approximation (dashed lines) along the DCIM path for the case of $d = 0.795$ mm, $\varepsilon_r = 2.35$, and a frequency of 7 GHz

Note that the accuracy of the approximation depends on the choice of T_0, N and M. In particular, T_0 should be selected so that the paths in Fig. A.3.1 do not pass too close to the surface wave poles which $f(k_p)$ may possess (indicted by '×' in the figure).

References

[1] Abdelmageed A.K., Michalski K.A., Analysis of EM scattering by conducting bodies of revolution in layered media using the discrete complex image method, *Proc. of IEEE Antennas and Propagation Society Int. Symp. 1995*, Vol. 1, pp. 402–405, 1995.

[2] Aksun M.I., Mittra R., Derivation of closed-form Green's functions for a general microstrip geometry, *IEEE Trans. Microwave Theory Tech.*, Vol. MTT-40, pp. 2055–2062, Nov. 1992.

[3] Al-Badwaihy K.A., Yen J.L., Extended boundary condition integral equations for perfectly conducting and dielectric bodies, *IEEE Trans. Antennas Propagat.*, AP-23, pp. 546–551, July 1975.

[4] Albertsen N.C., Hansen J.E., Jensen N.E., Computation of radiation from wire antennas on conducting bodies, *IEEE Trans. Antennas Propagat.*, AP-22, pp. 200–206, Mar. 1974.

[5] Anastassiu H.T., Volakis J.L., Filipovic D.S., Integral equation modeling of cylindrically periodic scatterers in the interior of a cylindrical waveguide, *IEEE Trans. Microwave Theory Tech.*, MTT-46, pp. 1713–1720, Nov. 1998.

[6] Andreasen M.G., Scattering from bodies of revolution, *IEEE Trans. Antennas Propagat.*, AP-13, pp. 303–310, Mar. 1965.

[7] Antar Y.M.M., Kishk A.A., Shafai L., Allan L.E., Radar backscattering from partially coated targets with axial symmetry, *IEEE Trans. Antennas Propagat.*, AP-37, pp. 564–575, May 1989.

[8] Barber P.W., Owen J.F., Chang R.K., Resonant scattering for characterization of axisymmetric dielectric objects, *IEEE Trans. Antennas Propagat.*, AP-30, pp. 168–172, Mar. 1982.

[9] Bertotto P., Cerri G., Russo P., Schiavoni A., Tribellini G., A MOM/FDTD hybrid method for the evaluation of the EM fields in penetrable objects, *13th International Zurich Symposium and Technical Exhibition on Electromagnetic Compatibility*, pp. 67–70, Zurich, Switzerland, 1999.

[10] Bilotti F., Toscano A., Vegni L., Full wave analysis of circular patch antennas with inhomogeneous substrate, *Proceedings of the International Conference on Electromagnetics in Advanced Applications*, Torino, Italy, pp. 281–284, Sept. 1999.

[11] Bleszynski E., Bleszynski M., Jaroszewicz T., AIM: adaptive integral method for solving large-scale electromagnetic scattering and radiation problems, *Radio Science*, Vol. 31, pp. 1225–1251, Sept.–Oct. 1996.

[12] Booton R.C., *Computational methods for electromagnetics and microwaves*, John Wiley & Sons, Inc., New York, Chichester, Brisbane, Toronto, Singapore, 1992.

[13] Boyse W.E., Seidl A.A., A hybrid finite element method for near bodies of revolution, *IEEE Trans. Magn.*, Vol. 27, pp. 3833–3836, Sept. 1991.

[14] Bretones A.R., Monorchio A., Manara G., Gomez Martin R., Mittra R., Hybrid technique combining finite element, finite difference and integral equation methods in time domain, *Electronics Letters*, Vol. 36, pp. 506–508, 16 March 2000.

[15] Brown W.J., Wilton D.R., EFIE and MFIE formulation for surfaces with curved triangular elements, *Proceedings of the International Conference on Electromagnetics in Advanced Applications*, Torino, Italy, pp. 325–328, Sept. 1995.

[16] Brown W.J., Wilton D.R., Singular basis function and curvilinear triangles in the solution of the electric field integral equation, *IEEE Trans. Antennas Propagat.*, AP-47, pp. 347–353, Feb. 1999.

[17] Burke G.J., Poggio A.J., Numerical electromagnetics code (NEC) – method of moments, Naval Ocean Systems Center, Tech. Doc. 116, AFWL-TR-76-320, July 1977.

[18] Canning F.X., Improved impedance matrix localization method (EM problems), *IEEE Trans. Antennas Propagat.*, AP-41, pp. 659–667, May 1993.

[19] Carvalho S.A., Mendes L.S., Scattering of EM waves by inhomogeneous dielectric with the use of the method of moments and 3-D solenoidal basis functions, *Microwave and Optical Technology Letters*, Vol. 23, pp. 42–46, 1999.

[20] Catedra M.F., Analysis of bodies of revolution composed of conductors and dielectrics using only electric equivalent currents: application to small horns with dielectric core, *IEEE Trans. Antennas Propagat.*, AP-36, pp. 1311–1317, Sept. 1988.

[21] Champagne N.J., Williams J.T., Wilton D.R., The use of curved segments for numerically modeling thin wire antennas and scatterers, *IEEE Trans. Antennas Propagat.*, AP-40, pp. 682–689, June 1992.

[22] Chang Y., Harrington R.F., A surface formulation for characteristic modes of material bodies, *IEEE Trans. Antennas Propagat.*, AP-25, pp. 789–795, Nov. 1977.

[23] Chen J., Kishk A.A., Glisson A.W., A 3D interpolation model for the calculation of the Sommerfeld integrals to analyze dielectric resonators in a multilayered medium, *Electromagnetics*, Vol. 20, pp. 1–15, Jan.-Feb. 2000.

[24] Chen K., A mathematical formulation of the equivalence principle, *IEEE Trans. Microwave Theory Techn.*, Vol. 37, pp. 1576–1581, Oct. 1989.

[25] Chen K.M., Guru B.S., Induced EM fields inside human bodies irradiated by EM waves of up to 500 MHz, *Journal of Microwave Power*, Vol. 12, pp. 173–183, 1977.

[26] Cheng N.C., Su H.C., Wong K.L., Leung K.W., Analysis of a broadband slot-coupled dielectric-coated hemispherical dielectric resonator antenna, *Microwave and Optical Technology Letters*, Vol. 8, pp. 13–16, 1995.

[27] Chew W.C., A quick way to approximate a Sommerfeld–Weyl-type integral, *IEEE Trans. Antennas Propagat.*, AP-36, pp. 1654–1657, Nov. 1988.

[28] Chew W.C., Habashy T., The use of vector transforms in solving some electromagnetic scattering problems, *IEEE Trans. Antennas Propagat.*, AP-34, pp. 871–879, July 1986.

[29] Chow Y.L., Yang J.J., Fang D.G., Howard G.E., A closed-form spatial Green's function for the thick microstrip substrate, *IEEE Trans. Antennas Propagat.*, AP-39, pp. 588–592, Mar. 1991.

[30] Cwik T., Zuffada C., Jamnejad V., Modeling three-dimensional scatterers using a coupled finite element – integral equation formulation, *IEEE Trans. Antennas Propagat.*, AP-44, pp. 453–459, April 1996.

[31] De Moerloose J., De Zutter D., Surface integral representation radiation boundary condition for the FDTD method, *IEEE Trans. Antennas Propagat.*, AP-41, pp. 890–896, July 1993.

[32] De Smedt R., Correction due to a finite permittivity for a ring resonator in free space, *IEEE Trans. Microwave Theory Tech.*, MTT-32, pp. 1288–1293, Oct. 1984.

[33] Donepudi K.C., Gang K., Song J.M., Jin J.M., Chew W.C., Higher-order MoM implementation to solve integral equations, *Proc. of IEEE Antennas and Propagation Society Int. Symp. 1999*, Vol. 3, pp. 1716–1719, 1999.

[34] Douglas M., Okoniewski M., Stuchly M.A., Accurate modeling of thin-wire antennas in the FDTD method, *Microwave and Optical Technology Letters*, Vol. 21, pp. 261–265, 20 May 1999.

[35] Dudley D.G., Error minimization and convergence in numerical methods, *Electromagnetics*, Vol. 5, pp. 89–97, 1985.

[36] Eibert T.F., Hansen V., 3-D FEM/BEM-hybrid approach based on a general formulation of Huygens' principle for planar layered media, *IEEE Trans. Microwave Theory Tech.*, MTT-45, pp. 1105–1112, July 1997.

[37] Fan Z., Antar Y.M.M., Ittipiboon A., Petosa A., Parasitic coplanar three-element dielectric resonator antenna subarray, *Electronic Letters*, Vol. 32, pp. 789–790, Apr. 1996.

[38] Fang J., Ren J., A locally conformed finite-difference time-domain algorithm of modeling arbitrary shape planar metal strips, *IEEE Trans. Microwave Theory Techn.*, Vol. 41, pp. 830–838, May 1993.

[39] Felsen L.B., Marcuvitz N., *Radiation and Scattering of Waves*, Englewood Cilffs, N.J.: Prentice Hall, 1973.

[40] Geng N., Carin L., Wide-band electromagnetic scattering from a dielectric BOR buried in a layered lossy dispersive medium, *IEEE Trans. Antennas Propagat.*, AP-47, pp. 610–619, Apr. 1999.

[41] Geng N., Jackson D.R., Carin L., On the resonances of a dielectric BOR buried in a dispersive layered medium, *IEEE Trans. Antennas Propagat.*, AP-47, pp. 1305–1313, Aug. 1999.

[42] Glisson A.W., Wilton D.R., Simple and efficient numerical methods for problems of electromagnetic radiation and scattering from surfaces, *IEEE Trans. Antennas Propagat.*, AP-28, pp. 593–603, Sept. 1980.

[43] Glisson A.W., An integral equation for electromagnetic scattering from homogeneous dielectric bodies, *IEEE Trans. Antennas Propagat.*, AP-32, pp. 173–175, Feb. 1984.

[44] Glisson A.W., Kajfez D., James J., Evaluation of modes in dielectric resonators using surface integral equation formulation, *IEEE Trans. Microwave Theory Tech.*, MTT-31, pp. 1023–1029, Dec. 1983.

[45] Golik W.L., Wavelet packets for fast solution of electromagnetic integral equations, *IEEE Trans. Antennas Propagat.*, AP-46, pp. 618–624, May 1998.

[46] Golik W.L., Sparsity and conditioning of impedance matrices obtained with semi-orthogonal and bi-orthogonal wavelet bases, *IEEE Trans. Antennas Propagat.*, AP-48, pp. 473–481, Apr. 2000.

[47] Gong Z., Glisson A.W., A hybrid equation approach for the solution of electromagnetic scattering problems involving two-dimensional inhomogeneous dielectric cylinders, *IEEE Trans. Antennas Propagat.*, AP-38, pp. 60–68, Jan. 1990.

[48] Govind S., Wilton D.R., Glisson A.W., Scattering from inhomogeneous penetrable bodies of revolution, *IEEE Trans. Antennas Propagat.*, AP-32, pp. 1163–1173, Nov. 1984.

[49] Graglia R.D., On the numerical integration of the linear shape functions times the 3-D Green's function or its gradient on a plane triangle, *IEEE Trans. Antennas Propagat.*, AP-41, pp. 1448–1455, Oct. 1993.

[50] Graglia R.D., Wilton D.R., Peterson A.F., Higher order interpolatory vector bases for computational electromagnetics, *IEEE Trans. Antennas Propagat.*, AP-45, pp. 329–342, Mar. 1997.

[51] Graglia R.D., Wilton D.R., Peterson A.F., Gheorma I.-L., Higher order interpolatory vector bases on prism elements, *IEEE Trans. Antennas Propagat.*, AP-46, pp. 442–450, Mar. 1998.

[52] Guan J.-M., Su C.-C., Precise computations of resonant frequencies and quality factors for dielectric resonators in MIC's with tuning elements, *IEEE Trans. Microwave Theory Tech.*, MTT-45, pp. 439–442, Mar. 1997.

[53] Gwarek W.K., Analysis of an arbitrarily-shaped planar circuit – a time-domain approach, *IEEE Trans. Microwave Theory Tech.*, MTT-33, pp. 1067–1072, Oct. 1985.

[54] Hagmann M.J., Gandhi O.P., Numerical calculation of electromagnetic energy deposition in models of man with grounding and reflector effects, *Radio Science*, Vol. 14, pp. 23–29, 1979.

[55] Hagmann M.J., Ghandhi O.P., Durney C.H., Numerical calculation of electromagnetic energy deposition for a realistic model of man, *IEEE Trans. Microwave Theory Tech.*, MTT-27, pp. 804–809, Sept. 1979.

[56] Hajny M., Mazanek M., Fišer O., Bi-static scattering function – radiation pattern calculation, COST 255 Meeting, 27 May 1998, CP51A09.

[57] Hansen R.C. (ed.), *Moment Methods in Antennas and Scattering*, Artech House, 1990.

[58] Harrington R.F., Matrix methods for field problems, *Proc. IEEE*, Vol. 55, pp. 136–149, Feb. 1967.

[59] Harrington R.F., Origin and development of the method of moments for field computations, Chapter 1 [in:] *Applications of the Method of Moments to Electromagnetic Fields*, B.J. Strait (ed.), SCEEE Press, 1980.

[60] Harrington R.F., Boundary integral formulations for homogeneous material bodies, *Journal of Electromagnetic Waves and Applications*, Vol. 3, No. 1, pp. 1–15, 1989.

[61] Harrington R.F., *Field Computation by Moment Methods*, New York: Macmillan, 1968.

[62] Harrington R.F., *Time-harmonic electromagnetic fields*, McGraw-Hill Book Company, 1961.

[63] Harrington R.F., Mautz J.R., Chang Y., Characteristic modes for dielectric and magnetic bodies, *IEEE Trans. Antennas Propagat.*, AP-20, pp. 194–198, Mar. 1972.

[64] Hodges R.E., Rahmat-Samii Y., The evaluation of MFIE integrals using vector triangle basis function, *Microwave and Optical Techn. Letters*, Vol. 14, pp. 9–14, Jan. 1997.

[65] Holland R., Simpson L., Kunz K.S., Finite-difference analysis of EMP coupling to lossy dielectric structures, *IEEE Trans. Electromagn. Compat.*, EMC-22, pp. 203–209, Aug. 1980.

[66] Hoppe D.J., Epp L.W., Lee J-F., A hybrid symmetric FEM/MOM formulation applied to scattering by inhomogeneous bodies of revolution, *IEEE Trans. Antennas Propagat.*, AP-42, pp. 798–805, June 1994.

[67] Hua Y., Sarkar T.K., Generalized pencil-of-function method for extracting poles of an EM system from its transient response, *IEEE Trans. Antennas Propagat.*, AP-37, pp. 229–234, Feb. 1989.

[68] Hubbing T.H., Survey of numerical electromagnetic modeling techniques, Report TR91-1-001.3, University of Missouri-Rolla, 1991.

[69] Huddleston P.L., Scattering from conducting finite cylinders with thin coatings, *IEEE Trans. Antennas Propagat.*, AP-35, pp. 1128–1136, Oct. 1987.

[70] Hurst M.P., Medgyesi-Mitschang L.N., Scattering from partial bodies of revolution, *IEEE Trans. Antennas Propagat.*, AP-38, pp. 69–75, Jan. 1990.

[71] Ishimaru A., *Electromagnetic Wave Propagation, Radiation, and Scattering*, Englewood Cliffs, N.J.: Prentice-Hall, 1991.

[72] Itoh T., Rudokas R.S., New method for computing the resonant frequencies of dielectric resonators, *IEEE Trans. Microwave Theory Tech.*, MTT-25, pp. 52–54, Jan. 1977.

[73] Jaworski M., Pospieszalski M.W., An accurate solution of the cylindrical dielectric resonator problem, *IEEE Trans. Microwave Theory Tech.*, MTT-27, pp. 639–643, July 1979.

[74] Jiangqi He, Tiejun Yu, Geng N., Carin L., Method of moments analysis of electromagnetic scattering from a general three-dimensional dielectric target embedded in a multilayered medium, *Radio Science*, Vol. 35, pp. 305–313, Mar.–Apr. 2000.

[75] Jones D.S., *Methods in Electromagnetic Wave Propagation*, New York, IEEE Press, 2nd ed., 1995.

[76] Johnson W.A., Dudley D.G., Real axis integration of Sommerfeld integrals: Source and observation points in air, [in:] *Moment Methods in Antennas and Scatterers*, R.C. Hansen (ed.), pp. 313–324, Boston: Artech House, 1990.

[77] Junker G.P., Glisson A.W., Kishk A.A., Input impedance of dielectric resonator antennas top loaded with high permittivity and conducting disks, *Microwave and Optical Techn. Letters*, Vol. 9, pp. 204–207, July 1995.

[78] Junker G.P., Kishk A.A., Glisson A.W., Input impedance of dielectric resonator antennas excited by a coaxial probe, *IEEE Trans. Antennas Propagat.*, AP-42, pp. 960–966, July 1994.
[79] Junker G.P., Kishk A.A., Glisson A.W., Input impedance of aperture-coupled dielectric resonator antennas, *IEEE Trans. Antennas Propagat.*, AP-44, pp. 600–607, May 1996.
[80] Junker G.P., Kishk A.A., Glisson A.W., Numerical analysis of dielectric resonator antennas in quasi-TE modes, *Electronics Letters*, Vol. 29, pp. 1810–1811, Oct. 1993.
[81] Junker G.P., Kishk A.A., Glisson A.W., Two port analysis of dielectric resonator antennas excited in TE_{01} mode, *Electronics Letters*, Vol. 32, pp. 617–618, Mar. 1996.
[82] Kajfez, D., Dual Resonance, *IEE Proceedings, Part H*, Vol. 135 (2), pp. 141–144, 1988.
[83] Kajfez D., Guillon P. (eds.), *Dielectric resonators*, Artech House, Dedham, MA, 1986.
[84] Kajfez D., Glisson A.W., James J., Computed modal field distributions for isolated dielectric resonators, *IEEE Trans. Microwave Theory Tech.*, MTT-32, pp. 1609–1616, Dec. 1984.
[85] Karwowski A., *Analysis of thin-wire radiating and scattering structures*, PWr, Wrocław, 1984 (in Polish).
[86] Kim H., Ling H., Wavelet analysis of radar echo from finite-size targets, *IEEE Trans. Antennas Propagat.*, AP-41, pp. 200–207, Feb. 1993.
[87] Kipp R.A., Chan C.H., Complex image method for sources in bounded regions of multilayer structures, *IEEE Trans. Microwave Theory Tech.*, MTT-42, pp. 860–865, May 1994.
[88] Kishk A.A., Elsherbeni A.Z., Radiation characteristics of dielectric resonator antennas loaded with a beam-forming ring, *Arch. Elek. Übertragung.*, Vol. 43, pp. 158–165, Mar. 1989.
[89] Kishk A.A., Shafai L., Improvement of the numerical solution of dielectric bodies with high permittivity, *IEEE Trans. Antennas Propagat.*, Vol. AP-37, pp. 1486–1490, Nov. 1989.
[90] Kishk A.A., Shafai L., Radiation characteristics of the short dielectric rod antenna: a numerical solution, *IEEE Trans. Antennas Propagat.*, AP-35, pp. 139–146, Feb. 1987.
[91] Kishk A.A., Ahn B., Kajfez D., Broadband stacked dielectric resonator antennas, *Electronic Letters*, Vol. 25, pp. 1232–1233, Aug. 1989.
[92] Kishk A.A., Ittipiboon A., Antar Y.M.M., Cuhaci M., Slot excitation of the dielectric disk radiator, *IEEE Trans. Antennas Propagat.*, AP-43, pp. 198–200, Feb. 1995.
[93] Kishk A.A., Zanoubi M.R., Kajfez D., A numerical study of a dielectric disk antenna above grounded dielectric substrate, *IEEE Trans. Antennas Propagat.*, AP-41, pp. 813–821, June 1993.
[94] Klees R., Numerical calculation of weakly singular surface integrals, *Journal of Geodesy*, Vol. 70, pp. 781–797, 1996.
[95] Knepp D.L., Goldhirsh J., Numerical analysis of electromagnetic radiation properties of smooth conducting bodies of arbitrary shape, *IEEE Trans. Antennas Propagat.*, AP-20, pp. 383–388, May 1972.
[96] Kottmann J.P., Martin O.J.F., Accurate solution of the volume integral equation for high-permittivity scatterers, *IEEE Trans. Antennas Propagat.*, AP-48, pp. 1719–1726, Nov. 2000.
[97] Krupka J., Derzakowski K., Abramowicz A., Computations of 3D electromagnetic field distributions in axially symmetric multilateral dielectric resonators by means of Galerkin–Rayleigh–Ritz method, *12th International Conference on Microwaves and Radar*, MIKON-98, Kraków (Poland), May 1998, pp. 491–495.
[98] Kucharski A.A., A body-of-revolution model for calculating electromagnetic fields excited inside human head, *Proc. of 14th International Wrocław Symposium and Exhibition on EMC*, June 23–25, 1998, pp. 286–290.
[99] Kucharski A.A., A method of moments solution of scattering by hydrometeors in resonance frequency region, *Proc. of Internat. Symposium on EMC. EMC '98 ROMA*, Rome, Italy, Sept. 14–18, 1998, pp. 375–379.

[100] Kucharski A.A., Resonances in inhomogeneous dielectric bodies of revolution placed in the multilayered media – TE modes, *Microwave and Optical Techn. Letters*, Vol. 21, pp. 1–4, Apr. 1999.

[101] Kucharski A.A., Resonances in inhomogeneous dielectric bodies of revolution placed in the multilayered media – HEM modes, *Microwave and Optical Techn. Letters*, Vol. 23, pp. 87–92, Oct. 1999.

[102] Kucharski A.A., Modeling of cylindrical dielectric antennas in a multilayer environment, *Proc. of the International Conference on Electromagnetics in Advanced Applications*, Torino, Italy, pp. 285–288, Sept. 1999.

[103] Kucharski A.A., Resonances in inhomogeneous dielectric bodies of revolution placed in the multilayered media – TM modes, *Microwave and Optical Techn. Letters*, Vol. 25, pp. 65–69, April 2000.

[104] Kucharski A.A., Resonances in Heterogeneous Dielectric Bodies with Rotational Symmetry – Volume Integral-Equation Formulation, *IEEE Trans. Microwave Theory Tech.*, MTT-48, pp. 766–770, May 2000.

[105] Kucharski A.A., A method of moments solution for electromagnetic scattering by inhomogeneous dielectric bodies of revolution, *IEEE Trans. Antennas Propagat.*, AP-48, pp. 1202–1210, Aug. 2000.

[106] Kucharski A.A., Cylindrical dielectric resonators in antenna applications – analysis using integral equations, accepted for publication in *Electronics and Telecommunications Quarterly*, (in Polish).

[107] Kucharski A.A., Electromagnetic scattering by inhomogeneous dielectric bodies of revolution embedded within stratified media, accepted for publication in *IEEE Trans. Antennas Propagat.*

[108] Kucharski A.A., Skrzypczyński J., Scattering by hydrometeors in resonance frequency region, *First Internat. Workshop on Radiowave Propagation Modelling for SatCom Services at Ku-band and above*, COST 255, European Space Agency, Nordwijk, Netherlands, 28–29 Oct. 1998, pp. 175–179.

[109] Leung K.W., Luk K.M., Chow K.Y., Yung E.K.N., Bandwidth enhancement of dielectric resonator antenna by loading a low-profile dielectric disk of very high permittivity, *Electronic Letters*, Vol. 33, pp. 725–726, Apr. 1997.

[110] Leviatan Y., Boag A., Analysis of electromagnetic scattering from dielectric cylinders using a multifilament current model, *IEEE Trans. Antennas Propagat.*, AP-35, pp. 1119–1136, Oct. 1987.

[111] Leviatan Y., Boag A., Boag A., Generalized formulations for electromagnetic scattering from perfectly conducting and homogeneous material bodies – theory and numerical solution, *IEEE Trans. Antennas Propagat.*, AP-36, pp. 1722–1734, Dec. 1988.

[112] Li Z., Wu C., Litva J., Adjustable frequency dielectric resonator antenna, *Electronic Letters*, Vol. 32, pp. 606–607, Mar. 1996.

[113] Li H.-B., Han G.-M., Mang H.A., A new method for evaluating singular integrals in stress analysis of solids by the direct boundary element method, *Internat. Journal for Numerical Methods in Engineering*, Vol. 21, pp. 2071–2098, 1985.

[114] Lindell I.V., *Methods for Electromagnetic Field Analysis*, New York, Oxford University Press, 1992.

[115] Ling F., Jin J.-M., Discrete complex image method for Green's functions of general multilayer media, *IEEE Microwave and Guided Wave Letters*, Vol. 10, pp. 400–402, Oct. 2000.

[116] Livesay D.E., Chen K-M., Electromagnetic fields induced inside arbitrarily shaped biological bodies, *IEEE Trans. Microwave Theory Tech.*, MTT-22, pp. 1273–1280, Dec. 1974.

[117] Long S.A., McAllister M.W., Shen L.C., The resonant cylindrical dielectric cavity antenna, *IEEE Trans. Antennas Propagat.*, AP-31, pp. 406–412, May 1983.

[118] Lu C.-C., Chew W.C., A multilevel algorithm for solving a boundary integral equation of wave scattering, *Microwave and Optical Techn. Letters*, Vol. 7, pp. 466–470, July 1994.

[119] Luk K.M., Leung K.W., Chow K.Y., Bandwidth and gain enhancement of a dielectric resonator antenna using a stacking element, *Microwave and Optical Techn. Letters*, Vol. 14, pp. 215–217, Mar. 1997.

[120] Maj Sz., Modelski J.W., Application of a dielectric resonator on microstrip line for a measurement of complex permittivity, *IEEE MTT-S Int. Microwave Symmp. Dig.*, San Francisco, CA, pp. 525–527, May 1984.

[121] Marx E., Integral equation for scattering by a dielectric, *IEEE Trans. Antennas Propagat.*, AP-32, pp. 166–172, Feb. 1984.

[122] Mautz J.R., Harrington R.F., A combined-source solution for radiation and scattering from a perfectly conducting body, *IEEE Trans. Antennas Propagat.*, AP-27, pp. 445–454, July 1979.

[123] Mautz J.R., Harrington R.F., Electromagnetic scattering from a homogeneous material body of revolution, *Arch. Elek. Übertragung.*, Vol. 33, pp. 71–80, Feb. 1979.

[124] Mautz J.R., Harrington R.F., H-field, E-field and combined-field solutions for conducting bodies of revolution, *Arch. Elek. Übertragung.*, Vol. 32, pp. 159–164, Apr. 1978.

[125] Mautz J.R., Harrington R.F., Radiation and scattering from bodies of revolution, *Appl. Sci. Res.*, Vol. 20, pp. 405–435, June 1969.

[126] Mautz J.R., A stable integral equation for electromagnetic scattering from homogeneous dielectric bodies, *IEEE Trans. Antennas Propagat.*, AP-37, pp. 1070–1071, Aug. 1989.

[127] McAllister M.W., Long S.A., Resonant hemispherical dielectric antenna, *Electronic Letters*, Vol. 20, pp. 657–659, Aug. 1984.

[128] Medgyesi-Mitschang L.N., Eftimiu C., Scattering from axisymmetric obstacles embedded in axisymmetric dielectrics: the method of moments solution, *Appl. Phys.*, Vol. 19, pp. 275–285, Feb. 1979.

[129] Medgyesi-Mitschang L.N., Putnam J.M., Electromagnetic scattering from electrically large coated flat and curved strips: entire domain Galerkin formulation, *IEEE Trans. Antennas Propagat.*, AP-35, pp. 790–801, July 1987.

[130] Medgyesi-Mitschang L.N., Putnam J.M., Electromagnetic scattering from axially inhomogeneous bodies of revolution, *IEEE Trans. Antennas Propagat.*, AP-32, pp. 797–806, Aug. 1984.

[131] Medgyesi-Mitschang L.N., Putnam J.M., Integral equation formulations for imperfectly conducting scatterers, *IEEE Trans. Antennas Propagat.*, AP-33, pp. 206–214, Feb. 1985.

[132] Michalski K.A., On the efficient evaluation of integrals arising in the Sommerfeld halfspace problem, [in:] *Moment Methods in Antennas and Scatterers*, R.C. Hansen (ed.), pp. 325–331, Boston: Artech House, 1990.

[133] Michalski K.A., On the scalar potential of a point charge associated with a time-harmonic dipole in a layered medium, *IEEE Trans. Antennas Propagat.*, AP-35, pp. 1299–1301, Nov. 1987.

[134] Michalski K.A., The mixed-potential electric field integral equation for objects in layered media, *Arch. Elek. Übertragung.*, Vol. 39, pp. 317–322, Sept.–Oct. 1985.

[135] Michalski K.A., Mixed-potential integral equation (MPIE) formulation for nonplanar microstrip structures of arbitrary shape in multilayered uniaxial media, *International Journal of Microwave and Millimeter-Wave Computer-Aided Engineering*, Vol. 3, pp. 420–431, 1993.

[136] Michalski K.A., Extrapolation methods for Sommerfeld integral tails, *IEEE Trans. Antennas Propagat.*, AP-46, pp. 1405–1418, Oct. 1998.

[137] Michalski K.A., Hsu C.-I.G., RCS computation of coax-loaded microstrip patch antennas of arbitrary shape, *Electromagnetics*, Vol. 14, pp. 33–62, 1994.

[138] Michalski K.A., Mosig J.R., Discrete complex image mixed-potential integral equation analysis of coax-fed coupled vertical monopoles in a grounded dielectric substrate: Two formulations, *Inst. Elect. Eng. Proc. Microwave Antennas Propagat.*, Vol. 142, pp. 269–274, June 1995.

[139] Michalski K.A., Mosig J.R., Discrete complex image mixed-potential integral equation analysis of microstrip patch antennas with vertical probe feeds, *Electromagnetics*, Vol. 15, pp. 377–392, July–Aug. 1995.

[140] Michalski K.A., Mosig J.R., Multilayered media Green's functions in integral equation formulations, *IEEE Trans. Antennas Propagat.*, AP-45, pp. 508–519, Mar. 1997.

[141] Michalski K.A., Zheng D., Electromagnetic scattering and radiation by surfaces of arbitrary shape in layered media, Parts I and II, *IEEE Trans. Antennas Propagat.*, AP-38, pp. 335–352, Mar. 1990.

[142] Michalski K.A., Zheng D., Integral equation analysis of arbitrarily shaped microstrip structures, unpublished draft, July 1990.

[143] Michalski K.A., Zheng D., Analysis of microstrip resonators of arbitrary shape, *IEEE Trans. Microwave Theory Tech.*, MTT-40, pp. 112–119, Jan. 1992.

[144] Michalski K.A., private communication.

[145] Mielewski J, Ćwikła A, Mrozowski M., Accelerated FD analysis of dielectric resonators, *IEEE Microwave Guided Wave Letters*, Vol. 8, pp. 375–377, Nov. 1998.

[146] Miller E.K., A selective survey of computational electromagnetics, *IEEE Trans. Antennas Propagat.*, AP-36, pp. 1281–1305, Sept. 1988.

[147] Miller E.K., Medgyesi-Mitschang L., Newman E.H. (eds.), *Computational Electromagnetics. Frequency-Domain Method of Moments*, IEEE Press, New York, 1992.

[148] Mitzner K.M., An integral equation approach to scattering from a body of finite conductivity, *Radio Science*, Vol. 2, pp. 1459–1470, 1967.

[149] Modelski J., Abramowicz A., *Rezonatory dielektryczne i ich zastosowanie*, (*Dielectric resonators and their applications*), PWN, Warszawa, 1990, (in Polish).

[150] Mongia R.K., Resonant frequency of cylindrical dielectric resonator placed in an MIC environment, *IEEE Trans. Microwave Theory Tech.*, MTT-38, pp. 802–804, June 1990.

[151] Morgan M.A., Mei K.K., Finite element computation of scattering by inhomogeneous penetrable bodies of revolution, *IEEE Trans. Antennas Propagat.*, AP-27, pp. 202–214, Mar. 1979.

[152] Morgan M.A., Chang S.K., Mei K.K., Coupled azimuthal potentials for electromagnetic field problems in inhomogeneous axially-symmetric media, *IEEE Trans. Antennas Propagat.*, AP-25, p. 413, 1977.

[153] Morita N., Surface integral representation for electromagnetic scattering from dielectric cylinders, *IEEE Trans. Antennas Propagat.*, AP-26, pp. 261–266, 1978.

[154] Morita, N., Kumagai N., Mautz J.R., *Integral equation methods for electromagnetics*, Boston: Artech House, 1990.

[155] Mosig J.R., Integral equation technique, Chapter 3 [in:] *Numerical techniques for microwave and millimeter-wave passive structures*, T. Itoh (ed.), John Wiley & Sons, 1989.

[156] Müller C., *Foundations of the Mathematical Theory of Electromagnetic Waves*, New York, Springer Verlag, 1969.

[157] Naylor P., Christopoulos C., A comparison between the time-domain and the frequency-domain diakoptic methods of solving field problems by transmission-line modelling, *International Journal of Numerical Modelling – Electronic Networks Devices & Fields*, Vol. 2, pp. 17–30, Mar. 1989.

[158] Naylor P., Christopoulos C., A new wire node for modeling thin wires in electromagnetic field problems solved by transmission line modeling, *IEEE Trans. Microwave Theory Techn.*, Vol. 38, pp. 328–330, Mar. 1990.

[159] Newman E.H., Forrai D., Scattering from a microstrip patch, *IEEE Trans. Antennas Propagat.*, AP-35, pp. 245–251, Mar. 1987.

[160] Newman E.H., Pozar D.M., Electromagnetic modeling of composite wire and surface geometries, *IEEE Trans. Antennas Propagat.*, AP-26, pp. 784–789, Nov. 1978.

[161] Newman E.H., Pozar D.M., Considerations for efficient wire/surface modeling, *IEEE Trans. Antennas Propagat.*, AP-28, pp. 121–125, Jan. 1980.
[162] Newman E.H., Tulyathan P., A surface patch model for polygonal plates, *IEEE Trans. Antennas Propagat.*, AP-30, pp. 588–593, July 1982.
[163] Oguchi T., Electromagnetic wave propagation and scattering in rain and other hydrometeors, *Proceedings of the IEEE*, Vol. 71, pp. 1029–1078, Sept. 1983.
[164] Okoniewski M, Stuchly M.A., A study of the handset antenna and human body interaction, *IEEE Trans. Microwave Theory Techn.*, Vol. 44, pp. 1855–1864, Oct. 1996.
[165] Peterson A.F., Ray S.L., Mittra R., *Computational Methods for Electromagnetics*, New York, IEEE Press, 1998.
[166] Poggio A.J., Miller E.K., Integral equation solutions of three-dimensional scattering problems, [in:] *Computer Techniques for Electromagnetics*, R. Mittra (ed.), Oxford, England, Pergamon, 1973, ch. 4.
[167] Przybyszewski P., Mrozowski M., A conductive wedge in Yee's mesh, *IEEE Microwave Guided Wave Letters*, Vol. 8, pp. 66–68, Feb. 1998.
[168] Rao S.M., Wilton D.R., Glisson A.W., Electromagnetic scattering by surfaces of arbitrary shape, *IEEE Trans. Antennas Propagat.*, AP-30, pp. 409–418, May 1982.
[169] Richmond J.H., Newman E.H., Dielectric coated wire antennas, *Radio Science*, Vol. 11, pp. 13–20, 1976.
[170] Richmond J.H., A wire-grid model for scattering by conducting bodies, *IEEE Trans. Antennas Propagat.*, AP-14, pp. 787–786, Nov. 1966.
[171] Richmond J.H., Digital computer solutions of the rigorous equations for scattering problems, *Proc. IEEE*, Vol. 53, pp. 796–804, Aug. 1965.
[172] Richmond J.H., Scattering by a dielectric cylinder of arbitrary cross section shape, *IEEE Trans. Antennas Propagat.*, AP-13, pp. 334–341, May 1965.
[173] Rumsey V.H., Reaction concept in electromagnetic theory, *The Physical Review*, Vol. 94, pp. 1483–1491, 1954.
[174] Sachse K., *Analysis and properties of transmission lines and waveguides with multilayered dielectric and semiconductor media*, PWr, Wrocław, 1991, (in Polish).
[175] Sarkar T.K., Arvas E., An integral equation approach to the analysis of finite microstrip antennas: volume/surface formulation, *IEEE Trans. Antennas Propagat.*, AP-38, pp. 305–312, Mar. 1990.
[176] Sarkar T.K., Arvas E., Ponnapoli S., Electromagnetic scattering from dielectric bodies, *IEEE Trans. Antennas Propagat.*, AP-37, pp. 673–676, May 1989.
[177] Sarkar T.K., Pereira O., Using the matrix pencil method to estimate the parameters of a sum of complex exponentials, *IEEE Antennas Propagat. Magazine*, Vol. AP-37, pp. 48–55, Feb. 1995.
[178] Schaubert D.H., Wilton D.R., Glisson A.W., A tetrahedral modeling method for electromagnetic scattering by arbitrarily shaped inhomogeneous dielectric bodies, *IEEE Trans. Antennas Propagat.*, AP-32, pp. 77–85, Jan. 1984.
[179] Shaeffer J.F., EM scattering from bodies of revolution with attached wires, *IEEE Trans. Antennas Propagat.*, AP-30, pp. 426–431, May 1982.
[180] Shum S.M., Luk K.M., Characteristics of a dielectric ring antenna with an air gap, *Electronics Letters*, Vol. 30, pp. 277–278, 1994.
[181] Singer H., Brüns H.-D., Kimmel M., Field analysis of EMC problems by an integral equation method – new features for SE computation, *Proc. of Workshop on Shielding Effectiveness*, Nov. 24–25, 1994, Budapest, Hungary, pp. 43–57.
[182] Singer H., Brüns H.-D., *CONCEPT II. User's manual*, Technical University of Hamburg–Harburg, Germany, 1996.

[183] Singh J., Adams A.T., A nonrectangular patch model for scattering from surfaces, *IEEE Trans. Antennas Propagat.*, AP-27, pp. 531–535, July 1979.
[184] Sivov A.N., Chuprin A.D., Synthesis of a resonant antenna enclosed in a dielectric, *Soviet Journal of Communications Technology & Electronics* (USA), Vol. 33, No. 4, pp. 1–6, Apr. 1988.
[185] Sommerfeld A., *Partial Differential Equations in Physics*, New York: Academic Press, 1949.
[186] Steinberg B.Z., Leviatan Y., On the use of wavelet expansions in the method of moments (EM scattering), *IEEE Trans. Antennas Propagat.*, AP-41, pp. 610–619, May 1993.
[187] St. Martin J.T.H., Antar Y.M.M., Kishk A.A., Ittipiboon A., Cuhaci M., Dielectric resonator antenna using aperture coupling, *Electronic Letters*, Vol. 26, pp. 2015–2016, Nov. 1990.
[188] Stratton J.A., *Electromagnetic theory*, McGraw-Hill, New York, 1941.
[189] Ström S., Zheng W., The null field approach to electromagnetic scattering from composite objects, *IEEE Trans. Antennas Propagat.*, AP-36, pp. 376–382, Mar. 1988.
[190] Su C.-C., Calculation of electromagnetic scattering from a dielectric cylinder using the conjugate gradient method and FFT, *IEEE Trans. Antennas Propagat.*, AP-35, pp. 1418–1425, Dec. 1987.
[191] Su C.-C., Electromagnetic scattering by a dielectric body with arbitrary inhomogeneity and anisotropy, *IEEE Trans. Antennas Propagat.*, AP-37, pp. 384–389, Mar. 1989.
[192] Taflove A., Brodwin M.E., Computation of the electromagnetic fields and induced temperatures within a model of the microwave-irradiated human eye, *IEEE Trans. Microwave Theory Tech.*, MTT-23, pp. 888–896, Nov. 1975.
[193] Tai C.-T., *Dyadic Green Functions in Electromagnetic Theory*, IEEE Press, New York, 1994.
[194] Tai C.-T., *Generalized Vector and Dyadic Analysis. Applied Mathematics in Field Theory*, IEEE Press, New York, 1997.
[195] Tsai C., Massoudi H., Durney C.H., Iskander M.F., A procedure for calculating fields inside arbitrarily shaped inhomogeneous dielectric bodies using linear basis function with the moment method, *IEEE Trans. Microwave Theory Tech.*, MTT-34, pp. 1131–1139, Nov. 1986.
[196] Tsuji M., Shigesawa H., Takiyama K., Analytical and experimental investigations on several resonant modes in open dielectric resonators, *IEEE Trans. Microwave Theory Tech.*, MTT-32, pp. 628–633, June 1984.
[197] Umashankar K., Taflove A., Rao S.M., Electromagnetic scattering by arbitrary shaped three-dimensional homogeneous lossy dielectric objects, *IEEE Trans. Antennas Propagat.*, AP-34, pp. 758–766, June 1986.
[198] Van Bladel J., Some remarks on Green's dyadic for infinite space, *IRE Trans. Antennas Propagat.*, pp. 563–566, Nov. 1961.
[199] Van Bladel J., *Electromagnetic Fields*, New York: Hemisphere Publ. Corp., 1985.
[200] Viola M.S., A new electric field integral equation for heterogeneous dielectric bodies of revolution, *IEEE Trans. Microwave Theory Tech.*, MTT-43, pp. 230–232, Jan. 1995.
[201] Viola M.S., A new electric field integral equation for heterogeneous dielectric bodies of revolution embedded within a stratified medium, *IEEE Trans. Antennas Propagat.*, AP-43, pp. 1116–1122, Oct. 1995.
[202] Vitebsky S., Sturgess K., Carin L., Short-pulse plane-wave scattering from buried perfectly conducting bodies of revolution, *IEEE Trans. Antennas Propagat.*, AP-44, pp. 143–151, Feb. 1996.
[203] Volakis J., Alternative field representations and integral equations for modeling inhomogeneous dielectrics, *IEEE Trans. Microwave Theory Tech.*, MTT-40, pp. 604–608, Mar. 1992.
[204] Wagner R.L., Chew W.C., A study of wavelets for the solution of electromagnetic integral equations, *IEEE Trans. Antennas Propagat.*, AP-43, pp. 802–810, Aug. 1995.
[205] Wang J.J.H, Richmond J.H., Gilbreath M.C., Sinusoidal reaction formulation for radiation and scattering from conducting surfaces, *IEEE Trans. Antennas Propagat.*, AP-23, pp. 376–382, May 1975.

[206] Wang J.J.H., Analysis of a three-dimensional arbitrarily shaped dielectric or biological body inside a rectangular waveguide, *IEEE Trans. Microwave Theory Techn.*, MTT-26, pp. 457–462, July 1978.

[207] Wang J.J.H., Numerical analysis of three-dimensional arbitrarily-shaped conducting scatterers by trilateral surface cell modelling, *Radio Science*, Vol. 13, pp. 947–952, Nov.–Dec. 1978.

[208] Wang J.J.H., *Generalized moment methods in electromagnetics*, John Wiley & Sons, New York, Chichester, Brisbane, Toronto, Singapore, 1991.

[209] Wang J.J.H., Dubberley J.R., Computation of fields in an arbitrarily-shaped heterogeneous dielectric or biological body by an iterative conjugate gradient method, *IEEE Trans. Microwave Theory Tech.*, MTT-37, pp. 1119–1125, July 1989.

[210] Wang J.J.H., Papanicolopulos C., A study of the analysis and measurements of three-dimensional arbitrarily-shaped dielectric scatterers, Rome Air Development Center, Rep. RADC-TR-30-372, Dec. 1980.

[211] Wang N.N., Richmond J.H., Gilreath M.C., Sinusoidal reaction formulation for radiation and scattering from conducting surfaces, *IEEE Trans. Antennas Propagat.*, AP-23, pp. 376–382, May 1975.

[212] Wilton D.R., Computational methods, [in:] *Scattering*, P. Sabatier, E.R. Pike (eds.), Ch. 1.5.5, London, Academic Press, 2001.

[213] Wilton D.R., Butler C.M., Effective methods for solving integral and integro-differential equations, *Electromagnetics*, Vol. 1, pp. 289–308, 1981.

[214] Wilton D.R., Rao S.M., Glisson A.W., Schaubert D.H., Al.-Bundak O.M., Butler C.M., Potential integrals for uniform and linear source distributions on polygonal and polyhedral domains, *IEEE Trans. Antennas Propagat.*, AP-32, pp. 276–281, Mar. 1984.

[215] Wilton D.R., Sharpe R.M., Electromagnetic scattering and radiation by discrete bodies of revolution, Technical Report Number 87-15, Applied Electromagnetics Laboratory, University of Houston, 1987.

[216] Wong K.L., Chen N.C., Analysis of a broadband hemispherical antenna with dielectric coating, *Microwave and Optical Technology Letters*, Vol. 7, pp. 73–76, 1994.

[217] Wu T., Electromagnetic fields and power deposition in body-of-revolution models of man, *IEEE Trans. Microwave Theory Tech.*, MTT-27, pp. 279–283, Mar. 1979.

[218] Wu T.K., Tsai L.L., Scattering from arbitrarily-shaped lossy dielectric bodies of revolution, *Radio Sci.*, Vol. 12, pp. 709–718, Sept. 1977.

[219] Xu X.-B., Yan W., Scattering of TM excitation by inhomogeneous cylinders near a media interface – a hybrid integral equation approach, *Journal of Electromagnetic Waves and Applications*, Vol. 7, No. 4, pp. 599–625, 1993.

[220] Xu X.-B., Yan W., A hybrid integral equation solution of scattering of TE excitation by inhomogeneous cylinders near a medium interface, *Journal of Electromagnetic Waves and Applications*, Vol. 7, No. 7, pp. 919–942, 1993.

[221] Yaghjian A.D., Electric dyadic Green's functions in the source region, *Proc. IEEE*, Vol. 68, pp. 248–263, Feb. 1980.

[222] Yeung M.S., Single integral equation for electromagnetic scattering by three-dimensional homogeneous dielectric objects, *IEEE Trans. Antennas Propagat.*, AP-47, pp. 1615–1622, Oct. 1999.

[223] Yousefi M., Chaudhuri S.K., Safavi-Naeini S., GIBC formulation for the resonant frequencies and field distributions of a substrate-mounted dielectric resonator, *IEEE Trans. Microwave Theory Tech.*, MTT-42, pp. 38–46, Jan. 1994.

[224] Yuan X., Lynch D.R., Strohbehn J.W., Coupling of finite element and moment methods for electromagnetic scattering from inhomogeneous objects, *IEEE Trans. Antennas Propagat.*, AP-38, pp. 386–393, Mar. 1990.

[225] Zheng W., Computation of complex resonance frequencies of isolated composite objects, *IEEE Trans. Microwave Theory Tech.*, MTT-37, pp. 953–961, June 1989.

[226] Zhuck N.P., Yarovoy A.G., Two-dimensional scattering from an inhomogeneous dielectric cylinder embedded in a stratified medium: case of TM polarization, *IEEE Trans. Antennas Propagat.*, AP-42, pp. 16–21, Jan. 1994.

Rozpraszanie fal elektromagnetycznych przez obiekty dielektryczne

1. Wprowadzenie

Zagadnienie rozpraszania fal elektromagnetycznych przez obiekty dielektryczne jest przedmiotem zainteresowania badaczy niemal od początku rozwoju elektrodynamiki. Przełom w analizie tego typu problemów nastąpił wraz z rozwojem metod numerycznych, stymulowanym wykorzystaniem komputerów o coraz większej mocy obliczeniowej. Zwróćmy uwagę, że pod pojęciem „rozwiązania" zagadnienia z dziedziny elektromagnetyzmu powszechnie rozumie się znalezienie rozwiązania równań Maxwella dla zadanych warunków początkowych i brzegowych.

W pracy skoncentrowano się na rozważaniu funkcji harmonicznych (założono, że zależność wszystkich wielkości od czasu wyraża się funkcją $e^{j\omega t}$). Do analizy wybrano metodę równań całkowych, rozwiązywanych przy użyciu tzw. metody momentów. Przedmiotem rozważań jest rozpraszanie fal eiektromagnetycznych przez obiekty czysto dielektryczne, aczkolwiek rozszerzenie opisanych metod na konfiguracje obejmujące struktury przewodzące nie nastręcza zasadniczych problemów. Analizowane obiekty dielektryczne mogą być zbudowane z materiałów stratnych (o skończonej przewodności). Szczególną uwagę poświęcono możliwości modelowania obiektów niejednorodnych, znajdujących coraz szersze zastosowanie w praktyce.

Z zagadnieniem rozpraszania fal elektromagnetycznych jest blisko związany problem tzw. rezonansów własnych obiektów. Metodom poszukiwania częstotliwości rezonansowych obiektów dielektrycznych, obliczania tzw. dobroci własnej oraz stowarzyszonych rozkładów przestrzennych pola elektromagnetycznego poświęcono w pracy stosunkowo dużo miejsca.

Główny dorobek autora stanowią metody analizy obiektów charakteryzujących się symetrią obrotową (ang. *BOR – Bodies-of-Revolution*). Wyprowadzono nowe klasy tzw. objętościowych równań całkowych, opisujących zagadnienie rozpraszania fal elektromagnetycznych. Przedstawiono także skuteczne metody numerycznego, przybliżonego rozwiązywania tych równań dla dwóch, ważnych z praktycznego punktu

widzenia, środowisk: tzw. swobodnej przestrzeni oraz ośrodków warstwowych o poziomej stratyfikacji.

2. Równania całkowe

W zagadnieniach elektromagnetyzmu dotyczących brył dielektrycznych, formułowanych za pomocą równań całkowych, wyróżnia się dwie podstawowe klasy: przypadek brył dielektrycznych jednorodnych (ewentualnie – partiami jednorodnych), w których model matematyczny konstruuje się na podstawie tzw. *powierzchniowego* równania całkowego, oraz przypadek ciał silnie niejednorodnych o przenikalności dielektrycznej zależnej od współrzędnych punktu wewnątrz bryły, dla których stosuje się opis wykorzystujący *objętościowe* równanie całkowe. Obydwa modele konstruuje się, wykorzystując *zasady równoważności*, które, w najbardziej ogólnej postaci, stwierdzają, że różne konfiguracje źródeł mogą w określonym obszarze generować ten sam przestrzenny rozkład pola elektrycznego i magnetycznego.

W przypadku brył jednorodnych sytuację oryginalną zastępuje się dwiema sytuacjami równoważnymi, konstruowanymi z myślą o obliczaniu pola elektromagnetycznego *wewnątrz* lub *na zewnątrz* analizowanej bryły. W obszarze dopełniającym postuluje się rozkłady pola wygodne do prowadzenia obliczeń. Zwróćmy uwagę, że przy takim podejściu w ogólności wprowadzamy *nieciągłość* składowych stycznych pola elektrycznego i magnetycznego na powierzchni bryły. Spełnienie warunków brzegowych wymaga wtedy wprowadzenia *fikcyjnych* prądów elektrycznego i magnetycznego. Fikcyjne (zastępcze) prądy określają rozkład pola elektromagnetycznego w interesującym nas obszarze, zagadnienie rozpraszania fal elektromagnetycznych sprowadza się zatem do znalezienia rozkładu tych zastępczych powierzchniowych źródeł pola.

Dla brył niejednorodnych wygodnie jest zastąpić ciało dielektryczne zastępczym *objętościowym* rozkładem prądu, promieniującym w środowisku, z którego obiekt niejednorodny został usunięty. W przypadku brył czysto dielektrycznych, czyli takich, w których przenikalność magnetyczna nie różni się od przenikalności środowiska, wystarczy posługiwać się *zastępczym prądem elektrycznym* zdefiniowanym zależnością

$$\boldsymbol{J}(\boldsymbol{r}) = j\omega(\varepsilon(\boldsymbol{r}) - \varepsilon_0)\boldsymbol{E}(\boldsymbol{r}), \tag{1}$$

gdzie $\boldsymbol{r}$ jest wektorem wskazującym punkt wewnątrz bryły, $\varepsilon(\boldsymbol{r})$ oznacza zależną od położenia przenikalność ciała dielektrycznego, ε_0 oznacza przenikalność dielektryczną ośrodka, a $\boldsymbol{E}(\boldsymbol{r})$ jest wektorem pola elektrycznego w punkcie $\boldsymbol{r}$.

Zastępczy prąd (1) jest w całej przestrzeni źródłem „rozproszonego" pola elektrycznego $\boldsymbol{E}^s$, co przy zadanym polu „padającym" $\boldsymbol{E}^i$ pozwala skonstruować równanie całkowe

$$\boldsymbol{E}\big|_V = \left(\boldsymbol{E}^i + \boldsymbol{E}^s(\boldsymbol{J})\right)\Big|_V, \tag{2}$$

gdzie symbol $|_V$ oznacza, że dziedziną działania operatorów są punkty leżące wewnątrz objętości bryły.

Równanie (2) stanowi podstawę konstrukcji szeregu specjalizowanych równań całkowych wyprowadzonych przez autora, dlatego zostało *explicite* podane w niniejszym streszczeniu.

Interesującą alternatywą jest zastosowanie w zagadnieniach, w których niejednorodna bryła dielektryczna została zanurzona w nietrywialnym środowisku, równania objętościowo-powierzchniowego. W podejściu takim pola na zewnątrz bryły są obliczane z użyciem całek powierzchniowych i właściwych dla danego środowiska funkcji Greena, podczas gdy kłopotliwe z punktu widzenia efektywności obliczeń całki objętościowe są obliczane tylko dla środowiska jednorodnego.

3. Obliczanie pól elektromagnetycznych dla zadanego rozkładu źródeł

Streszczone w poprzednim punkcie zasady konstruowania równań całkowych wymagają umiejętności obliczania pola elektrycznego i magnetycznego w dowolnym punkcie przestrzeni dla zadanego układu źródeł pola (prądów i ładunków). Takie obliczenia prowadzi się zwykle, wykorzystując pojęcie tzw. *funkcji Greena*. Wyrażają one związek pożądanej wielkości (np. pola elektrycznego lub magnetycznego) z elementarnym źródłem pola (np. dipolem elektrycznym, magnetycznym, ładunkiem, itp.). Jeśli dla danego środowiska są znane odpowiednie funkcje Greena, to pola w punkcie obserwacji oblicza się, wykorzystując zasadę superpozycji, sumując (całkując) pola pochodzące od źródeł elementarnych. Przykładowo pole elektryczne od zadanego rozkładu prądu elektrycznego znajdujemy z zależności

$$\boldsymbol{E} = \left\langle \underline{\underline{\boldsymbol{G}}}^{EJ}; \boldsymbol{J} \right\rangle, \tag{3}$$

gdzie symbol $\langle , \rangle$ oznacza całkę iloczynu dwóch funkcji oddzielonych przecinkiem we wspólnej dziedzinie przestrzennej, podczas gdy kropka nad przecinkiem oznacza iloczyn skalarny. Notacji $\underline{\underline{\boldsymbol{G}}}^{PQ}$ użyto dla oznaczenia diadowej funkcji Greena wiążą-

cej wielkość polową typu P (tutaj: pole elektryczne) w punkcie obserwacji z prądem typu Q (tu: elektrycznym) w punkcie źródłowym. Odpowiednie funkcje Greena dla swobodnej przestrzeni i ośrodków warstwowych zostały szczegółowo omówione.

Aby otrzymać przybliżone rozwiązanie zagadnień elektromagnetyzmu metodą momentów, należy obliczyć pola elektromagnetyczne dla punktów obserwacji położonych w obszarach źródłowych. Funkcje Greena charakteryzują się wtedy osobliwościami różnych rzędów, a obliczanie całek w rodzaju (3) wymaga specjalnych kroków. Jedną z możliwości jest wyodrębnienie z procesu całkowania bezpośredniego sąsiedztwa punktu osobliwego i obliczanie pozostałej całki w sensie *wartości głównej* Cauchy'ego. Metoda alternatywna, preferowana w pracy, polega na zredukowaniu osobliwości jąder całkowania przez zapisanie równań polowych z wykorzystaniem *potencjałów mieszanych*. Przykładowo zamiast równania (3) możemy zapisać

$$\boldsymbol{E} = -j\omega\boldsymbol{A} - \nabla\Phi = -j\omega\left\langle \underline{\underline{\boldsymbol{G}}}^{A}; \boldsymbol{J}\right\rangle - \nabla\left\langle G^{\Phi}; \nabla'\cdot\boldsymbol{J}\right\rangle, \tag{4}$$

gdzie $\boldsymbol{A}$ i Φ oznaczają odpowiednio potencjał wektorowy i skalarny, a symbol „prim" przy operatorze *nabla* wskazuje, że różniczkowanie odbywa się względem współrzędnych punktu źródłowego. Można wykazać, że funkcje podcałkowe w (4) charakteryzują się osobliwościami *całkowalnymi.*

Równanie dwupotencjałowe (4) charakteryzuje się ponadto następującymi właściwościami:

a) występuje w nim operator różniczkowania (gradient) na zewnątrz drugiej z całek, operator ten można jednak zneutralizować podczas algebraizacji równania całkowego, przenosząc jego działanie na tzw. funkcje wagowe (testowe);

b) drugi operator różniczkowania oddziałuje na rozkład prądu – wynika stąd, że funkcje użyte do aproksymacji rozkładu prądu (tzw. funkcje bazowe) powinny być różniczkowalne.

Zwróćmy uwagę, że znalezienie funkcji Greena dla potencjału wektorowego i skalarnego dla nietrywialnych środowisk nie jest zadaniem prostym. W monografii pokazano sposób konstruowania (jednego z wielu możliwych) równania dwupotencjałowego dla ośrodka warstwowego o dowolnej stratyfikacji. Omówiono także szczegółowe aspekty zastosowania równań takiego typu w modelach wykorzystujących prądy powierzchniowe i objętościowe.

4. Bryły o symetrii obrotowej

W wielu sytuacjach praktycznych liczba współczynników aproksymacji poszukiwanych podczas rozwiązywania równań całkowych stanowi poważne ograniczenie efektywności modeli numerycznych. Liczba ta może być znacznie zmniejszona, jeżeli

interesujący nas problem (w przypadku zagadnień poruszanych w monografii – bryła dielektryczna) charakteryzuje się pewnymi rodzajami symetrii. Jednym z takich rodzajów jest symetria obrotowa – ciała charakteryzujące się taką symetrią w literaturze anglojęzycznej określa się terminem *Bodies-of-Revolution*.

Równania dotyczące brył obrotowych wygodnie jest zapisywać w biegunowym układzie współrzędnych (ρ, z, ϕ), którego oś pokrywa się z osią symetrii bryły. Ponieważ parametry bryły nie zależą od współrzędnej azymutalnej ϕ, więc można rozłożyć wszystkie zmienne (prądy, ładunki, potencjały, natężenia pól) w szereg Fouriera względem ϕ. Jądra równań rozkładają się z kolei w szereg Fouriera względem różnicy współrzędnych azymutalnych punktu obserwacji i punktu źródłowego $\phi - \phi'$. Można dowieść, że jeżeli także pobudzenie (pole padające) daje się rozłożyć w szereg Fouriera, to równania całkowe dla poszczególnych *rodzajów* azymutalnych pola (odpowiadających poszczególnym składnikom w wykładniczym szeregu Fouriera) rozdzielają się, np. w miejsce równania (2) otrzymujemy szereg równań postaci

$$\boldsymbol{E}_m(\rho, z) = \boldsymbol{E}_m^i(\rho, z) + \boldsymbol{E}_m^s(\rho, z), \tag{5}$$

gdzie indeks m oznacza numer rodzaju.

Zwróćmy uwagę, że w równaniu (5) został zredukowany rząd problemu, gdyż w miejsce trzech współrzędnych przestrzennych (ρ, z, ϕ) posługujemy się wyłącznie współrzędnymi (ρ, z). W praktyce oznacza to, że w sformułowaniu problemu całki objętościowe redukują się do całek powierzchniowych, a całki powierzchniowe – do liniowych. Uważny czytelnik zwróci uwagę, że kosztem, jaki płacimy za tę redukcję, jest teoretycznie konieczność rozwiązywania nieskończonej liczby równań (5). Można jednak udowodnić, że w rzeczywistości rodzaje pola o odpowiednio dużych wartościach indeksu m wnoszą do wypadkowego rozwiązania pomijalnie mały wkład i w praktyce nie muszą być uwzględniane.

Jądra równań typu równania (5) mają zwykle dużo bardziej skomplikowaną postać niż ich „trójwymiarowe" odpowiedniki (obecne np. w równaniu (4)), np. dla przypadku środowiska warstwowego jądro stowarzyszone z potencjałem wektorowym ma postać

$$\underline{\underline{K}}_m^A = \begin{bmatrix} \dfrac{L_{tt}^{m-1} + L_{tt}^{m+1}}{2} & -\dfrac{L_{tz}^{m} + L_{tz}^{-m}}{2} & \dfrac{L_{tt}^{m-1} + L_{tt}^{m+1}}{2j} \\ -\dfrac{L_{zt}^{m-1} + L_{zt}^{-(m+1)}}{2} & L_{zz}^{m} & -\dfrac{L_{zt}^{m-1} - L_{zt}^{-(m+1)}}{2j} \\ \dfrac{L_{tt}^{m+1} + L_{tt}^{m-1}}{2j} & -\dfrac{L_{tz}^{m} - L_{tz}^{-m}}{2j} & \dfrac{L_{tt}^{m-1} + L_{tt}^{m+1}}{2} \end{bmatrix}, \tag{6}$$

gdzie

$$L_{tt}^{m} = \Im_{m0}\left\{V_i^h\right\}, \qquad L_{zz}^{m} = \frac{\mu_n}{\varepsilon_j}\Im_{m0}\left\{I_v^e + \frac{k_j^2}{k_\rho^2}\left(I_v^h - \frac{k_{zn}^2}{k_n^2} I_v^e\right)\right\},$$

$$L_{zt}^{m} = j\omega\mu_j \Im_{m1}\left\{\frac{I_i^h - I_i^e}{k_\rho^2}\right\}, \qquad L_{tz}^{m} = j\omega\mu_n \Im_{m1}\left\{\frac{V_v^h - V_v^e}{k_\rho^2}\right\}, \tag{7}$$

a jądro potencjału skalarnego wyraża się wzorem

$$K_m^{\phi} = \Im_{m0}\left\{\frac{V_i^h - V_i^e}{k_\rho^2}\right\}. \tag{8}$$

W powyższych formułach zakładamy, że współrzędna z jest w warstwie j, a z' – w warstwie n. $V_i^p, V_v^p, I_i^p, V_v^p$, gdzie $p = e$ lub h oznaczają odpowiednie *funkcje Greena zastępczych linii transmisyjnych*, ε i μ oznaczają odpowiednio przenikalność dielektryczną i magnetyczną, $k_{zn} = \sqrt{k_n^2 - k_\rho^2}$, gdzie k_n jest stałą propagacji warstwy n. Operator $\Im$ oznacza modalną całkę Sommerfelda

$$\Im_{mv}\{\cdot\} = \frac{1}{2\pi}\int_0^{\infty} dk_\rho k_\rho^{v+1} J_{m+v}\left(k_\rho \rho\right) J_m\left(k_\rho \rho'\right)\{\cdot\}, \tag{9}$$

a J_m jest funkcją Bessela rzędu m.

Równanie (5) odznacza się ciekawymi właściwościami dla przypadku $m = 0$. Równania charakteryzujące różne składowe pola ulegają wtedy dalszemu rozdzieleniu, co umożliwia wyodrębnienie i analizę pewnych charakterystycznych rodzajów pola.

5. Rozwiązywanie równań całkowych – metoda momentów

Znanym i typowym sposobem rozwiązywania równań całkowych jest ich algebraizacja, czyli sprowadzenie do rozwiązania układu równań liniowych za pomocą tzw. metody momentów. W metodzie tej definiuje się na wstępie dwa zestawy funkcji

pomocniczych. Tak zwane funkcje bazowe są podstawą skutecznej aproksymacji poszukiwanej wielkości (rozkładu prądu, pola), natomiast funkcji testowych (wagowych) używa się wraz z odpowiednio zdefiniowanym iloczynem skalarnym do algebraizacji równań. Szczególnym rodzajem metody momentów jest tzw. schemat Galerkina, w którym zbiory funkcji bazowych i wagowych są identyczne. Wariant ten szczególnie dobrze nadaje się do równań konstruowanych na podstawie metody potencjałów mieszanych, pozwala bowiem wyeliminować obliczanie gradientu potencjału skalarnego w równaniach typu (4).

W pracy omówiono szereg znanych w literaturze funkcji bazowych (wagowych), przydatnych zarówno w równaniach typu powierzchniowego, jak i objętościowego. Dodatkowo autor zaproponował nową klasę funkcji bazowych przydatną w rozwiązywaniu równań objętościowych dotyczących brył obrotowych (równanie (5)). Funkcje te zostały skonstruowane z myślą o aproksymacji indukcji elektrycznej $\boldsymbol{D}$. Dzięki „wbudowaniu" w definicje funkcji prawa Gaussa uzyskano znaczną redukcję (rzędu 2/3) liczby niewiadomych współczynników aproksymacji poszukiwanych w procesie rozwiązywania równań.

W wyniku zastosowania metody momentów rozwiązanie równania całkowego (np. (5)) sprowadza się do rozwiązania równania macierzowego

$$\boldsymbol{S}\left|\boldsymbol{D}\right\rangle = \left|\boldsymbol{E}^{i}\right\rangle, \tag{10}$$

gdzie $\boldsymbol{S}$ jest macierzą momentów, $\boldsymbol{D}$ jest wektorem nieznanych współczynników charakteryzujących poszukiwaną wielkość (tu: indukcję elektryczną), a $\boldsymbol{E}^{i}$ oznacza wektor pobudzenia zależny od pola padającego. Zwróćmy uwagę, że równanie (10) można w prosty sposób wykorzystać do poszukiwania tzw. rezonansów własnych struktury. Zjawiska takie definiuje się jako potencjalną możliwość istnienia w obiekcie niezerowych pól elektromagnetycznych, gdy brak pobudzenia. W zapisie równania (10) oznacza to możliwość niezerowych rozwiązań przy założeniu, że prawa strona (10) (wektor pobudzenia) jest zerowa. Sytuacja taka zachodzi, gdy

$$\det(\boldsymbol{S}) = 0. \tag{11}$$

Pierwiastków równania (11) poszukujemy na płaszczyźnie częstotliwości zespolonych. Oznacza to, że w równaniach każde $(j\omega)$ zastępujemy zmienną zespoloną s. Gdy znajdziemy zarówno część rzeczywistą jak i urojoną pierwiastka, otrzymujemy informację o częstotliwości rezonansowej oraz stowarzyszonej dobroci własnej struktury. Jeśli położenie pierwiastka na płaszczyźnie zespolonej jest określone z wystarczającą dokładnością, to równanie (11) może posłużyć do określenia, z dokładnością do stałej, rozkładu pola związanego z danym rezonansem.

Widzimy więc, że między zagadnieniem rozpraszania fal elektromagnetycznych a poszukiwaniem rezonansów własnych obiektów istnieje ścisły związek.

6. Pola padające

W zagadnieniach rozpraszania fal elektromagnetycznych typowym rozważanym pobudzeniem jest fala płaska o określonym kierunku propagacji i określonej polaryzacji. O ile matematyczny zapis pola elektrycznego i magnetycznego fali płaskiej dla przypadku swobodnej przestrzeni nie nastręcza trudności, o tyle sytuacja zmienia się, gdy rozważamy przypadek środowiska warstwowego. W pracy opisano metodę określania pól wzbudzanych w ośrodku warstwowym pod wpływem fali płaskiej padającej z górnej półprzestrzeni (założono dla uproszczenia, że obszar ten jest wypełniony powietrzem).

Pokazano, że dzięki odpowiedniemu rozdzieleniu zmiennych problem poszukiwania pól wzbudzonych w dowolnym punkcie środowiska warstwowego może być sprowadzony do problemu poszukiwania napięć i prądów w równoważnych liniach transmisyjnych pobudzanych napięciem zależnym od pola padającego.

W zagadnieniach dotyczących brył obrotowych interesuje nas rozkład pola padającego na poszczególne rodzaje azymutalne. W monografii zaproponowano prostą i elegancką metodę uzyskania takiego rozkładu dla fali płaskiej zarówno w swobodnej przestrzeni (rozkład taki jest opisany w literaturze), jak i w środowisku warstwowym (tu rozkład taki zaprezentowano po raz pierwszy).

7. Pole dalekie

W wielu sytuacjach praktycznych interesuje nas rozproszone (wtórne) pole elektromagnetyczne określane w dużej odległości od analizowanego obiektu. Obliczenia takiego pola (tzw. pola dalekiego) są zwykle dużo prostsze niż obliczenia pola w strefie bliskiej dzięki możliwości skorzystania z pewnych znanych *a priori* właściwości. Rozpatrzmy przypadek określenia pola elektrycznego wytwarzanego przez znany rozkład prądów elektrycznych. Okazuje się, że aby określić natężenie pola, wystarczy znaleźć w odległym punkcie dwie składowe potencjału wektorowego prostopadłe do kierunku wyznaczonego przez wektor łączący punkt wewnątrz analizowanego obiektu z punktem obserwacji. W strefie dalekiej składowa radialna pola zanika, co wynika ze znoszenia się składowej radialnej pochodzącej od potencjału wektorowego i składowej pola związanej z potencjałem skalarnym. Tak więc dla swobodnej przestrzeni możemy zapisać, że w strefie dalekiej

$$\boldsymbol{E}(\boldsymbol{r}) = j\omega\hat{\boldsymbol{r}} \times (\hat{\boldsymbol{r}} \times \boldsymbol{A}(\boldsymbol{r})). \tag{12}$$

Pole magnetyczne możemy obliczyć, korzystając ze znanej zależności

$$\boldsymbol{H}(\boldsymbol{r}) = \frac{1}{\eta_0} \hat{\boldsymbol{r}} \times \boldsymbol{E}(\boldsymbol{r}), \tag{13}$$

gdzie $\eta_0 = \sqrt{\mu_0 / \varepsilon_0}$ jest impedancją swobodnej przestrzeni, a $\hat{\boldsymbol{r}}$ oznacza wektor jednostkowy skierowany od punktu źródłowego do punktu obserwacji.

W przypadku środowiska warstwowego sposób obliczania pola dalekiego zależy od kierunku propagacji fali względem środowiska. W zagadnieniach antenowych rozważa się przypadek środowiska nieograniczonego od góry, tzn. takiego, gdzie górna warstwa jest jednorodną półprzestrzenią (zwykle wypełnioną powietrzem). W monografii podano przybliżone wzory opisujące pola w strefie dalekiej, zakładając, że nie interesuje nas propagacja wzdłuż granicy warstw (pozioma). W tym ostatnim przypadku propagacja jest zdominowana przez tzw. fale powierzchniowe i wymaga osobnego rozważenia – zagadnienie to opisano w literaturze.

W przypadku brył dielektrycznych należy znać formuły opisujące pole dalekie od poszczególnych rodzajów azymutalnych. W pracy podano odpowiednie wzory zarówno dla przypadku swobodnej przestrzeni, jak i środowiska warstwowego. Wzory dla tego ostatniego przypadku nie były dotąd, według wiedzy autora, publikowane w ogólnie dostępnej literaturze światowej.

Z zagadnieniem rozpraszania fali płaskiej wiąże się użyteczna miara rozproszenia, jaką jest tzw. *przekrój radarowy* definiowany jako

$$\sigma(\hat{\boldsymbol{r}}, \hat{\boldsymbol{k}}) = \lim_{r \to \infty} 4\pi r^2 \frac{|\boldsymbol{E}(\boldsymbol{r})|^2}{|\boldsymbol{E}^{\text{inc}}|^2}, \tag{14}$$

gdzie jednostkowy wektor $\hat{\boldsymbol{k}}$ określa kierunek propagacji płaskiej fali padającej, charakteryzującej się natężeniem pola elektrycznego $\boldsymbol{E}^{\text{inc}}$, a jednostkowy wektor $\hat{\boldsymbol{r}}$ definiuje kierunek obserwacji. Zwróćmy uwagę, że w świetle definicji (14) pole elektryczne określamy w strefie dalekiej.

8. Przykłady obliczeniowe

W monografii zaprezentowano szereg przykładów, na podstawie których zweryfikowano poprawność teorii przedstawionej wcześniej. Wyniki obliczeń porównano z danymi doświadczalnymi i obliczeniowymi dostępnymi w literaturze. W niektórych przypadkach, gdy w dostępnych źródłach nie znaleziono odpowiednich przykładów, wyniki obliczeń metodą własną autor porównał z wynikami obliczeń uzyskanych z użyciem komercyjnego pakietu oprogramowania CONCEPT II opracowanego na politechnice w Hamburgu.

Przykłady obejmują następujące zagadnienia:

1. Obliczenia rozkładów pola wewnątrz jednorodnych i niejednorodnych brył dielektrycznych oświetlonych falą płaską.
2. Obliczenia przekrojów radarowych brył dielektrycznych.
3. Określenie częstotliwości rezonansowych, stowarzyszonych współczynników dobroci własnej oraz rozkładów pola elektromagnetycznego cylindrycznych rezonatorów dielektrycznych.

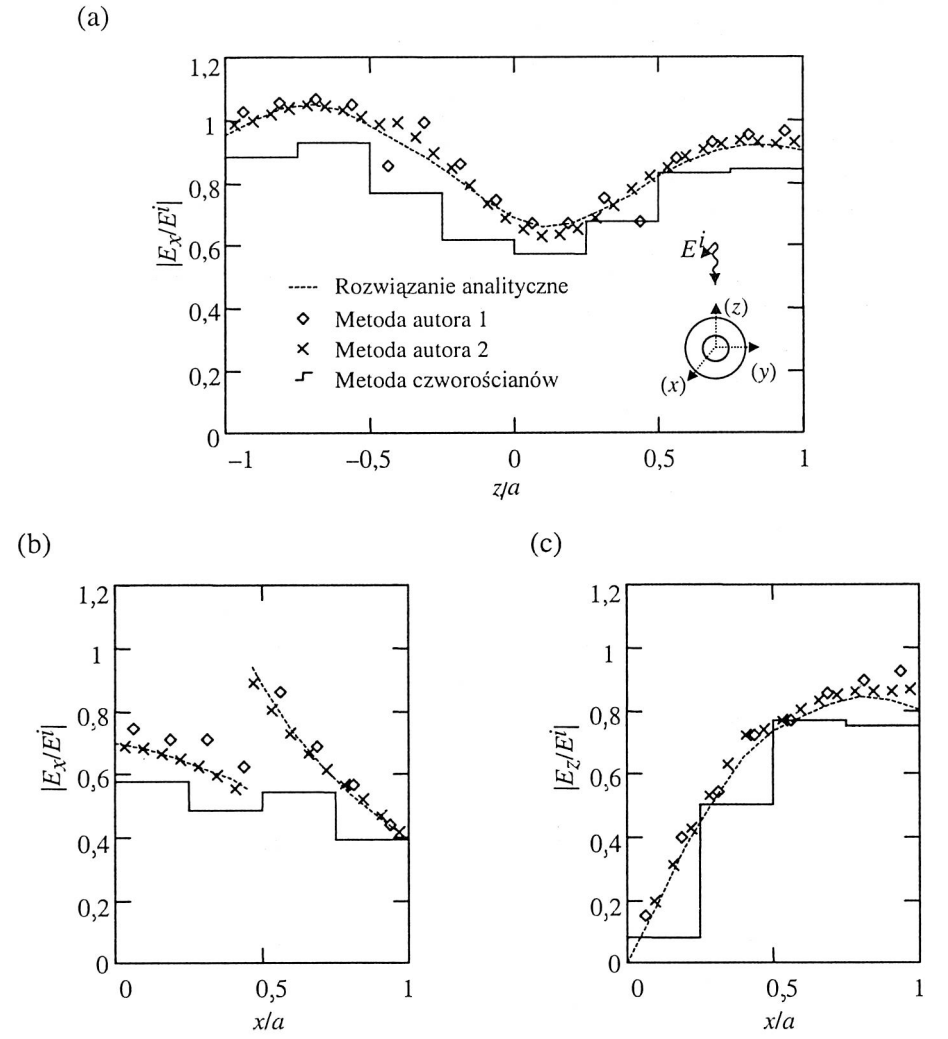

Rys. 1. Pole elektryczne wewnątrz niejednorodnej sfery: $\varepsilon_{r1} = 36$, $k_0 a_1 = 0{,}3738$, $\varepsilon_{r2} = 9$, $k_0 a_2 = 0{,}8168$. (a) Względna wartość E_x wzdłuż osi z. (b) Względna wartość E_x wzdłuż osi x. (c) Względna wartość E_z wzdłuż osi x. ([105], ©2000 IEEE)

Obliczenia prowadzono dla brył umieszczonych w swobodnej przestrzeni oraz w przykładowych środowiskach warstwowych. Dla tych ostatnich podano też szczegółową metodę obliczania całek Sommerfelda (por. wzór (9)) z wykorzystaniem tzw. metody dyskretnych obrazów zespolonych (ang. *DCIM – Discrete Complex Images Method*).

Jako przykłady poglądowe przytoczmy tu wyniki obliczeń pola elektrycznego wewnątrz niejednorodnej kuli oświetlonej falą płaską (rys. 1), obliczone częstotliwości rezonansowe i współczynniki dobroci własnej odosobnionego rezonatora dielektrycznego (tabele 1 i 2) oraz przekrój radarowy rezonatora dielektrycznego umieszczonego na ekranowanej od spodu warstwie dielektrycznej (rys. 2).

Te oraz szereg innych przykładów podanych w pracy wskazują na znakomitą wręcz zgodność wyników uzyskiwanych metodami rozwiniętymi przez autora z wynikami pomiarów i wynikami obliczeń autorów innych prac.

Tabela 1. Porównanie obliczonych i zmierzonych częstotliwości rezonansowych rezonatora o promieniu $a = 5{,}25$ mm, wysokości $h = 4{,}6$ mm i $\varepsilon_r = 38$. ([104], ©2000 IEEE)

Rodzaj pola	Częstotliwość [GHz]			
	Obliczona – metoda autora	Obliczona MoM [84]	Zmierzona [44]	Obliczona T-matrix [225]
TE_{01}	**4,861**	4,829	4,85	4,9604
TM_{01}	**7,594**	7,524	7,60	7,5384
HEM_{11}	**6,373**	6,333	–	6,3450
HEM_{12}	**6,657**	6,638	6,64	6,6520
HEM_{21}	**7,784**	7,752	7,81	7,7621

Tabela 2. Porównanie obliczonych i zmierzonych współczynników dobroci rezonatora o promieniu $a = 5{,}25$ mm, wysokości $h = 4{,}6$ mm i $\varepsilon_r = 38$. ([104], ©2000 IEEE)

Rodzaj pola	Q			
	Obliczona – metoda autora	Obliczona MoM [84]	Zmierzona [44]	Obliczona T-matrix [225]
TE_{01}	**40,7**	45,8	51	40,819
TM_{01}	**73,7**	76,8	86	76,921
HEM_{11}	**30,4**	30,7	–	30,853
HEM_{12}	**49,5**	52,1	64	50,316
HEM_{21}	**329,8**	327,1	204	337,66

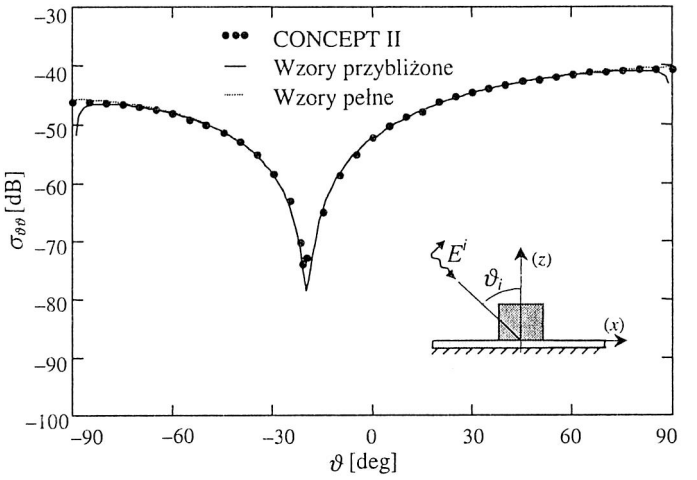

Rys. 2. Przekrój radarowy jednorodnego rezonatora dielektrycznego umieszczonego na uziemionym podłożu dielektrycznym: $\varepsilon_r = 36$, $a = 7$ mm, $h = 5$ mm, $d = 0{,}795$, $\varepsilon_{rs} = 2{,}35$, $k_0 a = 0{,}44$. Kąt padania $\vartheta_i = 45°$

Rozdział poświęcony obliczeniom uzupełniono dwoma przykładami wskazującymi na możliwość zastosowania opracowanych metod w zagadnieniach innych niż technika antenowa. W uproszczonym modelu głowy ludzkiej obliczono rozkład pola elektrycznego wytwarzanego pod wpływem płaskiej fali padającej z boku. Omówiono też zagadnienie rozpraszania fali elektromagnetycznej przez krople deszczu, co jest istotne w projektowaniu mikrofalowych łączy radiowych.

9. Podsumowanie

Celem niniejszej pracy było opracowanie wiarygodnych metod analizy rozpraszania fal elektromagnetycznych przez obiekty dielektryczne umieszczone w różnych środowiskach. Omówiono różne formy zasad równoważności przydatne w analizie ciał jednorodnych, partiami jednorodnych oraz niejednorodnych. Pokazano, że w połączeniu z ideą funkcji Greena metoda równań całkowych nadaje się do analizy wielu zagadnień elektromagnetyzmu, czego reprezentatywnymi przykładami są zagadnienia rozpraszania fal w tzw. swobodnej przestrzeni oraz w ośrodkach warstwowych. Specjalną uwagę poświęcono metodom wykorzystującym równanie skonstruowane na bazie tzw. potencjałów mieszanych.

Metody numeryczne omówione w pracy wymagają zwykle znacznej mocy obliczeniowej i/lub pamięci wykorzystywanych komputerów. Dlatego też pożądana jest

każda możliwa redukcja złożoności zagadnienia. Ważnym przykładem możliwości takiej redukcji są zagadnienia dotyczące brył o symetrii obrotowej. Poświęcono im w pracy szczególnie dużo uwagi.

Za swe główne osiągnięcia autor uważa:

- systematyczne przedstawienie różnych form zasady równoważności;
- zaproponowanie nowego objętościowo-powierzchniowego równania całkowego;
- ujednolicone przedstawienie zagadnień związanych z osobliwościami w równaniach całkowych;
- sformułowanie nowego równania całkowego opisującego zagadnienie rozpraszania fal elektromagnetycznych przez niejednorodne bryły dielektryczne o symetrii obrotowej;
- wprowadzenie nowej klasy bezdywergencyjnych funkcji bazowych przydatnych w aproksymacji indukcji elektrycznej – funkcje te umożliwiają znaczną redukcję liczby współczynników charakteryzujących problem;
- sformułowanie specjalizowanych form ogólnego równania całkowego przydatnych w opisie rodzajów azymutalnych w bryłach obrotowych;
- uogólnienie omówionych wyżej aspektów dla przypadku środowisk warstwowych;
- wyprowadzenie formuł opisujących rozkład płaskiej fali padającej na rodzaje azymutalne w środowisku warstwowym;
- wyprowadzenie wzorów definiujących tzw. pole dalekie dla poszczególnych rodzajów azymutalnych w środowisku warstwowym.

Wszystkie nowe wzory zaprezentowane w monografii zostały starannie zweryfikowane. Autor opracował własne programy komputerowe, a uzyskane wyniki porównał z danymi pomiarowymi i obliczeniowymi dostępnymi w literaturze, a także z wynikami otrzymanymi z użyciem oprogramowania komercyjnego.

Oprócz problemów kanonicznych, przydatnych do weryfikacji metod obliczeniowych, podano też wyniki o znaczeniu praktycznym. Przedstawione metody umożliwiają szczególnie łatwą identyfikację zjawisk rezonansowych w bryłach dielektrycznych o symetrii obrotowej. Wykorzystanie tej właściwości pozwoliło zaproponować nowe typy rezonatorów dielektrycznych o zwiększonej częstotliwościowej separacji rodzajów. Po raz pierwszy zaprezentowano także wyniki obliczeń przekrojów radarowych dielektrycznych anten rezonatorowych umieszczonych na uziemionym podłożu dielektrycznym.

Należy zauważyć, że choć zaprezentowane przykłady dotyczą głównie anten dielektrycznych, to opracowane metody są w pełni ogólne. Można je zastosować w wielu innych dziedzinach, jak np. propagacja fal radiowych przez kolumny deszczowe, interakcje pola elektromagnetycznego z ciałem człowieka, wykrywanie obiektów znajdujących się pod powierzchnią ziemi i prawdopodobnie w wielu innych.

Według autora dalsze badania w tej dziedzinie powinny dotyczyć:

- opracowania efektywnych algorytmów obliczania całek Sommerfelda dla różnych konfiguracji środowiska i umieszczenia w nim analizowanych obiektów;
- rozwinięcia koncepcji równań objętościowo-powierzchniowych;
- rozwinięcia koncepcji hybrydowych, łączących metodę równań całkowych z metodami siatkowymi;
- opracowania algorytmów pozwalających efektywnie analizować obiekty, których *fragmenty* są bryłami o symetrii obrotowej;
- uogólnienia dla przypadku ośrodków warstwowych technik dotyczących brył o innych rodzajach symetrii, np. tzw. *dyskretnych brył obrotowych*;
- przystosowania omówionych technik do innych niż zaprezentowane zastosowań;
- zastosowania algorytmów obliczeniowych do innych środowisk przez wykorzystanie odpowiednich funkcji Greena.

PRACE NAUKOWE INSTYTUTU TELEKOMUNIKACJI I AKUSTYKI
(wydane w latach 1993–2001)

Nr 71, Monografie nr 36, K. M. Abramski, *Metody analizy, kontroli i synchronizacji częstotliwości promieniowania laserów gazowych*, Wrocław 1993
Nr 72, Monografie nr 37, T. W. Więckowski, *Badania odporności elektronicznych na impulsowe narażenia elektromagnetyczne*, Wrocław 1993
Nr 73, Monografie nr 38, A. Prałat, *Zastosowanie pól elektromagnetycznych wielkiej częstotliwości do badania niejednorodności ośrodka skalnego*, Wrocław 1993
Nr 74, Konferencje nr 23, *V Sympozjum Inżynierii i Reżyserii Dźwięku*, Wrocław 1993
Nr 75, Monografie nr 39, B. Rudno-Rudzińska, *Modelowanie emisji i propagacji dźwięku do celów prognozowania klimatu akustycznego środowiska zurbanizowanego*, Wrocław 1994
Nr 76, Monografie nr 40, K. Gałkowski, *State-space realizations of n-D systems*, Wrocław 1994
Nr 77, Monografie nr 41, R. Makowski, *Wybrane zagadnienia ślepego rozplatania sygnałów udarowych*, Wrocław 1994
Nr 78, Konferencje nr 24, *XLI Otwarte Seminarium z Akustyki, Wrocław–Szklarska Poręba, 13–16 września 1994*, Wrocław 1994
Nr 79, Konferencje nr 25, *XVIIth National Conference. Circuit Theory and Electronic Networks*, tom I i II, Wrocław 1994
Nr 80, Konferencje nr 26, *VIII Krajowe Sympozjum Nauk Radiowych*, Wrocław 1995
Nr 81, Monografie nr 42, H. Trzaska, *Pomiary pól elektromagnetycznych do celów ochrony pracy i ochrony środowiska*, Wrocław 1996

Wydawnictwa Politechniki Wrocławskiej
są do nabycia w następujących księgarniach:
„Politechnika"
Wybrzeże Wyspiańskiego 27, 50-370 Wrocław
budynek A-1 PWr., tel. (0 71) 320 25 34;
„Tech"
plac Grunwaldzki 13, 50-377 Wrocław
budynek D-1 PWr., tel. (0 71) 320 32 5
Prowadzimy sprzedaż wysyłkową

ISSN 0324-9328